Dissertation

submitted to the

Combined Faculties of the Natural Sciences and Mathematics

of the Ruperto-Carola-University of Heidelberg, Germany

for the degree of

Doctor of Natural Sciences

Put forward by

M.Sc. Dennis Weiser

Born in Ehringshausen, Hessen, Germany

Oral Examination: February 07, 2019

Inclusive J/ψ production at mid-rapidity in pp and Pb–Pb collisions with ALICE

Referees:

apl. Prof. Dr. Klaus Reygers

Prof. Dr. Norbert Herrmann

Messung der inklusiven Produktion von J/ψ-Mesonen bei mittlerer Rapidität in pp- und Pb–Pb-Kollisionen mit ALICE

Die Messung von J/ψ-Mesonen in Schwerionenkollisionen wird als eine der Schlüsselmessungen angesehen. Es wird erwartet, dass die Präsenz eines Quark-Gluon-Plasmas Einfluss auf die Produktion von J/ψ-Mesonen hat. Bei hohen Kollisionsenergien, wie sie am LHC erreicht werden, wurde vorhergesagt, dass ein signifikanter Teil der J/ψ-Mesonen durch die (Re)kombination von freien Charm- und Anticharm-Quarks im Medium oder an der Phasengrenze gebildet wird. Modelle sagen voraus, dass dieser Produktionsmechanismus vor allem bei sehr niedrigen Impulsen wichtig ist.
In der vorliegenden Arbeit wird die Produktion von J/ψ-Mesonen bei mittlerer Rapidität ($|y| < 0.9$) in pp- und Pb–Pb-Kollisionen bei einer Kollisionsenergie von $\sqrt{s_{\mathrm{NN}}} = 5.02$ TeV mit ALICE untersucht. Diese werden im e^+e^--Zerfallskanal bis hinunter zu verschwindendem Transversalimpuls ($p_{\mathrm{T}} = 0$) rekonstruiert. Dabei werden die Elektronen und Positronen mittels des spezifischen Energieverlustes $\mathrm{d}E/\mathrm{d}x$ in der TPC identifiziert. Das J/ψ-Spektrum und der nukleare Modifikationsfaktor R_{AA} in zentralen Pb–Pb-Kollisionen zeigen eine Übereinstimmung mit Modellen, die die (Re)kombination von Charm- und Anticharm-Quarks an der Phasengrenze implementieren. Die Messung der ersten beiden Momente des p_{T}-Spektrums als Funktion der Zentralität zeigt, dass dieser Mechanismus wichtiger wird für zentralere Kollisionen.

Inclusive J/ψ production at mid-rapidity in pp and Pb–Pb collisions with ALICE

The measurement of J/ψ production in heavy-ion collisions is seen as a key measurement in the hunt for the Quark-Gluon Plasma. At high collision energies as reached at the LHC it was predicted that a significant fraction of the J/ψ yield is formed by (re)combination of deconfined charm and anticharm quarks in the medium or at the phase boundary. This mechanism is expected to be most important at very low transverse momentum.
In this thesis the production of J/ψ mesons is studied at mid-rapidity ($|y| < 0.9$) in pp and Pb–Pb collisions at a collision energy of $\sqrt{s_{\mathrm{NN}}} = 5.02$ TeV with ALICE. The J/ψ mesons are reconstructed in the e^+e^- decay channel down to vanishing transverse momentum ($p_{\mathrm{T}} = 0$). The electrons and positrons are identified using the specific energy loss $\mathrm{d}E/\mathrm{d}x$ in the TPC. The J/ψ spectrum and the nuclear modification factor R_{AA} in most central collisions are consistent with models which include (re)combination as a dominant source of J/ψ production. The measurement of the first two moments of the p_{T} distribution as a function of centrality shows that this mechanism becomes more important for more central collisions.

Contributions to physics analyses with ALICE

The work that is presented in this thesis is part of two papers which are currently prepared for publication. Below, these two papers are listed together with the most important contributions made within the scope of this thesis.

Paper: "Inclusive J/ψ production in pp collisions at $\sqrt{s} = 5$ TeV", in preparation

- Study and calibration of the TPC dE/dx
- Investigation and proposal of fitting signal extraction method
- Determination of the J/ψ $\langle p_{\mathrm{T}} \rangle$ and $\langle p_{\mathrm{T}}^2 \rangle$ with two independent methods

Paper: "Centrality and transverse momentum dependence of inclusive J/ψ production in Pb–Pb collisions at $\sqrt{s_{\mathrm{NN}}} = 5.02$ TeV", in preparation

- Study and calibration of the TPC dE/dx and parameterization of electron selection rules
- Measurement of the J/ψ p_{T} spectra in three centrality intervals
- Determination of the J/ψ $\langle p_{\mathrm{T}} \rangle$ and $\langle p_{\mathrm{T}}^2 \rangle$ with two independent methods

Contributions to the upgrade and operation of the ALICE detector

- Upgrade of the ALICE TRD FeeServer software packages improving radiation robustness of the front-end electronics operation
- Continuous support of the operation of the ALICE TRD including software adaptations to changing conditions

Contents

1 The Quark-Gluon Plasma **1**
- 1.1 Phase diagram of Quantum Chromodynamics . . . 4
- 1.2 Relativistic heavy-ion collisions . . . 7
  - 1.2.1 Space-time evolution . . . 7
  - 1.2.2 Geometrical aspects . . . 10
- 1.3 Quark-Gluon Plasma signatures . . . 15
  - 1.3.1 Thermal description of particle production . . . 15
  - 1.3.2 Collective flow . . . 16
  - 1.3.3 Parton energy loss . . . 19

2 Charmonium **21**
- 2.1 The charmonium spectrum . . . 21
- 2.2 Production in pp collisions . . . 23
- 2.3 Production in p–A collisions . . . 24
- 2.4 Production in A–A collisions . . . 27
  - 2.4.1 Early ideas and J/ψ suppression . . . 27
  - 2.4.2 High energy frontier and J/ψ (re)generation . . . 29
- 2.5 Photoproduction . . . 35

3 A Large Ion Collider Experiment at the Large Hadron Collider **37**
- 3.1 The Large Hadron Collider . . . 37
- 3.2 A Large Ion Collider Experiment . . . 39
  - 3.2.1 Inner Tracking System . . . 40
  - 3.2.2 Time Projection Chamber . . . 41
  - 3.2.3 Transition Radiation Detector . . . 44
  - 3.2.4 Other detectors . . . 46
- 3.3 Data reconstruction . . . 46
- 3.4 Data processing and analysis framework . . . 48
- 3.5 Charmonium measurement with ALICE . . . 49

4 Measurement of J/ψ yields in Pb-Pb collisions **51**
- 4.1 Datasets . . . 51
- 4.2 Event selection . . . 52
- 4.3 Track selection . . . 54
- 4.4 Electron identification with the TPC . . . 56
  - 4.4.1 One dimensional studies . . . 57
  - 4.4.2 PID post calibration . . . 59

4.4.3 Hadron exclusion . . . 60
4.5 Signal extraction . . . 63
4.6 Acceptance and reconstruction efficiency correction . . . 69
4.7 Systematic uncertainties . . . 73
4.8 Presenting results in wide bins . . . 75
4.9 Proton-proton reference . . . 79

5 Measurement of the J/ψ $\langle p_{\mathrm{T}} \rangle$ and $\langle p_{\mathrm{T}}^2 \rangle$ in pp and Pb-Pb collisions 81
5.1 Datasets . . . 81
5.2 Event and track selection . . . 81
5.3 Description of the method . . . 83
5.4 Efficiency correction . . . 84
5.5 Signal extraction . . . 85
5.6 Statistical uncertainties . . . 91
5.7 Systematic uncertainties . . . 92
5.8 Extracting moments using measured spectra . . . 94

6 Results 99
6.1 Centrality dependence of the nuclear modification factor . . . 99
6.2 Transverse momentum dependence of J/ψ production . . . 101
6.2.1 Results from pp collisions . . . 101
6.2.2 Results from Pb–Pb collisions . . . 103
6.3 Mean transverse momentum and mean squared transverse momentum 108
6.3.1 Results from pp collisions . . . 108
6.3.2 Results from Pb-Pb collisions . . . 109

7 Summary and outlook 119

Appendix 123

A Result tables 125

B Selection of electrons from photon conversions 127

C TPC PID studies in pp collisions 129

D Supplemental figures for statistical uncertainties of $\langle p_{\mathrm{T}} \rangle$ and $\langle p_{\mathrm{T}}^2 \rangle$ 131

E The TRD FeeServer and control engine 135
E.1 Front-end electronics . . . 135
E.2 Detector Control System . . . 136
E.3 FeeServer and control engine . . . 138
E.4 Upgrade of the control engine . . . 141
E.5 Implications for TRD operation in LHC Run 3 . . . 143

F Lists **145**
F.1 List of Figures 145
F.2 List of Tables 151

Bibliography **153**

Acknowledgements **173**

Deposition **175**

1 The Quark-Gluon Plasma

The foundation for contemporary nuclear physics research was established in the beginning of the 20th century by Ernest Rutherford. Very importantly, he found that the atomic mass is concentrated in the center of the atom [1], the atomic nucleus. Later Rutherford could show that atomic nuclei contain multiple hydrogen nuclei, thus discovering the proton as constituent [2]. Since the strong nuclear force was not known at that time Rutherford erroneously assumed that all nuclei must consist of protons and electrons [3]. After the discovery of the neutron by Chadwick in 1932 [4] this hypothesis was discarded and it became common understanding that atomic nuclei are made of protons and neutrons. However, now a very crucial question arose: How can the atomic nucleus be held together if the constituents are either charge neutral or have positive charge? In 1935 Yukawa postulated a massive exchange particle which should be responsible for the short range attractive force in the atomic nucleus [5]. Indeed, in 1947 the Yukawa particle was found in cosmic rays by Powell [6] and was labeled π-meson. Subsequently many more particles were discovered, building a full "zoo" of particles. In 1961 Gell-Mann's "eightfold way" [7], which was independently proposed by Ne'eman [8], was a successful attempt to understand the variety of newly observed particles by ordering them into multiplets. In 1964 Gell-Mann and Zweig [9, 10] proposed that all baryons and mesons could be constructed from hypothetical fundamental particles with non-integer electric charge, called "quarks"[1]. In a series of deep inelastic scattering experiments of electrons on protons at SLAC between 1967 and 1973 [11–13] direct evidence for these point-like constituents of the proton was found. According to Bjorken [14] a scaling behavior of the structure functions in deep inelastic scattering should exist in the case of point-like constituents of the protons, which was indeed observed.

A turning point at this time was the discovery of the J/ψ meson by the groups of Ting [15] and Richter [16] in p + Be and e^+e^- collisions in 1974. It finally helped the quark model to obtain credibility since the presence of this new particle implied the presence of a new quark, the charm quark. This quark had already been predicted in 1970 by Glashow, Iliopoulos and Maiani [17] and the discovery helped the progress in the theory of weak interactions.

In the meantime the theory of strong interactions (Quantum Chromodynamics (QCD)) had been developed [18, 19]. Fritzsch and Gell-Mann introduced color as a conserved quantum number in strong interaction. This solved the mystery of the wave function of the Ω^- baryon which seemed to not obey the Pauli principle. When color was introduced the wave function became antisymmetric under exchange of two quarks, thus following the Pauli principle. With three colors also the measured

[1] Initially Zweig used the word "aces"

cross-section ratio of electron-positron annihilation into hadrons compared to the annihilation into muon pairs could be explained. Fritzsch and Gell-Mann introduced QCD as a gauge theory with the color group as gauge group in which the interactions between quarks is mediated by massless gauge bosons, called gluons.
Gross, Wilczek and Politzer [20, 21] found that non-abelian gauge theories like QCD are asymptotically free, i.e. the coupling strength decreases with increasing energy. This behavior is demonstrated in Fig. 1.1.

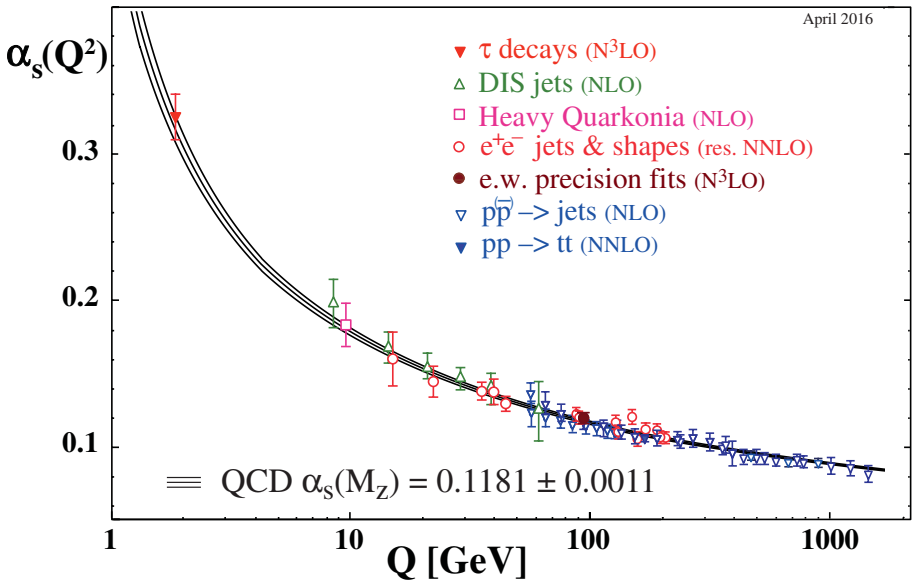

Figure 1.1: The strong coupling constant $\alpha_s(Q^2)$ as a function of the energy transfer Q, extracted from different measurements and compared to the QCD prediction. The order of QCD perturbation theory used for the extraction is given in brackets. The world average value of $\alpha_s(Q^2)$ at the mass of the Z^0 boson is given [22].

Shown are values of the strong coupling constant $\alpha_s(Q^2)$ as a function of the energy transfer Q as extracted from different processes. The measurements span the range between about 2 GeV and the TeV scale, being impressively consistent with the QCD prediction over the full range. The feature of asymptotic freedom allows for the perturbative treatment of QCD at high energy transfers. At low energy transfer the strong coupling gets larger and diverges at $\Lambda_{QCD} \approx 200$ MeV leading to a breakdown of perturbative treatments. This increase in the coupling strength is generally associated with the phenomenon of color confinement. The color carrying quarks and gluons can not be found freely, but only trapped inside colorless hadrons. Confinement is theoretically still far from understood and is connected to one of

the millenium problems of unsolved mathematical problems [23]. It is believed that color confinement is due to the self interaction of the gluons which is enabled by the non-commuting generators of the SU(3) symmetry group.
Confinement is closely related to the phenomenon of hadronization. When quark pairs are produced with high momentum in opposite directions they are moving against the color force which is binding them (see Fig. 1.2). Due to the specific shape of the QCD potential (discussed in Sec. 2.1) it is energetically favorable to create new light quark pairs out of the vacuum which happens in multiple stages. Finally, sprays of colorless hadrons, so-called jets, are observed.

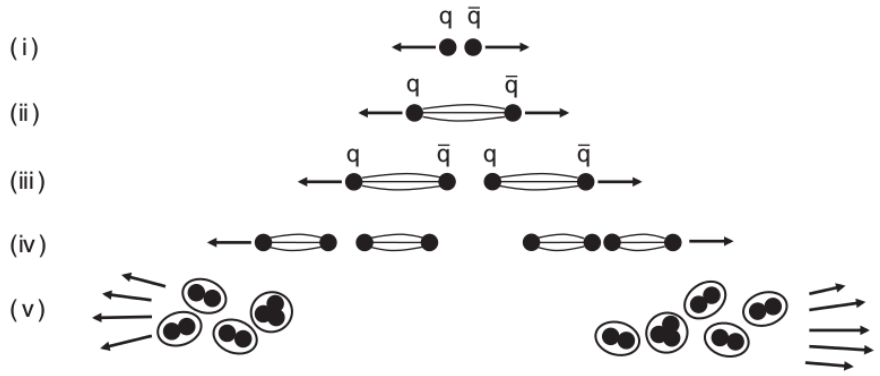

Figure 1.2: Qualitative picture of different stages of hadronization of a high momentum quark-antiquark pair [24].

While the process of hadronization is nowadays rather well modeled in event generators a precise understanding based on QCD is still lacking.
Together with the theory of electroweak interactions, pioneered in the 1960s [25–28], QCD builds the standard model of particle physics which describes the building blocks of matter and their interactions. The last big missing piece of the standard model, the Higgs boson, was discovered in 2012 by the ATLAS and CMS collaborations [29, 30].
Today, the research at colliders is focused on physics beyond the standard model and the understanding of different QCD phases and phase transitions. In the latter research field a great interest lies in the creation of a QCD many body system at high pressure and temperature where confinement is expected to be absent, the so-called Quark-Gluon Plasma (QGP).
In the next section the phase diagram of strongly interacting matter and the role of the QGP therein will be explained.

1.1 Phase diagram of Quantum Chromodynamics

It was realized early on that the hadronic world has to have a boundary at high temperature. Hagedorn described the exponentially growing number density of hadronic states with a statistical bootstrap model in 1965 [31]. He found that the partition function corresponding to this exponential mass spectrum diverges at $T = T_0 \approx 158$ MeV and concluded that this would be the highest possible temperature for strong interactions.
After the birth of QCD and the general acceptance of the quark model, ideas were put forward about a possible phase transition. Collins and Perry suggested that superdense matter as found in neutron star cores or the early universe consists of a quark soup with free quarks at sufficiently high densities [32]. Cabbibo and Parisi argued that exponentially growing hadronic state densities are not a sign of a limiting temperature as suggested by Hagedorn, but rather indicate the presence of a phase transition [33]. They suggested that either at high temperature or at high density a phase transition to a deconfined phase occurs, thus giving rise to a phase diagram.
Since the energy scale of hadronization is non-perturbative, perturbative methods cannot be applied to calculate the dynamics of the hadronic phase transition and the Quark-Gluon Plasma. Instead, lattice QCD is widely used today to perform those calculations [34, 35]. Lattice QCD was invented in 1974 by Wilson [36] and represents an approach to solve QCD on a discretized space-time lattice with lattice spacing a and the continuum limit $a \to 0$.
A conjectured QCD phase diagram reflecting the current understanding is shown in Fig. 1.3.

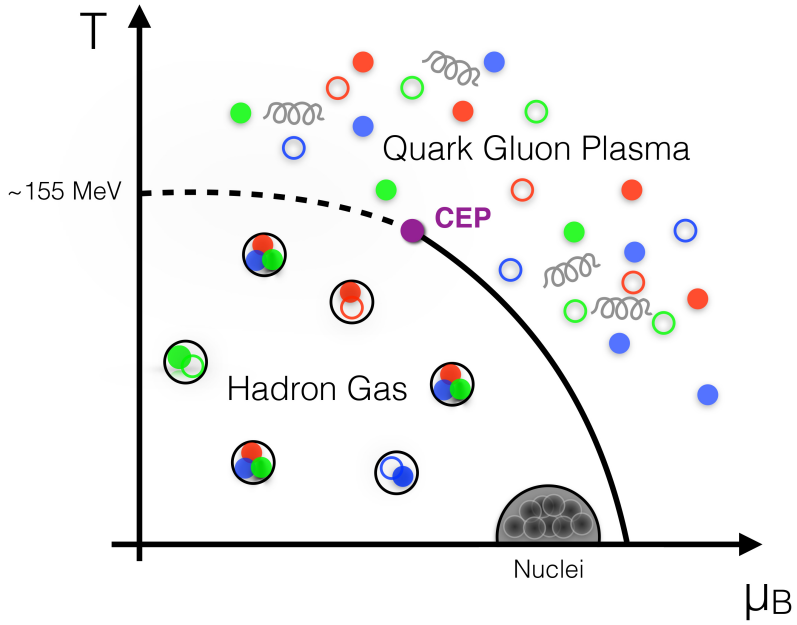

Figure 1.3: Sketch of a conjectured QCD phase diagram [34].

The temperature T is drawn on the ordinate while the baryochemical potential μ_B, a measure of the net baryon density, is drawn on the abscissa. At vanishing temperature and net baryon density of 1 the conditions for ordinary nuclear matter are fulfilled. Lowering the net baryon density or increasing the temperature lead to the state of a hadron gas. At $\mu_B = 0$ and a temperature around $T_c \approx 155$ MeV [37, 38] lattice QCD predicts a cross-over transition to a state of deconfined quarks and gluons [39].
Figure 1.4 shows thermodynamical bulk properties in the continuum extrapolation as calculated with lattice QCD [40]. It can be seen that pressure, energy density and entropy increase rapidly, but not abruptly, in the vicinity of T_c, indicating the cross-over type of the transition. For high temperatures the bulk observables undershoot the non-interacting limit which shows that even for very high temperatures quarks and gluons are still interacting strongly. Also indicated are predictions of the bulk observables in the framework of the hadron resonance gas which are compatible with the lattice results in the transition region. Even though the hadron resonance gas seems to give results compatible with lattice QCD also in a region $T > T_c$ it is argued in [34] that a description in terms of hadronic degrees of freedom is not valid any more in this region.

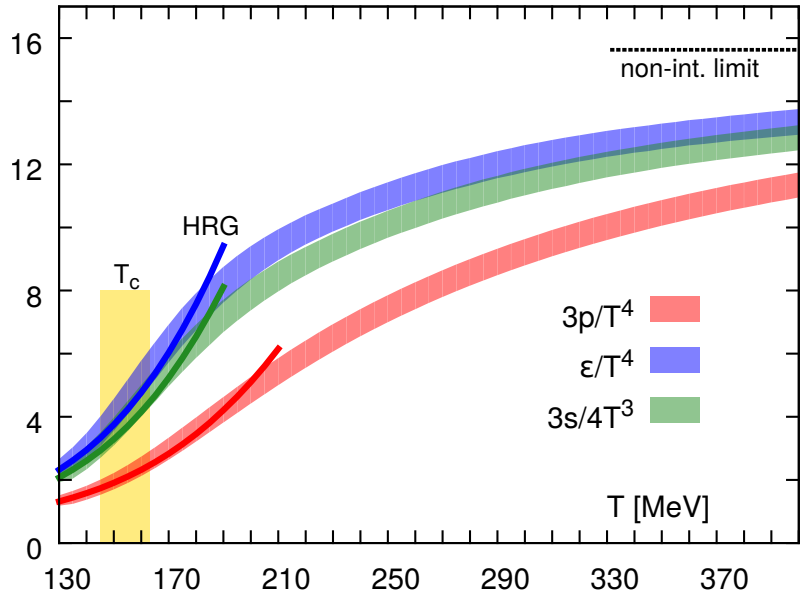

Figure 1.4: Thermodynamical bulk properties as calculated in lattice QCD [40].

The region of $\mu_B > 0$ is not directly accessible in lattice QCD due to the fermion sign problem. Different approaches have been developed over the years in order to make predictions for this interesting part of the phase diagram [41–45]. Some of those calculations suggest that a critical endpoint (CEP) followed by a first order phase transition may exist at high μ_B [46, 47]. The search for a critical endpoint is a topic of great interest in the beam energy scan at RHIC and at future facilities like

FAIR and NICA.
The region of very high μ_B and low temperature is largely unexplored terrain (not sketched in Fig. 1.3). It is expected that in this regime color superconductivity might play a role (see [48] for a review). However, direct lattice QCD predictions are not available and also tools like chiral effective field theory are only applicable at nuclear densities [49]. Interestingly, with the recent observation of a neutron-star merger it is already possible to constrain the Equation of State of neutron-star-matter at low densities [50] and it will be interesting to see if conclusions about the existence of quark matter inside neutron star cores can be drawn in the future.

The study of different QCD phases and phase transitions is of great importance for our understanding of matter and the strong interaction. According to Big Bang cosmology the universe underwent the QCD phase transition at almost vanishing μ_B few microseconds after the Big Bang [51]. The order of this phase transition has different cosmological implications [52]. For example, a first order phase transition could influence the dark matter power spectrum or the primordial density of gravitational waves [53, 54]. Thus, the experimental study of the Quark-Gluon Plasma phase and its phase transition at low μ_B is also relevant for the understanding of the evolution of the universe.
Experimentally, relativistic heavy-ion collisions are used to recreate and study this phase in the laboratory. Relativistic heavy-ion collisions will be introduced in the next section focusing on their space-time evolution and geometrical aspects.

1.2 Relativistic heavy-ion collisions

1.2.1 Space-time evolution

Shuryak already proposed in 1978 that a Quark-Gluon Plasma is produced in hadronic collisions [55]. He assumed that after some time a local thermal equilibrium builds up and that the system can be described by a temperature T. He developed the first picture of the space-time evolution of the system which was further developed by Bjorken assuming the applicability of hydrodynamics [56].
A schematic of the space-time evolution of heavy-ion collisions is shown in Fig. 1.5.

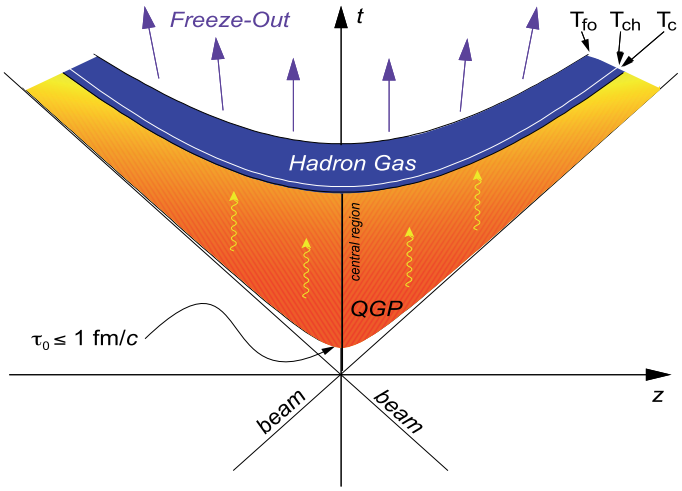

Figure 1.5: Schematic of the space-time evolution of ultra-relativistic heavy-ion collisions [57].

The z-axis represents the longitudinal direction in which the beams are approaching each other while the t-axis represents the time. The beams of Lorentz contracted nuclei meet and start to penetrate each other at $t = z = 0$. After the collision time of $t_{\mathrm{coll}} \approx 2.6 \cdot 10^{-3}$ fm/c (for Pb–Pb collisions at $\sqrt{s_{\mathrm{NN}}} = 5$ TeV)[2] and the equilibration time of $\tau_0 \leq 1$ fm/c the thermalized Quark-Gluon Plasma (QGP) state builds up. The QGP expands in longitudinal and radial direction due to pressure gradients and starts to cool down. After a lifetime of $\tau_{\mathrm{QGP}} \approx 10$ fm/c [58] the cross-over transition to a hadron gas takes place around the critical temperature T_{c}. The hadron abundances are fixed at the chemical freeze-out temperature T_{ch} when inelastic collisions no longer take place. In the hadron gas elastic collisions are still possible, fixing the hadron kinematics only at the kinetic freeze-out temperature T_{fo}. Let us emphasize here that particles measured in detectors underwent the full system evolution. Models which make predictions for heavy-ion collisions consequently need to incorporate knowledge about the initial state, the medium evolution and the freeze-out stages. Details about the relevant initial state (or nuclear) effects for

[2]For this estimation we used $t_{\mathrm{coll}} = 2R/\gamma_{\mathrm{cm}}$, with $R = 1.2$ fm $\cdot A^{1/3}$.

charmonium production will be given in Section 2.3.
The evolution of the QGP phase is often modeled using relativistic hydrodynamics. A review of relativistic hydrodynamics for heavy-ion collisions can be found in [59]. In the following we will explain the basics and derive observable properties which follow from hydrodynamic expansion.
Relativistic inviscid (ideal-fluid) hydrodynamics is based on the assumption of local thermodynamic equilibrium. In order to reach local equilibrium it is necessary that the mean free path of the particles is much smaller than a typical length scale of the system. Assuming a vanishing viscosity and local equilibrium may be only an approximation for the system created in heavy-ion collisions and deviations from this idealization are studied in viscous hydrodynamics [60, 61].
With the velocity $\vec{v}$ of the rest frame of a fluid element with respect to the laboratory frame the corresponding 4-velocity is (using c = 1):

$$u^\mu = (u_0, \vec{u}) = \left(\frac{1}{\sqrt{1-\vec{v}^2}}, \frac{\vec{v}}{\sqrt{1-\vec{v}^2}} \right). \tag{1.1}$$

The relativistic counterpart to the mass conservation is the baryon conservation with baryon density n:

$$\partial_\mu (n u^\mu) = 0. \tag{1.2}$$

With the energy-momentum tensor $T^{\mu\nu}$ the energy and momentum conservation equations are:

$$\partial_\mu T^{\mu\nu} = 0, \qquad T^{\mu\nu} = (\epsilon + P) u^\mu u^\nu - P g^{\mu\nu}, \tag{1.3}$$

with the energy density ϵ, pressure P and the metric tensor $g^{\mu\nu}$. These are the basic equations of inviscid relativistic hydrodynamics. In the following we are interested in the transverse expansion of the system. For this purpose we write down the energy-momentum conservation equations keeping only terms to first order in velocity:

$$\frac{\partial \epsilon}{\partial t} + \vec{\nabla} \cdot ((\epsilon + P)\vec{v}) = 0, \qquad \frac{\partial}{\partial t}((\epsilon + P)\vec{v}) + \vec{\nabla} P = 0. \tag{1.4}$$

For the transverse component we can consider the x (or y) component of Eq. 1.4:

$$\frac{\partial}{\partial t}((\epsilon + P) v_x) + \frac{\partial}{\partial x} P = 0. \tag{1.5}$$

Isotropy requires that momenta averaged over fluid cells vanish, yielding no preferred direction of motion. For fast thermalization times is it thus meaningful to assume

that the initial velocity components are zero: $v_x = v_y = 0$. With this assumption Eq. 1.5 can be simplified to:

$$\frac{\partial v_x}{\partial t} = -\frac{1}{\epsilon + P}\frac{\partial P}{\partial x} = -c_s^2 \frac{\partial \mathrm{ln}s}{\partial x}, \tag{1.6}$$

where we used the speed of sound $c_s = \left(\frac{\partial P}{\partial \epsilon}\right)^{1/2}$ and the identity $\frac{\mathrm{d}\epsilon}{\epsilon+P} = \frac{\mathrm{d}s}{s} = \mathrm{dln}s$. We assume a Gaussian entropy density profile (with widths σ_x, σ_y) at thermalization and obtain the velocities by integrating:

$$v_x = \frac{c_s^2 x}{\sigma_x^2} t, \qquad v_y = \frac{c_s^2 y}{\sigma_y^2} t. \tag{1.7}$$

These equations show that the initially vanishing transverse velocity is increasing linearly due to an interplay of the pressure gradient $\vec{\nabla} P$ and the inertia $\epsilon + P$.
Eventually the fluid cells have to be converted to free streaming particles which is often done using the "Cooper-Frye freeze-out picture" [62]. The basic assumptions for this picture are that the freeze-out does not influence the momentum distributions and that the particles in the fluid are independent. For the following considerations we will focus on fast particles which have an energy in the fluid rest frame exceeding their mass. By assuming that the momentum distributions are given by Boltzmann statistics, that the fluid is baryonless and that the expansion is radially symmetric one can derive an expression for the spectral shape:

$$\frac{\mathrm{d}N}{2\pi p_\mathrm{T} \mathrm{d}p_\mathrm{T} \mathrm{d}p_z} \propto \exp\left(\frac{-m_\mathrm{T} u_0 + p_\mathrm{T} u}{T}\right), \tag{1.8}$$

with transverse mass $m_\mathrm{T} = \sqrt{m^2 + p_\mathrm{T}^2}$ and the maximum fluid velocity u. In case of a stationary fluid ($u = 0$, $u_0 = 1$) the spectra are determined by the transverse mass of the particles ("m_T scaling"). However, if the fluid is expanding ($u > 0$) radially ("radial flow") the term $p_\mathrm{T} u/T$ is added in the exponent, leading to a (mass-dependent) flattening of the spectra. The kinetic energy associated with the collective flow ($mv^2/2$ in the non-relativistic case) is higher for heavier particles which hence get a larger momentum kick.
So far we have considered the radially symmetric case which is established in head-on (central) collisions. However, non-central collisions lead to an asymmetric overlap region of the nuclei and thus the mean velocities in Eq. 1.7 are different. This leads to an azimuthally asymmetric particle emission which is described by the elliptic flow coefficient v_2 in the Fourier decomposition of the azimuthal distribution:

$$\frac{\mathrm{d}N}{\mathrm{d}\phi} \propto 1 + 2v_2 \mathrm{cos}2\phi. \tag{1.9}$$

Using an azimuthally differential version of Eq. 1.8 an expression for v_2 can be derived:

$$v_2 = \frac{\alpha}{T}(p_T - v m_T), \tag{1.10}$$

with a positive coefficient α characterizing the strength of the asymmetry and v being the maximum fluid velocity averaged over ϕ. From this equation it can be immediately seen that also in the case of elliptic flow a mass ordering of different particles follows from the hydrodynamic expansion.
In summary, radial and elliptic flow and mass ordering of particles therein are the fingerprints of hydrodynamic evolution and are of great interest for heavy-ion physics. Before introducing more observables which are relevant to understand or characterize the produced medium we will first introduce the geometrical concepts which are applied in this research field.

1.2.2 Geometrical aspects

The initial geometry of the collision, i.e. the shape and size of the overlap region of the two nuclei is important for the understanding of the collision. In heavy-ion collisions it is a useful concept to understand the collisions in terms of geometrical quantities. The model which is used to relate observed particle distributions to the initial geometry is the Glauber model (see [63] and references therein).
Fig. 1.6 illustrates the geometrical concept used in heavy-ion collisions. Before the collision the centers of the Lorentz contracted nuclei are separated by the impact parameter b. During the collision the nucleons in the overlapping region (so-called participants) interact while the so-called spectator nucleons outside of the overlapping region continue their propagation approximately unaltered.

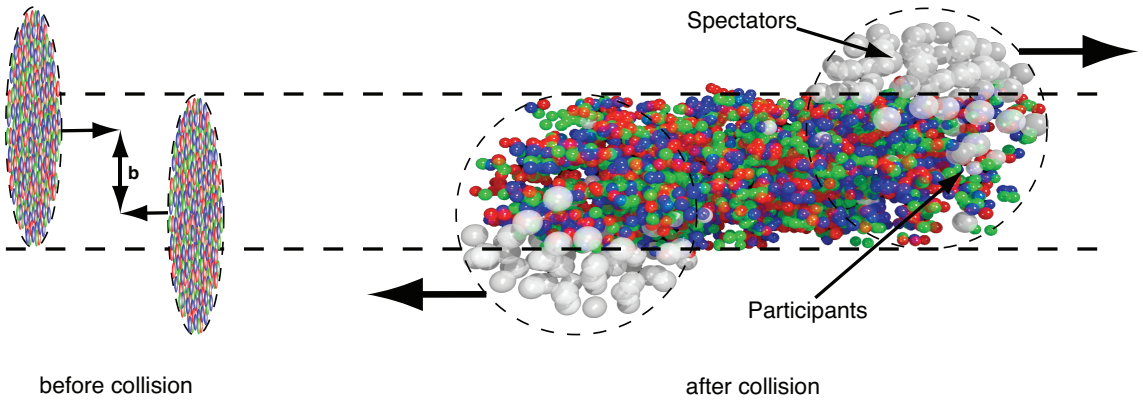

Figure 1.6: Illustration of the geometrical concept used in heavy-ion collisions. Left: Before the collision the incoming nuclei are separated by an impact parameter b. Right: During the collision the participant nucleons in the overlap region interact while the spectator nucleons outside of the overlap region continue propagating [64].

In Glauber model calculations several input parameters such as the inelastic nucleon-nucleon cross section or the nuclear charge densities have to be used. The nuclear charge densities are parameterized using a density distribution of Fermi-Dirac type:

$$\rho(r) = \rho_0 \cdot \frac{1 + w(r/R)^2}{1 + \exp(\frac{r-R}{a})}, \tag{1.11}$$

with the density in the center of the nucleus ρ_0, the nuclear radius R and parameters a and w which determine the steepness of the radial density decrease and the density shape modulation in the vicinity of R respectively. In the model it is assumed that the nucleons travel independently on straight lines and that the nucleon-nucleon cross-section is independent of the number of collisions which nucleons have undergone.

Specifically, in the so-called **optical-limit** analytical expressions for the geometrical quantities can be derived, as detailed in the following. Consider the situation of two Lorentz contracted nuclei approaching each other with separation in the transverse plane $\vec{b}$ as depicted in Fig. 1.7.

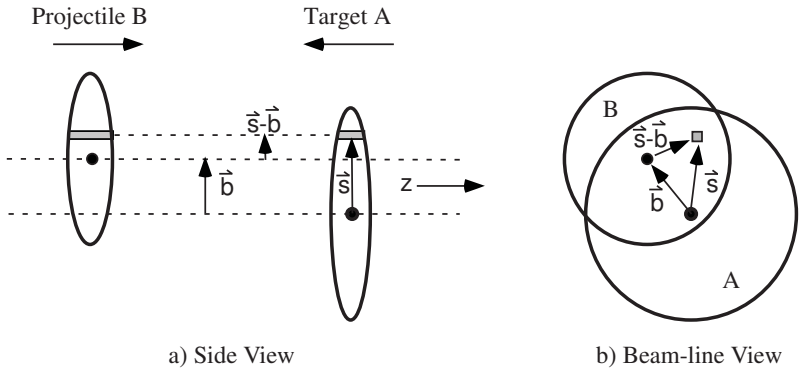

Figure 1.7: Illustration of optical Glauber model geometry shown in the transverse plane (left) and in beam direction (right) [63].

The tube of overlapping nucleons is located at $\vec{s}$ from the center of nucleus A and at $\vec{s} - \vec{b}$ from the center of nucleus B. The probability per unit area that a nucleon of nucleus A can be found in the flux tube is given by:

$$T_A(\vec{s}) = \int \rho_A(\vec{s}, z_A)\ \mathrm{d}z_A, \tag{1.12}$$

with $\rho_A(\vec{s}, z_A)$ being the probability per unit volume. The product of probabilities $T_A(\vec{s}) \cdot T_B(\vec{s} - \vec{b})\ \mathrm{d}^2 s$ yields the probability that nucleons of nucleus A and B can

be found in the overlapping area of size d^2s. Integrating over all possible flux tubes yields the so-called nuclear overlap function $T_{AB}(\vec{b})$ for a given impact parameter $\vec{b}$:

$$T_{AB}(\vec{b}) = \int T_A(\vec{s}) \cdot T_B(\vec{s} - \vec{b})\ \mathrm{d}^2s. \tag{1.13}$$

With the inelastic nucleon-nucleon cross section $\sigma_{\mathrm{inel}}^{\mathrm{NN}}$ the probability of an interaction is given by $p_{\mathrm{int}}(\vec{b}) = T_{AB}(\vec{b}) \cdot \sigma_{\mathrm{inel}}^{\mathrm{NN}}$. Consequently, the probability for n interactions out of AB possible nucleon nucleon combinations (assuming nucleus A contains A nucleons and nucleus B contains B nucleons) can be obtained by applying binomial statistics:

$$P(n, \vec{b}) = \binom{AB}{n} \left[T_{AB}(\vec{b}) \cdot \sigma_{\mathrm{inel}}^{\mathrm{NN}}\right]^n \left[1 - T_{AB}(\vec{b}) \cdot \sigma_{\mathrm{inel}}^{\mathrm{NN}}\right]^{AB-n}. \tag{1.14}$$

The number of nucleon-nucleon collisions N_{coll} is given by the expectation value:

$$N_{\mathrm{coll}}(\vec{b}) = \sum_{n=1}^{AB} n \cdot P(n, \vec{b}) = AB \cdot T_{AB}(\vec{b}) \cdot \sigma_{\mathrm{inel}}^{\mathrm{NN}}. \tag{1.15}$$

Finally, the number of nucleons which participate in inelastic collisions, denoted as N_{part}, can be obtained with the following expression:

$$\begin{aligned} N_{\mathrm{part}}(\vec{b}) \ = A \int T_A(\vec{s}) \left[1 - \left(1 - T_B(\vec{s} - \vec{b})\sigma_{\mathrm{inel}}^{\mathrm{NN}}\right)^B\right]\ \mathrm{d}^2s \ + \\ B \int T_B(\vec{s} - \vec{b}) \left[1 - \left(1 - T_A(\vec{s})\sigma_{\mathrm{inel}}^{\mathrm{NN}}\right)^A\right]\ \mathrm{d}^2s. \end{aligned} \tag{1.16}$$

An alternative approach to the optical-limit is the **Glauber Monte Carlo** approach. In this approach the geometrical entities are calculated on an event-by-event basis. For a single collision the two colliding nuclei are initialized by distributing their nucleons statistically in a three-dimensional space according to the density profile of the nucleus. The impact parameter of the collision is taken from a random sample of the geometrical cross-section $\mathrm{d}\sigma = 2\pi b\ \mathrm{d}b$ and the nucleons travel on straight lines. In a simple approach the nucleons undergo interactions if their distance in the transverse plane fulfills $d \leq \sqrt{\sigma_{\mathrm{inel}}^{\mathrm{NN}}/\pi}$ (black-disc approach, see Fig. 1.8).
Glauber Monte Carlo simulations can be used to map experimentally observed particle distributions to the geometrical entities. Typically the charged particle distribution $\mathrm{d}N_{\mathrm{evt}}/\mathrm{d}N_{\mathrm{ch}}$ is measured in an experiment and mapped to the distribution as obtained by a Glauber Monte Carlo simulation. Once this distribution is measured it can be sliced into percentiles of the total inelastic cross-section (centrality bins,

see Fig. 1.9). The convention is that low values of centrality (e.g. 0–5 %) correspond to the collisions with the highest overlap of the nuclei (most central collisions). The same slicing is done for the simulated Monte Carlo events and the average quantities in a given centrality class (e.g. $\langle N_{\mathrm{part}} \rangle$) are calculated.
How this procedure is carried out in ALICE will be explained in Sec. 3.3.

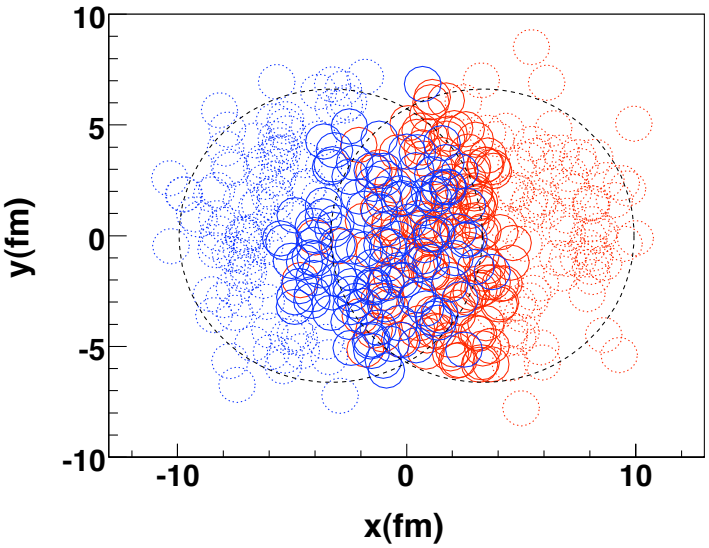

Figure 1.8: Glauber Monte Carlo simulation of a Pb–Pb collision at the LHC viewed in beam direction. Participating nucleons are represented with solid circles while spectator nucleons are marked with dotted circles [65].

It has been realized early on that particle production in heavy-ion collisions can be correlated with geometrical quantities. In hadron-nucleus collisions at 100 GeV/c^2 and nucleus-nucleus at various energies between 19.6 and 200 GeV/c^2 it has been found that the number of produced particles scales with N_{part} [66–68] . Since the total number of produced particles is dominated by the soft bulk it is expected that soft particle production scales with N_{part}. However, data from STAR and ALICE have indicated that this scaling is only approximate for the total number of produced particles and other processes need to be taken into account [69, 70].
Hard processes on the other hand are expected to scale with the nuclear overlap function T_{AA} or the number of binary collisions N_{coll} respectively. In order to quantify effects arising in hard processes in heavy-ion collisions of nuclei A and B in comparison with proton-proton collisions the nuclear modification factor R_{AB} is introduced:

$$R_{\mathrm{AB}}(p_{\mathrm{T}}) = \frac{\mathrm{d}N_x^{\mathrm{A\text{-}B}}/\mathrm{d}p_{\mathrm{T}}}{\langle T_{\mathrm{AB}} \rangle_{\mathrm{f}} \cdot \mathrm{d}\sigma^{\mathrm{pp}_x}/\mathrm{d}p_{\mathrm{T}}}, \tag{1.17}$$

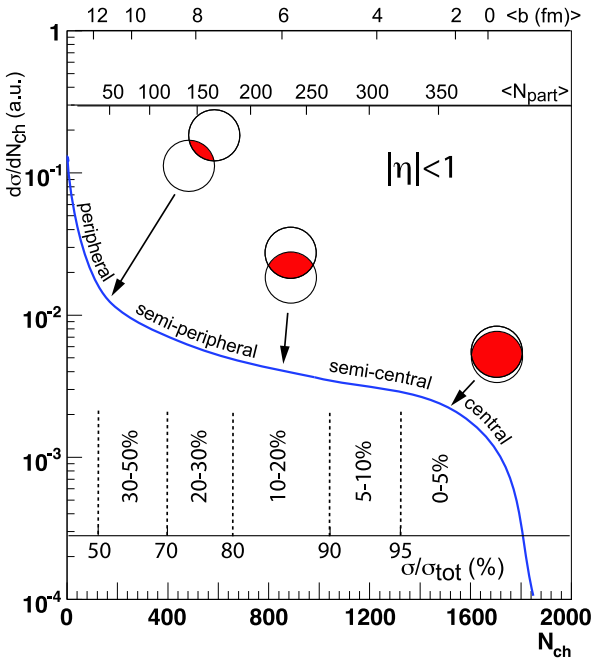

Figure 1.9: Sketch illustrating the slicing of the measured charged particle distribution into percentiles of the inelastic cross-section (centrality classes). The corresponding geometrical quantities like impact parameter $\langle b \rangle$ and $\langle N_{\mathrm{part}} \rangle$ can be obtained via a mapping procedure [63].

with the yield per event $\mathrm{d}N_x^{\mathrm{A\text{-}B}}/\mathrm{d}p_{\mathrm{T}}$, the cross-section in pp collisions $\mathrm{d}\sigma^{\mathrm{pp}_x}/\mathrm{d}p_{\mathrm{T}}$, the nuclear overlap function $\langle T_{\mathrm{AB}} \rangle_{\mathrm{f}}$ in centrality bin f for object x. Since hard processes are expected to scale with T_{AB} the nuclear modification factor should be $R_{\mathrm{AB}} = 1$ in absence of any effects in heavy-ion collisions. Compared to pp collisions, a suppression is present for $R_{\mathrm{AB}} < 1$ or an enhancement for $R_{\mathrm{AB}} > 1$ respectively.

The nuclear modification factor is a very important entity for measurements of hard processes in heavy-ion collisions. In the next section a few of the most striking observations in heavy-ion collisions at the LHC which are also relevant in the context of this thesis will be detailed.

1.3 Quark-Gluon Plasma signatures

Due to its great complexity the Quark-Gluon Plasma needs to be studied with many different measurements and observables in order to understand its properties. Let us introduce some of those measurements in the following and discuss which information can be deduced. We will start with basic observables in this section, while the special case of charmonium production in A–A collisions will be described in detail in Sec. 2.4.

1.3.1 Thermal description of particle production

Particle production yields of different species are a simple, yet powerful observable in heavy-ion collisions. Within the framework of thermal models those measurements can be linked to the QCD phase diagram by extracting the parameters T and μ_B [71].
The statistical hadronization model [72] is based on the partition function for a hadron resonance gas in the grand canonical ensemble:

$$\ln Z_i = \frac{V g_i}{2\pi^2} \int_0^\infty \pm p^2 \mathrm{d}p \, \ln\left[1 \pm \exp(-(E_i - \mu_i))/T\right], \tag{1.18}$$

where the plus sign corresponds to fermions and the minus sign to bosons, $g_i = (2J_i{+}1)$ is the spin degeneracy factor, $E_i = \sqrt{p^2 + m_i^2}$ is the energy of the particle, V is the volume of the system and T is the temperature. The particle density can be derived from the above equation:

$$n_i = N_i/V = -\frac{T}{V}\frac{\partial \ln Z_i}{\partial \mu} = \frac{g_i}{2\pi^2} \int_0^\infty \frac{p^2 dp}{\exp[(E_i - \mu_i)/T] \pm 1}. \tag{1.19}$$

The model is used to fit measured particle abundances and to extract the temperature, the baryochemical potential and the volume of the system. Please note that since particle abundances are fixed at chemical freeze-out the extracted temperature is the chemical freeze-out temperature $T = T_{\mathrm{chem}}$.
Figure 1.10 shows the statistical model fit to the particle abundances measured by ALICE at $\sqrt{s_{\mathrm{NN}}} = 2.76$ TeV in the 0–10% most central Pb–Pb collisions. Impressively, the particle yields are well described by the statistical model fit over 9 orders of magnitude which indicates that the system behaves thermally at freeze-out. The results of the fit are: $T = 156.5 \pm 1.5$ MeV, $\mu_B = 0.7 \pm 3.8$ MeV and $V_{\Delta y=1} = 5280 \pm 410$ fm^3. The chemical freeze-out temperature extracted from the fit coincides with the critical temperature extracted from Lattice QCD presented in Sec. 1.1 which might be taken as a hint of an occurring phase transition. The baryochemical potential is very low as expected for LHC energies due to the equal production of matter and antimatter [73].
The statistical model has also been used to fit particle abundances in e^+e^- and pp

collisions [74, 75]. Interestingly, the extracted temperatures are comparable to the one obtained in Pb–Pb collisions, however the description of the data is rather poor. Hence, it is argued that this might not indicate thermalization in small collisions systems but rather reflect the (statistical) nature of hadronization [76].

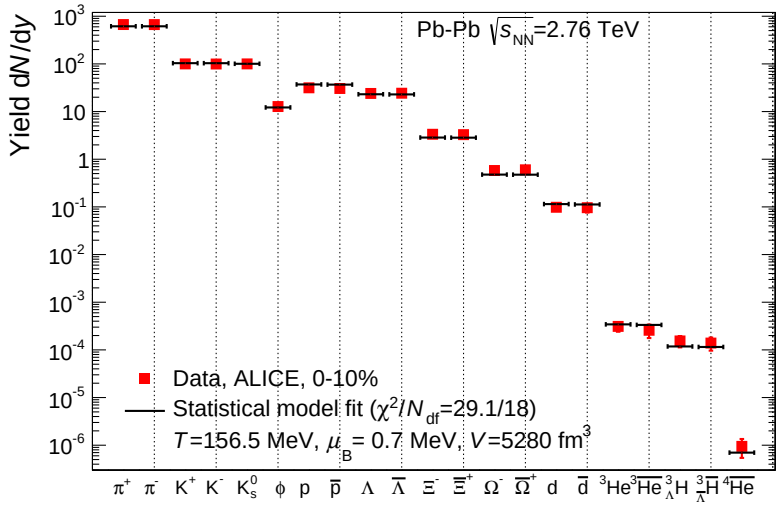

Figure 1.10: Statistical model fit to particle yields measured in the 0–10% most central collisions at $\sqrt{s_{\mathrm{NN}}} = 2.76$ TeV. Mean values of the result are given in the figure [72].

1.3.2 Collective flow

As detailed in Sec. 1.2.1 observations of radial or elliptic flow can naturally be explained with hydrodynamic behavior.
In the case of **radial flow** the expected flattening of the spectra can be described by a blast-wave model [77]. In the model it is assumed that particles are produced thermally from boosted sources with a radial velocity profile:

$$\beta_r(r) = \beta_s \left(\frac{r}{R}\right)^n, \tag{1.20}$$

where β_s is the surface velocity and R is the radius of the fireball. The particle spectrum is given as the superposition of individual thermal sources:

$$\frac{\mathrm{d}n}{m_{\mathrm{T}}\mathrm{d}m_{\mathrm{T}}} \propto \int_0^R r\ \mathrm{d}r\ m_{\mathrm{T}}\ I_0\left(\frac{p_{\mathrm{T}}\ \sinh\rho}{T_{\mathrm{kin}}}\right)\ K_1\left(\frac{m_{\mathrm{T}}\ \cosh\rho}{T_{\mathrm{kin}}}\right), \tag{1.21}$$

with $\rho = \tanh^{-1}\beta_r$ and the modified Bessel functions I_0 and K_1. Note that this model contains the kinetic freeze-out temperature T_{kin} as parameter since the hadron kinematics are only fixed at the kinetic freeze-out when elastic collisions cease.

Figure 1.11 shows a combined blast-wave fit to the spectra of light flavor hadrons measured by ALICE. The fit shows a good description of the data in general. Deviations of the fit to protons and pions at high p_{T} indicate the limit of a hydrodynamical description. The low p_{T} excess of the pion data over the fit is commonly understood by pion production in resonance decays [79]. Using fits of this kind to measured spectra the mean transverse velocity $\langle\beta_{\mathrm{T}}\rangle$ and the kinetic freeze-out temperature T_{kin} can be extracted. Figure 1.12 left panel shows the extraction of those parameters for ALICE and STAR data in different centrality classes. It can be observed that the transverse expansion velocity β_{T} increases with centrality and is about 10% higher at LHC than at RHIC. The decrease of the kinetic freeze-out temperature T_{kin} with centrality may indicate a longer lived fireball created in more central collisions. In the right panel of Fig. 1.12 the mean transverse momentum $\langle p_{\mathrm{T}}\rangle$ is shown in different centrality bins for different particle species as extracted from blast-wave fits to the measured spectra.

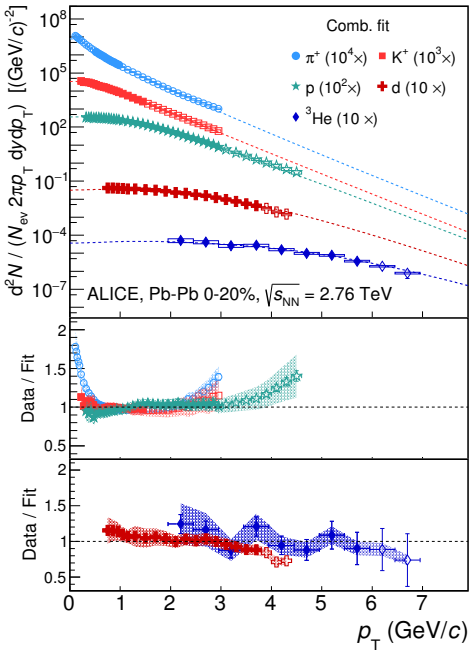

Figure 1.11: Blast wave fits to spectra of light flavor hadrons as measured by ALICE [78].

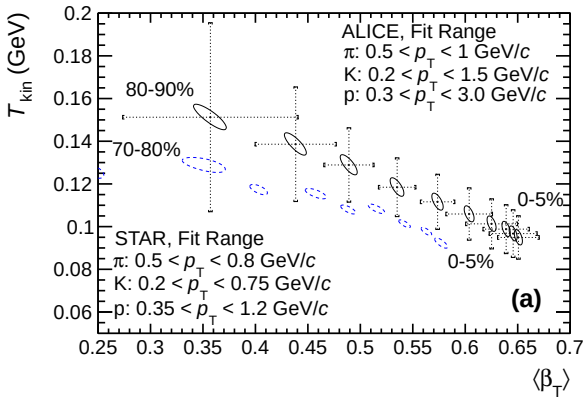

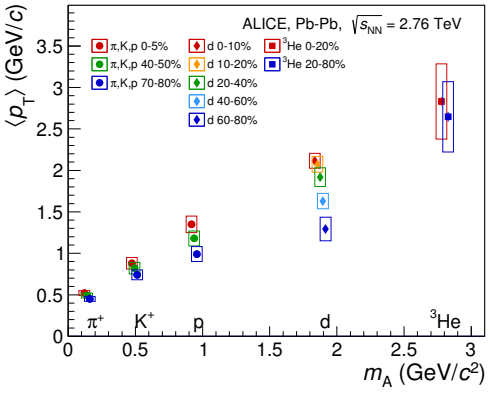

Figure 1.12: Left: Results for the kinetic freeze-out temperature T_{kin} and mean transverse expansion velocity $\langle\beta_{\mathrm{T}}\rangle$ as extracted from blast wave fits to ALICE and STAR data [78]. Right: Mean transverse momentum of different light flavor hadrons as function of centrality as extracted from blast wave fits [80] .

A clear hierarchy in centrality is observed: in more central collisions the mean transverse momentum $\langle p_{\mathrm{T}}\rangle$ is higher for all plotted particle types. This hierarchy is a

clear indication of hydrodynamical behavior due to the increasing radial momentum which is added by the flow field.

So far we discussed the radially symmetric flow, however, another interesting signature is the azimuthally anisotropic **elliptic flow** (for a review see [64]). Elliptic flow is generated by the initial spatial anisotropy of a non-central collision (see Fig. 1.13 left panel) which is converted into a momentum anisotropy of the outgoing particles due to the large pressure gradients. Elliptic flow is in particular sensitive to medium properties like the equation of state and the shear viscosity over entropy density ratio η/s. Experimentally elliptic flow is expressed as the second coefficient v_2 in the Fourier expansion of the particle azimuthal distribution:

$$E\frac{d^3N}{d^3p} = \frac{1}{2\pi}\frac{d^2N}{p_{\mathrm{T}}\mathrm{d}p_{\mathrm{T}}\mathrm{d}y}\left(1+\sum_{n=1}^{\infty}2v_n\cos(n(\phi-\Psi_{\mathrm{RP}}))\right), \tag{1.22}$$

where ϕ is the azimuthal angle of the particles of interest and Ψ_{RP} is the angle of the reaction plane spanned by the impact parameter and the beam direction. The reaction plane is not directly observable in heavy-ion collisions and needs to be estimated from measured particles. Details on the experimental methods can be found in [81].

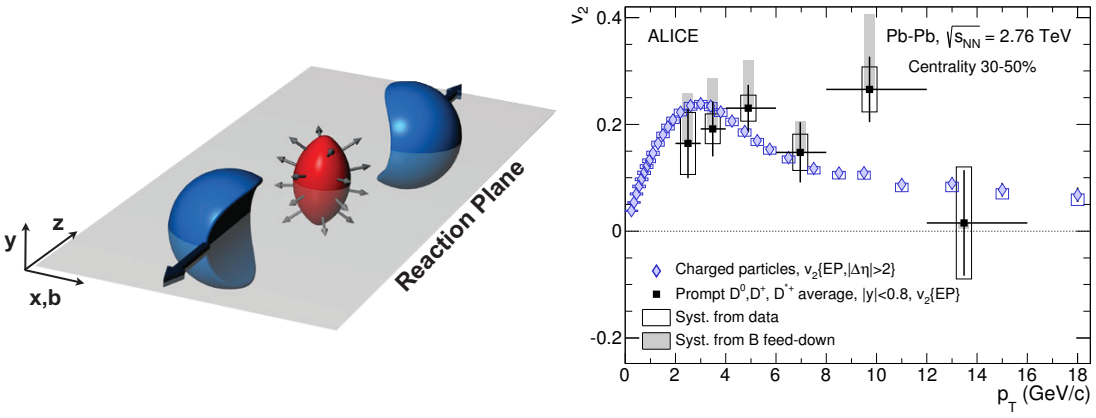

Figure 1.13: Left: Sketch of the almond shaped overlap zone created in semi-central heavy-ion collisions [64]. Right: ALICE measurement of the elliptic flow coefficient v_2 of inclusive charged particles and D mesons [82].

Figure 1.13 right panel shows the measurement of the elliptic flow coefficient v_2 in semi-central Pb–Pb collisions by ALICE for inclusive charged particles and D mesons. The v_2 of charged particles shows an initial increase with p_{T} which is almost linear as predicted by ideal hydrodynamics (see Eq. 1.10). Around $p_{\mathrm{T}} \approx 3$ GeV/c a plateau is reached which is attributed to viscous effects [83]. The behavior at high p_{T} is understood as an interplay of viscous effects and parton energy loss (explained in Sec. 1.3.3) [84]. Surprisingly, it was found that D mesons also exhibit a positive elliptic

flow, consistent in shape and magnitude with the charged particle v_2. This was taken as an indication that charm quarks might also thermalize and flow with the medium.

1.3.3 Parton energy loss

The energy loss of energetic partons traversing the medium was proposed early on as a signature of the Quark-Gluon Plasma by Bjorken [85]. He proposed that partons traversing the medium lose energy by elastic scattering with medium constituents. Experimentally an energy imbalance of back-to-back jets should be observable in this scenario. Indeed, a suppression of back-to-back dihadron correlations in central Au+Au collisions was observed by STAR at RHIC indicating significant interactions with the medium [86].
Since the early days the understanding of the energy loss processes has evolved: While Bjorken proposed the process of collisional energy loss in the medium more recent calculations indicate that parton energy loss is dominated by radiative energy loss at RHIC and LHC energies [87].
As expected, a strong suppression of high p_{T} hadrons was also observed at the LHC. In Fig. 1.14 the nuclear modification factor (introduced in Sec. 1.2.2) of different particle types as measured by ALICE and CMS is shown.

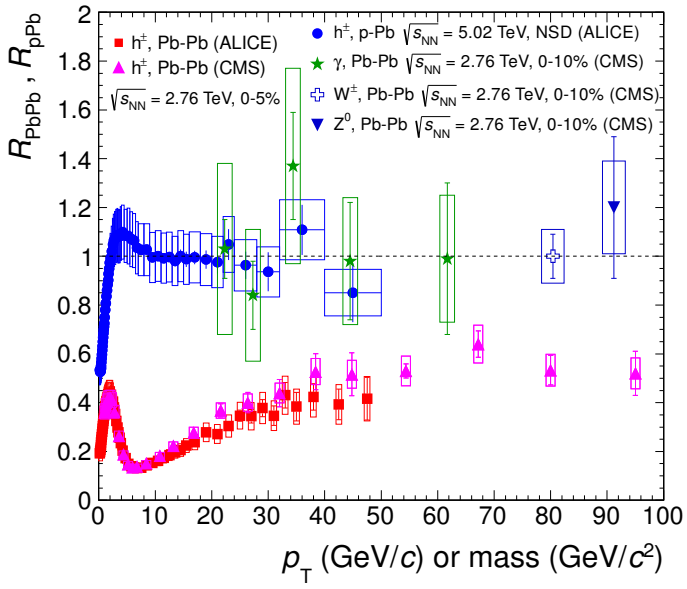

Figure 1.14: Results for the nuclear modification factor of different particle types in p–Pb and Pb–Pb collisions [88].

Inclusive hadrons measured in Pb–Pb collisions are found to have a nuclear modification factor far below unity, thus being strongly suppressed. The bump in the nuclear modification factor at low p_{T} can be explained by radial flow [89]. For higher transverse momenta the nuclear modification factor shows a rising trend. Using comparisons to model calculations it can be concluded that this is due to

a smaller relative energy loss with higher momentum [90]. In p–Pb collisions the nuclear modification factor is consistent with unity at high p_{T}. Thus, the observed suppression in Pb–Pb collisions can be related to strong medium effects present in this system. The measurement of high p_{T} direct photons and W/Z bosons confirms that T_{AA} scaling is valid for hard processes since electroweak observables are not expected to be influenced significantly by the medium.
Measurements of jet quenching have demonstrated that the medium is strongly interacting and has a large density. Nowadays these measurements can even be used to extract fundamental medium parameters like the jet transport parameter $\hat{q}$ and the mean free path λ_0 [91, 92].

2 Charmonium

2.1 The charmonium spectrum

Charmonia are bound states of $c\bar{c}$ quarks and are of interest since the discovery of their most prominent member, the J/ψ, in 1974 [15, 16]. Bottomonia, bound states of $b\bar{b}$ quarks, are also of interest in contemporary physics, however the discussion here will be focused on $c\bar{c}$ systems.
Already at the time of the discovery of the J/ψ its very narrow width smaller than the experimental resolution was noted [15, 16]. Today the decay width of the J/ψ is determined to be $\Gamma = 92.9 \pm 2.8$ keV [93] which translates to a lifetime of $\tau = \hbar/\Gamma = 7.09 \pm 0.21 \cdot 10^{-21}$ s. Thus compared to other particles which decay via strong interaction (like ρ or Δ) the J/ψ lives about three orders of magnitude longer. The long lifetime can be explained by the OZI rule: Since the J/ψ mass ($m_{\mathrm{J}/\psi} = 3.096900(6)$ GeV/c^2) is smaller than the mass of two D mesons ($2 \cdot m_{\mathrm{D}} \approx 3.73$ GeV/c^2, "open charm threshold") this decay is kinematically not allowed and the $c\bar{c}$ pair has to annihilate in the decay. For reasons of color and parity conservation the strong decay has to proceed via a 3 gluon exchange, thus being suppressed by α_{s}^3. Due to this OZI suppression the electromagnetic decay via a virtual photon can compete with the strong decay and leads to a sizeable branching into dielectron[1] pairs: BR(J/$\psi \to e^+e^-$) = 5.971(32)%.
The binding of the charm-anticharm system can be described with the phenomenological Cornell potential first suggested in [94]:

$$V(r) = -\frac{4}{3}\frac{\alpha_{\mathrm{s}}\hbar c}{r} + k \cdot r, \tag{2.1}$$

which contains a Coulomb-like part $\propto 1/r$ relevant at small radii r and a linearly increasing part $k \cdot r$ which is responsible for quark confinement. The constant k can be interpreted as the string tension which acts between the quark-antiquark pair. Based on the phenomenological potential the charmonium spectrum can be precisely calculated below the open charm threshold (see e.g. [95]).
In Fig. 2.1 the charmonium spectrum with the experimentally established states is shown. Singlett states are labeled η_{c} or h_{c}, while ψ or χ_{c} are triplett states. The open charm thresholds are indicated above which decays into different D meson types are possible. Above or in the vicinity of those thresholds non-conventional charmonium(-like) states X have been observed, possibly being of exotic nature [96]. The search for and the study of the nature of those states is subject to intense research today [97–99].

[1] Similar for dimuon pairs

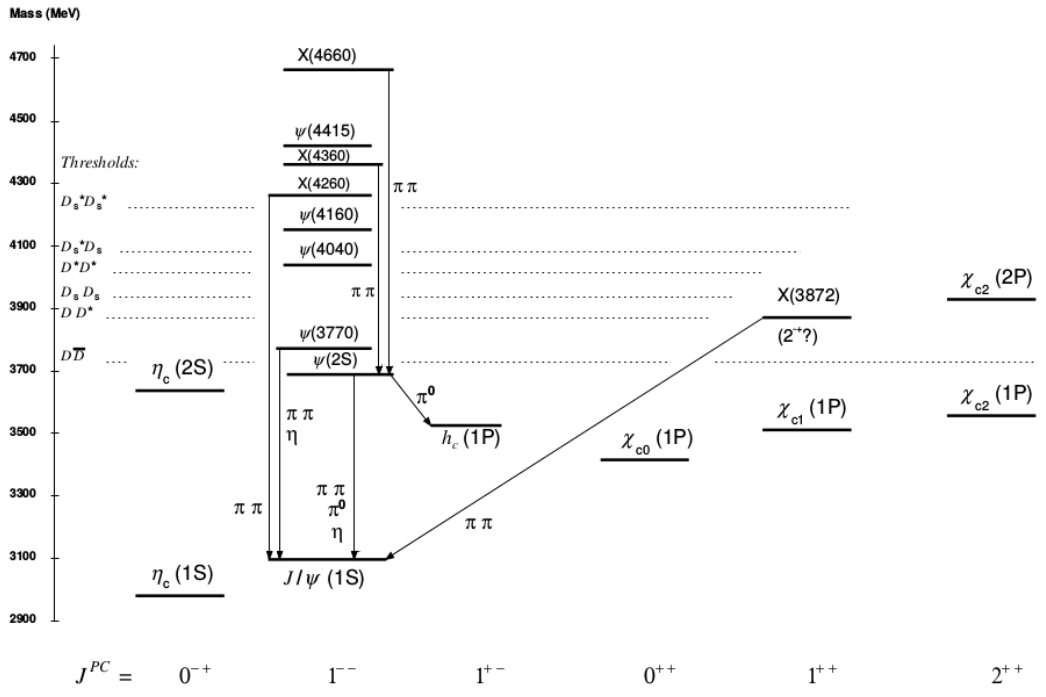

Figure 2.1: The spectrum of charmonia and non-conventional charmonium(-like) states X. Radiative transitions are not shown [93].

Charmonia are fascinating particles with an intrinsic multi-scale nature: While the production of charm quark pairs happens in hard processes ($q \gg \Lambda_{\mathrm{QCD}}$), the transition to the bound state must involve non-perturbative effects. Thus charmonia are an excellent tool to study QCD at different scales in pp and p–A collisions and also QCD many-body systems at high temperature and pressure in nucleus-nucleus collisions. In the following we will introduce the production mechanism relevant in pp, p–A and A–A collisions, highlighting the role of J/ψ as messenger of deconfinement in nucleus-nucleus collisions.

2.2 Production in pp collisions

Inclusive J/ψ production as relevant for this thesis can be divided into different sources: prompt J/ψ production and J/ψ production from weak decays of B mesons (non-prompt). The former component can be subdivided into direct production from a $c\bar{c}$ pair and feed-down contributions from higher charmonium states like χ_c or $\psi(2S)$.

The fraction of J/ψ from χ_c feed-down has been measured by CDF [104] and LHCb [105] and shows a slight increase from about 14% at $p_T = 2$ GeV/c to about 22% at 10 GeV/c. The fraction of J/ψ coming from ψ(2S) decays was determined to be around 10% integrated over p_T [106].
Non-prompt J/ψ can be identified by a displaced production vertex of the J/ψ due to the long timescale of weak decays and by making use of the good position resolution of silicon detectors. Figure 2.2 shows measurements of the fraction f_B of non-prompt J/ψ as function of transverse momentum. For low p_T the non-prompt fraction is around 10% and rises to about 30% at $p_T = 10$ GeV/c. No significant collision energy dependence can be observed considering the uncertainties of the measurements.

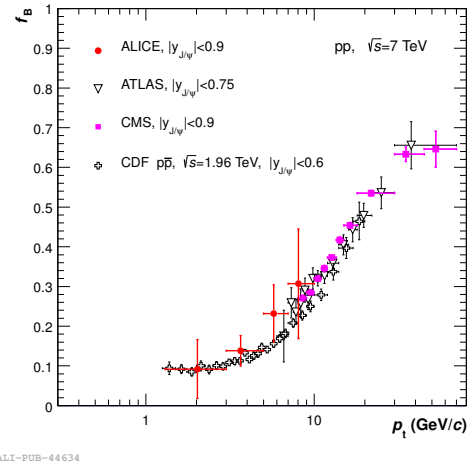

Figure 2.2: Fraction f_B of non-prompt J/ψ measured by CDF [100], ALICE [101], ATLAS [102] and CMS [103].

At the LHC the production of $c\bar{c}$ pairs is mainly due to gluon fusion processes caused by the dominant gluon distribution in the PDFs at the relevant Bjorken x range[2] of 10^{-2} – 10^{-4}.
The direct production of charmonia in pp collisions can be understood as a two-scale process. The initial production of the $c\bar{c}$ pair happens at high momentum transfer q^2 and can be described by perturbative QCD making use of an expansion in α_s. The transition of the $c\bar{c}$ pair to a bound charmonium state takes place at a nonperturbative scale and is currently only accessible by model approaches, e.g. color-singlet model (CSM) [107, 108], color-evaporation model (CEM) [109–111] and NRQCD [112]. In the CSM it is assumed that quarkonium states can only be formed if the $Q\bar{Q}$ pair is in a color singlett state and carries the quantum numbers of the final quarkonium state. Model parameters related to the $Q\bar{Q}$ wavefunction which are needed for the calculation of the production rate are extracted from data. In the CEM the production of a quarkonium state can only take place if the invariant mass of the $Q\bar{Q}$ pair is lower than the threshold for the production of an open

[2]Kinematic regime accessed so far by LHC experiments

heavy-flavor meson pair. Furthermore the probability of a $Q\bar{Q}$ pair to evolve into a given quarkonium state is assumed to be a constant and is extracted using the measurement of the total production cross-section of this state. Afterwards the CEM can predict the momentum distribution of the quarkonium production rate. NRQCD is an effective theory of QCD and makes use of an expansion in orders of α_s and the heavy-quark velocity v. The probability of a $Q\bar{Q}$ pair to evolve into a quarkonium is expressed with long-distance matrix elements which are extracted from data.
In order to justify the applicability of such model approaches it must be shown that the perturbative and nonperturbative effects can be separated from each other ("factorization"). Recently factorization has been proven to all orders in coupling constant in the NRQCD color octett mechanism [113].
NRQCD has been succesful in describing J/ψ production cross-sections at the LHC (see e.g. [103, 106, 114–116]). However, recent measurements of J/ψ polarization [117, 118] and correlations of J/ψ mesons with jets [119] are in tension with NRQCD predictions. A comprehensive theoretical description of different quarkonium observables in pp collisions has yet to be found.

2.3 Production in p–A collisions

For the interpretation of A–A results it is compulsory to gain a thorough understanding of p–A collisions where the production of a medium is not expected and the nuclear projectiles can be resolved locally. Effects observed in those collisions need to be incorporated in models which aim at describing A–A collisions. At LHC energies different effects might play a role such as the nuclear modification of the parton distribution functions (PDFs), the Color-Glass-Condensate (CGC) [120], coherent energy loss [121] and multiple scattering [122, 123].
The modifications of the quark distribution functions are known from deep-inelastic scattering (DIS) experiments. However, the modifications of the gluon PDFs are not directly measured in DIS and thus not very well constrained. The extraction of the nuclear PDFs is typically done in a global fit to experimental data at fixed order in perturbative QCD [124–127]. In the recent EPPS16 nPDFs LHC data on dijets and W/Z bosons have been included, however the region of low x and Q^2 is still widely unconstrained [127]. More data input is clearly needed.
The nuclear modification of the PDF of parton i is often expressed with the ratio:

$$R_i^A(x, Q^2) = f_i^{p/A}(x, Q^2)/f_i^p(x, Q^2), \tag{2.2}$$

with $f_i^{p/A}(x, Q^2)$ being the nuclear PDF of a proton p in nucleus A and the free proton PDF $f_i^p(x, Q^2)$. Figure 2.3 left panel shows an illustration of the function which is used for $R_i^A(x, Q^2)$ in the EPPS16 global fit while the right panel shows the extracted R_g^{Pb} at $Q^2 = 10$ GeV^2. Different effects are relevant for different ranges of Bjorken x. At small x shadowing suppresses the nPDFs compared to the proton PDFs. The suppression gets weaker for higher values of x until an enhancement is

reached in the antishadowing region. At higher values of x a local EMC minimum is reached until the nPDFs get larger than the proton PDFs at x close to unity due to the Fermi motion of the nucleons.

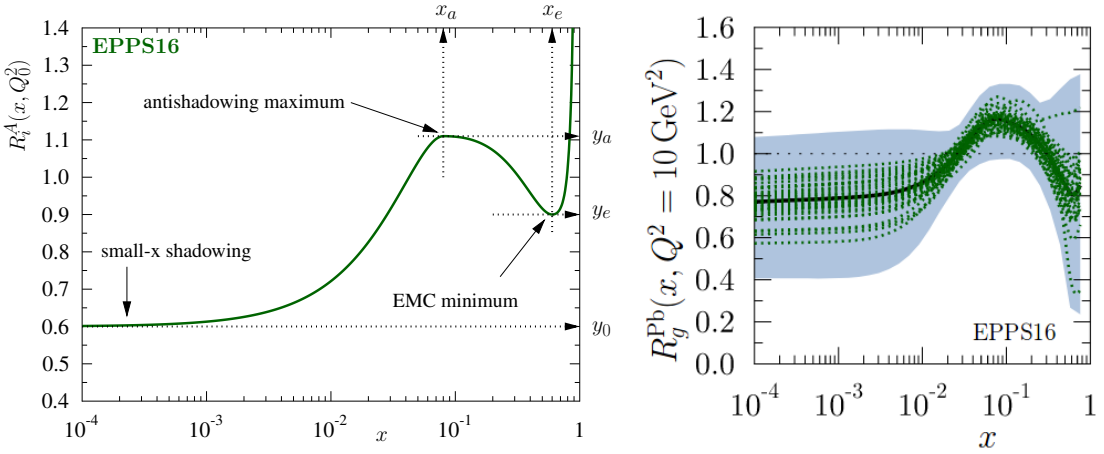

Figure 2.3: Left: Illustration of the fit function used in the extraction of the EPPS16 nPDFs. Right: Ratio R_g^{Pb} for gluons at $Q^2 = 10$ GeV^2. The mean value is indicated as black line while the total uncertainty is indicated as grey band. Both taken from [127].

Most authors agree that the reason for the shadowing depletion of the nPDFs at low x is multiple scattering of the resolved hadronic component of the virtual photon wave function with the nucleons in the nucleus [128]. The antishadowing enhancement can be explained by coherence effects while the origin the EMC effect is still debated [129].

The CGC approach considers the limit $x \to 0$ and $s \to \infty$. In this limit the number of partons in the nucleus increases dramatically due to QCD bremsstrahlung. Eventually the number of partons can not increase further due to recombination and color screening effects leading to saturation.

In the energy-loss model of Arleo and Peigné (see [121] and references therein) it is assumed that the $c\bar{c}$ pair is produced early in the collision in a color octet state and remains in that state for a longer time. Interference between initial and final state amplitudes leads to a medium induced radiation spectrum.

Kang and Qiu propose multiple scattering of the partons in the initial state as a source of transverse momentum broadening, i.e. the increase of $\langle p_{\mathrm{T}}^2 \rangle$ [122, 123]. In addition the final state scattering of the $c\bar{c}$ pair in the nucleus should further increase the broadening. Both contributions are added without considering possible coherence effects.

In Fig. 2.4 different measurements of J/ψ production in p–Pb collisions by ALICE are shown. In the left panel the measurement of the nuclear modification factor R_{pPb} is shown as a function of rapidity. At mid-rapidity the nuclear modification factor shows a suppression of the J/ψ yield which can in general be described by CGC, shadowing and shadowing + energy loss models within the experimental and theoretical

uncertainties. At forward rapidity (positive y) the data favor the CGC model by Ma et al. and models incorporating energy loss. At backward rapidity (negative y) the nuclear modification factor is consistent with unity which is reproduced by all model calculations. In the right panel of Fig. 2.4 the transverse momentum broadening is shown as a function of the average number of nucleon-nucleon collisions $\langle N_{\rm coll}^{\rm mult} \rangle$. It can be observed that the broadening increases as a function of $\langle N_{\rm coll}^{\rm mult} \rangle$ and more broadening is observed at forward rapidity. Forward rapidity can be associated with the beam configuration in which the proton penetrates the lead nucleus and fragments into the muon spectrometer. The transverse momentum broadening is well described by the multiple scattering model at forward and backward rapidity. The coherent energy loss model can describe the broadening at backward rapidity while slightly overpredicting the broadening at forward rapidity.

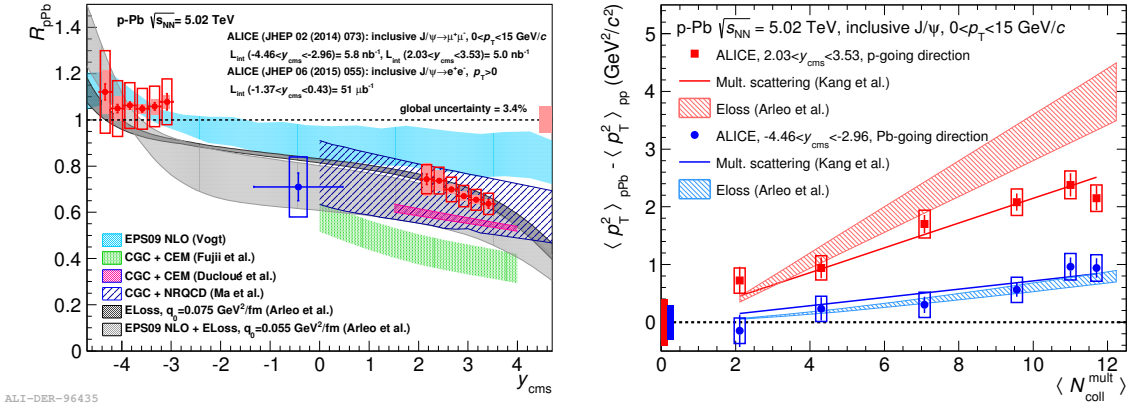

Figure 2.4: Left: ALICE measurement of the $R_{\rm pPb}$ of J/ψ as a function of rapidity compared to shadowing (EPS09), CGC and energy loss calculations [130, 131]. Right: Measurement of the transverse momentum broadening of J/ψ as a function of the average number of nucleon-nucleon collisions [132].

It can be concluded that in p–Pb collisions a suppression of the J/ψ yield is present at mid- and forward rapidity. At present the uncertainties of the data and the models do not allow us to conclude about the mechanism which is behind the suppression.

2.4 Production in A–A collisions

2.4.1 Early ideas and J/ψ suppression

The production of J/ψ mesons in nucleus-nucleus collisions is considered a key observable for deconfinement since the seminal paper by Matsui and Satz in 1986 [133]. In the initial proposal the produced $c\bar{c}$ pair is affected by the presence of the color charges in the deconfined QGP. Analogous to Debye screening in an electromagnetic plasma the color charges of the $c\bar{c}$ pair are screened by the neighboring color charges. The confining potential in Eq. 2.1 then becomes the screened potential:

$$V(r) = -\frac{\alpha_{\text{eff}}}{r} \cdot \exp(-r/r_{\text{D}}(T)), \tag{2.3}$$

with the effective coupling α_{eff} and the screening radius r_{D}. Matsui and Satz estimated that for temperatures just above T_{c} no J/ψ bound state formation can occur, thus yielding a J/ψ suppression in the presence of a QGP.
In this screening scenario it is illustrative to estimate the behavior of different charmonium states by considering their binding energy E_{B} and the average separation distance r_0 between the $c\bar{c}$ pair. The binding energy can be defined as the difference between the open charm threshold and the charmonium mass m_ψ:

$$E_{\text{B}} = 2m_{\text{D}} - m_\psi. \tag{2.4}$$

The binding energies and the separation distances of different charmonium states[3] can be calculated from Non-Relativistic Potential Theory [134]:

State	J/ψ	χ_{c}	$\psi(2S)$
m_ψ (GeV/c^2)	3.10	3.53	3.68
E_{B} (GeV)	0.64	0.20	0.05
r_0 (fm)	0.5	0.72	0.9

Table 2.1: Charmonium properties derived from Non-Relativistic Potential Theory. The different χ_{c} states are not resolved in this consideration.

Since higher lying charmonium states are closer to the open charm threshold their binding energy is smaller. Higher excitational states consequently possess greater separation distances of the charm quark pairs.
Now, for a fixed screening radius $r_{\text{D}}(T)$ states with a greater separation distance r_0 might already be screened while states with a smaller separation might still be bound in the plasma. Thus in the color screening scenario a sequential suppression

[3] We restrict the discussion to the three shown states, however, the general considerations can be applied to all states below the open charm threshold.

of charmonium states is expected. Since the screening radius $r_{\mathrm{D}}(T)$ is expected to depend on the temperature it is expected that the suppression pattern of quarkonia yields information about the medium temperature. Qualitatively this is also found in models employing potentials from Lattice QCD [135].
The left panel of Fig. 2.5 shows the measurement of J/ψ and ψ(2S) production in different p–A and A–A configurations at the CERN SPS. The results are normalized to the known nuclear absorption pattern and presented as a function of the effective pathlength L traveled through nuclear matter. In the case of nucleus-nucleus collisions at high effective pathlengths a suppression beyond the expectation from normal nuclear absorption is present for both J/ψ and ψ(2S). The suppression is stronger for ψ(2S) and also sets in already at a lower effective pathlength. Those results were interpreted as a possible sign of QGP formation at SPS energies. In the right panel of Fig. 2.5 results for the nuclear modification factor R_{AA} of J/ψ production in nucleus-nucleus collisions at SPS (NA38, NA50, NA60) and RHIC (PHENIX) are shown as a function of the number of participating nucleons N_{part}. The J/ψ suppression which is present in fixed-target Pb–Pb collisions at SPS at a center-of-mass energy[4] of $\sqrt{s_{\mathrm{NN}}} = 17.3$ GeV is also observed at RHIC in collider configuration with Au-Au collisions at higher center-of-mass energy of $\sqrt{s_{\mathrm{NN}}} = 200$ GeV.

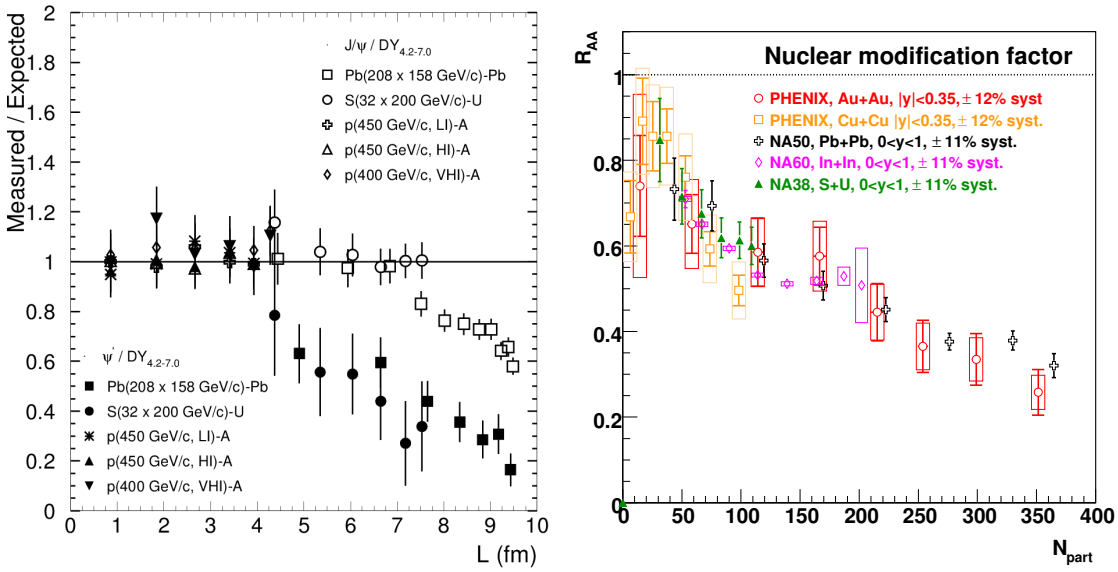

Figure 2.5: Left: Results for J/ψ and ψ(2S) production at SPS in different p–A and A–A configurations as a function of the effective traversed length in the nuclear medium [136]. Right: Nuclear modification factor of J/ψ measured at SPS and RHIC as a function of the number of participating nucleons [136].

[4]The energy given in the legend of the figure is the beam energy. Since the target is at rest the center-of-mass energy is $\sqrt{s_{\mathrm{NN}}} \approx \sqrt{2mE} = 17.3$ GeV.

2.4.2 High energy frontier and J/ψ (re)generation

In the year 2000 two different model approaches were put forward which suggest an additional J/ψ production source from deconfined charm and anticharm quarks in nucleus-nucleus collisions [137, 138]. At high collider energies as present at the LHC a J/ψ enhancement rather than a suppression should be observed according to those models.

The **statistical hadronization approach** (see [139–141] for more details) is an extension of the model presented in Sec. 1.3.1 incorporating charm. Since the mass of charm quarks is much bigger than expected QGP temperatures the charm production cannot be described thermally. Hence it is assumed that charm quark production takes place only in early hard scatterings, while all charmed mesons or charmonia are generated at the phase boundary with statistical weights. Furthermore it is assumed that charm is conserved throughout the system evolution:

$$\sigma_{c\bar{c}} = \frac{1}{2}(\sigma_{\mathrm{D}} + \sigma_{\Lambda_\mathrm{c}} + \sigma_{\Xi_\mathrm{c}} + \ldots) + (\sigma_{\eta_\mathrm{c}} + \sigma_{\mathrm{J}/\psi} + \sigma_{\chi_\mathrm{c}} + \ldots). \tag{2.5}$$

Since charm production is a hard process it is not expected that the total charm cross-section (left hand side of equation) is influenced by a medium creation. The presence of the QGP will only affect the right hand side by effectively leading to a redistribution of charm among hadrons. These considerations do not apply to lighter quark types as strange quarks since it cannot be assumed that the thermal production of those is negligible. The model implementation of charm conservation is the charm balance equation which is used to determine the fugacity factor g_c:

$$N_{c\bar{c}}^{\mathrm{dir}} = \frac{1}{2} g_\mathrm{c} N_{\mathrm{oc}}^{\mathrm{th}} \frac{I_1(g_\mathrm{c} N_{\mathrm{oc}}^{\mathrm{th}})}{I_0(g_\mathrm{c} N_{\mathrm{oc}}^{\mathrm{th}})} + g_\mathrm{c}^2 N_{c\bar{c}}^{\mathrm{th}}, \tag{2.6}$$

where $N_{c\bar{c}}^{\mathrm{dir}}$ is the number of produced $c\bar{c}$ pairs, $N_{\mathrm{oc}}^{\mathrm{th}}$ is the number of produced open charm mesons and $N_{c\bar{c}}^{th}$ is the number of produced charmonia. The total charm cross-section is input to the model and used to calculate $N_{c\bar{c}}^{\mathrm{dir}}$, while $N_{\mathrm{oc}}^{\mathrm{th}}$ and $N_{c\bar{c}}^{th}$ are calculated from their grand-canonical densities and the volume of the fireball. Afterwards the yield of open charm hadrons and charmonia can be calculated.
Let us emphasize again that in this model the production of charmonia takes place at the phase boundary from the combination of charm and anticharm quarks. Thus the J/ψ yield is expected to scale with the number of charm quarks squared ($\propto N_\mathrm{c}^2$). Since the charm cross-section is increasing with center-of-mass energy of the collision the statistical production of J/ψ at the phase boundary should be relevant only at the highest collision energies. Figure 2.6 shows a pictorial representation of the relevance of collision energy for the statistical production of J/ψ at the phase boundary. At low collision energy at RHIC only few $c\bar{c}$ pairs are produced in a collision. Due to color screening no J/ψ can be formed and the charm quarks propagate through the

medium. At the phase boundary they will most likely pick up a light quark from the medium and hadronize. However, at the LHC the number of produced charm quarks is very high (up to 200 in a central collision [142]). From time scale arguments it follows that bound states cannot be formed before the QGP and hence deconfined charm quarks are able to travel through the medium. Finally, at the phase boundary they might pick up an anticharm quark (or vice-versa) from the medium to form a J/ψ.

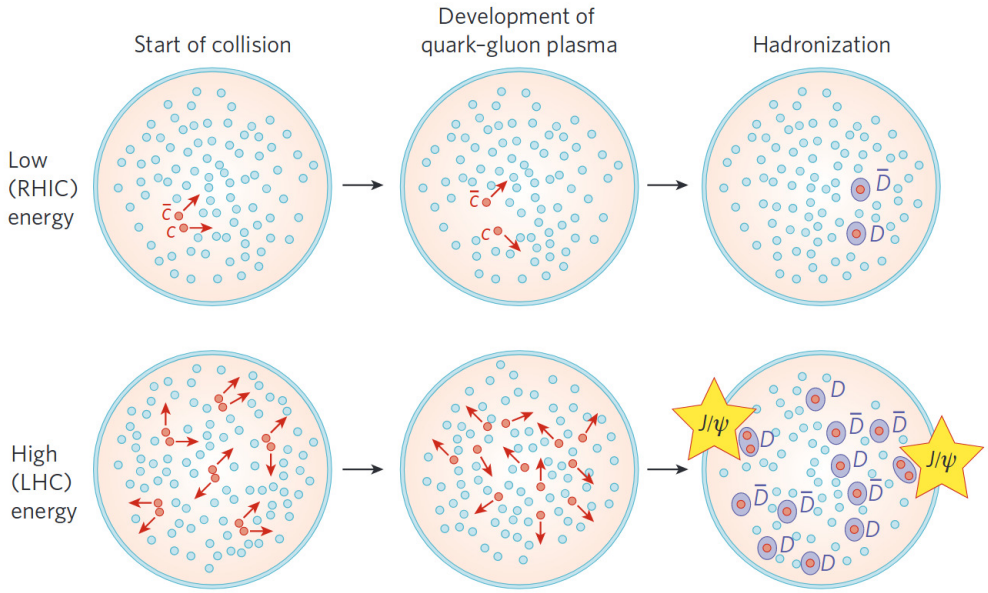

Figure 2.6: Sketch of the dynamics of $c\bar{c}$ pairs produced in nucleus-nucleus collisions. At low collision energy the charm quarks are separated due to color screening and form open charm mesons at freeze-out. At high collisions energy J/ψ might be formed by combinations of charm and anticharm quarks from the medium due to their large abundance [142].

While in the statistical hadronization model all J/ψ are generated at the phase boundary **transport models** [143–146] implement a partial destruction and (re)generation of J/ψ during the lifetime of the medium. In particular, J/ψ mesons are transported through an expanding fireball which is modeled by hydrodynamics (Zhou et al. [145, 146]) or a hydro-like approach (Rapp et al. [143, 144]).
In the fireball the charmonia (Ψ) undergo interactions with the medium constituents. Zhou et al. assume that the break up process is gluon dissociation: $\Psi + \mathrm{g} \rightarrow c + \bar{c}$. Rapp et al. calculate the dissociation rate using partonic scattering $p + \Psi \rightarrow p + c + \bar{c}$ in a quasi-free approximation in which the binding of the $c\bar{c}$ pair is neglected. The reverse process facilitates the production of charmonium by deconfined charm quarks in the medium.
Transport models use a Boltzmann equation to describe the space-time evolution of the J/ψ phase space distribution function. From the Boltzmann equation Rapp et

al. derive the time evolution ("rate equation") of the charmonium yield:

$$\frac{\mathrm{d}N_\psi}{\mathrm{d}\tau} = -\Gamma_\psi(T)\left[N_\psi - N_\psi^{eq}(T)\right], \tag{2.7}$$

where Γ_ψ is the dissociation (and formation) rate and $N_\psi^{eq}(T)$ is the number of charmonia in the thermal equilibrium limit. Hence the time evolution of the charmonium state ψ is governed by a gain and a loss term where the gain term is only active below the J/ψ dissociation temperature (above no state can be formed). Figure 2.7 shows a schematic of the time evolution of a $c\bar{c}$ pair as implemented in a transport approach. After an initial formation time of the pair and its wave function the charm quarks start to equilibrate with the medium which is assumed to occur on a timescale of about 5 fm. When the temperature of the medium drops below the dissociation temperature charmonium states can be formed within the medium. By interactions with the medium constituents charmonia can be broken up and recombined again. Finally the $c\bar{c}$ pair hadronizes to build a charmonium state.

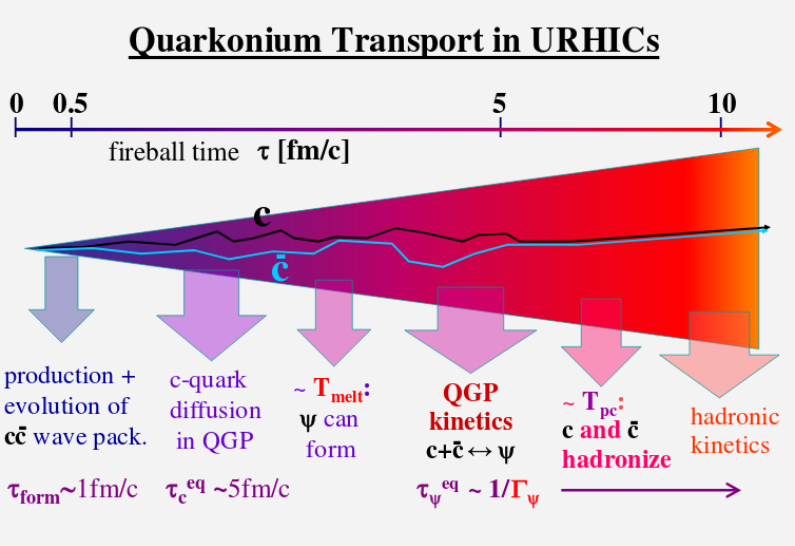

Figure 2.7: Time evolution of a $c\bar{c}$ pair in an expanding fireball within a transport model [147].

Since in the transport models charm quarks only thermalize incompletetly in the medium the (re)generated charmonium yield is lower than in the limit of the statistical hadronization model. However, the total charm cross-section which is experimentally often not determined precisely is input to both models which makes the predictions sensitive to its particular choice.

Comover models have been developed to describe the SPS results of charmonia by final state interactions of $c\bar{c}$ pairs with comoving hadrons [148, 149]. However,

in a recent version of a comover model aimed at describing Pb–Pb collisions at the LHC the comoving medium is considered to be a dense partonic medium [150]. In particular $c\bar{c}$ pairs which have been broken up by the medium can (re)combine to form charmonium states. Analogous to transport models the time dependence of the J/ψ density is given by a rate equation with loss and gain terms:

$$\tau \frac{\mathrm{d}N_{\mathrm{J}/\psi}}{\mathrm{d}\tau}(b,s,y) = -\sigma_{\mathrm{co}} \left[N^{\mathrm{co}}(b,s,y) N_{\mathrm{J}/\psi}(b,s,y) - N_c(b,s,y) N_{\bar{c}}(b,s,y) \right], \quad (2.8)$$

with the J/ψ dissociation cross section σ_{co}, the density of the co-moving medium N^{co} and the charm density N_c. The dissociation cross section σ_{co} is fixed by fits to low-energy data. The density of the co-moving medium is estimated from the charged particle density in pp collisions scaled by the number of binary collisions and corrected for shadowing contributions using Glauber-Gribov theory. The density of charm is again an input parameter of the model.

In LHC Run 1 Pb–Pb collisions have been recorded at $\sqrt{s_{\mathrm{NN}}} = 2.76$ TeV and have shown indications that indeed at LHC energies the production of J/ψ by (re)combination of $c\bar{c}$ pairs is important. Figure 2.8 left panel shows the nuclear modification factor of J/ψ as function of centrality. It stays roughly constant while the suppression is significantly smaller in most central collisions compared to the suppression observed at lower collision energy (Fig. 2.5). The results are compared to statistical hadronization and transport model predictions. The models can reproduce the data within the uncertainties, however, the transport models seem to slightly undershoot the data.

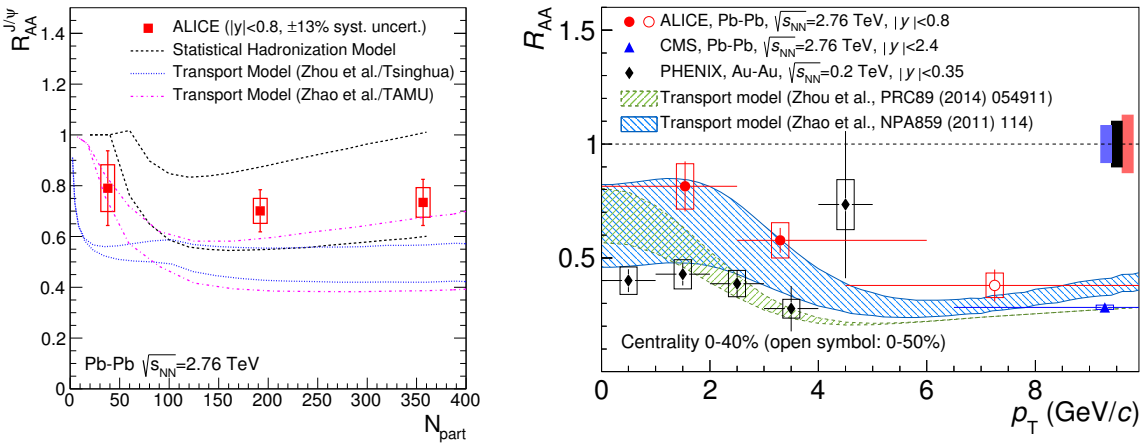

Figure 2.8: Left: Centrality dependence of the nuclear modification factor compared to model predictions [151]. Right: Transverse momentum dependence of the nuclear modification factor compared to transport model predictions and lower energy results from PHENIX [152]. In both cases the model uncertainties reflect the imprecise knowledge of the charm cross-section in Pb–Pb collisions.

In the right panel of Fig. 2.8 the transverse momentum dependence of the nuclear modification factor in 0–40% (0–50%) most central collisions is shown together with transport model predictions and lower energy results from PHENIX. At the LHC the nuclear modification factor is highest at low transverse momentum which is reproduced by the transport model by Zhao et al. In the (re)combination picture J/ψ are produced from deconfined thermalized charm quarks which should move with the bulk. Consequently it is expected that the regenerated J/ψ mesons should be dominant at low p_{T}.

Special interest in the centrality dependence of the second moment of the p_{T} distribution $\langle p_{\mathrm{T}}^2 \rangle$ has been aroused since the proposal of Zhou et al. [145]. It should be specifically sensitive to the nature of the produced medium and allows one to differentiate the systems which are produced at different collisions energies. As shown in the left panel of Fig. 2.9 the ratio $r_{\mathrm{AA}} = \langle p_{\mathrm{T}}^2 \rangle_{\mathrm{AA}} / \langle p_{\mathrm{T}}^2 \rangle_{\mathrm{pp}}$ divides the different collision energies into different regimes.

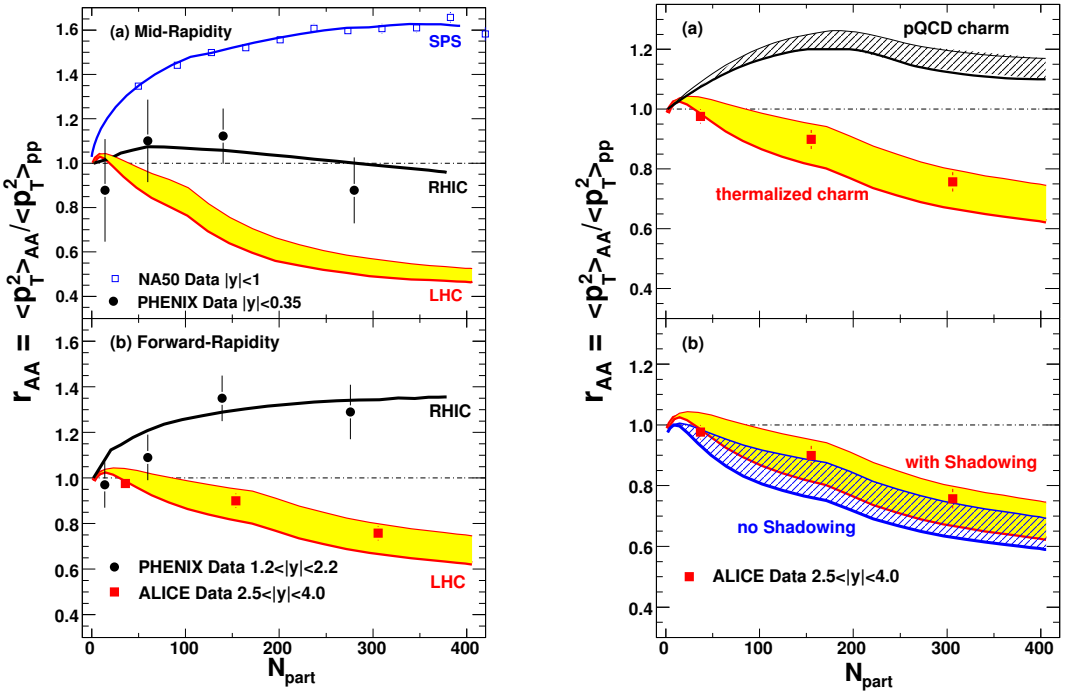

Figure 2.9: Left: Transport model predictions for the centrality dependence of r_{AA} at different collision energies compared to available data from SPS, RHIC and LHC. Right: Expectation for a hard pQCD charm quark distribution (a) and effect of nuclear shadowing of the PDFs (b) [145].

While at the SPS the J/ψ mesons are subject to transverse momentum broadening the production via (re)combination starts to become important at RHIC and leads to an almost flat r_{AA}. At LHC energies where the production from deconfined

thermalized charm quarks might become dominant for the bulk of the produced J/ψ the ratio drops below unity. The smooth decrease with centrality is caused by a greater importance of the production via (re)generation for more central collisions. The right panel part (a) of Fig. 2.9 shows the prediction for r_{AA} for the scenario of thermalized charm in the QGP and the expectation for a non-thermal pQCD charm quark distribution obtained from a simulation. For the hard charm quark distribution the r_{AA} exceeds unity which clearly separates the two scenarios. It is also shown in (b) that the observable r_{AA} is not very sensitive to the nuclear shadowing of the PDFs.
At the time Fig. 2.9 was published no mid-rapidity measurement by ALICE was available yet. A later measurement of the first two moments of the transverse momentum distribution of J/ψ $\langle p_{\mathrm{T}} \rangle$ and $\langle p_{\mathrm{T}}^2 \rangle$ showed indeed a suppression below unity [152]. However, the centrality dependence of both moments at mid-rapidity was inconclusive due to the limited precision of the measurement.

The motivation for a measurement of J/ψ production at $\sqrt{s_{\mathrm{NN}}} = 5$ TeV as presented in this thesis is twofold. Firstly, due to the increase of the charm cross-section (about a factor of 1.5 compare to 2.76 TeV [72]) a larger (re)generation component is expected which should be seen in the measurements. Secondly, due to a larger dataset the observables can be measured more precisely. In particular, the J/ψ spectrum in most central collisions and the transverse momentum dependence of the nuclear modification factor have not been determined with great accuracy yet at mid-rapidity. The J/ψ p_{T} spectrum in most central collisions carries information about deconfinement and thermalization of charm at low transverse momenta. In addition, a more precise measurement of the centrality dependence of the first two moments of the p_{T} distribution $\langle p_{\mathrm{T}} \rangle$ and $\langle p_{\mathrm{T}}^2 \rangle$ should improve the understanding of the onset of deconfinement and thermalization of charm in nucleus-nucleus collisions at the highest available collision energy.

2.5 Photoproduction

When the impact parameter of hadrons or nuclei is larger than the sum of the radii of the projectiles ($b > R_{\mathrm{A}} + R_{\mathrm{B}}$) they can still interact electromagnetically. The Lorentz contracted electric fields of the projectiles can be expressed as an equivalent photon flux based on the Weizsäcker-Williams method [154, 155] (see Fig. 2.10). These photons can induce interactions with the target nucleus (γ–A) or with another photon (γ–γ). These types of collisions are typically referred to as "ultraperipheral collisions" (UPC), reviews of the topic can be found in [153, 156]. Typically it is differentiated whether the interactions are of coherent or incoherent type. In the coherent case the photons are radiated by the nucleus as a whole and vector mesons or dilepton pairs are produced exclusively (i.e. the nuclei remain intact and no other particles are produced, see Fig. 2.11). In the transverse direction no Lorentz contraction is acting on the nuclei. Hence the uncertainty principle sets an upper limit on the mean photon wavelength which leads to a low[5] transverse momentum of the coherently produced J/ψ ($\langle p_{\mathrm{T}} \rangle \approx 60$ MeV/c [157]). In the incoherent case the transverse momentum of J/ψ is higher ($\langle p_{\mathrm{T}} \rangle \approx 500$ MeV/c) and the target nucleus breaks up.

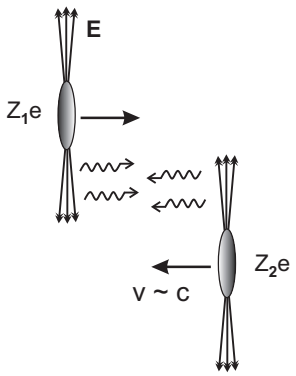

Figure 2.10: Sketch of the equivalent photon flux in UPC [153].

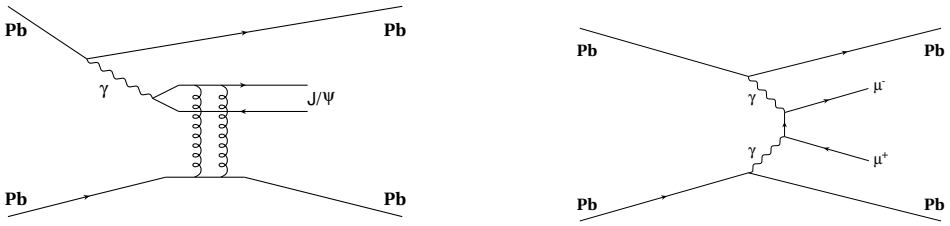

Figure 2.11: Exclusive photoproduction of J/ψ (left) and dilepton pairs (right) [158].

ALICE has measured exclusive J/ψ and e^+e^- photoproduction in UPC at forward and mid-rapidity at $\sqrt{s_{\mathrm{NN}}} = 2.76$ TeV. In the left panel of Fig. 2.12 the transverse momentum distribution of exclusively produced e^+e^- pairs is shown. The individual contributions are obtained using a fit with templates obtained from a simulation. The distribution is dominated by coherent J/ψ photoproduction and $\gamma\gamma \to e^+e^-$ at low transverse momentum. Measurements of this type are extremely useful since they can constrain the nuclear gluon PDFs in range $10^{-5} < x < 10^{-2}$ [157].
However, it has been realized that J/ψ photoproduction not only occurs in UPC

[5] compared to the mean transverse momentum of hadronically produced J/ψ mesons.

but also in heavy-ion collisions with hadronic interactions. The right panel of Fig. 2.12 shows the p_{T} distribution of dimuon pairs in Pb–Pb collisions with centrality 70–90%. A peak at very low transverse momentum is observed consistent with the expectation of coherent photoproduction of J/ψ. This excess is also present in semi-central collisions, however, the extraction becomes more difficult. With a larger dataset it might be possible to extract the signal also in central collisions in the future. Photoproduced J/ψ would be a unique external probe of the QGP and could constrain the suppression scenarios in model calculations. However, for measurements of hadronically produced or (re)generated J/ψ the photoproduction represents a background which has to be removed.

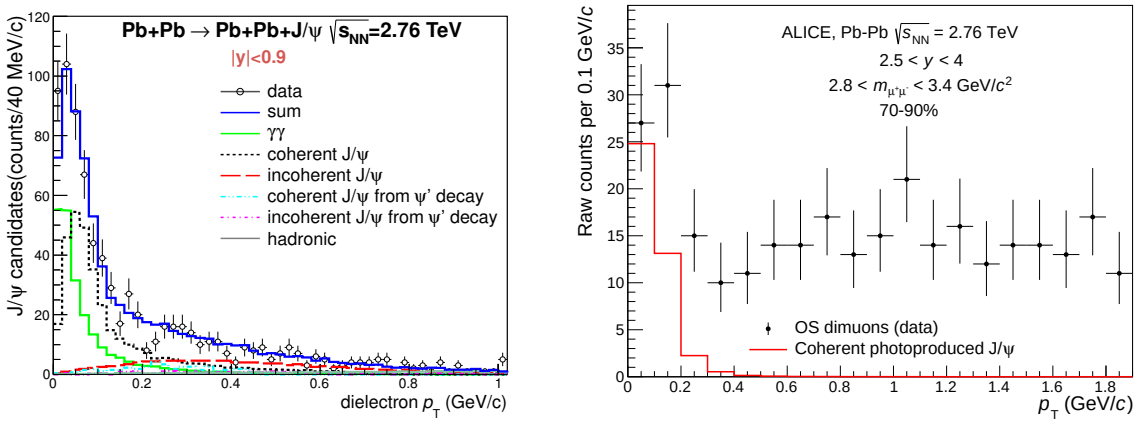

Figure 2.12: Left: Measurement of e^+e^- pair transverse momentum in exclusive events at mid-rapidity in the mass interval $2.2 < m_{e^+e^-} < 3.2$ GeV/c. The contributions are obtained from a fit based on simulated templates [159]. Right: Observation of an excess at very low p_{T} in the dimuon transverse momentum distribution consistent with photoproduced J/ψ in 70–90% Pb–Pb collisions at forward-rapidity [160].

3 A Large Ion Collider Experiment at the Large Hadron Collider

The purpose of this chapter is to introduce the experimental infrastructure which is required to study J/ψ production in Pb–Pb collisions with A Large Ion Collider Experiment (ALICE). The Large Hadron Collider (LHC) facilitates the collisions of heavy-ions and will be described in Sec. 3.1. The detection of produced particles takes place with ALICE which will be introduced in Sec. 3.2. The ALICE subsystems which are relevant for charmonium detection at mid-rapidity will be described therein. Finally, after a description of the ALICE data reconstruction procedure and the software framework, the ALICE approach to charmonium measurements will be described.

3.1 The Large Hadron Collider

The Large Hadron Collider [161] is a two-ring hadron collider located near Geneva in Switzerland and France. With its superconducting magnets operating at 8.33 T and its circumference of 26.7 km it is designed to enable pp collisions at a center-of-mass energy of up to $\sqrt{s}$ =14 TeV and Pb–Pb collisions at up to $\sqrt{s_{\mathrm{NN}}} = 5.5$ TeV. The tunnel was inherited from the previous LEP collider and is situated 45 m - 170 m below ground level. The CERN accelerator complex with the LHC and its accelerator chain [162] is shown in Fig. 3.1. For operation with protons hydrogen is injected into a duoplasmatron to strip off the electrons with the applied electrical field. Afterwards protons are delivered to the injection chain Linac2 — Proton Synchrotron Booster (PSB) — Proton Synchrotron (PS) — Super Proton Synchrotron (SPS) for subsequent acceleration before injection into the LHC. The protons are delivered in bunches of about $1.15{\cdot}10^{11}$ protons of which the LHC is designed to circulate up to 2808 with a spacing of 25 ns in one beam ring.
For operation with Pb beams the ions are generated by a plasma source which contains a small oven for Pb evaporation. In Linac3 the extracted Pb^{27+} ions are accelerated and afterwards partially stripped with a carbon foil. In the Low Energy Ion Ring (LEIR) Pb^{54+} ions are accumulated and cooled to create short high-density bunches before they are injected into the PS. Between the PS and the SPS the Pb ions are fully stripped with an aluminum foil resulting in a beam of Pb^{82+}. In the case of Pb beams the LHC is filled with 592 bunches per beam, each consisting of about $7{\cdot}10^7$ ions.
In the LHC the last acceleration step to the final collision energy takes place. The beams can be brought to collision in distinct interaction points where experiments

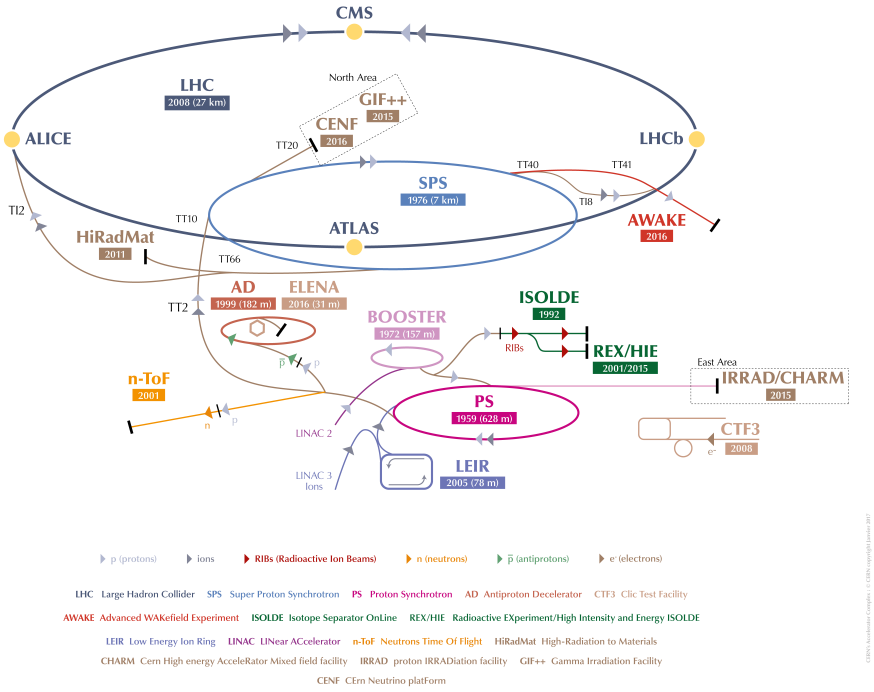

Figure 3.1: The CERN accelerator complex with the LHC and its accelerator chain [163].

are situated. When the beam intensity is significantly reduced or the beams become unstable they can be dumped into a carbon block surrounded by steel and concrete shielding (beam dump).

At the LHC there are four major experiments placed at the four interaction points: ATLAS [164], CMS [165], LHCb [166, 167] and ALICE [168]. Three smaller experiments share the interaction points of the larger experiments: LHCf [169], MoEDAL [170] and TOTEM [171].
ATLAS and CMS are high luminosity general purpose experiments with large acceptance at mid-rapidity. Great interest lies in the detection of the Higgs boson and studies of its properties. In addition, searches for new physics like supersymmetry, massive vector bosons and extra dimensions drive the research. Standard model studies and studies of high p_{T} or electroweak observables in heavy-ion collisions top off their program.
LHCb is running at lower luminosity and it situated at forward rapidity. It is focused on measurements of CP violation in the heavy quark sector. Also access to new physics can be gained by indirect searches. Recently LHCb has joined the heavy-ion research recording p–Pb and Pb–Pb collisions.
LHCf is situated at very forward rapidity up- and downstream ($\pm$ 140 m) of the interaction point used by ATLAS. Its purpose is to measure photons and neutral pions

in the very forward region in order to deliver important input for the understanding of cosmic ray physics.
MoEDAL is placed behind the LHCb detector at forward rapidity. Its objectives are the search for magnetic monopoles and highly ionizing massive particles.
TOTEM consists of tracking telescopes and Roman Pots up- and downstream of the interaction point of CMS. It is designed to measure elastic and diffractive scattering at small angles and to determine the total proton-proton cross-section.
The ALICE experiment will be described in detail in the next section.

3.2 A Large Ion Collider Experiment

ALICE [168, 172] is the dedicated heavy-ion experiment at the LHC. It is designed to study nuclear matter at extreme conditions of temperature and energy density as they were present in the early universe. ALICE is operating in the very low μ_b regime of the QCD phase diagram where a cross-over transition to a Quark-Gluon Plasma state is expected (see Sec. 1.1). It is the goal of relativistic heavy-ion research to observe and to characterize the produced medium and its phase transition. The variety of observables which are relevant for relativistic heavy-ion physics is reflected in the complex detector design of ALICE. Figure 3.2 shows the schematic layout of the experiment.

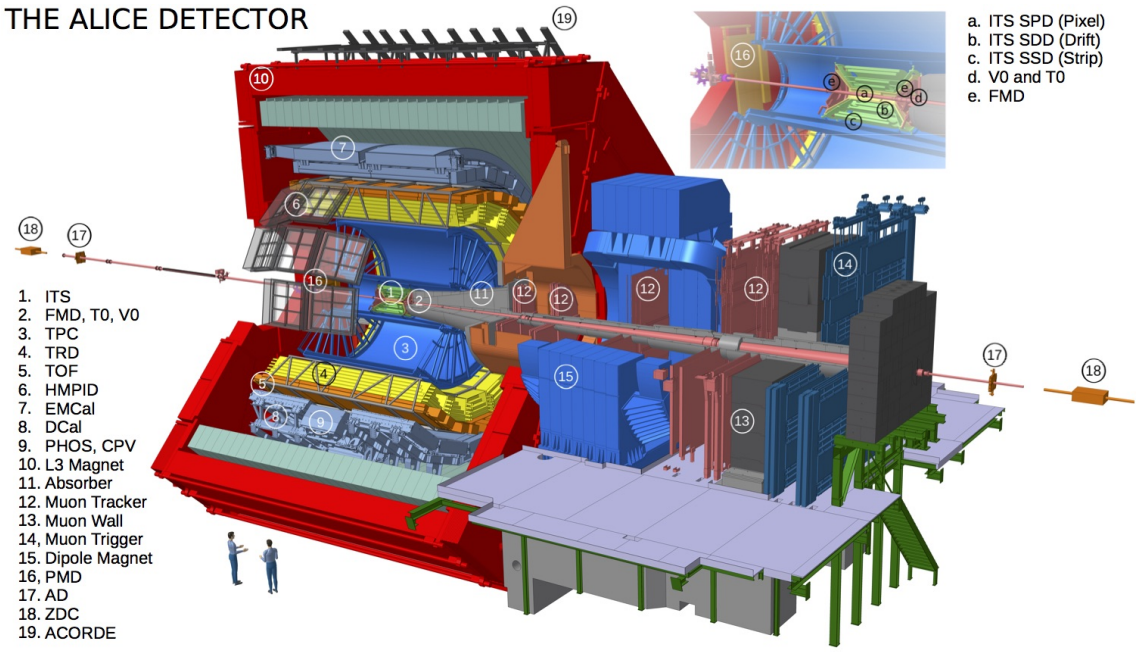

Figure 3.2: Schematic view of the ALICE detector [173].

ALICE has the approximate dimensions 16×16×26 m^3 and weighs about 10000 t. It consists of a central barrel which is contained in the L3 magnet and a muon spectrometer behind an absorber. Important detectors at mid-rapidity are the Inner

Tracking System (ITS), the Time Projection Chamber (TPC), the Transition Radiation Detector (TRD), the Time Of Flight Detector (TOF) and the calorimeters EMCAL/DCAL and Photon Spectrometer (PHOS). At mid-rapidity the detector choices can be understood by the necessity for high precision tracking, vertexing and particle identification in the high occupancy environment of central Pb–Pb collisions. Important observables at mid-rapidity are identified particle spectra/flow, heavy flavor and quarkonium production at low p_{T}, direct and thermal photon production and the dilepton continuum at low masses.
The muon spectrometer behind the composite absorber is designed to reconstruct quarkonium states via their $\mu^+\mu^-$ decays at forward rapidity ($2.5 < y < 4$). It consists of 10 detection planes, a dipole magnet and four planes equipped with trigger chambers. It is designed to have an invariant mass resolution of about 100 MeV/c^2 in the Upsilon mass range in order to resolve the different states.

For the interpretation of Pb–Pb collisions it is important that ALICE takes also pp and p–Pb collision data as a baseline. In addition, it is interesting to study those systems exclusively. Due to its great tracking and PID capabilities at low transverse momentum ALICE can contribute significantly to the understanding of QCD in a domain where the dynamics are governed by an interplay of hard and soft processes. Furthermore the question has been raised whether a QGP is formed also in high multiplicity pp or p–A collisions where effects are observed which are typically attributed to QGP formation ([174] and references therein).

The ALICE coordinate system uses the nominal interaction point as origin. The z-axis points counterclockwise along the LHC (away from the muon spectrometer) and is parallel to the mean beam direction. The x axis points towards the center of the LHC while the y axis points vertically upwards [172].

In the following we will describe the detectors which are relevant for the work presented in this thesis in more detail.

3.2.1 Inner Tracking System

As shown in Fig. 3.2 the Inner Tracking System (ITS) (described in detail in [168, 172]) is the innermost ALICE detector close to the interaction point surrounding the beam pipe. It consists of six cylindrical layers of silicon detectors with a combined acceptance of $|\eta| < 0.9$. The first layer has a larger pseudorapidity acceptance of $|\eta| < 1.98$ in order to allow for a continuous coverage of charged particle multiplicity measurements together with the Forward Multiplicity Detector (FMD). The granularity of the ITS layers decreases in outward direction because of the lower track density. Due to the large expected multiplicity in Pb–Pb collisions the two innermost layers are Silicon Pixel Detectors (SPD) with a very high granularity. The two intermediate layers are Silicon Drift Detectors (SDD) while the two outermost layers are Silicon Strip Detectors (SSD). The SDD and SSD have analogue readout

and allow for particle identification of low momentum particles.
The tasks of the ITS are:

- Localization of the primary interaction vertex with a precision better than 100 μm
- Reconstruction of secondary vertices from decays of hyperons, D and B mesons
- Tracking and particle identification of particles with momentum below 200 MeV/c
- Increasing the lever arm for track reconstruction and thus improving the momentum and position resolution of the tracking

3.2.2 Time Projection Chamber

The Time Projection Chamber (TPC) [175] is among the most important detectors in ALICE due its capacity to provide track reconstruction, momentum measurements and particle identification (PID) in a high occupancy environment. It was designed to cope with occupancies as high as $dN_{\mathrm{ch}}/d\eta = 8000$ which corresponds to 20000 charged primary and secondary tracks in the acceptance. The TPC covers the pseudorapidity $|\eta| < 0.9$ for tracks with full track length while tracks with reduced track length can be reconstructed up to $|\eta| = 1.5$. It covers the full azimuthal angle and provides precision momentum measurements in the region 0.1 GeV/c < p_{T} < 100 GeV/c. The TPC has a cylindrical shape with a length of 5 m in beam direction, an inner radius of about 85 cm and an outer radius of about 250 cm. The left panel of Fig. 3.3 shows the geometry of the TPC.

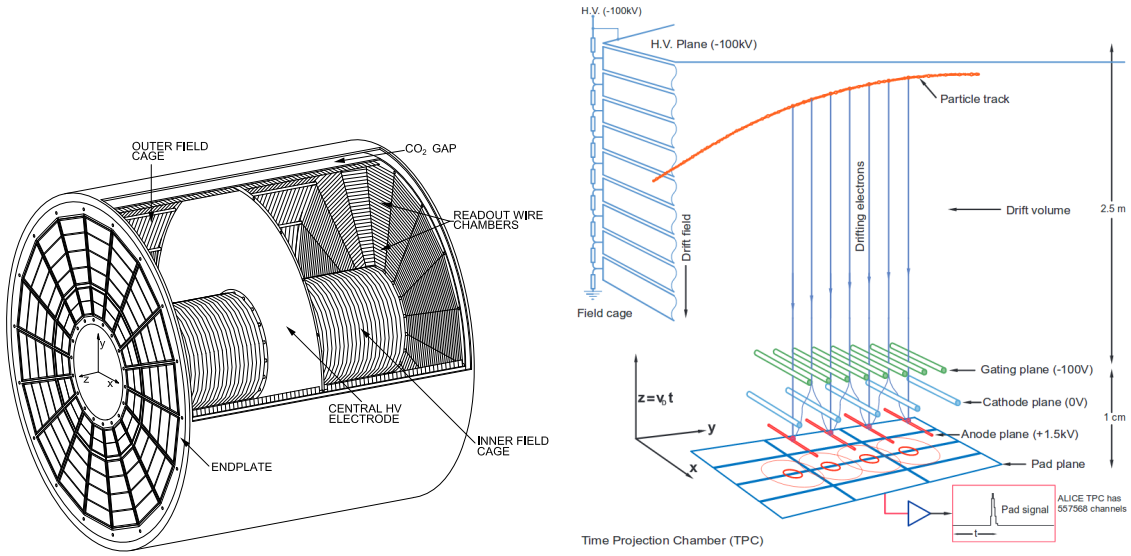

Figure 3.3: The ALICE TPC. Left: Geometry [175]. Right: Sketch of the working principle [176].

In the center a central electrode generates a drift field in the volume. On each end cap 18 multi-wire proportional chamber (MWPC) chambers with cathode pad readout are installed which are responsible for the signal creation and readout. The 90 m^3 gas volume was initially filled with a $Ne/CO_2/N_2$ (85.7/9.5/4.8) mixture [177]. Before the start of LHC Run 2 in 2015 the gas was replaced by Ar/CO_2 (88/12) to allow for a more stable running.
The working principle is sketched in the right panel of Fig. 3.3. When a charged particle traverses the gas volume it ionizes the gas along its path. The created electrons drift towards the end caps due to the applied electric field. In the vicinity of the anode plane the electrons are strongly accelerated and an avalanche is created. The ions which are created in the avalanche slowly drift away from the anode plane and induce a signal on the pads in the pad plane. The cathode wire plane separates the electron drift volume from the amplification volume and is designed to collect the back drifting ions. However, simulations showed that back drifting ions are also collected on the pad plane and in some cases at the gating grid, giving rise to a complex signal tail structure [177]. The Gating Plane has been designed to mitigate its penetration by drifting electrons or back drifting ions in the absence of a collision trigger. Blocking back drifting of ions is necessary to avoid severe distortions of the drift field.
At the central electrode a voltage of 100 kV is applied which leads to a drift field of 400 V/cm and a drift time of 94 μs respectively. After the electron drift time the gating grid is closed for 200 μs (Ne) or 400 μs (Ar) in order to block back drifting ions [178]. Together with the readout time of the front-end electronics this limits the maximum readout rate of the TPC. In 2010 the maximum readout rate was 2.7 kHz in pp collisions and 656 Hz in Pb–Pb collisions [179].
The TPC delivers full 3D reconstruction of the particle tracks. The x and y information is deduced from the projection of the track on the pad plane. The drift time with respect to a collision trigger gives information about the z coordinates of the clusters of each track. Since a nominal magnetic field of 0.5 T is applied in z direction, the tracks are bent in the $x-y$ plane and their momentum can be calculated from the track curvature. The initial ionization of the gas depends on the momentum and mass of the traversing particles. Thus, the collected signal can be related to the energy loss of the particle $\mathrm{d}E/\mathrm{d}x$.

The **particle identification** (PID) with the TPC is based on the specific energy loss $\mathrm{d}E/\mathrm{d}x$ of the charged particles propagating through the active volume. The mean energy loss of a particle per traversed unit length of material $\langle\frac{dE}{dx}\rangle$ can be calculated with the Bethe-Bloch equation. However, in order to calculate track ionization in drift chambers the energy loss calculation must be restricted to processes below a certain energy transfer E_{cut} which are typically not identified to be associated to the

track (e.g. δ electrons). The restricted energy loss formula reads [180]:

$$\left\langle \frac{\mathrm{d}E}{\mathrm{d}x} \right\rangle \propto \frac{z^2}{\beta^2} \left[\ln \frac{\sqrt{2m_e c^2 E_{\mathrm{cut}}}\beta\gamma}{I} - \frac{\beta^2}{2} - \frac{\delta}{2} \right], \tag{3.1}$$

with the relativistic factors β, γ, the charge of the ionizing particle z, the electron mass m_{e}, the effective excitation energy of the ionized material I and the density effect correction factor δ. Prefactors containing natural or material constants have been omitted for clarity and can be found in [181]. For particles with intermediate velocities ($\beta\gamma < 0.5$) the energy loss decreases as $1/\beta^2$. At higher velocities around $\beta\gamma \approx 4$ they reach the minimum ionizing region. Increasing the velocity leads to a contraction of the electric field lines of the penetrating particles. The field lines are stretched in the direction perpendicular to the propagation and the energy loss increases as $\ln\beta\gamma$ ("relativistic rise"). For even higher velocities the lateral extension of the electric field is attenuated due to a polarization of the penetrated medium. Thus, the restricted energy loss becomes constant at the highest energies and leads to the "Fermi plateau".
Experimentally, the energy loss is reconstructed from a maximum number of 159 independent measurements in the 159 pad rows in the TPC readout chambers. The individual charge deposition ΔQ can be obtained by integrating the charge (Q_{tot}) or the maximum charge deposition (Q_{max}). In order to obtain a single value of the energy loss of a particle the individual measurements need to be combined. However, since the underlying ionization distribution is a Landau distribution a simple mean calculation is affected by outlier fluctuations [182]. Instead, the energy loss distribution is truncated to contain only the entries with the lowest 60% charge depositions. The obtained truncated mean then yields a reliable estimate of the energy loss and is approximately Gaussian. Figure 3.4 shows the TPC $\mathrm{d}E/\mathrm{d}x$ as a function of the rigidity p/z for the Pb–Pb data relevant for this thesis.
The shape of the distributions of the different particles can be explained with the above mentioned regimes in the restricted Bethe-Bloch equation considering their mass and charges.
The TPC $\mathrm{d}E/\mathrm{d}x$ is parameterized with functions of Bethe-Bloch type as a function of momentum[1] (see [182] for more details). Since not everywhere in the momentum space particles can be clearly separated, the parameterization is carried out on clean topologically selected V^0 daughter tracks. In addition the resolution is parameterized so that the measured $\mathrm{d}E/\mathrm{d}x$ of a particle can be expressed in terms of the deviation to the expectation:

$$n_{\sigma,TPC}^{\mathrm{species}} = \frac{\mathrm{d}E/\mathrm{d}x - \mathrm{d}E/\mathrm{d}x_{\mathrm{expected}}^{\mathrm{species}}}{\sigma_{\mathrm{expected}}^{\mathrm{species}}}. \tag{3.2}$$

This variable allows for a quantitative selection of the desired particles.

[1] also η and multiplicity corrections are applied depending on the dataset

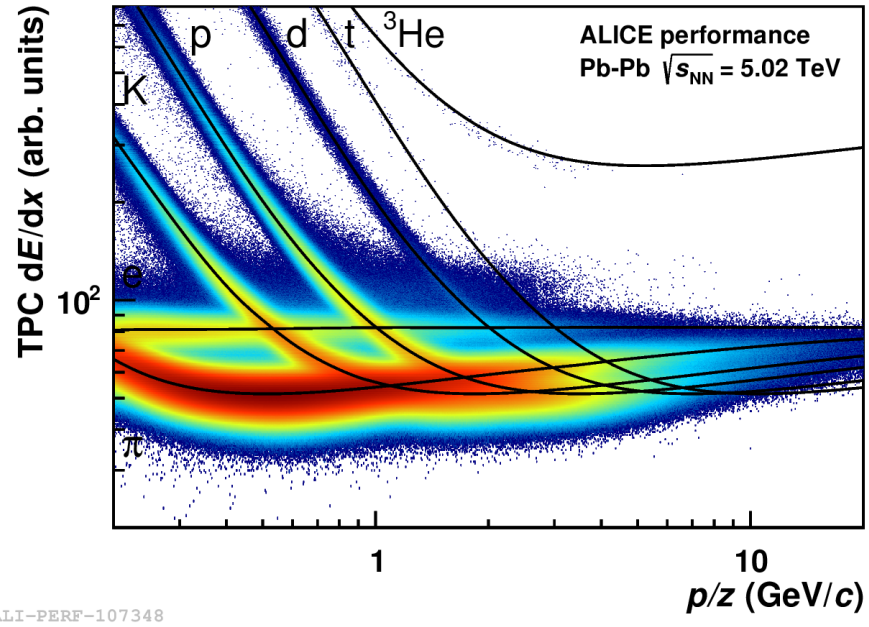

Figure 3.4: Specific energy loss $\mathrm{d}E/\mathrm{d}x$ as a function of the rigidity p/z measured with the TPC in Pb–Pb collisions at 5.02 TeV. Solid lines represent the expected energy loss for different particles [173].

3.2.3 Transition Radiation Detector

The TRD [183] was designed to provide electron identification at high transverse momentum ($p_{\mathrm{T}} > 1$ GeV/c) in order to enable measurements of light and heavy vector mesons as well as the dilepton continuum and electrons from open heavy flavor decays. In addition its triggering capabilities should enhance the samples of Υ, high p_{T} J/ψ, high mass dilepton pairs and jets at high transverse momentum. Besides its electron identification and triggering capabilities it also contributes to the calibration and track reconstruction at mid-rapidity [184].

As shown in Fig. 3.5 the TRD is situated just outside of the TPC. It covers the pseudorapidity range $-0.84 < \eta < 0.84$ and the full azimuthal angle. The 18 TRD supermodules contain in general 5 stacks of 6 layers of readout chambers. Three stacks in front of the PHOS detector are omitted, totaling to 522 readout chambers in the TRD. More information about the front-end electronics and its detector control system can be found in Appendix E.
The TRD is filled with $\mathrm{Xe/CO_2}$ with a nominal admixture of 85/15. The particle identification power of the TRD is based on ionization of the gas plus the emission of transition radiation (TR) by highly relativistic electrons. Transition radiation is emitted when a highly relativistic particle ($\gamma \gtrsim 1000$) propagates across the boundary between two materials with different dielectric constants. In order to increase the radiation yield many layers are necessary which is realized in the TRD by a radiator

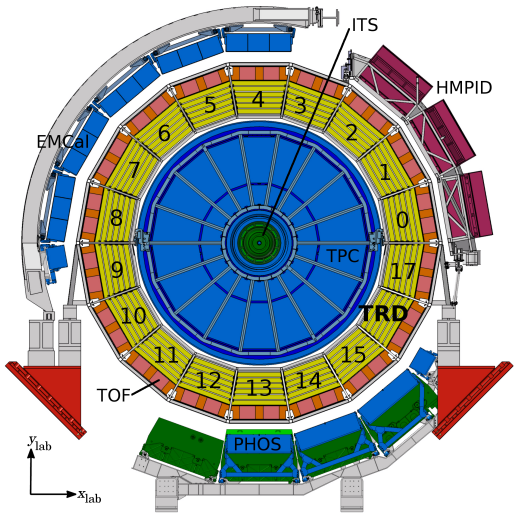

Figure 3.5: Slice of the ALICE central barrel in beam direction [184].

made of a fibre/foam sandwich. The radiation is in the X-ray domain and very forward peaked. For typical TR photon energies the absorption length in Xe is less than a centimeter giving rise to a unique ionization signature at the beginning of the gas layer in case of TR emission. In the left panel of Fig. 3.6 a scheme of the TRD working principle is shown.

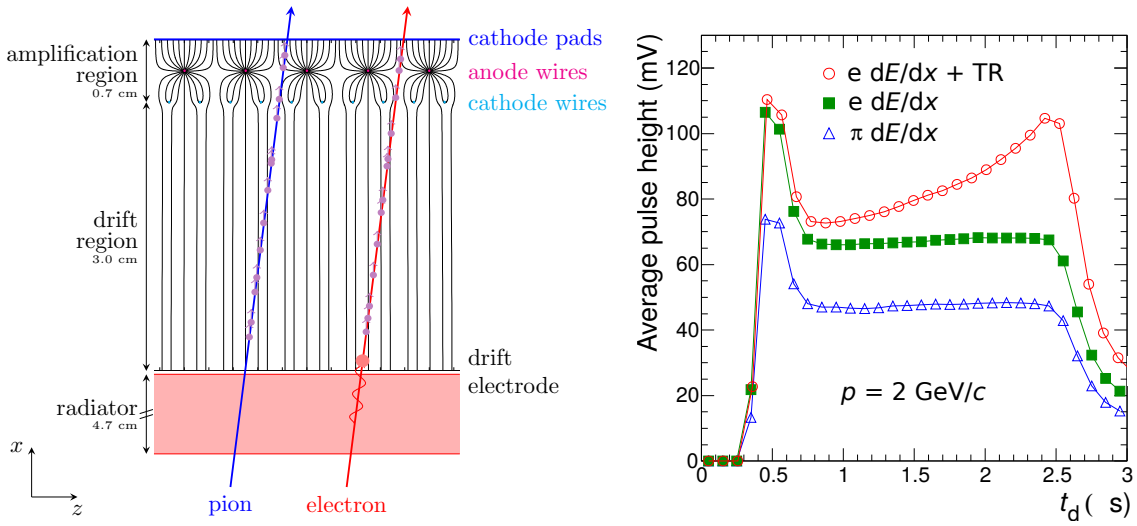

Figure 3.6: Left: Illustration of generated ionization along the path of electrons and pions through a TRD chamber. Right: Measured average puls height distribution as a function of the signal arrival time. Both taken from [184].

Since pions are not yet highly relativistic ($\gamma < 1000$) in the momentum range of interest no TR is released upon penetration of the radiator. Nevertheless they ionize the gas according to the Bethe-Bloch equation. However, in case an electron passes through the radiator TR is released and absorbed in the beginning of the drift region.

The gas volume is also ionized by the passage of the electron in addition. The generated charges are drifting towards the amplification region where avalanches are created and signals are induced on the cathode pads. The right panel of Fig. 3.6 shows the average signal as a function of its arrival time for pions and electrons (with and without TR). At early times avalanches are created from two sides of the anode wires in the amplification region yielding a pronounced peak. Afterwards the ionization from the drift region is detected where the TR induced ionization yields a peak at late times. The time structure of the signal is exploited with different PID methods in order to effectively separate electrons and pions [184].

3.2.4 Other detectors

The **V0** detector consists of two scintillator arrays **V0A** and **V0C** covering $2.8 < \eta < 5.1$ and $-3.7 < \eta < -1.7$ respectively. It provides the minimum bias trigger which is used in all collision systems by requiring a coincident signal in both arrays. It also enables measurements of the multiplicity in the event which is used for the centrality determination in Pb–Pb collisions. Based on the signal arrival time in both detectors beam induced background events can be rejected [172].

The **Zero Degree Calorimeters (ZDC)** are a set of neutron (**ZN**) and proton (**ZP**) calorimeters placed 112.5 m away from the IP on both sides of the ALICE detector close to the beam pipe. They are designed to detect spectator neutrons and protons. In addition there are two electromagnetic calorimeters (**ZEM**) placed 7.3 m away from the IP. When the measurements of the ZDCs and the ZEMs are combined an independent centrality determination can be carried out. Also, parasitic beam collisions which take place outside of the fiducial vertex region $|z_{\mathrm{vtx}}| \leq 10$ cm can be rejected using timing information from the ZN calorimeters. Very importantly, electromagnetic dissociation events can be rejected based on the correlation of energy measurements in the neutron calorimeters.

Details on the **other ALICE detectors** which were not described in this chapter can be found in [168].

3.3 Data reconstruction

The **event and track reconstruction** in ALICE is carried out in multiple steps as depicted in Fig. 3.7. First, the detector signals need to be converted to clusters which contain information about the time and space coordinates and the signal. This is done for each detector individually. Afterwards a preliminary determination of the primary vertex is carried out based on the space point of convergence of most SPD tracklets[2].

[2] A tracklet is a straight line connecting clusters. In case of the SPD a tracklet is formed by the positions of the clusters in the first and second layer.

The track reconstruction is based on an inward-outward-inward scheme starting at the outer radius of the TPC. The seeds are propagated inward and updated with clusters newly assigned to the track. A special algorithm takes care that the same track is not reconstructed twice by comparing the number of shared cluster between two tracks. The TPC tracks are finally propagated to the outer radius of the ITS where they are used as seeds. In the ITS tracking the tracks are updated with all clusters within a fiducial distance, giving rise to multiple seeds at each step. Penalty factors are added to the χ^2 of the track in case no associated cluster was found in a given layer. The tracks with the best quality are checked for shared clusters and the best one is used. In order to increase the detection efficiency of low momentum pions and protons which are subject to energy loss and multiple scattering in the material an ITS standalone tracking is carried out in addition. Afterwards the tracks are propagated to their closest approach to the preliminary vertex and are propagated outwards, updating the track kinematics subsequently. Outside the TPC the tracks are matched to tracklets in the TRD and the TOF clusters if possible. Further outwards propagation is used for the matching to the EMCAL, PHOS and HMPID detectors. The (primary) track reconstruction is finalized by a last full inwards propagation. For the final vertex determination the tracks are propagated inwards to find the point of their closest approach and to carry out a precision vertex fit. The event reconstruction in finalized by secondary vertex and cascade finding.

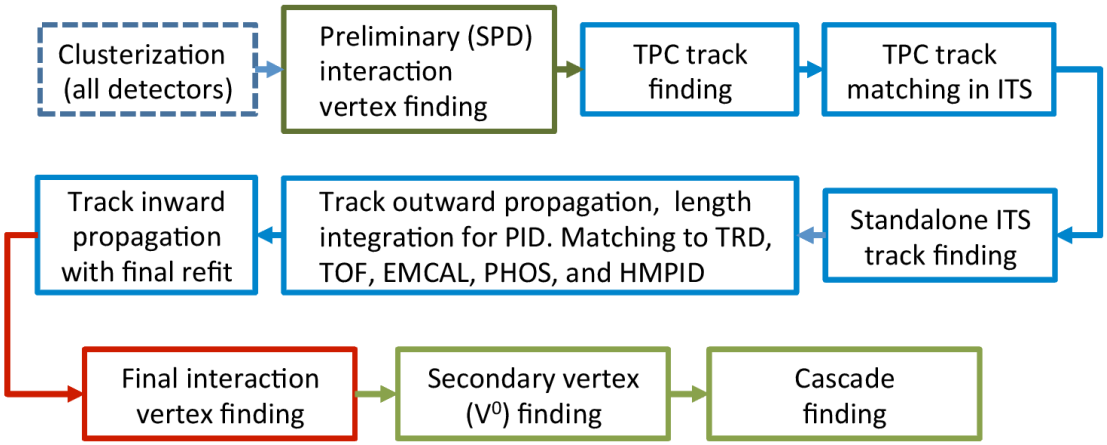

Figure 3.7: Schematic of the event reconstruction sequence [172].

After the Pb–Pb data reconstruction the **centrality determination** [185] is carried out based on the Glauber Monte Carlo approach (see Sec. 1.2.2). The centrality is defined in ALICE as a percentile of the total hadronic cross-section. The Glauber Monte Carlo is used to simulate the geometry of Pb–Pb collisions event-by-event. The geometrical quantities are obtained by integrating over a large simulation sample. In order to reproduce the experimentally measured multiplicity distribution in the V0 scintillators the Glauber Monte Carlo is coupled to a two-component particle

production model which is based on a negative binomial distribution (NBD). The NBD-Glauber model is then fit to the measured V0 amplitude distribution (see Fig. 3.8). Afterwards the V0 amplitude distribution is sliced into centrality percentiles and the mean geometrical quantities therein ($\langle N_{\mathrm{part}} \rangle$, $\langle N_{\mathrm{coll}} \rangle$ and $\langle T_{\mathrm{Pb-Pb}} \rangle$) are extracted using the model. The centrality determination is only carried out up to a centrality of 90% due to the contamination with electromagnetic processes in the very peripheral events.

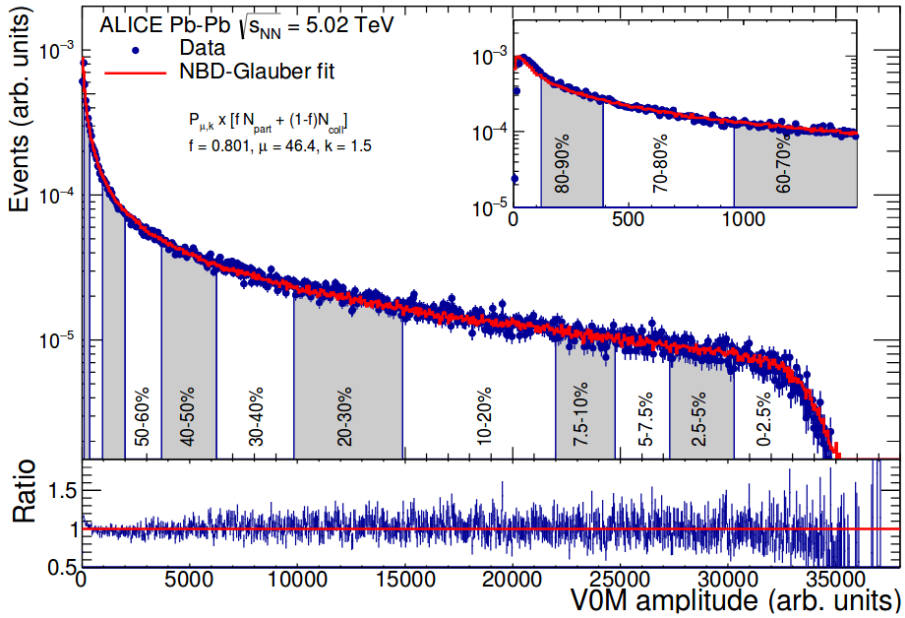

Figure 3.8: Fit of the V0 amplitude distribution with the NBD-Glauber model. Centrality percentiles are indicated as slices of the distribution [185].

3.4 Data processing and analysis framework

The ALICE offline software which is used to process and analyze the recorded data is based on ROOT [186]. ROOT is a C++ based environment which provides the framework for simulations, reconstruction and data analysis. In order to have a framework which is fully adapted to the needs of ALICE the ROOT based AliRoot [187] and AliPhysics [188] frameworks have been developed. AliRoot contains detector specific implementations which are required for reconstruction and calibration while AliPhysics contains the analysis tools of the different physics working groups.
During the reconstruction the raw data is processed and the results are written into Event Summary Data (ESD) objects. These contain the reconstructed vertices, tracks, particles reconstructed in the calorimeters and also V^0 and cascade candidates. Data analysis can be carried out directly on the ESDs or they can be filtered to Analysis Object Data (AOD) in order to reduce the occupied disk space and to

reduce the processing time. The AODs contain information which can be tailored to the needs of the physics working groups. For J/ψ analysis at mid-rapidity it has turned out to be useful to create reduced trees from the ESDs. These reduced trees contain already a loose selection of electron candidates and track information which is user definable. With this data format the data volume from one Pb–Pb data taking period can be less than 1 TB and even few GB for a pp data taking period. The small occupied disk space enables data analysis on small computing farms or even on user laptops with the reducedTree framework. The reducedTree framework contains all the basic classes and methods which are required for a J/ψ analysis. It contains classes which hold the event and track properties, enable selection criteria, implement the background models and signal extraction techniques. Within the scope of the work presented in this thesis a significant contribution to the reducedTree framework was made by debugging and developing code.

3.5 Charmonium measurement with ALICE

In ALICE charmonium measurements can be carried out at mid-rapidity with the central barrel detectors ($|y| < 0.9$) or at forward rapidity with the muon spectrometer ($2.5 < y < 4$). The muon spectrometer is placed behind an absorber to remove the hadronic background. With this system the non-prompt component of J/ψ cannot be resolved and thus all measurements are inclusive. However, due to the operation with dedicated muon triggers large luminosity samples can be recorded. In addition, no particle identification is necessary due to the thick absorber.
At mid-rapidity charmonia can be reconstructed with the central barrel detectors (ITS, TPC, TRD) in the dielectron decay channel. Due to the good tracking and position resolution with the ITS the prompt and non-prompt components of the J/ψ can be separated based on the distance of production from the primary vertex. At mid-rapidity the dominant data taking strategy is to collect minimum bias data for low p_{T} physics. Together with the aforementioned readout rate limitations (see Sec. 3.2.2) this stringently limits the amount of acquired statistics. TRD triggers which would enhance the collected charmonium sample are only available in pp and p–Pb collisions. In addition, scarcely produced electrons need to be identified from the abundant pion, kaon and proton background in a high occupancy environment.
However, in both rapidity windows J/ψ can be reconstructed down to $p_{\mathrm{T}} = 0$ which is unique at the LHC. Figure 3.9 shows the kinematic acceptances of the different LHC experiments participating in J/ψ measurements in Pb–Pb collisions based on the Run 1 publications.
ATLAS and CMS are using dedicated muon triggers with a single track p_{T} threshold for their measurements of J/ψ production in Pb–Pb collisions which limits their acceptance to the high p_{T} region. LHCb has joined the Pb-Pb data taking only recently and is limited by the current tracking algorithm to peripheral events with centrality larger than 50% [190].

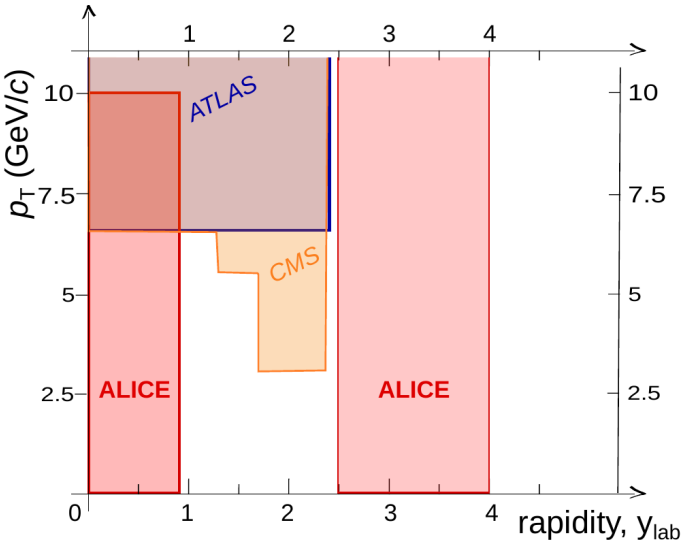

Figure 3.9: Kinematic acceptance of the LHC experiments for J/ψ measurements in Pb–Pb collisions based on Run 1 publications [189].

4 Measurement of J/ψ yields in Pb-Pb collisions

The objective of this chapter is the measurement of J/ψ yields in Pb–Pb collisions at $\sqrt{s_{\mathrm{NN}}} = 5.02$ TeV. The measurement of the J/ψ yields as a function of centrality, rapidity and transverse momentum was carried out in common efforts within the ALICE analysis group J/$\psi \to e^+e^-$. The contributions which have been made within the scope of this thesis will be described in this chapter.

4.1 Datasets

The Pb–Pb collision data that are used for the analyses presented in this thesis were recorded at the end of 2015 in a dedicated Pb–Pb running period of the LHC. The intensity of the beams and the interaction rate were increased gradually during this period. The beams consisted of a maximum number of 518 Pb bunches spaced by 150 ns and were colliding at a maximum interaction rate of 7.5 kHz. The probability for the readout of more than one collision during the detector readout time ("pile-up") can be estimated using the average number of inelastic collisions within one bunch crossing:

$$\mu = \frac{f_{\mathrm{int}}}{f_{\mathrm{rev}} \cdot N_{\mathrm{b,coll}}}, \tag{4.1}$$

with the inelastic interaction rate f_{int}, the LHC revolution frequency f_{rev} and the number of colliding bunches $N_{\mathrm{b,coll}}$. Using the Poissonian distribution for the number of inelastic collisions the probability of having more than one interaction per bunch crossing is estimated to be around 10^{-6}. Even if more than one interaction took place during one bunch crossing the good resolution of the vertex determination including SPD information is expected to resolve possible pile-up vertices. Thus, same bunch pile-up is considered to be negligible. On the other hand the 94 μs readout time of the TPC integrates over a few hundred bunch crossings for the bunch spacing schemes relevant for this data. If more than one interaction occurs within this time the occupancy in the TPC will be higher and might lead to a deterioration of its performance. It is estimated that this is the case for about 31 % of the recorded events assuming the highest interaction rate for all of them. Surely, this can be considered as an upper limit due to the gradual increase of the beam intensity and interaction rates during data taking. The implications of these considerations on the event selection will be described in Sec. 4.2.

In order to correct measured J/ψ distributions for acceptance and efficiency of the ALICE apparatus a dedicated Monte Carlo (MC) simulation was produced. In the simulation collisions of Pb nuclei are generated with HIJING [191] while the transport of produced particles through the simulated ALICE detector is carried out with GEANT3 [192]. Since J/ψ mesons are only scarcely produced in minimum bias simulations and the reconstruction of Pb–Pb events can take quite long due to the high track density the following strategy was used: Primary and non-prompt J/ψ mesons produced by PYTHIA 6 [193] are injected into the Pb–Pb events in the ratio 70:30. The prompt component is separated into three parts: At low to intermediate p_{T} (0–6 GeV/c) J/ψ mesons are generated with a smooth p_{T} spectrum. This spectrum is derived from an interpolation procedure of PHENIX, CDF and LHC measurements according to [194]. In order to enhance the low ($p_{\mathrm{T}} < 0.5$ GeV/c) and high p_{T} ($p_{\mathrm{T}} > 6$ GeV/c) components J/ψ mesons with a flat p_{T} spectrum are additionally generated in those regions (see Fig. 4.1). The low p_{T} J/ψ signals are especially important for the analysis of the J/ψ photoproduction in Pb–Pb collisions which is currently carried out [195]. The different components of the prompt J/ψ sources are injected with the ratio 10:3:3 while about 12 J/ψ are injected in total per event into the acceptance. The implications of the different p_{T} shapes of the injected J/ψ mesons for the efficiency calculation will be discussed in Sec. 4.6. Finally, the J/ψ mesons are forced to decay into an electron and a positron which is handled by the EvtGen [196] package which uses PHOTOS [197] for the calculation of the QED final state radiation. In total 1.1×10^6 simulated Pb–Pb events have been analyzed.

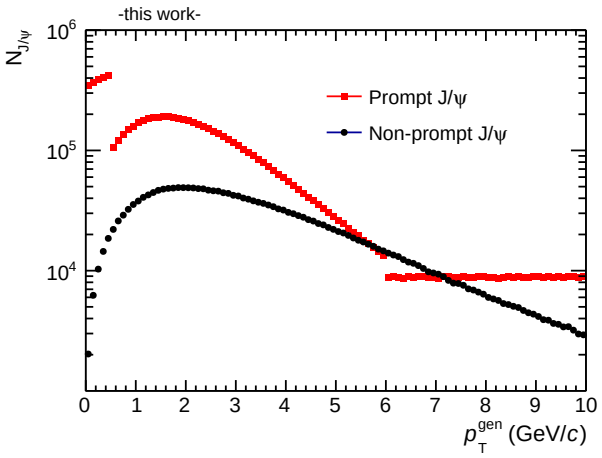

Figure 4.1: Transverse momentum distribution of generated J/ψ signals.

4.2 Event selection

The Pb–Pb dataset used for this work was recorded with minimum bias triggers provided by coincident signals in the V0 detectors. Beam induced background and

electromagnetic interactions are rejected as explained in Sec. 3.2.4.
In addition it is required that a vertex could be reconstructed for the events and that the z coordinate of the vertex position lies within $|z| < 10$ cm from the nominal interaction point. The latter requirement is used to reject events with a reduced acceptance compared to events which occur close to the nomimal vertex position in ALICE.

The data were recorded in the beam period "LHC15o" and were split into different samples for the reconstruction. An initial dataset was recorded at low interaction rates of 300–400 Hz ("LHC15o_lowIR"), constituting only 3% of the overall sample. The dominating sample was taken at interaction rates of 1–7.5 kHz and is split into "LHC15o_highIR" and "LHC15o_pidfix". For all the samples dedicated TPC PID parameterizations are provided due to a slightly different TPC performance.
During the quality assurance of the data the effect of pile-up in the TPC mentioned in Sec. 4.1 was investigated. In Fig. 4.2 the multiplicity measured in the V0 scintillators for a given triggered event is shown versus the number of tracks in the TPC[1]. In case of a low interaction rate scenario (left panel) the two multiplicity estimators show a narrow correlation (except for a few outliers which will be explained later). This indicates that in a heavy-ion collisions the multiplicity at forward rapidity and the multiplicity at mid-rapidity are strongly correlated. However, in a high interaction rate scenario (right panel) also detector effects become important. Since the TPC readout time is on the order of a few hundred bunch crossings for this data also tracks which originate from a different bunch crossing are detected in the TPC. This leads to the population of the plot on the right side of the main correlation. In these events the triggered event is overlapped by one or more collisions from a different bunch crossing in the TPC. This leads to the observation that the TPC occupancy is higher than expected by the physics correlation.

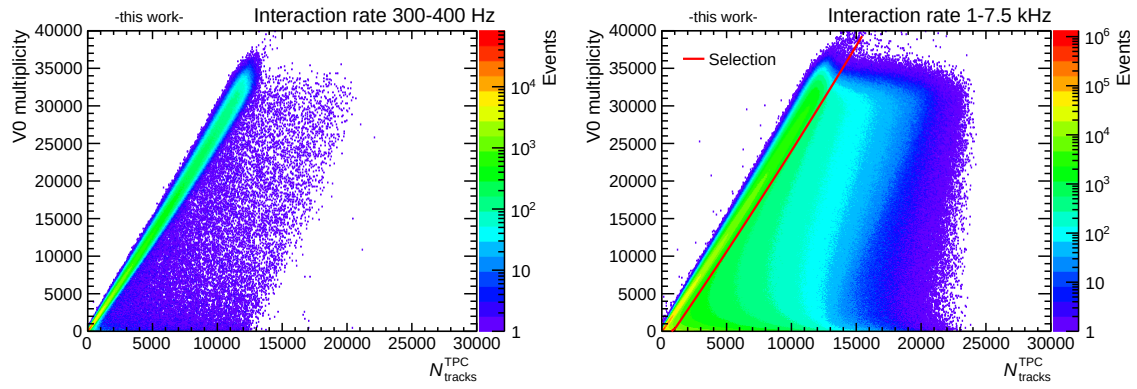

Figure 4.2: Multiplicity measured in V0 scintillators versus number of tracks in the TPC. Left: Low interaction rate data. Right: High interaction rate data.

The triggered events which are overlapped by collisions from a different bunch crossing

[1] A TPC track is defined here as a track which is reconstructed in the TPC and reaches its outer radius

in the TPC have been investigated in detail within the collaboration [198]. It was found that the TPC tracking and PID performance are significantly deteriorated by the higher occupancy. Since J/ψ analyses require a very good tracking and particle identification it was decided to use the following strategy: Based on the correlation of V0 multiplicity and TPC multiplicity observed in low interaction rate data a selection was applied to the events in high interaction rate data (see Fig. 4.2 right panel). With this selection the events in which the pile-up from a different bunch crossing in the TPC is relevant are rejected.
Figure 4.3 shows the distribution of the z position of the interaction vertex and the centrality distributions for the selected events. The distribution of the z coordinate of the vertex shows the typical Gaussian shape while the centrality distribution is flat on a percent level. These plots demonstrate that the obtained event sample is unbiased.

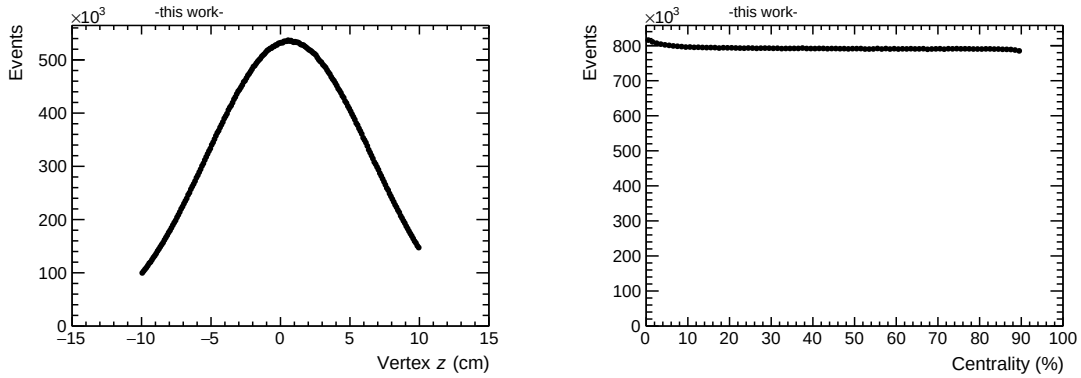

Figure 4.3: Left: Distribution of the z coordinate of the interaction vertex for the selected events. Right: Centrality distribution of the selected events.

The event statistics of the datasets which are used for the Pb–Pb analysis presented in this thesis is summarized in Tab. 4.1. Due to the very low statistics and the necessity for an additional PID calibration the low interaction rate data is not used for the J/ψ measurement.

	LHC15o_highIR	LHC15o_pidfix	Total
$N_{\text{events, selected}}$	45.69 $\times 10^6$	25.68 $\times 10^6$	71.37 $\times 10^6$

Table 4.1: Number of events after selection for the datasets used in the Pb–Pb analysis presented in this thesis.

4.3 Track selection

The analysis of J/ψ in the e^+e^- decay channel requires the selection of good candidate tracks. The acceptance of the tracks is defined to be $p_{\mathrm{T}} > 1.0$ GeV/c and $|\eta| < 0.9$.

The rationale for the minimum transverse momentum is the high low p_{T} electron background originating from photon conversions or semileptonic heavy flavor decays. With the mentioned selection J/ψ mesons can still be reconstructed down to p_{T} = 0 since J/ψ produced at rest will decay into electrons with momenta of about[2] $m_{\mathrm{J}/\psi}/2 \approx 1.55$ GeV/c. The pseudorapidity acceptance is given by the requirement of full track length in the TPC. In order to benefit from the larger resolution and low pile-up contributions the tracks are required to have a refit in the ITS besides the TPC. In addition, tracks are required to have a hit in one of the two innermost layers (SPD) to reject a substantial part of electrons from photon conversions. The distance of closest approach (DCA) of the track to the primary vertex is selected to be within 1 cm in the $x - y$ plane and within 3 cm in the z direction. This loose selection assures that the reconstruction efficiency of prompt and non-prompt J/ψ are similar. Tracks which originate from a kink topology (e.g. weak decay products) are rejected. In addition, quality selection criteria related to the number of clusters in the TPC and the χ^2 of the track fit in the ITS and TPC are applied. A track can have a maximum number of 159 clusters in the TPC corresponding to 159 TPC pad rows in radial direction. The maximum number of clusters is divided into 8 consecutive segments. A segment is considered to be active if at least 5 clusters have been found. A selection of a minimum number of TPC segments assures a uniform distribution of clusters along the tracks (to avoid tracks with e.g. missing TPC parts). A summary of the applied track selection criteria can be found in Tab. 4.2.

Variable	Selection
p_{T}	> 1 GeV/c
$\lvert\eta\rvert$	< 0.9
$\lvert\mathrm{DCA}_{xy}\rvert$	< 1 cm
$\lvert\mathrm{DCA}_{z}\rvert$	< 3 cm
ITS refit	true
TPC refit	true
Rejection of kink daughters	true
Hit in which SPD layers	any
ITS χ^2/cluster	< 10
TPC cluster	> 70
TPC segments	>5 (> 6 in 0–10% centrality)
TPC χ^2/cluster	$< 1.9 + 1.1{\cdot}10^{-4}{\cdot}\ N_{\mathrm{tracks}}^{\mathrm{TPC}}$ (< 2.5 in 0–10% centrality)
Fraction of TPC shared clusters	< 0.3
Ratio of TPC crossed rows and findable clusters	$\in [0.8, 2.0]$

Table 4.2: Summary of applied track selection criteria.

[2]neglecting the small momenta taken away by the photon in the NLO decay J/$\psi \to e^+e^-\ \gamma$ and bremsstrahlung in the detector

Finally, in order to select electrons from the vast amount of other particles (e.g. pions, kaons and protons) a particle identification needs to be carried out. The strategy followed in this analysis will be detailed in the next section.

4.4 Electron identification with the TPC

In the ALICE central barrel several detectors have electron identification capabilities. With the ITS and TOF detectors electrons can be identified at low momenta of $p < 200$ MeV/c (ITS) and $p < 1$ GeV/c (TOF). In the TPC electrons can be identified over a wide range in momentum which is only limited by the ambiguities in the crossing of the kaon, proton and pion bands at intermediate and high momentum, respectively (see Fig. 3.4). The TRD was designed to provide electron identification in the central barrel for electrons above momenta of 1 GeV/c. However, the crossing of the pion and electron band in the TPC only becomes relevant for momenta larger than $p \approx 5$ GeV/c.
Since the TPC is a central part of the tracking in the central barrel the efficiency of a PID signal is close to 100% for a reconstructed track. The more outward detectors TRD and TOF are only matched to an ITS-TPC track if possible and thus those detectors suffer from finite matching efficiencies. The TOF matching efficiency was around 70% at $p_{\mathrm{T}} = 1$ GeV/c in the 2013 p–Pb collision sample [172]. The matching efficiency to tracks with at least 4 out of 6 TRD layers[3] was found to be around 50% at $p_{\mathrm{T}} = 1$ GeV/c in pp collisions at $\sqrt{s} = 13$ TeV [184]. For a pair analysis at low transverse momentum one may approximate the resulting penalty factor by the square of the matching efficiency $\epsilon^2_{\mathrm{matching}}$. Hence an inclusion of those detectors in the PID strategy for a pair analysis is not straight forward. The proton and pion contamination of the electron sample selected with the TPC can also be rejected by excluding particles which are consistent with this hypothesis within a given window. Let us emphasize that TRD and TOF could also be used only in the regions of ambiguities in the TPC in order to enhance the electron sample. However, since the net gain is expected to be small for low p_{T} J/ψ mesons the presented analysis is based solely on TPC PID which will be studied in the following. Possible future applications of a combined PID approach will be discussed in Chapter 7.
As explained in Sec. 3.2.2 the TPC dE/dx is parameterized in order to derive n_σ distributions. Since J/ψ analyses require a very good particle identification it is necessary to study the TPC PID thoroughly. In order to do so abundant electrons from photon conversions can be selected based on the reaction topology. The selection criteria for those V^0 electrons are summarized in Appendix B. Photon conversion processes typically take place in locations of high material density, e.g. in the beam pipe, in the ITS or at the TPC inner and outer wall. Hence they emerge at larger radii than J/ψ leg candidates which are produced in close vicinity of the primary vertex. In order to assure that both electron types have similar TPC PID properties we require conversion electrons to be produced before the entrance to the TPC. In

[3]The TRD PID methods require a minimum of 4 layers

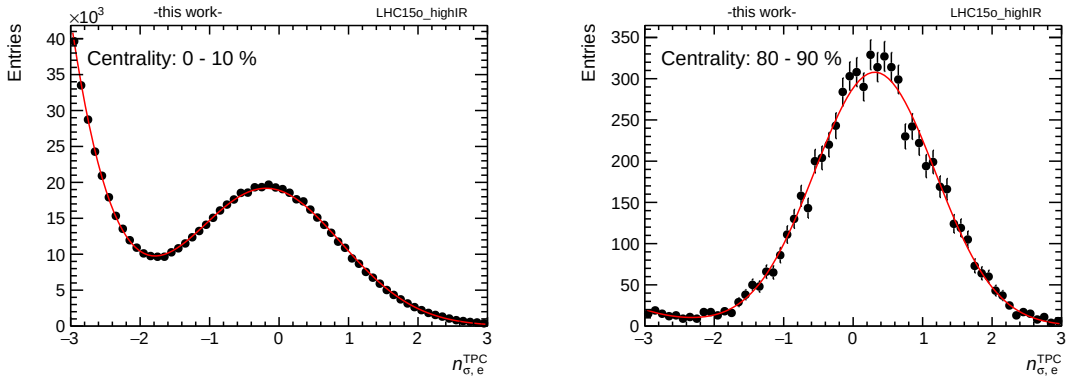

Figure 4.4: Double Gaussian fit to the $n^{\mathrm{TPC}}_{\sigma,\mathrm{e}}$ distribution of conversion electrons in most central (left) and most peripheral collisions (right).

this way the path length of both electron types in the TPC is similar. The number of TPC clusters associated with a track is directly connected to the resolution of the $\mathrm{d}E/\mathrm{d}x$ determination. It was explicitly verified that both types of electrons exhibit similar TPC cluster distributions.

4.4.1 One dimensional studies

In order to evaluate the TPC PID performance it is useful to study the $n^{\mathrm{TPC}}_{\sigma,\mathrm{e}}$ distribution of the conversion electrons in slices of different variables. As explained in Sec. 3.2.2 we expect the truncated PID signal to be Gaussian with a mean of zero and a width of one. Hence we fit the $n^{\mathrm{TPC}}_{\sigma,\mathrm{e}}$ distribution with a Gaussian to determine the mean and the width. In central Pb–Pb collisions the topologically selected conversion electrons are contaminated by combinatorial pion background as visible in Fig. 4.4. This contribution is fit with another Gaussian. Afterwards the results of both fits are used as input for a final double-Gaussian fit to the $n^{\mathrm{TPC}}_{\sigma,\mathrm{e}}$ distribution (also shown in Fig. 4.4). From the electron Gaussian we finally extract the mean and the width. The centrality dependence of both parameters is shown in Fig. 4.5. As visible in Fig. 4.5 the electron $n^{\mathrm{TPC}}_{\sigma,\mathrm{e}}$ distribution shows a centrality dependence for both data periods. In most central collisions the mean of the Gaussian is lower than zero and is increasing towards peripheral collisions. The width of the distribution is highest in most central collisions and decreases to more peripheral collisions. Those observations can be understood by different effects. Most central collisions lead to the highest occupancies in the TPC. As mentioned in Sec. 3.2.2 the TPC signal has a complex tail structure which is actually negative as opposed to the main signal peak. In a high occupancy environment new signals might end up on top of the tail of a previous signal. In this case the obtained $\mathrm{d}E/\mathrm{d}x$ and its resolution is lower than in a low occupancy environment. This is consistent with the observation of an increasing mean and decreasing width of the $n^{\mathrm{TPC}}_{\sigma,\mathrm{e}}$ distribution.
In Fig. 4.6 the pseudorapidity dependence of the mean and the width is shown. The

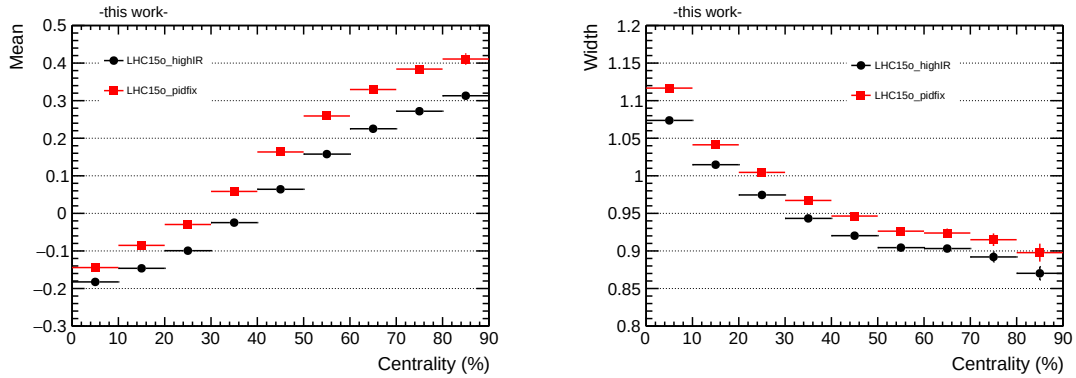

Figure 4.5: Centrality dependence of the mean and the width of the electron Gaussian in the fit for both data periods.

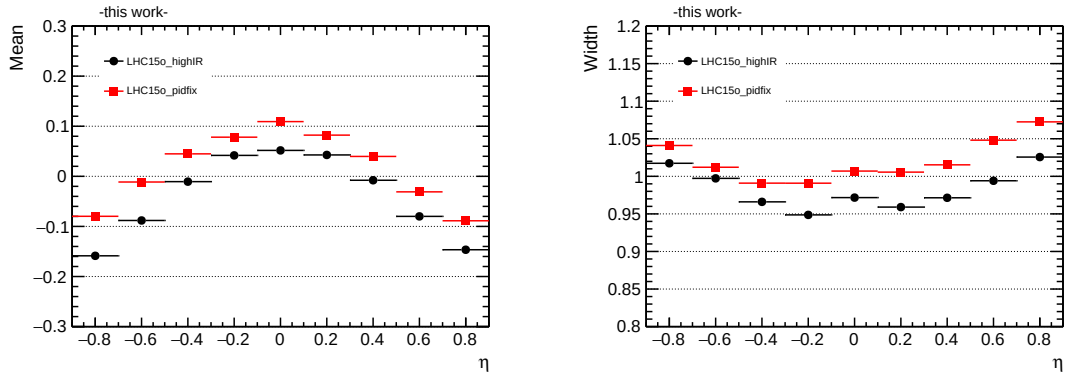

Figure 4.6: Pseudorapidity dependence of the mean and the width of the electron Gaussian in the fit for both data periods.

TPC dE/dx signal also depends on pseudorapidity which can be explained by the track length component in beam direction: In case of $\eta = 0$ the track length is minimal while for $|\eta| > 0$ the track length is larger. In the latter case the measured dE/dx is larger since a larger ionization length is projected to the same pad. For the analyzed data a correction for the pseudorapidity dependence is already applied in the dE/dx parameterization. So the dependencies shown in Fig. 4.6 can be understood as a residual imperfection of the dE/dx parameterization. The momentum dependence of the dE/dx signal has also been explicitly studied. Since electrons with momenta of $p = 1$ GeV/c are highly relativistic ($\beta\gamma \approx 2000$) no strong momentum dependence of the energy loss is expected. Indeed, as shown in Fig. 4.7 the variations with momentum are very small. In the first bin below 1.5 GeV/c a proton contamination of the conversion electrons may play a role and may distort the distribution. Thus this bin is excluded for further considerations.

In the analysis of the simulation data the tune-on-data option is used. In this case the

$n_{\sigma,\mathrm{e}}^{\mathrm{TPC}}$ for true reconstructed electrons is calculated from the data parameterization assuming a Gaussian distribution. By construction the $n_{\sigma,\mathrm{e}}^{\mathrm{TPC}}$ agrees with the data expectation of a Gaussian response with a mean of zero and a width of one. It was explicitly verified that this is indeed the case for the dimensions studied in this section. Hence the real data needs to be post calibrated to the data expectation in order to match with the simulation which will be described in the next section.

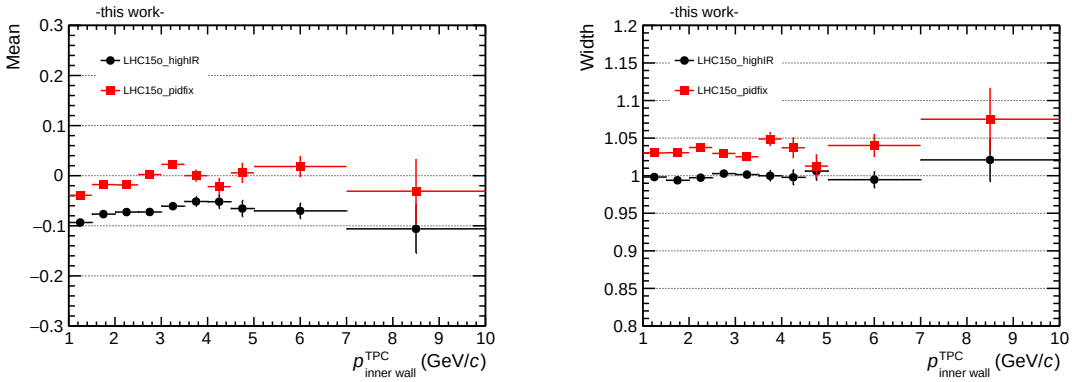

Figure 4.7: Momentum dependence of the mean and the width of the electron Gaussian in the fit for both data periods.

4.4.2 PID post calibration

The observed dependencies of the mean and width of the electron $n_{\sigma,\mathrm{e}}^{\mathrm{TPC}}$ distributions need to be corrected in order to assure a uniform PID performance. This guarantees a proper agreement of the simulation and the collision data.
Since the momentum dependence is found to be negligible it is not considered in the correction procedure. In order to derive correction factors we carry out the same fit procedure as in Sec. 4.4.1, but take into account possible correlations between the pseudorapidity and centrality dependence. To assure a clean electron sample we require a minimum momentum of $p > 1.5$ GeV/c. The obtained two dimensional calibration maps are shown in Fig. 4.8. The correction factors do not differ strongly between the two periods as expected from the studies in Sec. 4.4.1.
Using those post calibration factors the corrected $n_{\sigma,\mathrm{e}}^{\mathrm{TPC,\ corr}}$ values are calculated according to:

$$n_{\sigma,\mathrm{e}}^{\mathrm{TPC,\ corr}} = \frac{n_{\sigma,\mathrm{e}}^{\mathrm{TPC}} - \mathrm{mean}(\eta, \mathrm{centrality})}{\mathrm{width}(\eta, \mathrm{centrality})}. \tag{4.2}$$

After applying those PID corrections the mentioned studies have been repeated in order to assess the quality of the calibration. In order to check the sensitivity to the TPC occupancy estimator the calibration was studied as a function of the number of tracks at mid-rapidity instead of the centrality. It was found that the calibration is better than 2% in all cases in the considered phase space.

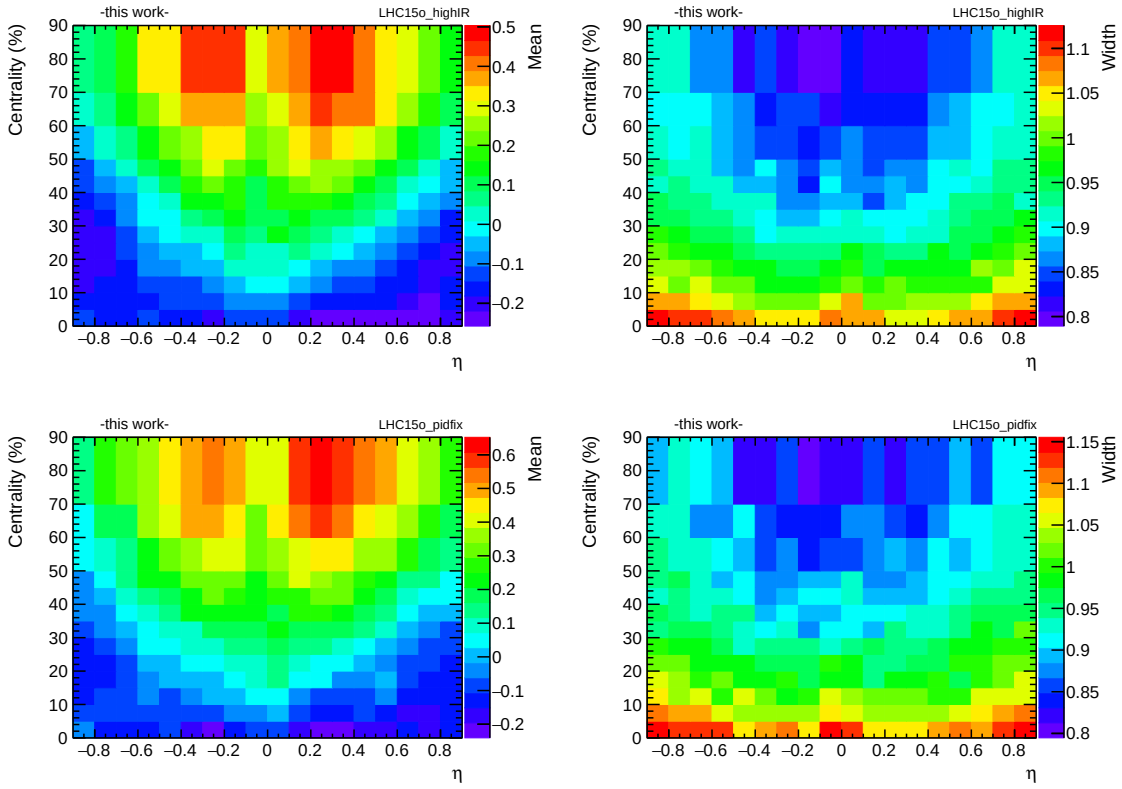

Figure 4.8: Correction maps for the mean and the width of the electron $n_{\sigma,\mathrm{e}}^{\mathrm{TPC}}$ distribution for the two data periods.

4.4.3 Hadron exclusion

As mentioned earlier the electron selection in the TPC is not unambiguous due to the crossing of the e.g. proton and pion bands. These particles are very abundant in heavy-ion collisions and constitute a large background source. However, they can be removed by rejecting particles which are consistent with the proton or pion hypothesis (within e.g. 3.5 σ). Figure 4.9 shows the selected electrons after excluding particles consistent with the proton and pion hypothesis within 3.5 σ.
The protons are rejected at low momenta while the pions are crossing at high momenta. In order to compare the representation of the hadron exclusion in the simulation and collision data we define the electron selection efficiency as:

$$\epsilon_{\mathrm{PID}} = \frac{N_{\mathrm{electrons}}(-2.0 < n_{\sigma,\mathrm{e}}^{\mathrm{TPC,\ corr}} < 3.0 \ \&\ n_{\sigma,\mathrm{p}}^{\mathrm{TPC}} > 3.5 \ \&\ n_{\sigma,\pi}^{\mathrm{TPC}} > 3.5)}{N_{\mathrm{electrons}}(-2.0 < n_{\sigma,\mathrm{e}}^{\mathrm{TPC,\ corr}} < 3.0)}. \tag{4.3}$$

As a first step we calculate this efficiency based on J/ψ decay legs using the Monte Carlo simulation. Since finally we want to compare to collision data where pure electrons can only be selected using photon conversions we also calculate the selection efficiency in the simulation using conversion electrons. Both simulation efficiencies

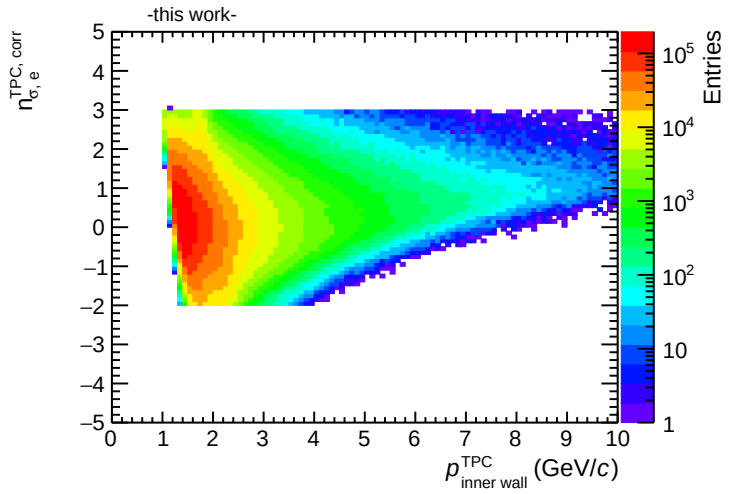

Figure 4.9: Selected calibrated electrons after applying a selection of -2 $< n_{\sigma,\mathrm{e}}^{\mathrm{TPC,\ corr}} <$ 3 and excluding protons and pions by requiring $n_{\sigma,\mathrm{p}}^{\mathrm{TPC}} > 3.5$ and $n_{\sigma,\pi}^{\mathrm{TPC}} > 3.5$.

are compared in Fig. 4.10 and found to agree very well. Thus, it is justified to use conversion electrons to study the selection efficiency in data.

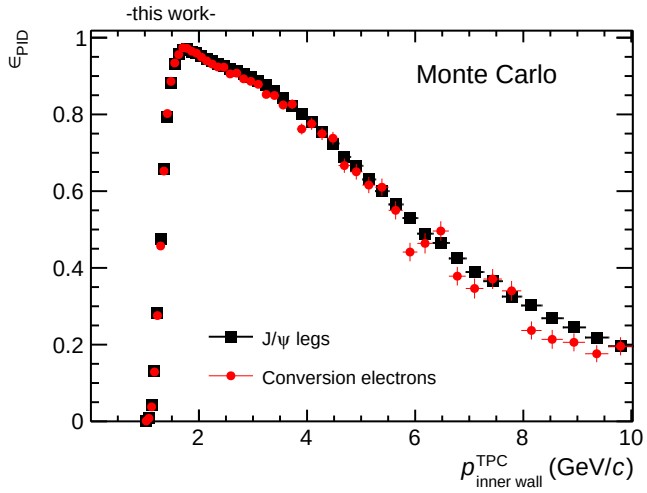

Figure 4.10: Comparison of electron selection efficiency defined in Eq. 4.3 for J/ψ legs and conversion electrons in the simulation.

However, one needs to make sure that the conversion electrons in data are sufficiently pure in order to deduce valuable information. The purity of the conversion electron sample was studied using double Gaussian fits to the electron and pion distribution and calculating the relative contamination fraction by integration. It was found that only in case of peripheral collisions (70–90% centrality) the contamination is negligible in the window -2.0 $< n_{\sigma,\mathrm{e}}^{\mathrm{TPC,\ corr}} <$ 3.0. In order to study also more

central collisions it would be required to significantly improve the conversion electron selection. However, it is not clear if negligible contamination fractions can ever be achieved in most central collisions. Thus we restrict the study to the peripheral collisions. Figure 4.11 shows the electron selection efficiency in data compared to J/ψ legs in the simulation.

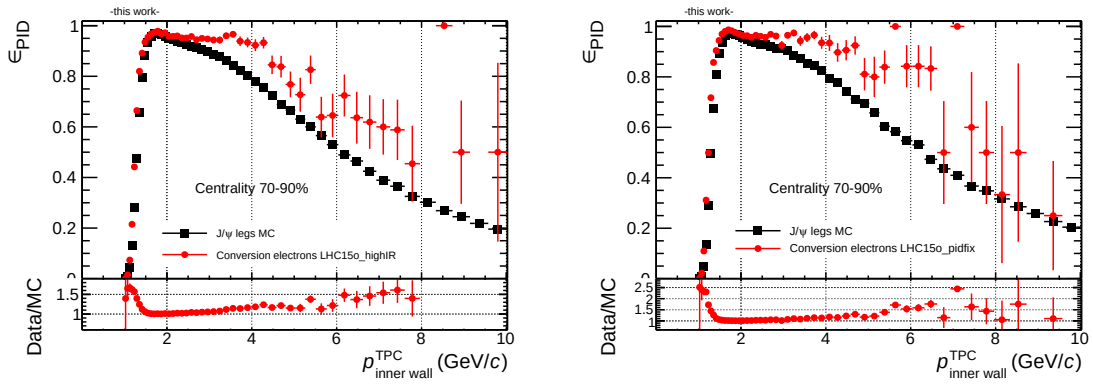

Figure 4.11: Comparison of electron selection efficiency in the simulation compared to the data periods LHC15o_highIR (left) and LHC15o_pidfix (right).

It is observed that the efficiency is systematically higher in data compared to the simulation up to a factor 1.5 or 2.5 in the proton rejection region. In the pion rejection region the mismatch is also significant, however less pronounced. In the intermediate region where there is only a weak hadron rejection the agreement is satisfactory. In order to assure that the selection efficiency is well matched in the simulation we parameterize the exclusion of the hadrons in terms of $n_{\sigma,\mathrm{e}}^{\mathrm{TPC,\ corr}}$. This way the selection only depends on the description of the electron $n_{\sigma,\mathrm{e}}^{\mathrm{TPC,\ corr}}$ distribution which is already calibrated such that it matches the simulation. The parameterization can then be consistently applied to data and simulation. An example of the parameterizations is shown in Fig. 4.12 and they are carried out as follows.
The momentum dependent $n_{\sigma,\mathrm{e}}^{\mathrm{TPC,\ corr}}$ distribution after 3 σ electron selection and 3.5 σ proton and pion rejection is separated into different centrality classes. In each class the borders of the distribution are fit with polynomials of third order. In order to improve the stability of the parameterizations against fluctuations at least 8% of the maximum number of entries in each momentum slice are required to define the borders. The procedure is carried out for both data periods and for the centrality bins $\{0, 5, 10, 15, 20, 30, 40, 60, 90\}$ separately. The pseudorapidity dependence of the hadron exclusion curves was also studied, however the variation with centrality was found to be stronger. By repeating the study shown in Fig. 4.11 it was verified that the electron selection efficiency ϵ_{PID} in the simulation and the data agree after the parameterized hadron rejections are applied.
For the J/ψ analysis the following PID selections are applied: Electrons are included within $-2 < n_{\sigma,\mathrm{e}}^{\mathrm{TPC,\ corr}} < 3$. The protons and pions are rejected using the centrality

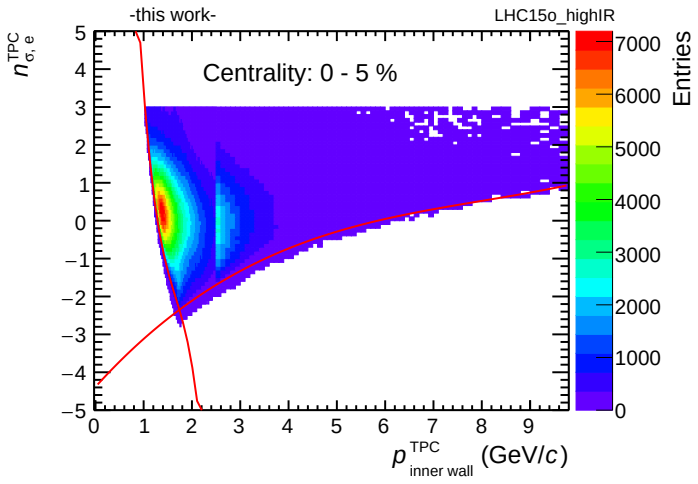

Figure 4.12: Example of the parameterization of the hadron rejection lines in the centrality class 0–5%.

dependent parameterization of the 3.5 σ exclusion curves determined above. For the most central collisions (0–20%) a more restrictive selection is applied by using additive constants (+0.25 for proton rejection and +0.7 for pion rejection) in order to reject pseudorapidity dependent contaminations. In order to retain signal sensitivity at high transverse momentum the pion exclusion is applied such that no particles are rejected above $n_{\sigma,\mathrm{e}}^{\mathrm{TPC,\ corr}} = 0$.

4.5 Signal extraction

After the leg candidates have been selected the J/ψ reconstruction can be carried out. The J/ψ candidates are built from all e^+e^- (unlike sign) pairs in a given event. In order to suppress background from photon conversions e^+e^- pairs with an invariant mass $m_{e^+e^-} < 50$ MeV/c^2 are rejected and the legs are removed from the pairing. In [199] it was verified that this rejection does not influence the J/ψ reconstruction efficiency. Due to the pseudorapidity selection of the tracks the J/ψ rapidity is limited to $|y| < 0.9$. The pair is required to have a minimum transverse momentum of $p_{\mathrm{T}} > 0.15$ GeV/c in order to reject J/ψ produced by photoproduction in peripheral collisions as explained in Sec. 2.5. This selection is applied in all centrality classes in order to assure consistency.
The different sources contributing to the background in the e^+e^- decay channel were also studied in [199]. The background electrons were identified to originate from photon conversions, heavy-flavor decays or misidentified pions and protons. The shape of the background $m_{e^+e^-}$ distribution is influenced by the minimum electron transverse momentum requirement in conjunction with the proton rejection. This selection leads to a maximum in the background invariant mass distribution at lower invariant masses. The background distribution can be modeled using

different approaches such as fitting, like-sign or event mixing techniques. Fitting the background at very low signal to background ratios as present in Pb–Pb collisions can be very sensitive to the choice of the background function and is thus disfavored. In the like-sign technique e^+e^+ or e^-e^- pairs are constructed in the same event as used for the creation of the unlike-sign signal candidate pairs. This technique has been used for the first ALICE publication of J/ψ production in pp collisions [199]. The disadvantage of this technique is that the statistical uncertainty of the background distribution is relevant and is propagated into the statistical uncertainty of the extracted signal as $\Delta S = \sqrt{S + 2B}$. In the event mixing technique e^+e^- pairs can be constructed from electrons and positrons from different events. This procedure can be carried out for many events such that the statistical uncertainty of the background description becomes negligible. In this case the statistical uncertainty of the extracted signal reduces to $\Delta S = \sqrt{S + B}$. For this reason the mixed event technique is favored for the presented analysis. Note that in this case the statistical uncertainty of the mixed event normalization is neglected. In this analysis, however also imperfections in the description of the background are relevant and are exploited in the study of the systematic uncertainties. This uncertainty reflects to some extent also the statistical uncertainty of the normalization.
By construction mixed event pairs can only describe the combinatorial background. However, due to the high number of electrons present in Pb–Pb collision events correlated background may not be relevant. Possible residual correlations in the background have to be included in the systematic uncertainty of the background description. In order to apply the event mixing technique it needs to be assured that events which are mixed have similar properties such as collisions geometry, detector occupancy or detector condition. The latter condition is fulfilled by mixing events only within a continuous data taking time in which the detector conditions are stable ("run"). The former conditions can be fulfilled by separating the events into different categories. In the presented analysis the events have been categorized into classes of centrality, number of TPC tracks and event plane. The transverse momentum dependent signal extraction for the centrality intervals 0–20%, 20–40% and 40–90% is shown in Figs. 4.13, 4.14 and 4.15. The signal is extracted in four bins in p_{T} in all cases: 0.15–1.3 GeV/c, 1.3–3 GeV/c, 3–5 GeV/c and 5–10 GeV/c. The mixed event distribution is normalized to the same event distribution in the intervals [2.2, 2.5] GeV/c^2 and [3.2, 3.5] GeV/c^2 using the weighted average of the normalization factors obtained in both regions. The lower panel shows the signal distribution which is obtained by subtracting the mixed event distribution from the same event distribution. Also drawn is the J/ψ signal shape which is expected based on the full detector simulation. It is extracted from the non-prompt J/ψ component in the simulation in order to avoid potential shape biases due to the injected signal kinematics (see Fig. 4.1). It is normalized such that the integral matches the number of counts in the signal extraction window $2.92 < m_{e^+e^-} < 3.16$ GeV/c^2. The tail of the peak towards lower masses represents the contributions from the NLO decay J/$\psi \rightarrow e^+e^- \gamma$ and bremsstrahlung losses which are not recovered by the tracking algorithm. The quality of the agreement of the background description can be judged

from the χ^2 between the data and the MC shape and is very good in all cases. The significance $\frac{S}{\sqrt{S+B}}$ is larger than five in most of the cases corresponding to a statistical uncertainty lower than 20%. The signal to background ratio is lowest in most central collisions at low transverse momentum where it is approximately 2%. It is increasing towards higher transverse momenta and more peripheral collisions due to the lower electron abundance. Finally the signal is extracted in the window $2.92 < m_{e^+e^-} < 3.16$ GeV/c^2 by bin counting. Since not all signal is contained within this window the signal loss is taken into account in the efficiency calculation.

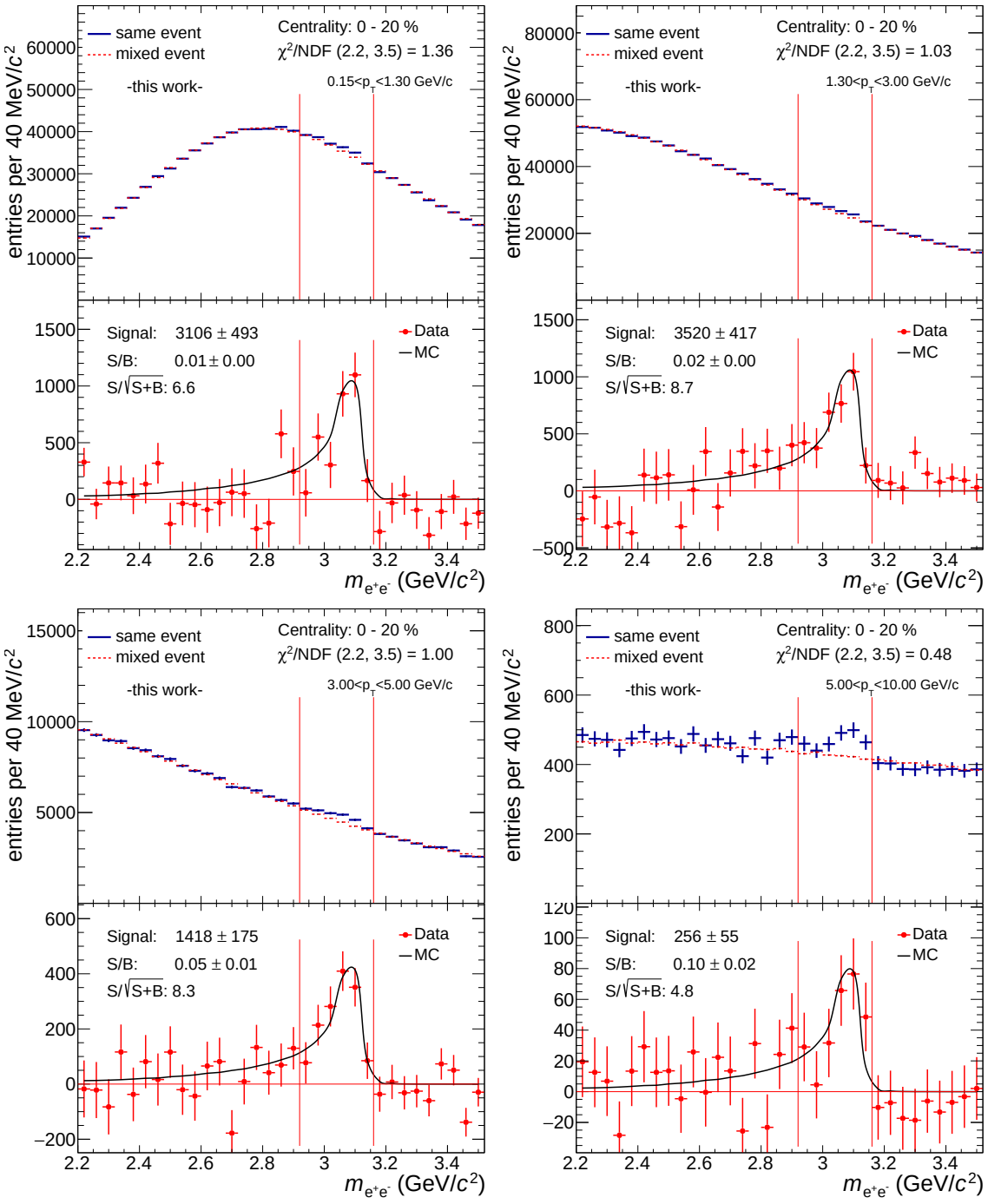

Figure 4.13: Transverse momentum dependent signal extraction in the centrality class 0–20%.

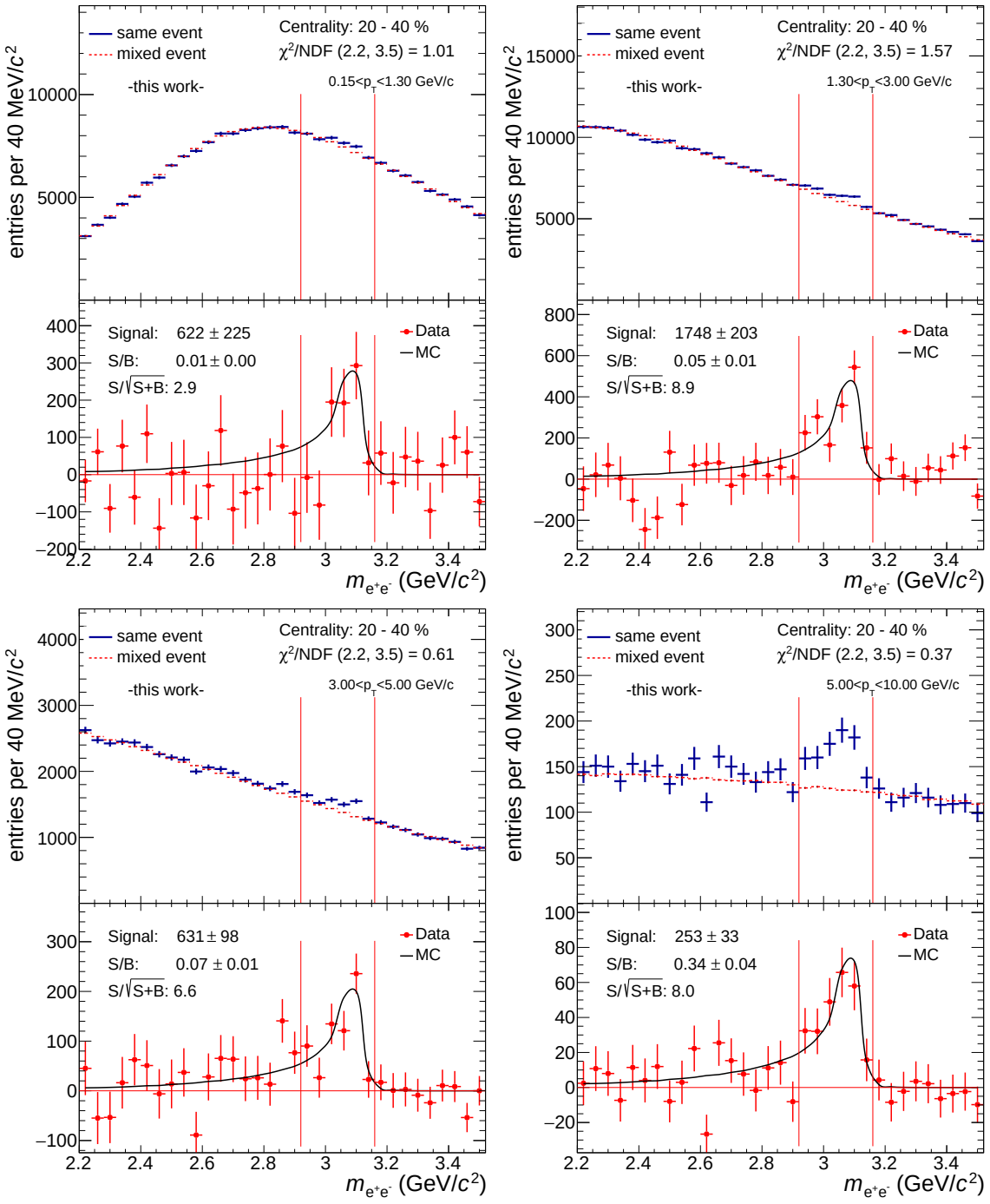

Figure 4.14: Transverse momentum dependent signal extraction in the centrality class 20–40%.

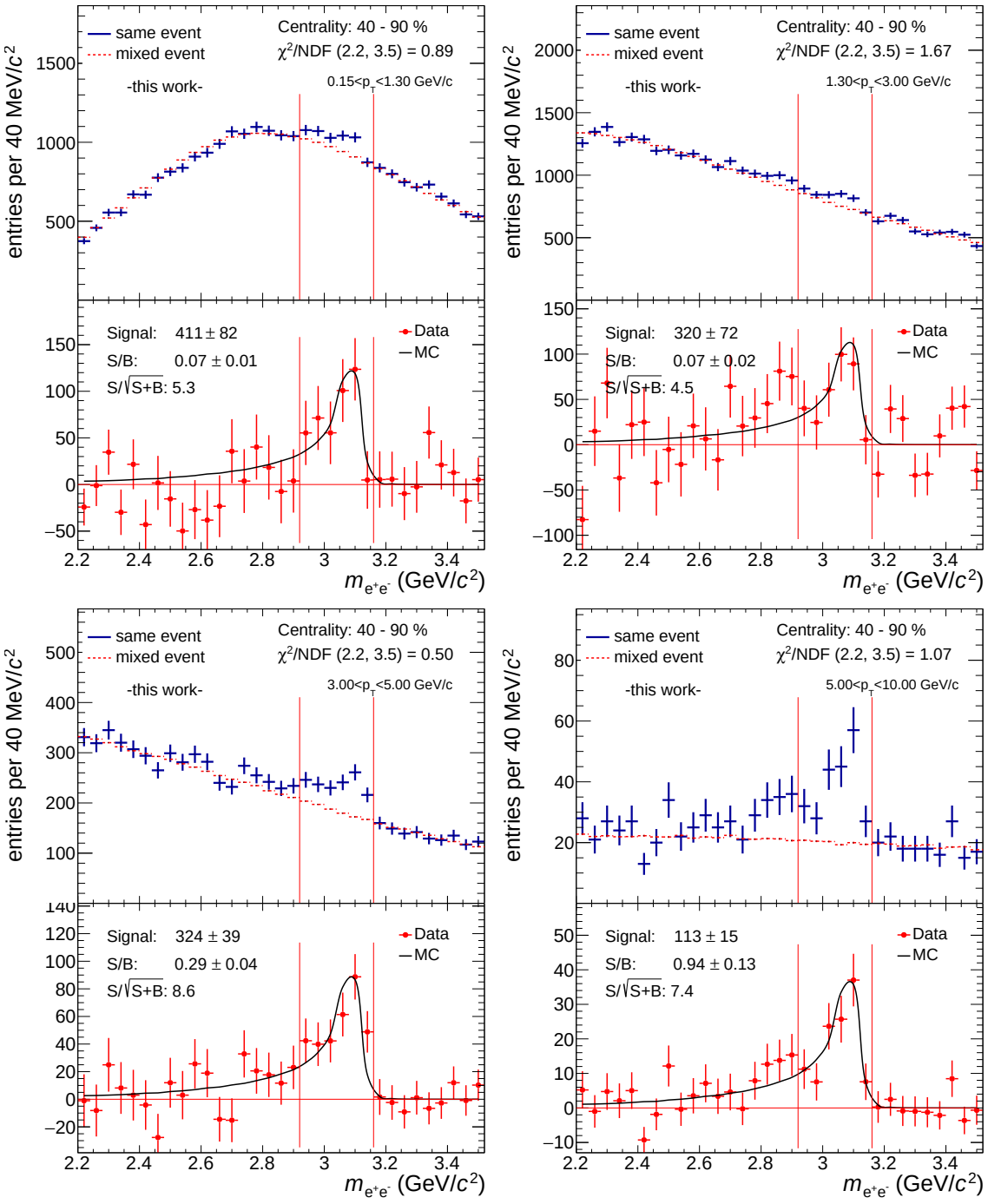

Figure 4.15: Transverse momentum dependent signal extraction in the centrality class 40–90%.

4.6 Acceptance and reconstruction efficiency correction

The extracted J/ψ raw yields need to be corrected for the acceptance and the reconstruction efficiency of the ALICE central barrel. The correction factors are obtained from the full detector simulation described in Sec. 4.1. The acceptance $\times$ efficiency ($A \times \epsilon$) factors as function of p_{T} are calculated from the number of generated and reconstructed J/ψ as:

$$A \times \epsilon(p_{\mathrm{T}})\Big|_{|y|<0.9} = \frac{N^{\mathrm{rec}}_{\mathrm{J}/\psi}(p^{\mathrm{rec}}_{\mathrm{T}})\Big|_{|y|<0.9}}{N^{\mathrm{gen}}_{\mathrm{J}/\psi}(p^{\mathrm{gen}}_{\mathrm{T}})\Big|_{|y|<0.9}}. \tag{4.4}$$

For the calculation of the number of reconstructed J/ψ the specific track selection is taken into account. Also it is assured that reconstructed J/ψ mesons have been generated to avoid counting of background particles. In Fig. 4.16 the $A \times \epsilon$ factors as function of p_{T} are shown in centrality intervals.

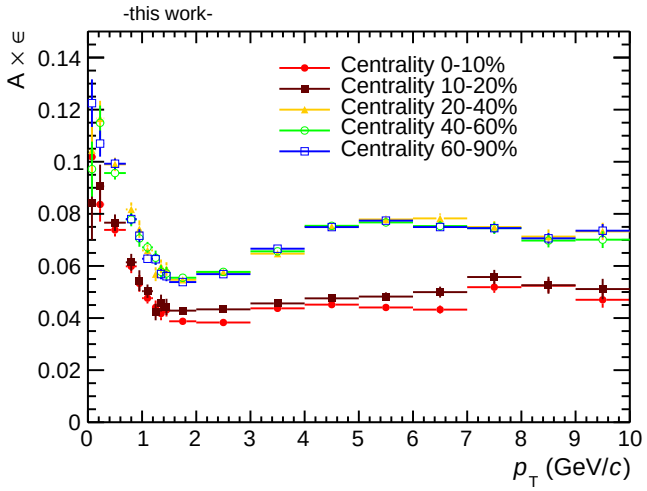

Figure 4.16: Obtained $A \times \epsilon$ factors as a function of p_{T} shown in centrality intervals.

The $A \times \epsilon$ factors lie between 4% and 12% and are lowest for the 0–20% most central collisions due to the stronger PID selection (see Sec. 4.4). The difference between the 0–10% and 10–20% centrality class can be attributed to the slightly different TPC χ^2 requirements. The $A \times \epsilon$ distributions are similar for the semi-central and peripheral collisions due to the similar track selections (see Sec. 4.3). The shape of the $A \times \epsilon$ factors as a function of p_{T} can be understood when they are decomposed

into the different contributions:

$$\begin{aligned} A \times \epsilon &= \frac{N^{\mathrm{rec}}_{\mathrm{J}/\psi}}{N^{\mathrm{gen}}_{\mathrm{J}/\psi}} \\ &= \frac{N^{\mathrm{rec}}_{\mathrm{J}/\psi}}{N^{\text{rec, no mass}}_{\mathrm{J}/\psi}} \cdot \frac{N^{\text{rec, no mass}}_{\mathrm{J}/\psi}}{N^{\text{rec, no mass, no PID}}_{\mathrm{J}/\psi}} \cdot \frac{N^{\text{rec, no mass, no PID}}_{\mathrm{J}/\psi}}{N^{\text{gen, selected}}_{\mathrm{J}/\psi}} \cdot \frac{N^{\text{gen, selected}}_{\mathrm{J}/\psi}}{N^{\mathrm{gen}}_{\mathrm{J}/\psi}} \\ &= \epsilon_{\mathrm{mass}} \cdot \epsilon_{\mathrm{PID}} \cdot \epsilon_{\mathrm{tracking}} \cdot A, \end{aligned} \tag{4.5}$$

where $N^{\text{rec, no mass}}_{\mathrm{J}/\psi}$ is the number of reconstructed J/ψ without mass window selection and $N^{\text{rec, no mass, no PID}}_{\mathrm{J}/\psi}$ is the number of reconstructed J/ψ without PID requirements and mass window selection. The number of generated J/ψ after leg acceptance requirements (p_{T}, η) is denoted $N^{\text{gen, selected}}_{\mathrm{J}/\psi}$. The four fractions in Eq. 4.5 define the partial efficiencies related to the mass window selection ϵ_{mass}, PID selection ϵ_{PID} and track reconstruction $\epsilon_{\mathrm{tracking}}$ while the last fraction defines the acceptance A. The indices related to the rapidity and p_{T} intervals have been omitted. The p_{T} dependence of the $A \times \epsilon$ is shown together with the acceptance and the partial efficiencies in Fig. 4.17 for the most central and most peripheral collisions.

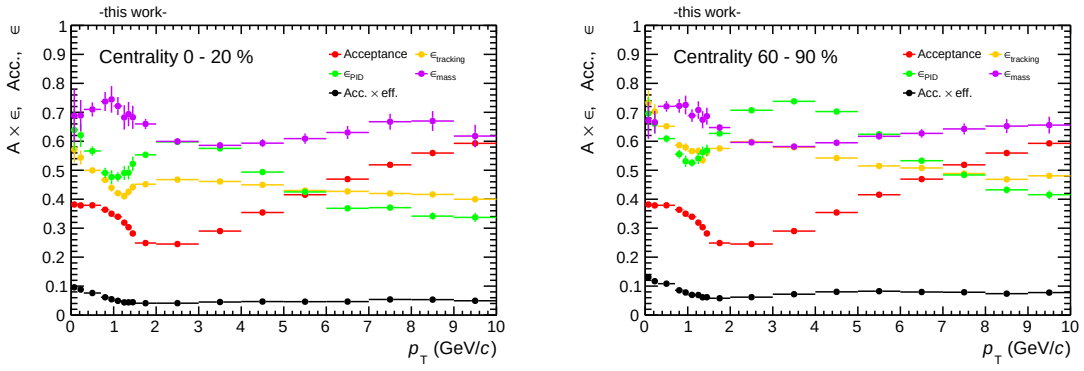

Figure 4.17: Transverse momentum dependence of the $A \times \epsilon$ shown together with its partial efficiencies and the acceptance for the most central (left) and most peripheral collisions (right).

The p_{T} dependence of the acceptance shows a pronounced dip at about 2 GeV/c and the acceptance increases towards the highest momenta. The dip in the acceptance can be understood considering the decay kinematics. At $p_{\mathrm{T}} = 0$ the J/ψ decays into dielectrons which are approximately back-to-back in azimuth. The p_{T} of the legs can be approximated with $m_{\mathrm{J}/\psi}/2$ in this situation. Clearly both legs are fulfilling the leg p_{T} requirement of 1 GeV/c in this case. However, for $p_{\mathrm{T}} > 0$ the transverse momenta of the legs become asymmetric in the lab frame due to the boost and the assumed isotropy of the decay in the rest frame: If a leg is emitted in the opposite direction as the J/ψ propagation direction the momentum of the leg is reduced and can fall below the minimum accepted leg p_{T}. This effect gets less important for

higher transverse momenta. In addition the average opening angle of the J/ψ legs in the lab frame decreases with increasing momentum due to the boost. Both effects lead to an increase of the acceptance for $p_{\mathrm{T}} > 2$ GeV/c.
As mentioned before the J/ψ decay is assumed to be isotropic in the rest frame, i.e. the J/ψ is assumed to be unpolarized. Measurements of the J/ψ polarization in pp collisions at low p_{T} have shown a polarization consistent with zero at forward rapidity at the LHC [117, 118]. At mid-rapidity J/ψ polarization has been measured for $p_{\mathrm{T}} > 14$ GeV/c at the LHC and was found to be consistent with zero [200]. At the Tevatron the J/ψ polarization has been measured down to $p_{\mathrm{T}} \geq 5$ GeV/c at mid-rapidity [201]. A small polarization was observed which was consistent with zero at the lowest p_{T}. To date there is no measurement of the J/ψ polarization in p–Pb or Pb–Pb collisions available. In the absence of such measurements at low p_{T} at mid-rapidity J/ψ mesons are assumed to be unpolarized.
The shape of the PID efficiency can be understood as follows: At very low p_{T} it can be compared to the shape of the acceptance since the proton rejection acts effectively as a minimum momentum requirement. At intermediate p_{T} the influence of the proton and pion rejection is weakest and thus a local maximum is observed. At high p_{T} the pion rejection gains importance and consequently the PID efficiency drops. The PID efficiency is smallest in the 0–20% centrality case due to the already mentioned tighter PID selection. As shown in Fig. 4.16 the $A \times \epsilon$ factors are comparable in the more peripheral centrality classes. Hence, only the efficiency steps for the most peripheral collisions are shown in the right panel of Fig. 4.17.
The shape of the tracking efficiency can be related to the TPC track finding efficiency shown in [172]. At low p_{T} (< 0.5 GeV/c) it is decreased due to energy loss in the material while at higher momenta the geometry related cluster loss plays a role. The tracking efficiency in 0–20% centrality is lower than in more peripheral collisions due to the higher TPC segments and χ^2 requirements.
The $A \times \epsilon$ correction is applied as bin-by-bin correction factors:

$$N_{\mathrm{J}/\psi}(p_{\mathrm{T}}, \Delta p_{\mathrm{T}})\Big|_{|y|<0.9} = \frac{N^{\mathrm{raw}}_{\mathrm{J}/\psi}(p_{\mathrm{T}}, \Delta p_{\mathrm{T}})\Big|_{|y|<0.9}}{A \times \epsilon(p_{\mathrm{T}}, \Delta p_{\mathrm{T}})\Big|_{|y|<0.9}}, \tag{4.6}$$

where $N^{\mathrm{raw}}_{\mathrm{J}/\psi}(p_{\mathrm{T}}, \Delta p_{\mathrm{T}})\Big|_{|y|<0.9}$ is the number of J/ψ obtained from the signal extraction in a given p_{T} interval. Bin migration effects caused by the finite momentum resolution are small since the single track resolution is around 1% in the relevant p_{T} ranges in p–Pb collisions which is expected to be only slightly deteriorated in Pb–Pb collisions at high p_{T} [172]. However, this is only true if the MC J/ψ p_{T} spectrum is close in shape to the true spectrum. Due to the flat p_{T} distribution of the injected signals at low and high p_{T} in the prompt component in the simulation bin migration effects may be overestimated. It was estimated that this leads to a bias in the efficiencies of up to 2% at the highest transverse momenta. Hence, only the non-prompt component is used for the $A \times \epsilon$ determination in this analysis. It was verified that the $A \times \epsilon$ of

the prompt and non-prompt components agree in the transverse momentum range where no injected signals are present ($0.5 < p_{\mathrm{T}} < 6$ GeV/c).
Since the J/ψ yields are obtained in p_{T} bins with sizable width the determined $A \times \epsilon$ is sensitive to the MC J/ψ p_{T} input spectrum. In order to correct for this effect the $A \times \epsilon$ factors are weighted with the spectra measured at forward rapidity before combining them into the bins of the J/ψ signal extraction. The spectra are parameterized using the functional form:

$$\frac{\mathrm{d}^2N}{\mathrm{d}p_{\mathrm{T}}\mathrm{d}y} = C_0 \cdot \frac{p_{\mathrm{T}}}{(1 + (p_{\mathrm{T}}/p_0)^2)^n}. \tag{4.7}$$

The spectra together with their parameterizations are obtained from [202]. The parameterizations of the spectra in the different measured centrality intervals are shown in Fig. 4.18.

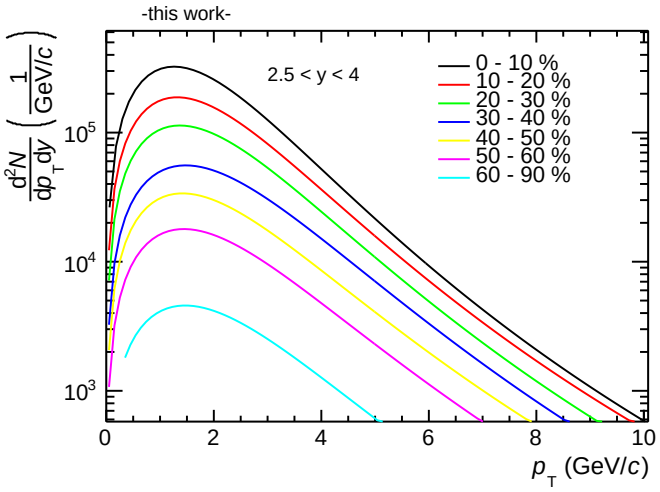

Figure 4.18: Fits to the J/ψ spectra measured at forward rapidity in Pb–Pb collisions at $\sqrt{s_{\mathrm{NN}}} = 5.02$ TeV in different centrality bins.

The reweighting of the $A \times \epsilon$ factors is carried out as follows: First the parameterizations of the forward spectra are added to obtain spectra in the same centrality intervals as used in this analysis. Afterwards the $A \times \epsilon$ factors are summed up to the bins used in the signal extraction using the effective forward spectra as weights. The differences of the obtained $A \times \epsilon$ factors to the ones calculated without reweighting are on the level of 2% or smaller. Possible differences introduced by the different rapidity window of the spectra used for reweighting are expected to be small due to the smallness of the correction factors and are expected to be covered by the systematic uncertainty of the MC input shape.
In addition the necessity of a weighting of the $A \times \epsilon$ factors for differences in collision data and MC statistics has been investigated. Typically MC events are generated

in a constant fraction of the collision data events for every run. However, the event selection shown in Fig. 4.2 may reject more events in runs at higher interaction rate than in runs at lower interaction rate. This would lead to a difference in the fraction of collision data to MC events for every run. Together with the run dependence of the $A \times \epsilon$ factors this might induce a bias in the correction factors. This effect was assessed by summing runwise the $A \times \epsilon$ factors using the number of events in data as weights. The difference was found to be negligible and hence this procedure is not carried out for the $A \times \epsilon$ correction.

4.7 Systematic uncertainties

In this section the estimation of the systematic uncertainties relevant for this analysis will be discussed. The uncertainties are grouped into different categories: The uncertainty related to the signal extraction procedure, to the particle identification, to the tracking or to the simulation kinematics.
The signal extraction procedure is sensitive to the imperfection in the background description due to the particular choice of the background scaling windows. In addition the choice of the signal extraction mass window is sensitive to the description of the detector material budget which gives rise to the bremsstrahlung tail of the signal. In order to estimate those uncertainties the background scaling windows are varied away from the standard choice. It is done such that either more weight is given to the region on the high mass side or on the low mass side of the signal compared to the standard choice. The signal extraction mass window is either made wider or smaller compared to the standard choice. For all systematic choices the fully corrected yield is calculated. The standard deviation of the obtained results is taken as systematic uncertainty for the signal extraction.
The particle identification is in principle sensitive to the agreement of the parameterization of the electron, proton and pion bands in data and MC. However, the parameterized PID selection developed in Sec. 4.4.3 reduces this sensitivity to the description of the electron band. The parameterization of the electron band is post calibrated as explained in Sec. 4.4.2 to match the MC. Since the calibration is better than 2% on the single track level the PID uncertainty should be lower than 4%. In order to estimate the uncertainty the electron selection curves have been varied independently in the momentum region of the proton and pion rejection. The standard deviation of the obtained corrected yields is taken as PID uncertainty.
The uncertainty for the tracking arises from the imperfection of the modeling of the detector in the simulation which translates to a difference in the tracking performance. The choices of the tracking related quantities are summarized in Tab. 4.2. The description of the track related quantities in the simulation is tested by varying the selection criteria away from the standard choice. In case of the numerical selection criteria this is done by selecting a stronger and a weaker selection than the standard choice. The DCA selection criteria have not been varied since they are almost fully efficient for the signal. The requirements of ITS refit, TPC refit

and kink rejection have not been varied since omitting these requirements would be a too extreme variation. The requirement of a hit in any of the SPD layers has only been tightened to a requirement of both layers since without SPD requirement the background is too high for a reasonable signal extraction. For every systematic choice the corrected yield is calculated. Since not all variations might have enough sensitivity to their imperfect description in the simulation a rejection of those cases based on the Barlow criterion [203] is applied. By choosing a specific variation either a statistical sub- or superset is analyzed. In this case the statistical uncertainty of the difference of two choices $\Delta = N_1 - N_2$ is given by $\sigma_\Delta = \sqrt{|\sigma_1^2 - \sigma_2^2|}$, where σ_1 and σ_2 are the statistical uncertainties of the individual choices. If the deviation of two choices is smaller than $\sigma_\Delta = \sqrt{|\sigma_1^2 - \sigma_2^2|}$ it is likely that the difference of the two results is due to a statistical fluctuation and not a systematic effect. After a rejection of those cases the standard deviation of the corrected yield distributions of the remaining cases is assigned as tracking uncertainty.
As mentioned in Sec. 4.6 the calculated efficiencies are sensitive to the J/ψ p_{T} spectrum used in the simulation. This effect is corrected by using a reweighting technique based on weights obtained from fits to the measured forward spectra. The uncertainties of the obtained fit result gives rise to an uncertainty of the reweighting factors and thus the obtained correction factors. This uncertainty has been studied in [198]. In order to also take into account possible differences introduced by the different rapidity ranges the uncertainty estimation is done using fits to the measured mid-rapidity spectra. The fit parameters have been varied randomly and independently according to their uncertainties in order to derive variations of the fit function. The $A \times \epsilon$ factors have been calculated each time and the standard deviation of the $1/A \times \epsilon$ distribution is assigned as uncertainty.
The summary of the systematic uncertainties is shown in Tab. 4.3. The total systematic uncertainty is obtained by adding the uncertainties of the different categories in quadrature. The final result is defined as the mean of all systematic variations in order to be less sensitive to specific choices. For the statistical uncertainty of the result the mean of the statistical uncertainties of the different systematic cases is taken.
For the calculation of the nuclear modification factor also the uncertainty of the nuclear overlap function is relevant. It was studied within the ALICE collaboration [185] and the values are also given in in Tab. 4.3.

Source	p_{T} (GeV/c)			
	0.15 – 1.3	1.3 – 3	3 – 5	5 – 10
	Centrality 0–20%			
Signal extraction	3.2	3.4	1.7	7.3
PID	3.5	1.9	2.8	6.2
Tracking	8.7	5.8	8	8.9
Simulation kinematics	1	1	1.5	1.5
T_{AA}	2.1			
	Centrality 20–40%			
Signal extraction	10.2	3.1	7.5	4.6
PID	14.3	3.5	3.8	7.1
Tracking	15.6	8	7.3	6.5
Simulation kinematics	1	1	1	1
T_{AA}	3.1			
	Centrality 40–90%			
Signal extraction	7.9	8.7	3.5	4.6
PID	3.8	5.4	3.2	2.6
Tracking	11.4	15.5	11.2	7.8
Simulation kinematics	4	1	2	2
T_{AA}	2.0			

Table 4.3: Summary of systematic uncertainties of the fully corrected J/ψ yields and the nuclear overlap function in percent.

4.8 Presenting results in wide bins

It is a prominent problem of statistically limited analyses that a large width of result bins complicates the comparison to smooth prediction curves. It was demonstrated in [204] that neither plotting the result point in the middle of the bin nor at the mean position of the x value is appropriate. Instead, it was shown that the correct x position to present the data is x_{lw} which lies on the smooth true distribution and is defined by:

$$g(x_{\mathrm{lw}}) = \frac{1}{\Delta x} \int_{x_1}^{x_2} g(x)\, dx, \tag{4.8}$$

where x_1 and x_2 are the lower and upper bin limits, $\Delta x = x_2 - x_1$ is the bin width and $g(x)$ is the true distribution of the quantity which is measured.
A possible approach to obtain the x_{lw} values for J/ψ spectra was developed in the course of this thesis. The method is demonstrated based on a study using the J/ψ spectrum measured in 0–10% central collisions at forward rapidity (the spectrum was

obtained from [202]). The parameterization of the spectrum is assumed to be the true distribution. This distribution is sampled in the bins used for the J/ψ spectrum measurement presented in this chapter in order to derive a toy measurement of the true distribution. Both are shown in the left panel of Fig. 4.19 together with the bin centers, $\langle p_{\mathrm{T}} \rangle$ and x_{lw}.

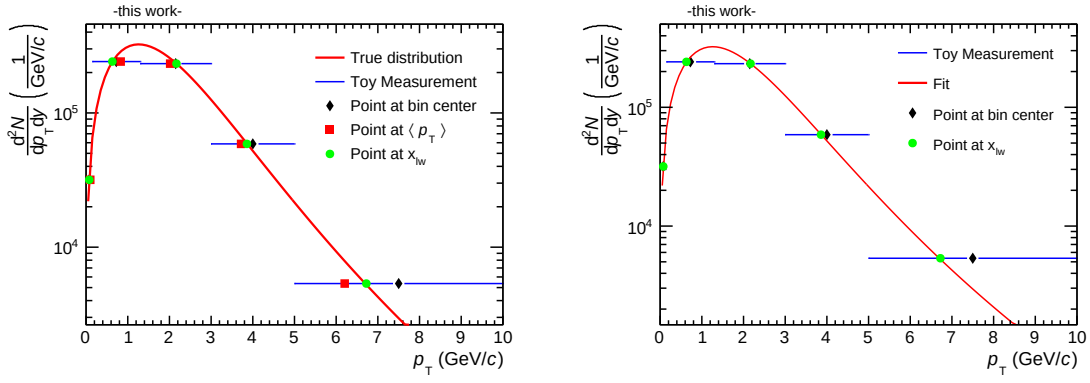

Figure 4.19: Left: Toy measurement obtained from sampling the parameterization of the forward J/ψ spectrum in 0–10% centrality drawn together with different drawing positions. Right: Fit to the toy measurement together with the true x_{lw}.

This figure illustrates that x_{lw} is the correct position for the representation of the measured data. In the right panel of Fig. 4.19 a fit[4] to the sampled distribution with a function as defined in Eq. 4.7 is shown together with the x_{lw} value which is obtained from the true distribution. It can be observed that the fit function coincides with the true x_{lw} values. In addition it was verified that the true x_{lw} and the obtained x_{lw} agree with a precision better than 10^{-4} in this study. Hence, this method is used to obtain the x_{lw} values for the measured spectra.
The fits to the measured mid-rapidity spectra are shown in Fig. 4.20. The x_{lw} in each bin is retrieved using the definition in Eq. 4.8. For the uncertainty estimation the mean value of the function parameters μ_i and their covariance matrix Σ is considered:

$$\vec{\mu} = \begin{pmatrix} \mu_{C_0} \\ \mu_{p_0} \\ \mu_n \end{pmatrix}, \qquad \Sigma = \begin{pmatrix} \sigma^2_{C_0} & C_{C_0 p_0} & C_{C_0 n} \\ C_{p_0 C_0} & \sigma^2_{p_0} & C_{p_0 n} \\ C_{n C_0} & C_{n p_0} & \sigma^2_n \end{pmatrix}. \tag{4.9}$$

It is observed that the uncertainties related to the amplitude are negligible in comparison with the other uncertainties and thus the covariance matrix can be reduced to:

$$\Sigma_{p_0,n} = \begin{pmatrix} \sigma^2_{p_0} & C_{p_0 n} \\ C_{n p_0} & \sigma^2_n \end{pmatrix} = \begin{pmatrix} \sigma^2_{p_0} & \rho \sigma_{p_0} \sigma_n \\ \rho \sigma_{p_0} \sigma_n & \sigma^2_n \end{pmatrix}, \tag{4.10}$$

[4]The fit is set to integrate the bin contents.

with the correlation coefficient ρ. In this case the mean values μ_{p_0} and μ_n and the covariance matrix $\Sigma_{p_0,n}$ define a bivariate normal distribution:

$$\begin{aligned} f(p_0, n) =& \frac{1}{2\pi\sigma_{p_0}\sigma_n\sqrt{1-\rho^2}} \cdot \\ & \exp\left(-\frac{1}{2(1-\rho^2)}\left[A(p_0) + A(n) - 2\rho A(p_0)A(n)\right]\right), \end{aligned} \tag{4.11}$$

with:

$$A(p_0) = \frac{(p_0 - \mu_{p_0})^2}{\sigma_{p_0}^2}, \qquad A(n) = \frac{(n - \mu_n)^2}{\sigma_n^2}. \tag{4.12}$$

In order to estimate the uncertainties of the x_{lw} the bivariate Gaussian is sampled to extract variations of p_0 and n taking into account their correlation. Each time the corresponding function is evaluated and the x_{lw} values are retrieved. The standard deviation of this distribution is assigned as uncertainty. The spectrum fits and the x_{lw} determination procedure is carried out using the quadratic sum of statistical and systematic uncertainties assigned to the spectrum. Hence, the results are given with the total uncertainty in Tab. 4.4.

Centrality	p_{T} (GeV/c)			
	0.15 – 1.3	1.3 – 3	3 – 5	5 – 10
0–20%	0.66 ± 0.03	2.24 ± 0.06	3.88 ± 0.03	6.69 ± 0.17
20–40%	0.67 ± 0.03	2.29 ± 0.09	3.91 ± 0.03	6.82 ± 0.13
40–90%	0.67 ± 0.06	2.31 ± 0.15	3.93 ± 0.04	6.94 ± 0.19

Table 4.4: Results for x_{lw} (GeV/c) for the different centrality intervals and p_{T} bins.

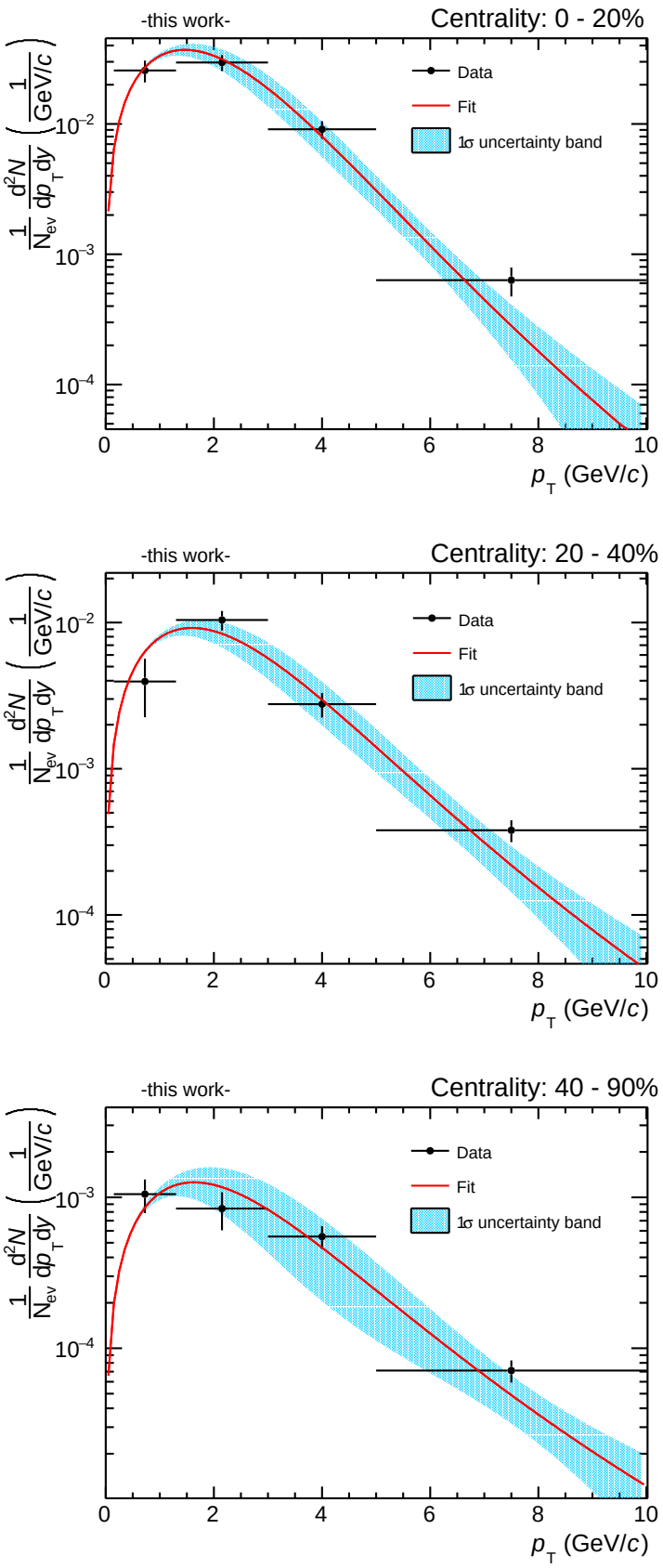

Figure 4.20: Fits to measured spectra together with 1σ uncertainty band.

4.9 Proton-proton reference

For the calculation of the nuclear modification factor the pp reference cross section is a necessary input. At the time of the data analysis the extraction of the pp reference cross section from the high statistics 2017 pp data sample at $\sqrt{s} = 5$ TeV was not yet finalized. Hence the reference is constructed using an interpolation procedure based on the approach presented in [194, 205] and was carried out within the ALICE collaboration.
The approach makes use of the universal behavior which is observed for J/ψ spectra measured at different energies: When the p_{T} spectra are normalized to unity and the p_{T} is replaced by $z_{\mathrm{T}} = p_{\mathrm{T}}/\langle p_{\mathrm{T}} \rangle$ the different spectra can be described by a universal function of type:

$$\frac{1}{\mathrm{d}\sigma/\mathrm{d}y}\frac{\mathrm{d}^2\sigma}{\mathrm{d}z_{\mathrm{T}}\mathrm{d}y} = 2a^2(n-1)\cdot\frac{z_{\mathrm{T}}}{(1+a^2z_{\mathrm{T}}^2)^n}, \tag{4.13}$$

with $a = \Gamma(3/2)\Gamma(n-3/2)/\Gamma(n-1)$. Once the fit to the different spectra has been carried out a p_{T} differential reference cross section can hence be constructed from interpolated values of the inclusive cross section and the $\langle p_{\mathrm{T}} \rangle$.
The interpolation of the inclusive cross section is carried out as detailed in [131]. Mid-rapidity cross section measurements are interpolated using empirical functions of exponential, logarithmic and power law type, yielding $\mathrm{d}\sigma/\mathrm{d}y = 6.19 \pm 1.03$ μb. The $\langle p_{\mathrm{T}} \rangle$ interpolation is shown in Fig. 4.21. Logarithmic and polynomial functions are used to interpolate the measurements. Due to the high precision of the CDF data point the precision of the interpolation is very good in its vicinity.

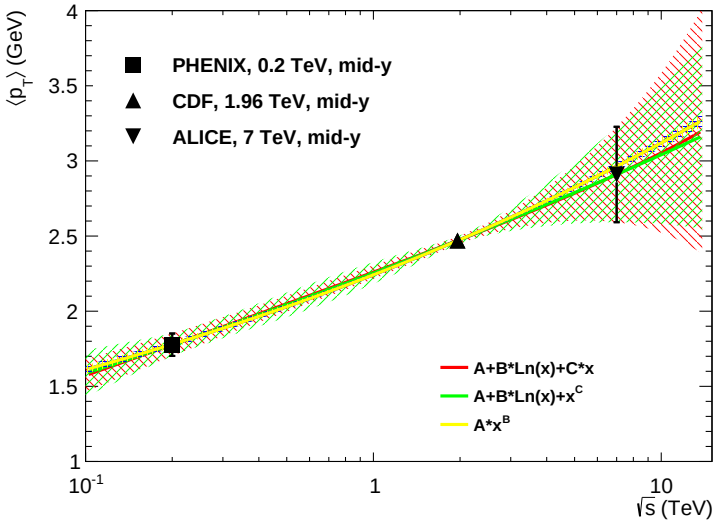

Figure 4.21: Interpolation of the J/ψ $\langle p_{\mathrm{T}} \rangle$ at mid-rapidity [206].

The results of the $\langle p_{\mathrm{T}} \rangle$ interpolation for the $\langle p_{\mathrm{T}} \rangle$ and $\langle p_{\mathrm{T}}^2 \rangle$ for $p_{\mathrm{T}} < 10$ GeV/c are

listed in Tab. 4.5. Both values are an important reference for the measurement of the $\langle p_{\mathrm{T}} \rangle$ and $\langle p_{\mathrm{T}}^2 \rangle$ in Pb–Pb collisions presented in Chapter 5. The obtained values for the $\langle p_{\mathrm{T}} \rangle$ and the inclusive cross section are used to construct the p_{T} differential pp reference cross section using Eq. 4.13. The p_{T} differential cross section results are listed in Tab. 4.6. The uncertainty which arises from the inclusive cross section is correlated among all p_{T} bins while the uncertainty of the $\langle p_{\mathrm{T}} \rangle$ gives rise to an uncorrelated uncertainty.

$\langle p_{\mathrm{T}} \rangle$ (GeV/c)	$\langle p_{\mathrm{T}}^2 \rangle$ (GeV^2/c^2)
2.72 ± 0.05	10.36 ± 0.29

Table 4.5: Results of the $\langle p_{\mathrm{T}} \rangle$ interpolation at $\sqrt{s} = 5$ TeV for $p_{\mathrm{T}} < 10$ GeV/c.

p_{T} range	$\mathrm{d}^2\sigma/\mathrm{d}y\mathrm{d}p_{\mathrm{T}}$ (μb)
0.15 – 1.3 GeV/c	1.06 ± 0.18 (corr.) ± 0.07 (uncorr.)
1.3 – 3 GeV/c	1.60 ± 0.27 (corr.) ± 0.07 (uncorr.)
3 – 5 GeV/c	0.78 ± 0.13 (corr.) ± 0.04 (uncorr.)
5 – 10 GeV/c	0.126 ± 0.021 (corr.) ± 0.015 (uncorr.)

Table 4.6: Results of the p_{T} differential pp cross section interpolation at $\sqrt{s} = 5$ TeV. The values reflect the integral in the p_{T} ranges.

5 Measurement of the J/ψ $\langle p_{\mathrm{T}} \rangle$ and $\langle p_{\mathrm{T}}^2 \rangle$ in pp and Pb-Pb collisions

In this chapter the measurement of the $\langle p_{\mathrm{T}} \rangle$ and $\langle p_{\mathrm{T}}^2 \rangle$ of J/ψ mesons in Pb–Pb and pp collisions will be presented.

5.1 Datasets

For the measurement the Pb–Pb dataset used in Chapter 4 with the corresponding simulation is also used here. In addition, a high statistics pp dataset recorded at the end of 2017 is used. It is split into two subsets named "LHC17p" and "LHC17q" where the former was taken at a low interaction rate of about 55 kHz and constitutes the dominating part of the statistics. The latter is collision data from a single LHC fill with a minimum bias interaction rate of about 200 kHz. The probability of pile-up is estimated with the same methodology as in Sec. 4.1. The probability of same-bunch pile-up is estimated to be smaller than 10^{-5} for LHC17p and smaller than 10^{-4} for LHC17p and is hence considered to be negligible. The issue of pile-up from different bunch crossings in the TPC as described in Sec. 4.1 is not important in pp collisions due to the much lower occupancy.

For the pp collision dataset a dedicated detector simulation was produced. The pp events are generated by PYTHIA 6 [193] where one J/ψ is injected additionally per event in order to enhance the statistics. Prompt and non-prompt J/ψ are injected with the ratio 70:30 where both sources exhibit a natural p_{T} spectrum. Also in this simulation J/ψ are forced to decay into an electron and a positron where PHOTOS [197] is used for the calculation of the QED final state radiation. The transport of the particles through the ALICE detector model is done with GEANT3 [192]. In total about $56{\times}10^6$ simulation events have been generated.

5.2 Event and track selection

The event an track selection which is used in Pb–Pb collisions is described in detail in Sec. 4.2 and 4.3. The particle identification strategy in Pb–Pb collisions is reported in Sec. 4.4 and is also exploited here.

The analyzed pp collision data were also recorded with the minimum bias trigger issued by coincident signals of the V0 scintillators. For the analysis of the data it is required that a collision vertex was reconstructed from at least one contributing

track. The z coordinate of the vertex is required to be within $|z| < 10$ cm of the nominal vertex position to assure a uniform acceptance. The number of selected events which are used for the analysis are summarized in Tab. 5.1.

	Pb–Pb	pp
$N_{\text{events, selected}}$	71.4 $\times 10^6$	925.6 $\times 10^6$

Table 5.1: Number of events after selection for the Pb–Pb and pp datasets used in the analysis presented in this chapter.

The large size of the pp sample was reached by the exclusion of the slow SDD detector in the readout in a large fraction of the events. In the other event fraction where the SDD was part of the readout it was disabled for the data reconstruction in order to assure uniformness of the reconstructed data. The electron selection criteria which are used in the analysis of pp collisions are summarized in Tab. 5.2.

Variable	Selection
p_{T}	> 1 GeV/c
$\lvert\eta\rvert$	< 0.9
$\lvert\mathrm{DCA}_{xy}\rvert$	< 1 cm
$\lvert\mathrm{DCA}_{z}\rvert$	< 3 cm
ITS refit	true
TPC refit	true
Rejection of kink daughters	true
Hit in which SPD layers	any
ITS χ^2/cluster	< 10
TPC cluster	> 70
TPC χ^2/cluster	< 4
$\lvert n_{\sigma,\mathrm{e}}^{\mathrm{TPC,\ corr}} \rvert$	< 3
$n_{\sigma,\mathrm{p}}^{\mathrm{TPC}}$	> 3.5
$n_{\sigma,\pi}^{\mathrm{TPC}}$	> 3.5

Table 5.2: Summary of applied electron selection criteria used in pp collisions.

The TPC PID is corrected for a small momentum and η dependence as described in Appendix C. The proton and pion exclusion bands are not additionally parameterized since the mismatch between data and MC is small in this dataset [198]. In pp collisions softer TPC track requirements could be used due to the lower TPC track density.

In pp collisions the same pair selection criteria are applied as in Pb–Pb collisions. However, no exclusion of a photoproduction component is necessary in pp collisions and hence the transverse momentum of the J/ψ is only restricted to be $p_{\mathrm{T}} < 10$ GeV/c.

5.3 Description of the method

For the extraction of the $\langle p_{\mathrm{T}}\rangle$ and $\langle p_{\mathrm{T}}^2\rangle$ of J/ψ mesons different methods can be considered. One option is to fit J/ψ spectra with a function as defined in Eq. 4.7 and to extract the moments from the function. However, one disadvantage in Pb–Pb collisions is that this extraction method is restricted to centrality intervals in which spectra are measured. Also, since the spectrum fit method relies on the validity of a chosen function this approach is disfavored. This method is however used as a cross-check and will be presented in Sec. 5.8. At the time of the analysis no J/ψ spectrum was available at mid-rapidity in pp collisions at $\sqrt{s} = 5.02$ TeV and hence this method could also not be applied there. Due to these reasons a different method is used in both collision systems where the moments are extracted directly from data. It is based on the elliptic flow extraction technique proposed in [207] and applied in e.g. [208]. In this approach the $\langle p_{\mathrm{T}}\rangle$ of the opposite sign pairs $\langle p_{\mathrm{T}}(m_{e^+e^-})_{\mathrm{S+B}}\rangle$ is expressed with the $\langle p_{\mathrm{T}}\rangle$ of the signal S and background B as:

$$\langle p_{\mathrm{T}}(m_{e^+e^-})_{\mathrm{S+B}}\rangle = \frac{N_{\mathrm{B}}(m_{e^+e^-}) \cdot \langle p_{\mathrm{T}}^{\mathrm{B}}(m_{e^+e^-})\rangle + N_{\mathrm{S}}(m_{e^+e^-}) \cdot \langle p_{\mathrm{T}}^{\mathrm{S}}\rangle}{N_{\mathrm{S}}(m_{e^+e^-}) + N_{\mathrm{B}}(m_{e^+e^-})}, \tag{5.1}$$

where $N_{\mathrm{S}}(m_{e^+e^-})$ is the number of signal pairs, $N_{\mathrm{B}}(m_{e^+e^-})$ is the number of background pairs, $\langle p_{\mathrm{T}}^{\mathrm{B}}(m_{e^+e^-})\rangle$ is the $\langle p_{\mathrm{T}}\rangle$ of the background and $\langle p_{\mathrm{T}}^{\mathrm{S}}\rangle$ is the $\langle p_{\mathrm{T}}\rangle$ of the signal. The number of signal and background pairs and the $\langle p_{\mathrm{T}}\rangle$ of the background depend on the invariant mass of the dielectron pair and are hence distributions. The $\langle p_{\mathrm{T}}\rangle$ of the signal is assumed to be independent of the invariant mass since the mass resolution at the J/ψ peak ($\sigma \approx 23$ MeV/c^2 in pp collisions at $\sqrt{s} = 5$ TeV [206]) is very small compared to expected $\langle p_{\mathrm{T}}\rangle$ values.
The distributions of the number of signal and background pairs are obtained from the inclusive signal extraction as explained in Sec. 5.5. The $\langle p_{\mathrm{T}}^{\mathrm{B}}(m_{e^+e^-})\rangle$ distribution is obtained either by event mixing or a parameterization of the background outside of the signal region as explained in Sec. 5.5.
In order to perform the acceptance and efficiency correction in this measurement the correction factors are applied before the $\langle p_{\mathrm{T}}\rangle$ extraction as follows. When building the $\langle p_{\mathrm{T}}(m_{e^+e^-})_{\mathrm{S+B}}\rangle$ and $\langle p_{\mathrm{T}}^{\mathrm{B}}(m_{e^+e^-})\rangle$ profiles the inverse correction factors $(A \times \epsilon)^{-1}$ are taken as a weight in the average calculation. The extracted raw numbers of signal and background pairs ($N_{\mathrm{S}}(m_{e^+e^-})$ and $N_{\mathrm{B}}(m_{e^+e^-})$) are not corrected for acceptance and efficiency since the correction factors drop out in the ratio on the right hand side of Eq. 5.1. This was explicitly verified in pp collision by performing a p_{T} dependent $A \times \epsilon$ correction prior to the inclusive signal extraction.
Finally the same event distribution $\langle p_{\mathrm{T}}(m_{e^+e^-})_{\mathrm{S+B}}\rangle$ can be fit with the right hand side of Eq. 5.1 where $\langle p_{\mathrm{T}}^{\mathrm{S}}\rangle$ is the only free parameter and can be extracted. The extraction of the $\langle p_{\mathrm{T}}^2\rangle$ can be done analogously by replacing the $\langle p_{\mathrm{T}}\rangle$ distributions in Eq. 5.1 by $\langle p_{\mathrm{T}}^2\rangle$. Since the terms on the right hand side of Eq. 5.1 represent distributions (or templates) this method is referred to as "template fit method" in the following.

More details about the efficiency correction and the signal and $\langle p_{\mathrm{T}} \rangle$ ($\langle p_{\mathrm{T}}^2 \rangle$) extraction are given in Sec. 5.4 and 5.5.

5.4 Efficiency correction

In this section the efficiency correction for the $\langle p_{\mathrm{T}} \rangle$ and $\langle p_{\mathrm{T}}^2 \rangle$ extraction in pp and Pb–Pb collisions will be described.
Due to the slight transverse momentum dependence of the acceptance × efficiency (see e.g. Fig. 5.1 right panel) J/ψ are reconstructed with different probability at different transverse momenta. Hence, when averaging transverse momenta of J/ψ this p_{T} dependence of the acceptance × efficiency needs to be taken into account. In case of a perfectly flat $A \times \epsilon$ this would not be necessary since the shape of the p_{T} spectrum would not be changed by the detector response. Since the $A \times \epsilon$ is the relevant quantity for the transformation of the true spectra to the reconstructed level, the inverse ($(A \times \epsilon)^{-1}$) is the relevant quantity for the transformation back to the true level. Hence, in order to obtain back the true p_{T} spectrum shape the inverse of the acceptance × efficiency is applied as weight in the calculation of the $\langle p_{\mathrm{T}} \rangle$ (see Eq. 5.2). In the case of the $\langle p_{\mathrm{T}}^2 \rangle$ the correction is applied in the same way.

$$\langle p_{\mathrm{T}} \rangle_{\mathrm{corrected}} = \frac{\sum p_{\mathrm{T}} \cdot (A \times \epsilon)^{-1}}{\sum (A \times \epsilon)^{-1}}, \qquad \langle p_{\mathrm{T}}^2 \rangle_{\mathrm{corrected}} = \frac{\sum p_{\mathrm{T}}^2 \cdot (A \times \epsilon)^{-1}}{\sum (A \times \epsilon)^{-1}} \tag{5.2}$$

In Pb–Pb collisions the $A \times \epsilon$ is additionally centrality dependent (see Sec. 4.6). Since we aim to study the $\langle p_{\mathrm{T}} \rangle$ and $\langle p_{\mathrm{T}}^2 \rangle$ as a function of centrality this needs to be taken into account in the correction. Hence, a map of the $A \times \epsilon$ is created as a function of centrality and p_{T} (see Fig. 5.1 left panel).

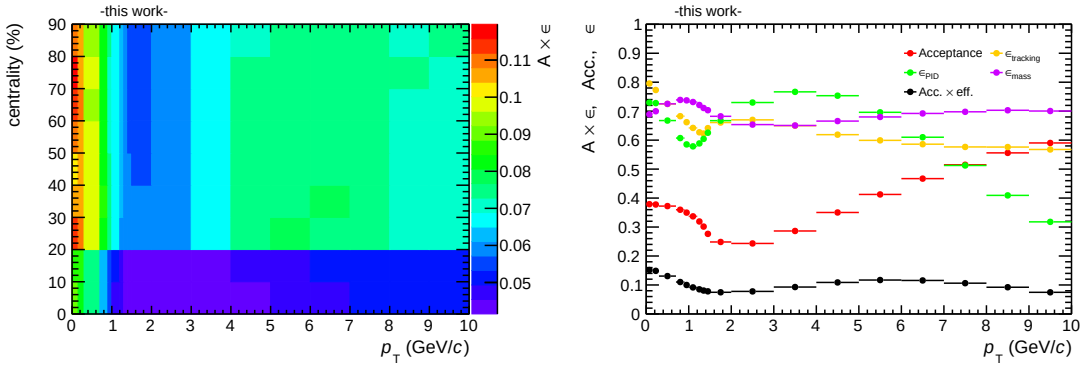

Figure 5.1: Left: Acceptance × efficiency map used for the correction of the Pb–Pb data. Right: Acceptance × efficiency as function of p_{T} with its different steps in pp collisions.

The $A \times \epsilon$ factors are taken from this map and dielectron pairs from a given interval in centrality and p_{T} are corrected using the corresponding correction factor. The $A \times \epsilon$ for pp collisions is shown in Fig. 5.1 right panel together with its different

steps. The shapes of the different steps have already been explained for the Pb–Pb case in Sec. 4.6. In pp collisions they are very similar, however, the overall $A \times \epsilon$ is slightly higher due to the softer electron selection criteria. In pp collisions the correction of the $\langle p_{\mathrm{T}} \rangle$ and $\langle p_{\mathrm{T}}^2 \rangle$ is done using only the p_{T} dependent $A \times \epsilon$ as weight. The known rapidity dependence of the $A \times \epsilon$ is not considered in the weighting since the moments are not extracted as a function of rapidity.

5.5 Signal extraction

As explained in Sec. 5.3 the inclusive J/ψ signal extraction has to be carried out in order to derive the distributions for the number of signal and background pairs. In the inclusive signal extraction the p_{T} of the J/ψ is required to be below $p_{\mathrm{T}} < 10$ GeV/c. In Pb–Pb collisions it is additionally required to be above $p_{\mathrm{T}} > 0.15$ GeV/c in order to exclude the photoproduction component mentioned in Sec. 2.5. The implication of this minimum transverse momentum requirement on the $\langle p_{\mathrm{T}} \rangle$ and $\langle p_{\mathrm{T}}^2 \rangle$ is discussed in Sec. 6.3.
In Pb–Pb collisions the background is described using the event mixing technique. Here the same event mixing categories are used as in Sec. 4.5. The Pb–Pb signal extraction is done in five bins in centrality and is shown in Fig. 5.2 and 5.3 (left panel). The mixed event background is scaled to the same event distributions in the ranges $2.0 < m_{e^+e^-} < 2.5$ GeV/c^2 and $3.2 < m_{e^+e^-} < 4.0$ GeV/c^2 using the weighted average of the obtained normalization factors. The signal is extracted by bin counting in the window $2.92 < m_{e^+e^-} < 3.16$ GeV/c^2. The obtained significances are around $\frac{\mathrm{S}}{\sqrt{\mathrm{S+B}}} \approx 8$ or higher, corresponding to statistical uncertainties lower than 13%. The background description is sufficiently good as can be judged from the reduced χ^2 between the background subtracted distribution and the normalized MC shape. As in Sec. 4.5 the signal to background ratio improves towards peripheral collisions due to the lower amount of electrons per event.
In pp collisions a different signal extraction approach is followed. Due to the high precision of the data and the low amount of electrons per event in pp collisions correlated background becomes non-negligible. Hence the event mixing technique is not suitable for the modeling of the background. Instead, the background is described using a polynomial of order four in the range 2–4 GeV/c^2. This polynomial function is combined with the J/ψ MC shape derived from the dedicated detector simulation corresponding to this data taking campaign. The sum of the background polynomial and the MC shape is fit to the opposite sign invariant mass distribution in the range 2–4 GeV/c^2 using a likelihood fit (see Fig. 5.3 right panel). Since the shape of the J/ψ distribution is fixed, only the amplitude of the distribution is a free parameter in the fit. The description of the opposite sign invariant mass distribution with the combined fit is very good as demonstrated by the reduced χ^2 of the fit.

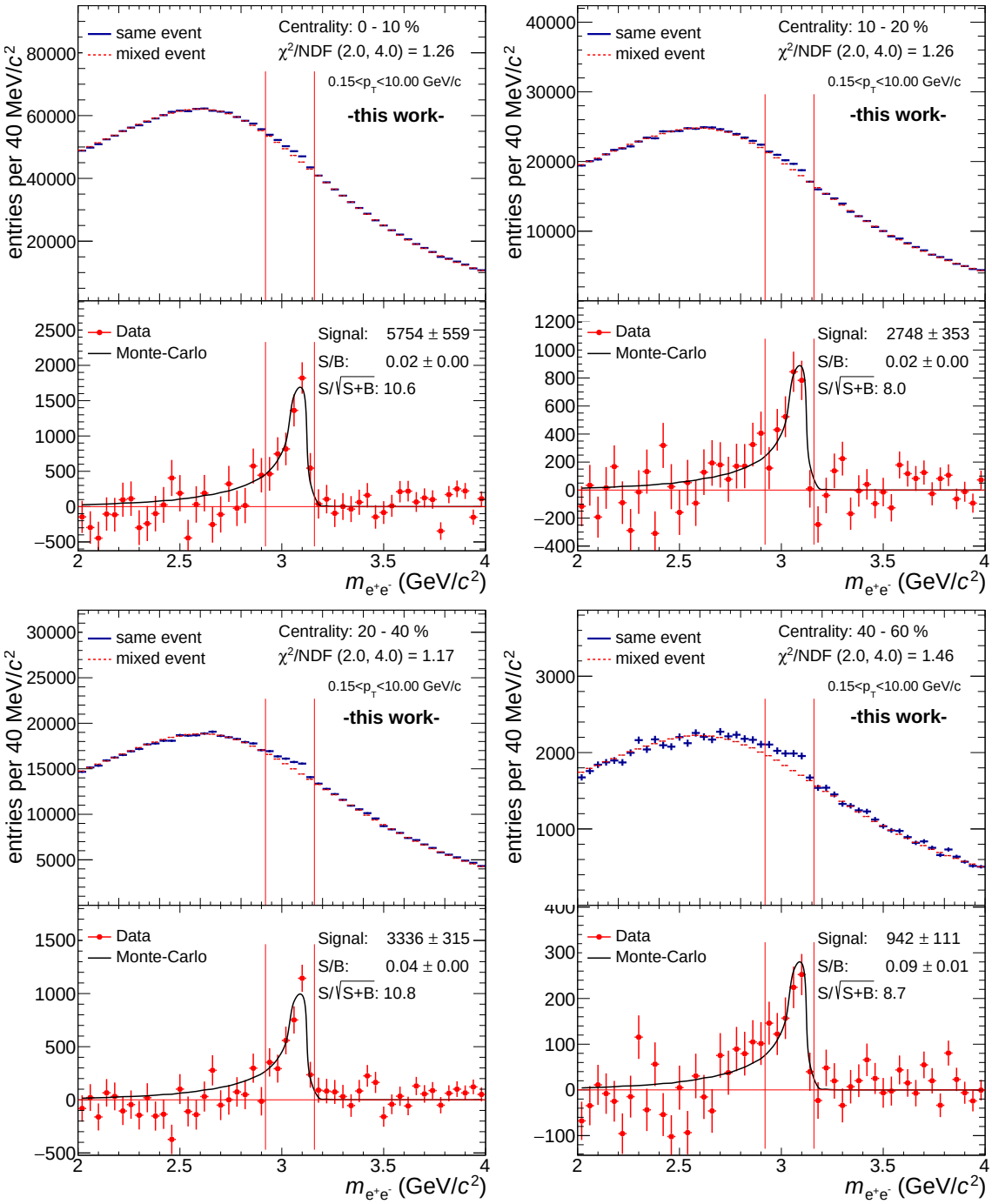

Figure 5.2: Inclusive signal extraction in Pb–Pb collisions in the centrality intervals up to 60%.

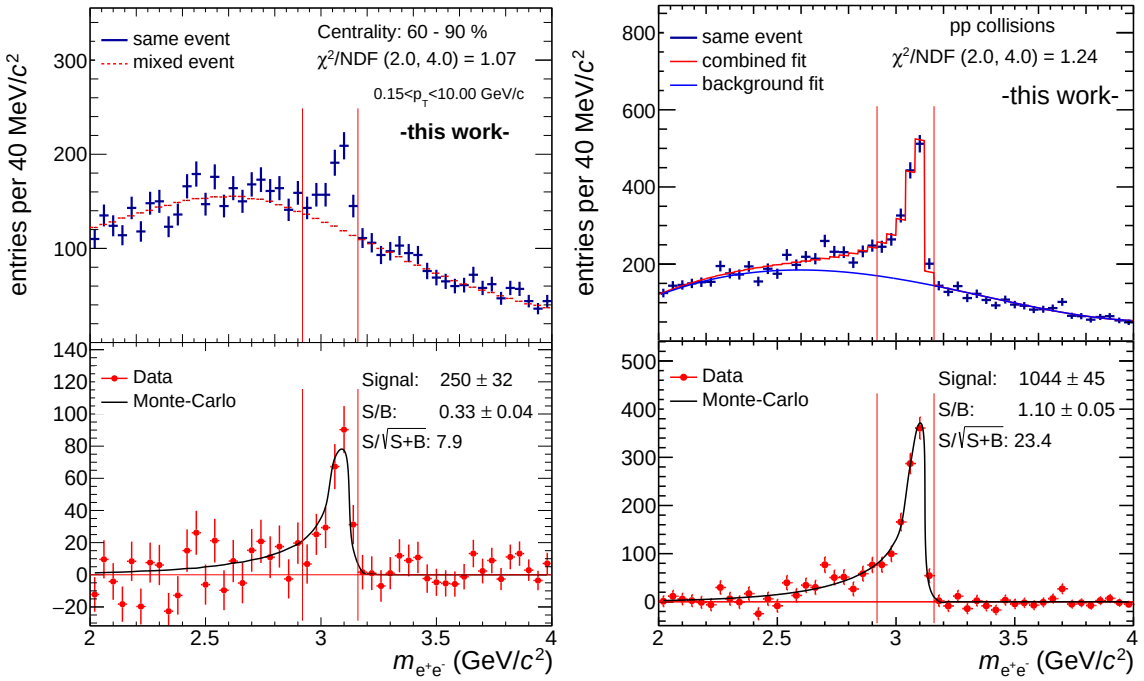

Figure 5.3: Inclusive signal extraction for Pb–Pb collisions in the centrality interval 60–90% (left) and for pp collisions (right).

At around $m_{e^+e^-} \approx 3.7$ GeV/c^2 a hint of a ψ(2S) signal can be seen. In this case it is still consistent with a fluctuation and hence does not influence the fit quality to an observable degree. In higher statistics datasets in the future the ψ(2S) contribution needs to be taken into account in the signal extraction employing background fits. Also, the detection of ψ(2S) represents a great physics opportunity as will be discussed in Chapter 7. The signal is finally also extracted via bin counting in the window $2.92 < m_{e^+e^-} < 3.16$ GeV/c^2.
In pp collisions in total a signal of $S = 1044 \pm 45$ could be extracted with a signal to background ratio of $S/B \approx 1.1$. Hence the statistical uncertainty of the signal is as low as 4.3%.

Finally for the signal distribution $N_{\mathrm{S}}(m_{e^+e^-})$ the MC shape of the respective dataset normalized to the number of extracted counts in the counting window is taken. In case of Pb–Pb collisions the normalized mixed event distribution is taken as the background distribution $N_{\mathrm{B}}(m_{e^+e^-})$. In pp collisions the background function which is obtained from the fit is taken as $N_{\mathrm{B}}(m_{e^+e^-})$.

In Pb–Pb collisions the background $\langle p_{\mathrm{T}}^{\mathrm{B}}(m_{e^+e^-}) \rangle$ distribution is obtained using the event mixing technique with the same categories as in the inclusive signal extraction. The pair transverse momentum range selection which is applied to the same event pairs is also applied to the mixed event pairs in order to assure the same kinematic selection. The distribution is constructed by weighting with the corresponding $A \times \epsilon$

correction factors as explained in Sec. 5.4. The same correction procedure is applied to the same event $\langle p_{\mathrm{T}}(m_{e^+e^-})_{\mathrm{S+B}} \rangle$ distribution.
In pp collisions the background $\langle p_{\mathrm{T}}^{\mathrm{B}}(m_{e^+e^-}) \rangle$ distribution is obtained from a fit to the same event $\langle p_{\mathrm{T}}(m_{e^+e^-})_{\mathrm{S+B}} \rangle$ distribution after the $A \times \epsilon$ correction is applied. In this fit the signal region (2.5–3.2 GeV/c^2) is spared and the distribution is fit with a polynomial of order two ($\langle p_{\mathrm{T}} \rangle$) or order four ($\langle p_{\mathrm{T}}^2 \rangle$) as shown in Fig. 5.4.

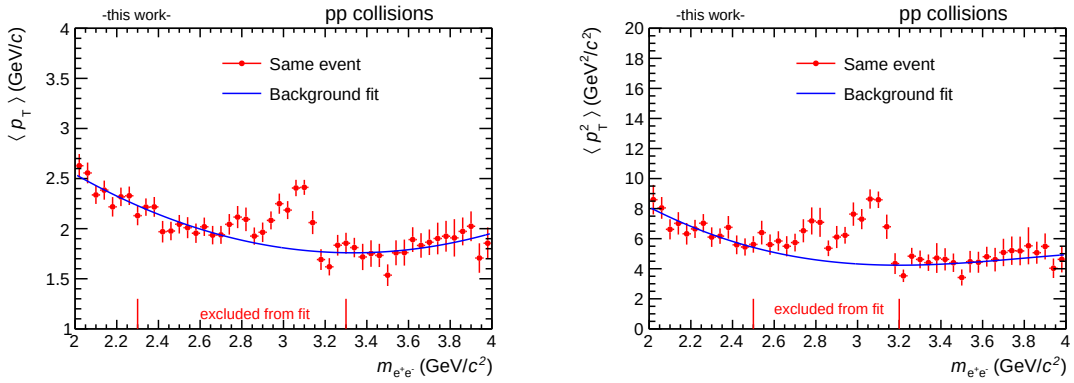

Figure 5.4: Parameterization of the background $\langle p_{\mathrm{T}} \rangle$ and $\langle p_{\mathrm{T}}^2 \rangle$ in pp collisions.

Finally the $A \times \epsilon$ corrected $\langle p_{\mathrm{T}} \rangle$ is extracted by fitting the $\langle p_{\mathrm{T}}(m_{e^+e^-})_{\mathrm{S+B}} \rangle$ distribution with the right hand side of Eq. 5.1. This fit is carried out in the mass interval 2.92 $< m_{e^+e^-} <$ 3.16 GeV/c^2 in both pp and Pb–Pb collisions. The choice of the window in which the fit is carried out is considered in the systematic uncertainties as described in Sec. 5.7. The extraction of the $\langle p_{\mathrm{T}} \rangle$ is shown in Fig. 5.5 for the different centrality bins in Pb–Pb collisions as well as for pp collisions. Since the $\langle p_{\mathrm{T}} \rangle$ of the J/ψ is higher than the $\langle p_{\mathrm{T}} \rangle$ of the background a peak can be observed at the J/ψ mass. This peak gets more pronounced towards more peripheral collisions due to the increasing signal to background ratio (and partly due to a higher $\langle p_{\mathrm{T}} \rangle$). The width of the peak does not directly reflect the detector resolution in this case since the number of J/ψ distribution $N_{\mathrm{S}}(m_{e^+e^-})$ is modulated by the mass dependent $N_{\mathrm{S}}(m_{e^+e^-})/(N_{\mathrm{S}}(m_{e^+e^-}) + N_{\mathrm{B}}(m_{e^+e^-}))$ ratio.
The template fit extraction of the $\langle p_{\mathrm{T}}^2 \rangle$ is shown in Fig. 5.6 and is carried out in a similar way. For the extraction of the $\langle p_{\mathrm{T}}^2 \rangle$ the $\langle p_{\mathrm{T}} \rangle$ terms in Eq. 5.1 are replaced by $\langle p_{\mathrm{T}}^2 \rangle$, however their determination methods remain the same.
Overall all $\langle p_{\mathrm{T}} \rangle$ and $\langle p_{\mathrm{T}}^2 \rangle$ fits show a good performance as can be seen in the good agreement of the fit result and the same event distributions.
The estimation of the relevant uncertainties will be discussed in Sec. 5.6 and 5.7.

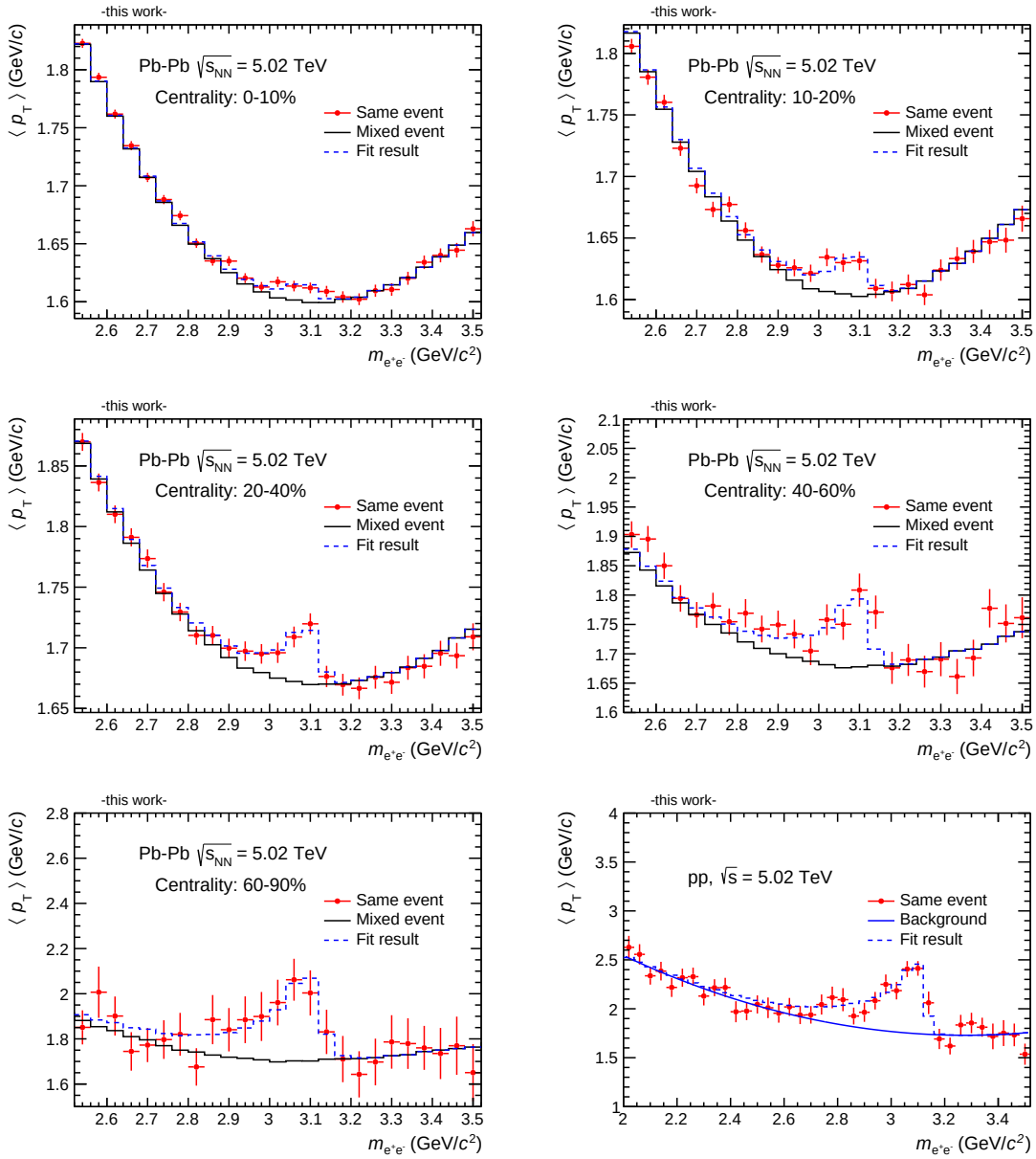

Figure 5.5: Extraction of the J/ψ $\langle p_{\mathrm{T}} \rangle$ with the template fit method in Pb–Pb and pp collisions.

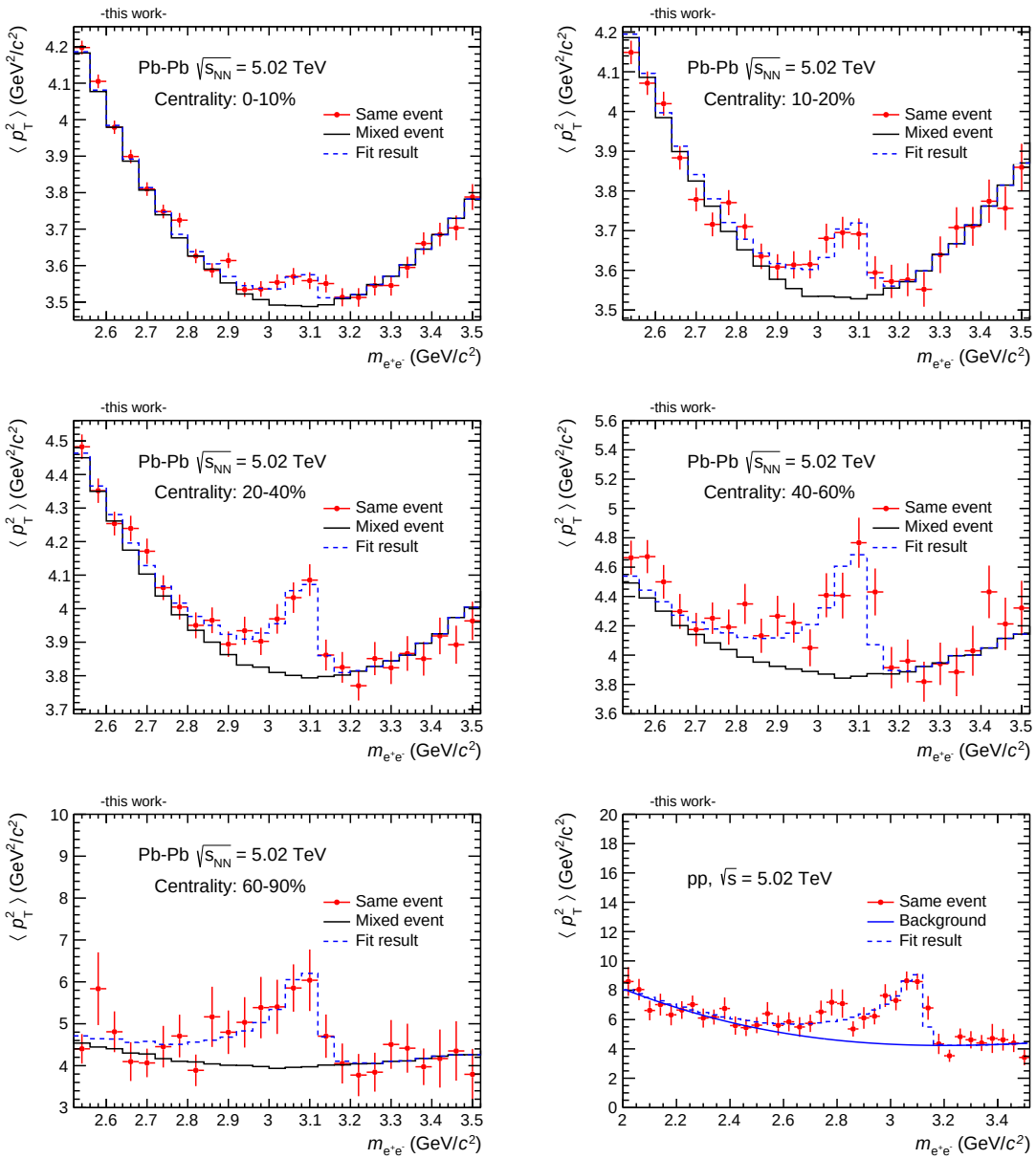

Figure 5.6: Extraction of the J/ψ $\langle p_{\mathrm{T}}^2 \rangle$ with the template fit method in Pb–Pb and pp collisions.

5.6 Statistical uncertainties

The estimation of the statistical uncertainties of the $\langle p_{\mathrm{T}} \rangle$ and $\langle p_{\mathrm{T}}^2 \rangle$ determination is described in this section. In the used template fit extraction method in principle multiple sources add to the statistical uncertainty as visible in Eq. 5.1. However, if the background is described by event mixing or a functional fit the statistical uncertainty of the background distribution can be considered as negligible. Possible imperfections in the background description are treated as systematic uncertainty and will be discussed in Sec. 5.7. Hence, only the statistical uncertainty of the same event distribution $\langle p_{\mathrm{T}}(m_{e^+e^-})_{\mathrm{S+B}} \rangle$ and the statistical uncertainty of the number of J/ψ $N_{\mathrm{S}}(m_{e^+e^-})$ constitute to the overall statistical uncertainty.
In order to evaluate the statistical uncertainty related to the same event $\langle p_{\mathrm{T}}(m_{e^+e^-})_{\mathrm{S+B}} \rangle$ distribution the following approach is used: Every point of the distribution is smeared randomly around its central value using a Gaussian probability density with a width which corresponds to the statistical uncertainty of the point. Once this is done the $\langle p_{\mathrm{T}} \rangle$ is extracted from the smeared distribution and the distribution is unsmeared again. This procedure is carried out $\mathcal{O}(10^4)$ times in order to obtain a result distribution. This distribution is fit with a Gaussian and the width is extracted (shown in Fig. D.1 and D.2 in Appendix D).
The evaluation of the statistical uncertainty related to the extracted number of J/ψ counts is estimated in the following way: The extracted signal is varied randomly according to its statistical uncertainty using a Gaussian probability distribution. The varied number of counts is used to create a signal distribution $N_{\mathrm{S}}(m_{e^+e^-})$ and the $\langle p_{\mathrm{T}} \rangle$ extraction is carried out. This procedure is also repeated $\mathcal{O}(10^4)$ times and the width of the result distribution is extracted using a Gaussian fit (see Fig. D.3 and D.4 in Appendix D).
The obtained relative statistical uncertainties in Pb–Pb collisions are summarized in Fig. 5.7.

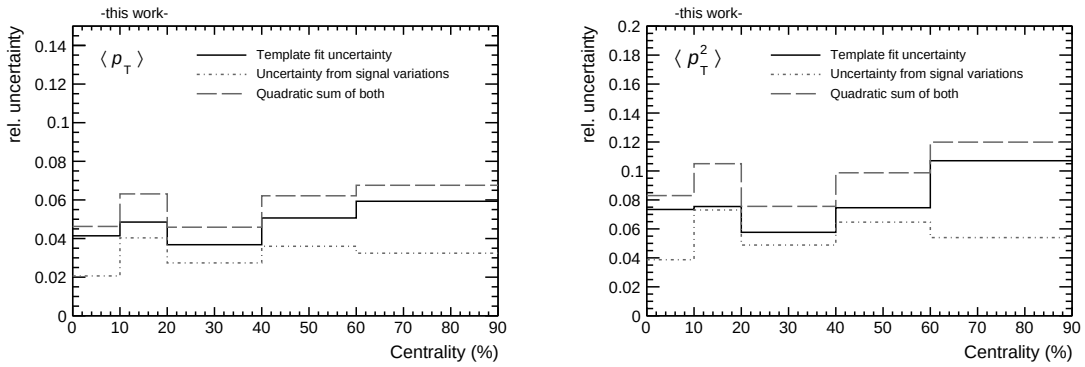

Figure 5.7: Summary of the relative statistical uncertainties of the $\langle p_{\mathrm{T}} \rangle$ and $\langle p_{\mathrm{T}}^2 \rangle$ in Pb–Pb collisions.

It is found that the statistical uncertainty related to the same event $\langle p_{\mathrm{T}}(m_{e^+e^-})_{\mathrm{S+B}} \rangle$ ("template fit uncertainty") is the dominating source of statistical uncertainty. Also,

this uncertainty coincides with the uncertainty returned by the minimizer algorithm since the uncertainties of the templates on the right hand side of Eq. 5.1 are not considered in the fit. Hence the latter is taken in further analysis steps in order to reduce the complexity of the analysis chain. The uncertainty related to the number of J/ψ distribution is smaller in every case. This can be understood by the suppressed influence of the uncertainty of $N_{\mathrm{S}}(m_{e^+e^-})$ in the ratio

$$N_{\mathrm{S}}(m_{e^+e^-})/(N_{\mathrm{S}}(m_{e^+e^-}) + N_{\mathrm{B}}(m_{e^+e^-}))$$

in Eq. 5.1.
The obtained statistical uncertainties in pp collisions are summarized in Tab. 5.3.

Source	Rel. stat. $\langle p_{\mathrm{T}} \rangle$ (%)	Rel. stat. $\langle p_{\mathrm{T}}^2 \rangle$ (%)
Template fit uncertainty	2.6	5.0
Uncertainty from signal variation	0.7	1.1
Total	2.6	5.1

Table 5.3: Summary of statistical uncertainties for $\langle p_{\mathrm{T}} \rangle$ and $\langle p_{\mathrm{T}}^2 \rangle$ in pp collisions.

Both sources are added in quadrature in order to define the total statistical uncertainty.

5.7 Systematic uncertainties

The estimation of the systematic uncertainties is carried out in a similar way as for the J/ψ spectra measurement. In general the systematic uncertainties are grouped into signal extraction, PID, tracking and MC kinematics.
The signal extraction uncertainty here contains all uncertainties which are relevant for the template fit extraction according to Eq. 5.1. The influence of the fixed fit range was assessed by increasing the window to $2.72 < m_{e^+e^-} < 3.36$ GeV/c^2 and $2.52 < m_{e^+e^-} < 3.56$ GeV/c^2. In addition the sensitivity of the template fit extraction to the bin size was tested by doubling it to 80 MeV/c^2. In Pb–Pb collisions at $\sqrt{s_{\mathrm{NN}}}$ = 2.76 TeV this variation led to a large uncertainty in peripheral collisions [205], however here it was found to yield smaller deviations than other typical variations. In Pb–Pb collisions also the ranges of the mixed event normalization in the inclusive signal extraction are varied away from the standard choice by increasing the sidebands or by giving more weight to the lower or higher mass regions. The influence of the mass window choice used in the inclusive signal extraction is tested in the same fashion. In pp collisions the background description in the inclusive signal extraction is tested by changing the fitting range. This is also done by giving once more weight to the lower mass side and once to the higher mass side. In the end the standard deviation of the obtained result distribution is taken as uncertainty.
For the tracking and PID uncertainties the description of the associated variables

in the simulation is important. However, since the $A \times \epsilon$ correction is applied as a relative correction only p_{T} dependent mismatches between the data and the simulation should be important. Hence, it is expected that the relative systematics are smaller here than in the yield extraction.
The PID and track selection criteria have been varied away from the standard choices. Each choice is individually made stronger or weaker when possible. In Pb–Pb collisions due to greater number of track selection criteria variations the Barlow criterion has been exploited to exclude variations which are consistent with fluctuations (in the same way as in Sec. 4.7). In the PID and tracking categories also the standard deviation of the result distributions are assigned as systematic uncertainty.
In the measurement of the J/ψ spectra an uncertainty is assigned to the MC kinematics. This uncertainty arises since the underlying J/ψ p_{T} distribution is not precisely known and thus $A \times \epsilon$ correction factors obtained in wide p_{T} bins are sensitive to the underlying spectral shape. In the case of the $\langle p_{\mathrm{T}} \rangle$ and $\langle p_{\mathrm{T}}^2 \rangle$ analysis however the $A \times \epsilon$ correction is applied in much finer bins in p_{T} as in the spectrum measurement. Hence no uncertainty is assigned to the MC kinematics.
Finally as result value the mean of all systematic variations is quoted. For the statistical uncertainty the mean of all statistical uncertainties is taken where the uncertainty related to the signal variations is added in the end.
In the tables 5.4 and 5.5 the assigned uncertainties are listed for the $\langle p_{\mathrm{T}} \rangle$ and $\langle p_{\mathrm{T}}^2 \rangle$ respectively.

Centrality (%)	Relative systematic uncertainty $\langle p_{\mathrm{T}} \rangle$ (%)			
	Signal extraction	PID	Tracking	Total
0–10	0.8	1.9	2.8	3.5
10–20	1.0	1.9	4.1	4.7
20–40	1.2	1.0	2.2	2.7
40–60	1.2	1.2	3.5	3.9
60–90	0.9	1.8	1.5	2.5
pp collisions	0.6	2.1	0.7	2.3

Table 5.4: Summary of systematic uncertainties for the $\langle p_{\mathrm{T}} \rangle$ analysis.

Centrality (%)	Relative systematic uncertainty $\langle p_{\mathrm{T}}^2 \rangle$ (%)			
	Signal extraction	PID	Tracking	Total
0–10	1.5	2.6	4.8	5.6
10–20	1.9	3.3	5.8	7.0
20–40	2.1	1.5	3.5	4.4
40–60	2.1	2.2	2.9	4.2
60–90	1.2	3.6	3.8	5.4
pp collisions	1.4	2.1	1.3	3.4

Table 5.5: Summary of systematic uncertainties for the $\langle p_{\mathrm{T}}^2 \rangle$ analysis.

5.8 Extracting moments using measured spectra

As explained in Sec. 5.3 the $\langle p_{\mathrm{T}} \rangle$ and $\langle p_{\mathrm{T}}^2 \rangle$ of J/ψ can also be extracted using fits to measured spectra. Typically the following functional shape is used for fits of J/ψ $\mathrm{d}N/\mathrm{d}p_{\mathrm{T}}$ spectra (as in e.g. [114, 209, 210]):

$$f(p_{\mathrm{T}}) = C_0 \cdot \frac{p_{\mathrm{T}}}{(1 + (p_{\mathrm{T}}/p_0)^2)^n}, \tag{5.3}$$

with three parameters C_0, p_0 and n. The moments of this function can be obtained from integrating that function in a given range $a \leq p_{\mathrm{T}} \leq b$:

$$\langle p_{\mathrm{T}} \rangle \Big|_a^b = \frac{\int_a^b p_{\mathrm{T}} \cdot f(p_{\mathrm{T}})\ \mathrm{d}p_{\mathrm{T}}}{\int_a^b f(p_{\mathrm{T}})\ \mathrm{d}p_{\mathrm{T}}}, \qquad \langle p_{\mathrm{T}}^2 \rangle \Big|_a^b = \frac{\int_a^b p_{\mathrm{T}}^2 \cdot f(p_{\mathrm{T}})\ \mathrm{d}p_{\mathrm{T}}}{\int_a^b f(p_{\mathrm{T}})\ \mathrm{d}p_{\mathrm{T}}}. \tag{5.4}$$

The estimation of the uncertainties of the moments can be done in different ways. The uncertainty of the normalization constant C_0 does not influence the determination of $\langle p_{\mathrm{T}} \rangle$ and $\langle p_{\mathrm{T}}^2 \rangle$ and hence can be neglected. Hence only the uncertainties of p_0 and n have to be propagated. However, these parameters are typically strongly correlated which has to be taken into account. One option of uncertainty estimation is to sample randomly the 1 σ ellipsoid in the $p_0 - n$ space and extract the variations of the moments from the function variations. This was done in e.g. [211]. However, it has the disadvantage that not the full phase space is sampled resulting in a spiked result distribution which is sensitive to fluctuations. A way to sample the full phase space is described in Sec. 4.8. Another option is to use general error propagation employing the elements V_{ij} of the covariance matrix:

$$\sigma_y^2 \approx \sum_{i,j=1}^{N} \left[\frac{\partial y}{\partial x_i} \frac{\partial y}{\partial x_j} \right]_{\vec{x}=\vec{\mu}} V_{ij}, \tag{5.5}$$

where y depends on N parameters. In case of the two parameters p_0 and n this equation reduces to:

$$\sigma_y^2 \approx \left(\frac{\partial y}{\partial p_0}\right)^2\Big|_{\vec{\mu}} V_{p_0p_0} + 2\frac{\partial y}{\partial p_0}\frac{\partial y}{\partial n}\Big|_{\vec{\mu}} V_{p_0n} + \left(\frac{\partial y}{\partial n}\right)^2\Big|_{\vec{\mu}} V_{nn}, \tag{5.6}$$

with $\vec{\mu} = (\hat{p_0}, \hat{n})$ being the central result and $y = \langle p_{\mathrm{T}}^j\rangle$ $(j = 1, 2)$. With $x_k \in \{p_0, n\}$ the derivatives are given by:

$$\frac{\partial}{\partial x_k}\langle p_{\mathrm{T}}^j\rangle\Big|_a^b = \frac{\partial}{\partial x_k}\frac{\int_a^b p_{\mathrm{T}}^j \cdot f(p_{\mathrm{T}}, x_k)\ \mathrm{d}p_{\mathrm{T}}}{\int_a^b f(p_{\mathrm{T}}, x_k)\ \mathrm{d}p_{\mathrm{T}}} \tag{5.7}$$

The derivative of the fraction can be evaluated:

$$\begin{aligned}\frac{\partial}{\partial x_k}\langle p_{\mathrm{T}}^j\rangle\Big|_a^b \ = \ & \frac{\frac{\partial}{\partial x_k}\int_a^b p_{\mathrm{T}}^j \cdot f(p_{\mathrm{T}}, x_k)\ \mathrm{d}p_{\mathrm{T}} \cdot \int_a^b f(p_{\mathrm{T}}, x_k)\ \mathrm{d}p_{\mathrm{T}}}{(\int_a^b f(p_{\mathrm{T}}, x_k)\ \mathrm{d}p_{\mathrm{T}})^2} \\ & - \frac{\int_a^b p_{\mathrm{T}}^j \cdot f(p_{\mathrm{T}}, x_k)\ \mathrm{d}p_{\mathrm{T}} \cdot \frac{\partial}{\partial x_k}\int_a^b f(p_{\mathrm{T}}, x_k)\ \mathrm{d}p_{\mathrm{T}}}{(\int_a^b f(p_{\mathrm{T}}, x_k)\ \mathrm{d}p_{\mathrm{T}})^2}\end{aligned} \tag{5.8}$$

Since $f(p_{\mathrm{T}}, x_k)$ is a smooth function and the variables in the integration and derivative are different the integration and derivation can be exchanged:

$$\begin{aligned}\frac{\partial}{\partial x_k}\langle p_{\mathrm{T}}^j\rangle\Big|_a^b \ = \ & \frac{\int_a^b p_{\mathrm{T}}^j \cdot \frac{\partial}{\partial x_k} f(p_{\mathrm{T}}, x_k)\ \mathrm{d}p_{\mathrm{T}} \cdot \int_a^b f(p_{\mathrm{T}}, x_k)\ \mathrm{d}p_{\mathrm{T}}}{(\int_a^b f(p_{\mathrm{T}}, x_k)\ \mathrm{d}p_{\mathrm{T}})^2} \\ & - \frac{\int_a^b p_{\mathrm{T}}^j \cdot f(p_{\mathrm{T}}, x_k)\ \mathrm{d}p_{\mathrm{T}} \cdot \int_a^b \frac{\partial}{\partial x_k} f(p_{\mathrm{T}}, x_k)\ \mathrm{d}p_{\mathrm{T}}}{(\int_a^b f(p_{\mathrm{T}}, x_k)\ \mathrm{d}p_{\mathrm{T}})^2}\end{aligned} \tag{5.9}$$

The two derivatives (with respect to p_0 or n) can be calculated analytically (omitting intermediate steps for clarity):

$$\frac{\partial}{\partial p_0} f(p_{\mathrm{T}}) = \frac{2np_{\mathrm{T}}^3\left(1 + \frac{p_{\mathrm{T}}^2}{p_0^2}\right)^{-1-n}}{p_0^3}, \tag{5.10}$$

$$\frac{\partial}{\partial n} f(p_{\mathrm{T}}) = -p_{\mathrm{T}}\left(1 + \frac{p_{\mathrm{T}}^2}{p_0^2}\right)^{-n}\ln\left(1 + \frac{p_{\mathrm{T}}^2}{p_0^2}\right). \tag{5.11}$$

After the derivatives have been calculated the integration in the desired p_{T} range $a \le p_{\mathrm{T}} \le b$ can be carried out. This is done numerically in this work to avoid further complications. Finally inserting the terms into Eq. 5.6 yields the uncertainty of the

desired moment.
The advantage of the procedure of first calculating the derivatives and integrating afterwards is that the derivatives can be calculated analytically. The analytical integration can yield very complex terms in case of $a > 0$ and $b < \infty$. It has been verified that both options lead to the same results in case of $a = 0$ and $b = \infty$ for the uncertainty estimation of the moments in Pb–Pb collisions.
In the course of this work several measured spectra have been fitted in order to derive $\langle p_{\mathrm{T}} \rangle$ and $\langle p_{\mathrm{T}}^2 \rangle$ values. The fits to the Pb–Pb J/ψ spectra obtained in Sec. 4 are shown in Sec. 4.8. In addition fits to the ALICE $\sqrt{s} = 7$ TeV pp J/ψ spectrum and PHENIX $\sqrt{s} = 200$ GeV have been carried out and are shown in Fig. 5.8 and 5.9. The extracted values of the $\langle p_{\mathrm{T}} \rangle$ and $\langle p_{\mathrm{T}}^2 \rangle$ can be found in Appendix A.
When deriving results for the $\langle p_{\mathrm{T}} \rangle$ and $\langle p_{\mathrm{T}}^2 \rangle$ from the fits to spectra the following strategy is used: The central result is defined by a fit to the spectrum using the quadratic sum of statistical and systematic uncertainties as error on the points. In order to propagate the statistical and systematic uncertainty the spectra are fit separately where once only the statistical and once only the systematic uncertainties are assigned to the points. Each time the full error propagation according to Eq. 5.6 is carried out.
Another option to derive the $\langle p_{\mathrm{T}} \rangle$ and $\langle p_{\mathrm{T}}^2 \rangle$ values from measured spectra is the numerical calculation. In case spectra are measured in very fine bins Eq. 5.12 can be discretized:

$$\langle p_{\mathrm{T}} \rangle \Big|_a^b = \frac{\sum_a^b p_{\mathrm{T}} \cdot f(p_{\mathrm{T}})\ \Delta p_{\mathrm{T}}}{\sum_a^b f(p_{\mathrm{T}})\ \Delta p_{\mathrm{T}}}, \qquad \langle p_{\mathrm{T}}^2 \rangle \Big|_a^b = \frac{\sum_a^b p_{\mathrm{T}}^2 \cdot f(p_{\mathrm{T}})\ \Delta p_{\mathrm{T}}}{\sum_a^b f(p_{\mathrm{T}})\ \Delta p_{\mathrm{T}}}. \tag{5.12}$$

In this case $f(p_{\mathrm{T}})$ represents the measured cross-section (or yield) values.

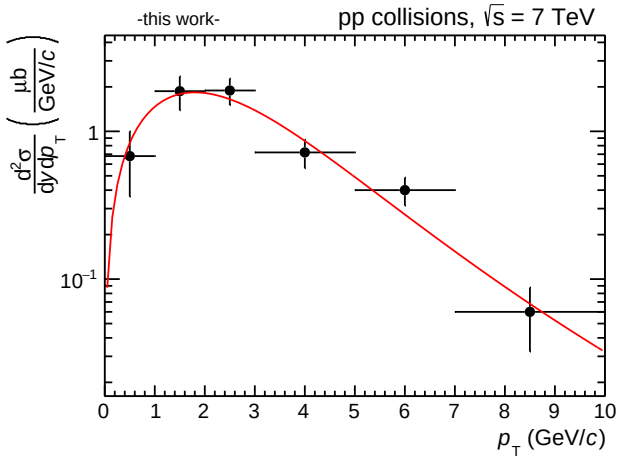

Figure 5.8: Fit to the ALICE J/ψ spectrum measured at $\sqrt{s} = 7$ TeV where the quadratic sum of statistical and systematic uncertainty is assigned to the points. In the fit the integral of the bins is used. The data is taken from [101, 199].

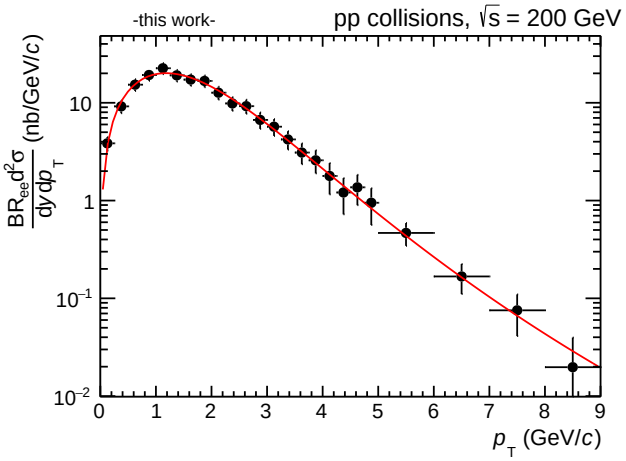

Figure 5.9: Fit to the PHENIX J/ψ spectrum measured at $\sqrt{s} = 200$ GeV where the sum of statistical and systematic uncertainty is assigned to the points. In the fit the integral of the bins is used. The data is taken from [212].

6 Results

In this chapter the results of this work will be presented. The results are separated into three blocks: Firstly the centrality and rapidity dependence of the nuclear modification factor will be presented in Sec. 6.1. The J/ψ transverse momentum spectra and the transverse momentum dependence of the nuclear modification factor are presented in Sec. 6.2. Finally, the results for the J/ψ $\langle p_{\mathrm{T}} \rangle$ and $\langle p_{\mathrm{T}}^2 \rangle$ are presented in Sec. 6.3.

6.1 Centrality dependence of the nuclear modification factor

The PID studies and calibrations presented in Sec. 4.4 enabled the measurement of the inclusive J/ψ nuclear modification factor. The final determination of the J/ψ yields as a function of centrality was carried out in [213]. The results are presented also here since an important contribution was made towards these results within the scope of this thesis. In addition it is the goal to provide a full picture of J/ψ production in Pb–Pb collisions.

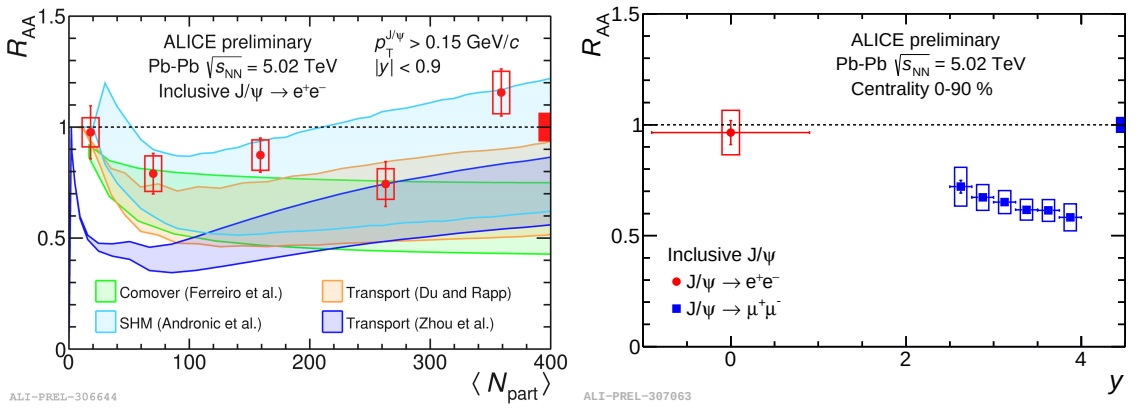

Figure 6.1: Left: Centrality dependence of the J/ψ nuclear modification factor compared to model calculations. Right: Rapidity dependence of the nuclear modification factor. The correlated uncertainty only represents the reference uncertainty of the forward measurement. The figures are taken from [214].

In the left panel of Fig. 6.1 the nuclear modification factor of J/ψ is shown as a function of centrality. The pp reference cross-section used here became available during the writing of this thesis and is obtained from the pp data by the collaboration. The

measured value is $\mathrm{d}\sigma_{\mathrm{J}/\psi}/\mathrm{d}y = 5.64 \pm 0.22$ (stat.) ± 0.33 (syst.) ± 0.12 (luminosity) μb. The error bar around unity represents the correlated uncertainty from the pp reference cross section and the nuclear overlap function. The nuclear modification factor is found to be rather flat as a function of centrality with a hint of an increase in most central collisions. The measurement is compared to model predictions which include J/ψ production by (re)combination. The models are described in detail in Sec. 2.4.2. In the statistical hadronization model (SHM) [215] it is assumed that all charm quarks are equilibrated with the medium near the critical temperature T_{c}. The production of J/ψ takes place solely at the phase boundary. Transport models [143–146] on the other hand assume that an initial J/ψ fraction survives during the medium evolution and the other fraction is continuously dissolved and (re)generated. Hence a lower yield of (re)generated J/ψ is expected in general. However, in specific cases the J/ψ yield is sensitive to the model input parameters such as the charm cross-section in pp collisions and the assumed level of shadowing. In the Co-mover model [150] J/ψ mesons are broken up due to interactions with the co-moving partonic medium. With the same probability J/ψ mesons can also be formed by (re)combination. In case the (re)combination component is not considered the model leads to an under-prediction of the J/ψ data at $\sqrt{s_{\mathrm{NN}}} = 2.76$ TeV (see [150]).
The uncertainty bands of the models represent the J/ψ production cross-section in pp collisions and the shadowing uncertainty in case of the statistical hadronization model. In the case of the transport models the uncertainties reflect different assumptions on the shadowing strength, neglecting the uncertainty of the charm cross-section. In the case of the co-mover model the uncertainty band reflects only the uncertainty of the charm cross-section, neglecting the shadowing uncertainty. The model input parameters are summarized in Tab. 6.1. The shadowing factors can be understood as the factor by which the $c\bar{c}$ cross-section is reduced in the models.

Model	$\mathrm{d}\sigma_{c\bar{c}}/\mathrm{d}y$ (mb)	Shadowing
SHM	0.8 ± 0.1	0.56 ± 0.2 (data driven)
Transport (Du and Rapp)	0.85	$(0.5 \pm 0.5) \cdot$ EPS09
Transport (Zhou et al.)	0.86	$(0.5 \pm 0.5) \cdot$ EPS09
Co-mover	0.925 ± 0.175	Glauber-Gribov theory

Table 6.1: Summary of model input parameters. The charm cross section is listed prior to the shadowing reduction. The values are obtained by private communication with the authors.

Within the quoted uncertainties the models including (re)combination can describe most of the data points. The transport model by Zhou et al. however underestimates the J/ψ yield in peripheral collisions. In central collisions the data seems to favor the statistical hadronization model which predicts a nuclear modification factor around unity. In the transport models the upper uncertainty band corresponds to the scenario where shadowing is neglected. The lower uncertainty band corresponds

to a shadowing according to EPS09. Given the p–Pb measurements (see Sec. 2.3) both assumptions might underestimate the magnitude of the relevant p–Pb effects. In case of EPS09 shadowing or even stronger p–Pb effects the models underestimate the data. In order to clearly distinguish between the models in the future it will be necessary to improve the experimental uncertainties of the model input parameters. Very importantly the models also need to converge to common input parameters.
The rapidity dependence of the nuclear modification factor is shown in the right panel of Fig. 6.1. The centrality integrated nuclear modification factor at mid-rapidity is calculated from the centrality dependent measurement and is found to be close to unity. Together with the forward rapidity data a clear increasing trend of the R_{AA} towards mid-rapidity is observed. In the picture of J/ψ production by (re)combination this trend is expected due to the increasing charm cross-section towards mid-rapidity.

6.2 Transverse momentum dependence of J/ψ production

6.2.1 Results from pp collisions

During the writing of this thesis the J/ψ production cross-section measurement by the collaboration based on the high statistics pp data sample mentioned in Chapter 5 became available. The p_{T} dependent cross-section result is shown in Fig. 6.2. In the left panel of Fig. 6.2 the measured p_{T} dependent cross-section is compared to model predictions for the prompt J/ψ cross-section. Since the measured cross-section is obtained for inclusive J/ψ the fraction of J/ψ from beauty feed-down is obtained from FONLL [216, 217] and added to the prompt J/ψ model predictions.

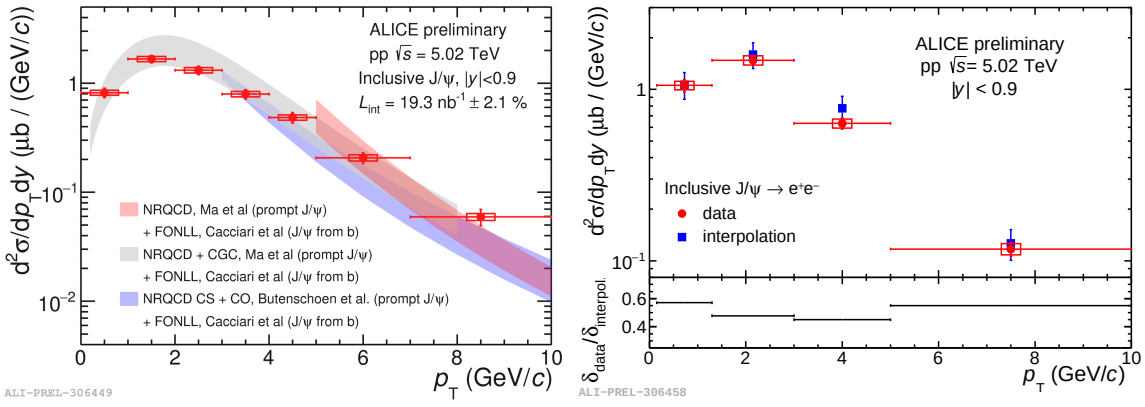

Figure 6.2: Transverse momentum dependent J/ψ production cross-section in pp collisions. Left: Comparison to model predictions. Right: Comparison to the reference obtained from the interpolation explained in Sec. 4.9. The figures are taken from [214].

The model by Ma et al. [218] in which the CGC approach at low p_{T} is coupled to the

NRQCD approach at intermediate p_{T} covers the full p_{T} range up to 8 GeV/c. The agreement with the data is very good in the full range. At high p_{T} it is complemented by the exclusive NRQCD model [219]. The color singlett and color octett model by Butenschoen et al. [220] covers the transverse momentum range above $p_{\mathrm{T}} = 3$ GeV/c. The combined prediction with FONLL seems to slightly undershoot the data.
In the right panel of Fig. 6.2 a comparison of the measured cross-section to the interpolated one is shown in the bins used for the calculation of the nuclear modification factor. The uncertainties quoted for the interpolated reference are the quadratic sum of correlated and uncorrelated uncertainties. As can be seen from the figure the measurement and the interpolation agree within uncertanties while the uncertainties of the reference are dramatically reduced with the measured cross-section.
Given the good agreement of the model calculations with the measured cross-section more differential studies are encouraged. The fragmentation of charm quarks into different final states is studied experimentally using ratios of p_{T} differential cross-sections [221, 222]. In the scope of this work the fragmentation of charm quarks into J/ψ relative to D mesons is studied. In the left panel of Fig. 6.3 the cross-sections of prompt D^0 [222] and J/ψ mesons is shown. In order to study charm fragmentation the J/ψ cross-section shown in Fig. 4.9 has to be corrected for the beauty feed-down component. This is done using a parameterization of the world's data of the fraction of J/ψ from beauty feed-down f_{b}. Since the fraction of J/ψ from beauty feed-down lies only between 10% and 30% for $p_{\mathrm{T}} < 10$ GeV/c and the parameterization of the world's data is quite well constrained the uncertainty of the parameterization is neglected. In the right panel of Fig. 6.3 the ratio of the cross-sections of prompt J/ψ and prompt D^0 mesons is shown.

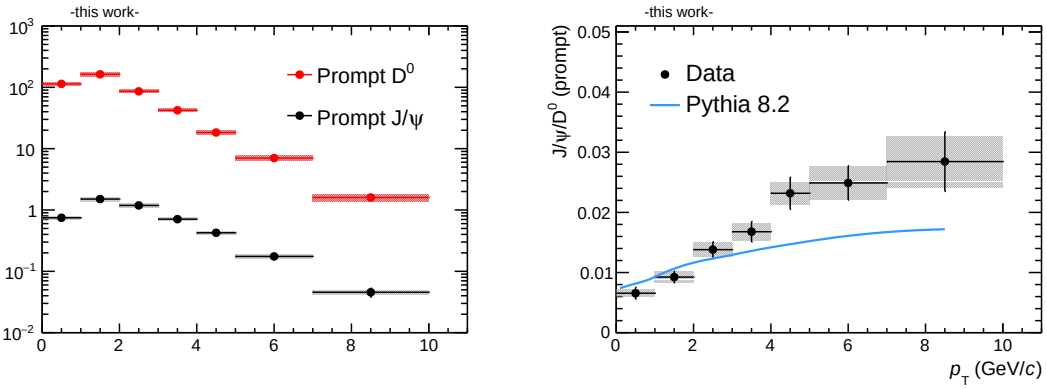

Figure 6.3: Left: Transverse momentum differential cross-section of prompt J/ψ and prompt D^0 mesons. Right: Ratio of J/ψ and D^0 cross-sections. The D^0 meson data is taken from [222].

The ratio shows initially a linear increase until $p_{\mathrm{T}} \approx 5$ GeV/c where it is consistent with a flat behavior. Also a prediction by PYTHIA 8.2 [223] is shown. In PYTHIA 8.2 J/ψ are produced using leading order NRQCD color singlett and color octett contributions. At low p_{T} the PYTHIA prediction is consistent with the data while

above $p_{\mathrm{T}} = 4$ GeV/c the prediction clearly undershoots the data. This departure can have different origins. In the correction for the non-prompt component a universality of the f_{b} is assumed when parameterizing the world's data. However, the world's data is dominated by the CDF data measured at $\sqrt{s} = 1.96$ TeV. A measurement of the f_{b} at $\sqrt{s} = 5.02$ TeV using the high statistics data could verify this assumption of universality. However, if the f_{b} parameterization reflects the true f_{b} to a high degree, the departure of PYTHIA from the data could be seen as an insufficient modeling of the J/ψ production mechanism. A departure from the (LO) NRQCD prediction as implemented in PYTHIA was also seen in the measurement of J/ψ production in jets by LHCb [119] and could be related to the observed departure here.

6.2.2 Results from Pb–Pb collisions

The measurement of the J/ψ spectra in Pb–Pb collisions has been described in Chapter 4. The obtained spectra are shown in Fig. 6.4 where the data points are placed at the calculated x_{lw} values as described in Sec. 4.8. For the most central and semi-central collisions the prediction of the statistical hadronization model [224] is shown. This dynamic version of the statistical hadronization model is shortly described in the following: In [224] the classically stationary statistical hadronization model is coupled to viscous hydrodynamic simulations in order to derive a prediction for the transverse momentum spectra. The simulations are used to constrain parameters of the blast-wave function (see Eq. 1.21). The blast wave function is then used to predict the low p_{T} part of the J/ψ spectrum. The uncertainty band of the model is driven by the imprecise knowledge of the charm cross section in pp collisions and the shadowing uncertainty as described in Sec. 6.1. At low transverse momentum where the J/ψ production is dominated by (re)combination from thermalized deconfined $c\bar{c}$ quarks in the model the description of the data is very good. At high transverse momentum the statistical J/ψ production becomes less important in the model and is dominated by a "corona" part for $p_{\mathrm{T}} > 5$ GeV/c [206]. This corona part is modeled as independent pp collisions scaled by a fraction of N_{coll} using an interpolated pp spectrum. Hence possible effects which may be relevant at high p_{T} in Pb–Pb collisions such as color screening or parton energy loss are not taken into account. The disagreement of the data and the model at high p_{T} suggests that additional effects of this type may play a role there.
In order to compare the p_{T} differential J/ψ yields with the ones obtained in pp collisions the nuclear modification factor R_{AA} is computed. The p_{T} differential cross-section is taken from the measurement at $\sqrt{s} = 5$ TeV. The uncertainties which are correlated among all p_{T} bins (luminosity in pp collisions (2.1% [225]) and T_{AA}) are shown as a box around unity. The statistical and systematic uncertainties of the pp reference cross-section are propagated into the statistical and systematic uncertainties of the points. The x_{lw} correction of the points can not be carried out for the R_{AA} since the obtained values in Pb–Pb and pp might not coincide and hence the R_{AA} is quoted in p_{T} bins. The obtained values for the R_{AA} are shown in Fig. 6.5 for the

three centrality bins. For the 0–20% centrality class a hint of an enhancement above unity is observed in the lowest momentum bin. For increasing p_{T} the points show an increasing suppression. The nuclear modification factors in the centrality classes 20–40% and 40–90% show a less steep shape, indicating that the high p_{T} suppression is more relevant in central collisions. This stronger suppression at high p_{T} in central collisions compared to peripheral collisions is also observed for inclusive charged particles [226] and D mesons [227]. There it is interpreted as an effect of parton energy loss in the hot and dense medium created in central collisions. A new measurement by the ATLAS collaboration for $p_{\mathrm{T}} > 9$ GeV/c lends support to the energy loss hypothesis, although the data is also consistent with the color screening scenario [228].

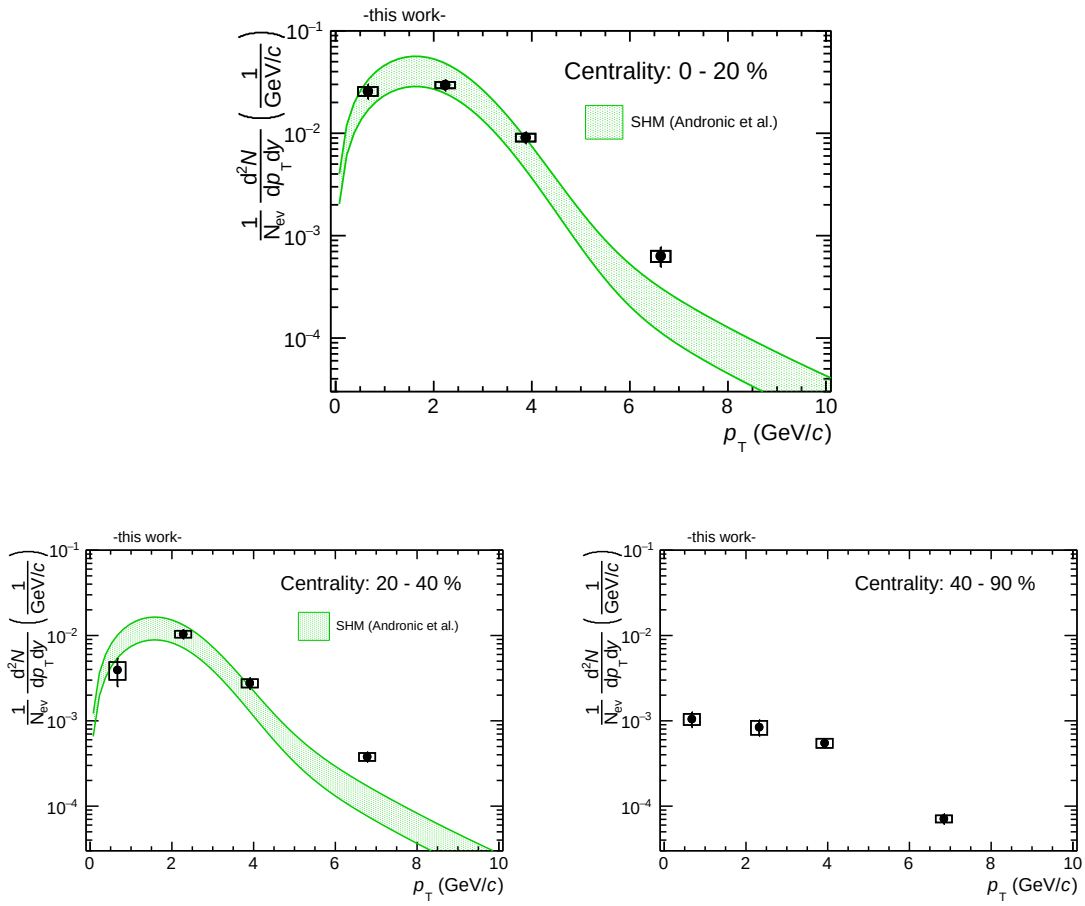

Figure 6.4: J/ψ transverse momentum spectra in three centrality classes together with statistical hadronization model [224] predictions.

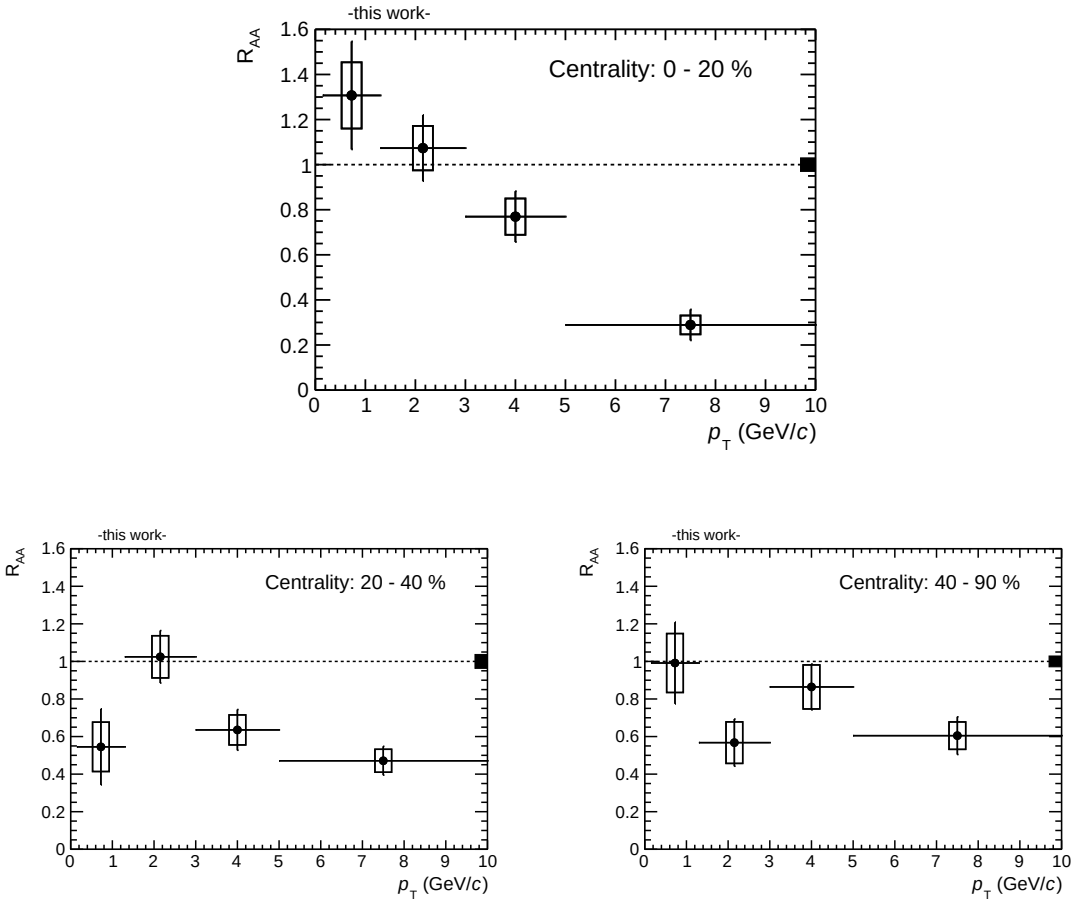

Figure 6.5: Transverse momentum dependent nuclear modification factor of J/ψ in three centrality classes. Statistical uncertainties are indicated with vertical error bars while systematic uncertainties are indicated with boxes around the points. The horizontal error bars reflect the bin width of the measurement. The box around unity reflects the correlated systematic uncertainty (luminosity in pp collisions and T_{AA}).

The nuclear modification factor is also compared to model predictions in Fig. 6.6. The statistical hadronization model [224] and the transport model [143, 144] exhibit similar shapes. At low p_{T} a higher J/ψ yield is expected due to the production of J/ψ by (re)combination of low p_{T} thermal charm quarks. This yield is predicted to be larger by the SHM since all charm quarks can contribute to this production mechanism in the model. In the SHM the R_{AA} is even expected to be above unity at low p_{T}, meaning that the yield in Pb–Pb collisions exceeds the yield of binary scaled pp collisions. In the transport model only partial charm thermalization is realized and a fraction of J/ψ can even exist in the medium. Hence a lower J/ψ yield is expected at low p_{T} in the model. In addition the choice of the total charm cross-section in pp collisions and its translation to Pb–Pb collisions via the relevant p–Pb effects plays a role for the model predictions. The relevant model input parameters are summarized in Tab. 6.1. In the case of the transport model the upper edge of the uncertainty

band corresponds to a scenario of no shadowing while the lower limit corresponds to a shadowing according to EPS09. This treatment might underestimate the relevant effects given the p–Pb measurements where a suppression at the level of at least EPS09 is observed [130, 131]. However, given the current precision of the data and the models no prediction is clearly favored. At high p_{T} the SHM undershoots the data as already discussed for the spectra results. The transport model seems to better describe the high p_{T} part where the J/ψ dissociation by partonic scatterings is relevant in the model.

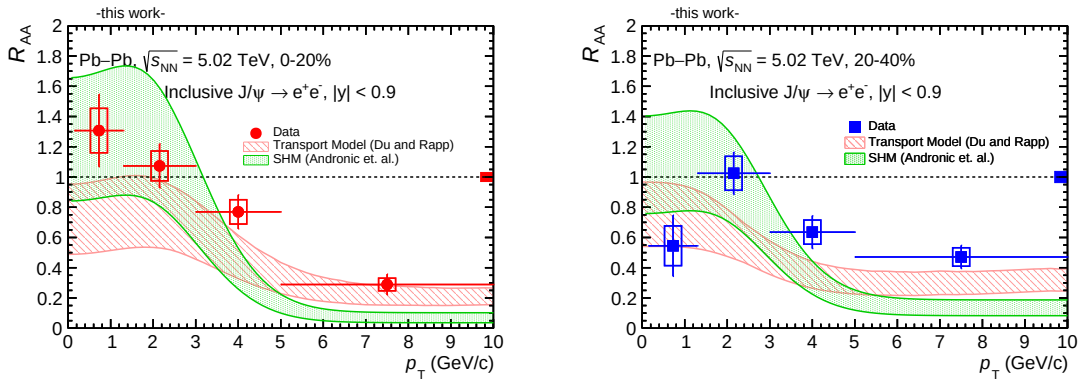

Figure 6.6: Transverse momentum dependent nuclear modification factor compared to predictions by the SHM and the transport model by Du and Rapp. Statistical uncertainties are indicated with vertical error bars while systematic uncertainties are indicated with boxes around the points. The horizontal error bars reflect the bin width of the measurement. The box around unity reflects the correlated systematic uncertainty (luminosity in pp collisions and T_{AA}).

In Fig. 6.7 the p_{T} dependent nuclear modification factor is compared to the forward rapidity measurement [229] for the most central collisions. The suppression at the highest transverse momenta is observed to be similar. However, at low transverse momentum the mid-rapidity data indicates a higher yield than the forward rapidity data. In the (re)combination picture this is expected since the charm cross-section increases towards mid-rapidity and hence more J/ψ can be produced.

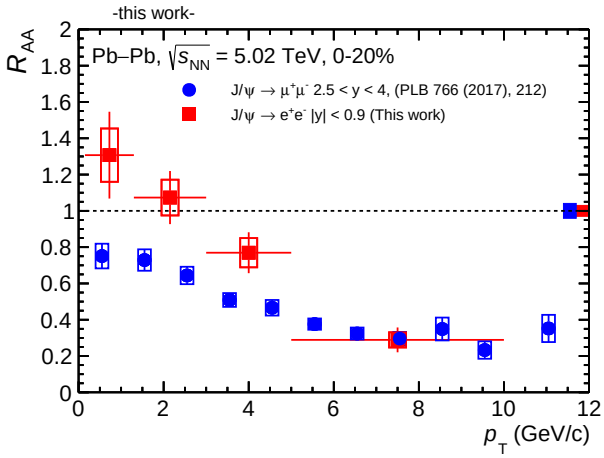

Figure 6.7: Transverse momentum dependent nuclear modification factor compared to the forward rapidity measurement. Statistical uncertainties are indicated with vertical error bars while systematic uncertainties are indicated with boxes around the points. The horizontal error bars reflect the bin width of the measurement. The box around unity reflects the correlated systematic uncertainty (luminosity in pp collisions and T_{AA}).

6.3 Mean transverse momentum and mean squared transverse momentum

6.3.1 Results from pp collisions

The mean transverse momentum and the mean transverse momentum squared have been obtained for $p_{\mathrm{T}} < 10$ GeV/c from pp collisions in Chapter 5. The results are shown in Fig. 6.8 compared to the values obtained by the interpolation procedure as explained in Sec. 4.9. The values of both procedures are consistent with each other while the uncertainties are slightly larger for data, mostly driven by the statistical uncertainty.

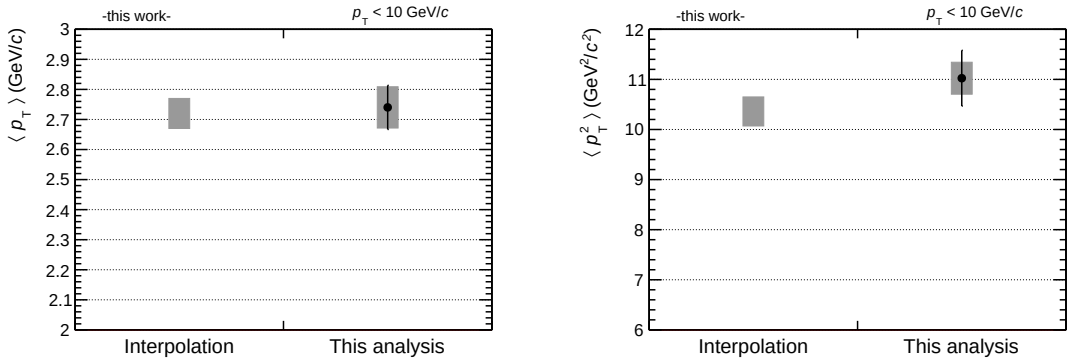

Figure 6.8: Results for $\langle p_{\mathrm{T}} \rangle$ and $\langle p_{\mathrm{T}}^2 \rangle$ in pp collisions compared to the values obtained by the interpolation.

Figure 6.9 shows the world's data for $\langle p_{\mathrm{T}} \rangle$ and $\langle p_{\mathrm{T}}^2 \rangle$ of J/ψ mesons measured at mid-rapidity.

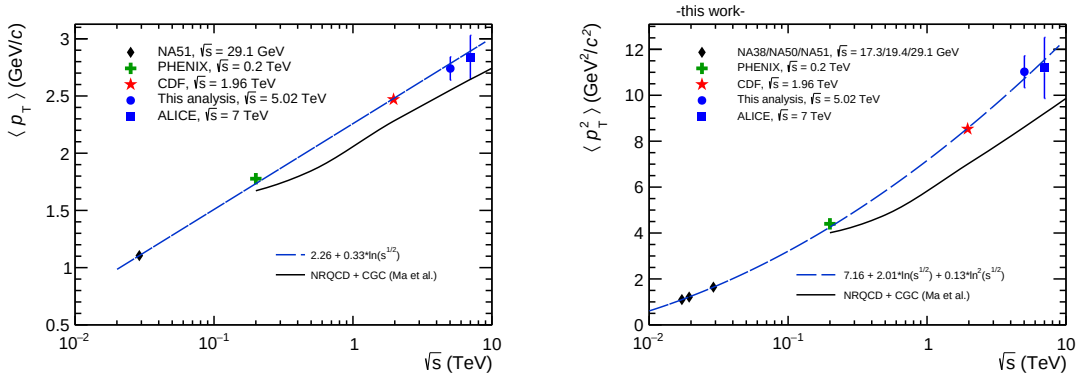

Figure 6.9: World data for J/ψ $\langle p_{\mathrm{T}} \rangle$ and $\langle p_{\mathrm{T}}^2 \rangle$ at mid-rapidity in pp collisions. Error bars represent the quadratic sum of statistical and systematic uncertainties.

The values from NA38, NA50 and NA51 are taken from [230]. The values for

PHENIX and ALICE at $\sqrt{s} = 7$ TeV are taken from fits to the spectra as detailed in Sec. 5.8. Due to the high granularity of the CDF spectrum measurement the values are calculated according to the discretized scheme described in Sec. 5.8. The PHENIX values are obtained for $p_{\mathrm{T}} < 9$ GeV/c while the values for CDF, ALICE and the ones from this analysis are obtained for $p_{\mathrm{T}} < 10$ GeV/c. A clear increasing trend of both moments is observed as function of the center of mass energy. Due to the high precision of the measurement the point obtained in this work can constrain the high-energy limit. Interestingly, the increase can be nicely described with a logarithmic function up to the highest collision energies. This logarithmic scaling is typically attributed to the increase of the available phase space.
Also shown is a prediction by the NRQCD + CGC model by Ma et al. [218]. In this model the CGC approach is used at low p_{T} and is coupled to an NRQCD approach at intermediate p_{T} up to $p_{\mathrm{T}} = 8$ GeV/c. However, in the model only prompt J/ψ production is considered. Non prompt J/ψ mesons are known to exhibit a slightly harder spectrum than prompt J/ψ mesons. However, they constitute only around 10% of the inclusive yield around the maximum of the spectrum (see Sec. 2.2). The different kinematic range and the non-existence of the non-prompt J/ψ component in the model hampers the comparability to data. However, the model follows a similar trend as the data.

6.3.2 Results from Pb-Pb collisions

The J/ψ $\langle p_{\mathrm{T}} \rangle$ and $\langle p_{\mathrm{T}}^2 \rangle$ are obtained as described in Chapter 5 in the transverse momentum range $0.15 < p_{\mathrm{T}} < 10$ GeV/c. The pp reference values are obtained in the range $p_{\mathrm{T}} < 10$ GeV/c since no exclusion of a low p_{T} photoproduction component is necessary. The effect of this minimum transverse momentum requirement was studied in the interpolation framework in pp collisions. For both moments the effect is smaller than 0.5% and hence neglected.
The results for the J/ψ $\langle p_{\mathrm{T}} \rangle$, $\langle p_{\mathrm{T}}^2 \rangle$ and r_{AA} are shown in Fig. 6.10. A centrality dependence of both moments is observed: In peripheral collisions the $\langle p_{\mathrm{T}} \rangle$ and $\langle p_{\mathrm{T}}^2 \rangle$ are consistent with the pp value within the uncertainties. Towards central collisions the moments decrease where the most central points are separated from the pp data points by 4.59 σ ($\langle p_{\mathrm{T}} \rangle$) and 5.80 σ ($\langle p_{\mathrm{T}}^2 \rangle$). In case the interpolated pp reference is used for this calculation the separation of the most central Pb–Pb data points and the pp data points are 5.48 σ ($\langle p_{\mathrm{T}} \rangle$) and 6.64 σ ($\langle p_{\mathrm{T}}^2 \rangle$) due to the smaller uncertainty. Hence a softening of the J/ψ spectra is observed in Pb–Pb collisions which is significant for the most central collisions (0–10% centrality). The relative suppression of the most central Pb–Pb data points compared to the pp data points is around 25% in the case of $\langle p_{\mathrm{T}} \rangle$ and around 45% in the case of $\langle p_{\mathrm{T}}^2 \rangle$.
The results are compared to model predictions in Fig. 6.11. The statistical hadronization model can describe the most central point of the $\langle p_{\mathrm{T}} \rangle$, but slightly underestimates the centrality dependence. The second moment is slightly underestimated by the SHM which can be explained by the under-prediction of the spectra at high p_{T} (see Fig. 6.4).

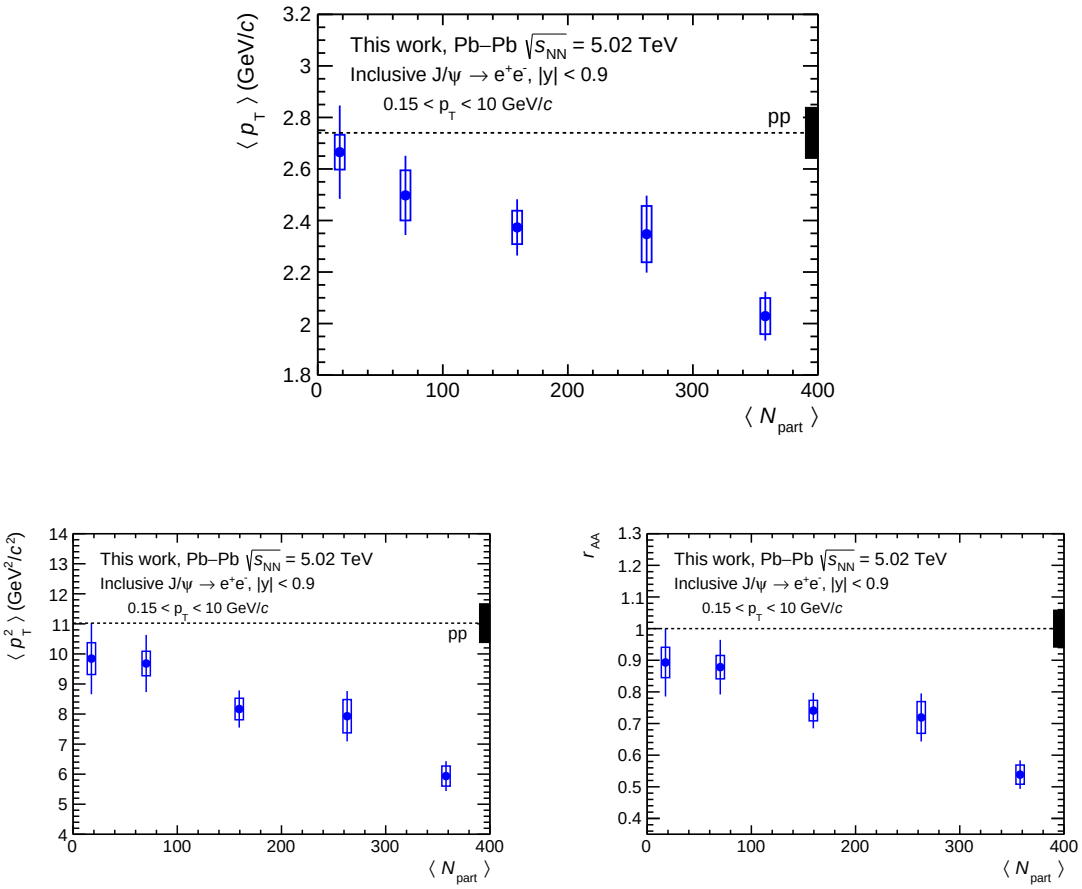

Figure 6.10: Results for $\langle p_{\mathrm{T}} \rangle$, $\langle p_{\mathrm{T}}^2 \rangle$ and $r_{\mathrm{AA}} = \langle p_{\mathrm{T}}^2 \rangle^{\mathrm{Pb–Pb}} / \langle p_{\mathrm{T}}^2 \rangle^{\mathrm{pp}}$ as a function of centrality in Pb–Pb collisions. Also shown is the pp data point as a reference.

In general the second moment is more sensitive to discrepancies at high p_{T} than the mean. The transport model by Rapp et al. can describe the initial decrease in peripheral collisions for both moments. However, the most central points of the $\langle p_{\mathrm{T}} \rangle$ and r_{AA} indicate a slight overestimation by the model. The lower uncertainty band in this model represents the scenario of no shadowing while the upper band represents the scenario according to EPS09. Again, this treatment is somewhat debatable given the inclusive p–Pb measurements. In the model of Rapp et al. the softening of both moments is due to the J/ψ production by (re)combination of soft charm quarks. The spectra of primordial J/ψ which are not dissolved in the medium show a hardening in the model due to the Cronin effect [231]. However, the net effect on all J/ψ is still a softening due to the importance of the production by (re)combination which increases with centrality. The transport model by Zhou et al. under-predicts the data in a wide range while being consistent with the data in peripheral collisions. The tremendous softening is somewhat surprising for a transport model in which not all J/ψ are formed by (re)combination. The non-existence of uncertainty bands raises the question whether the relevant effects observed in p–Pb collisions are taken

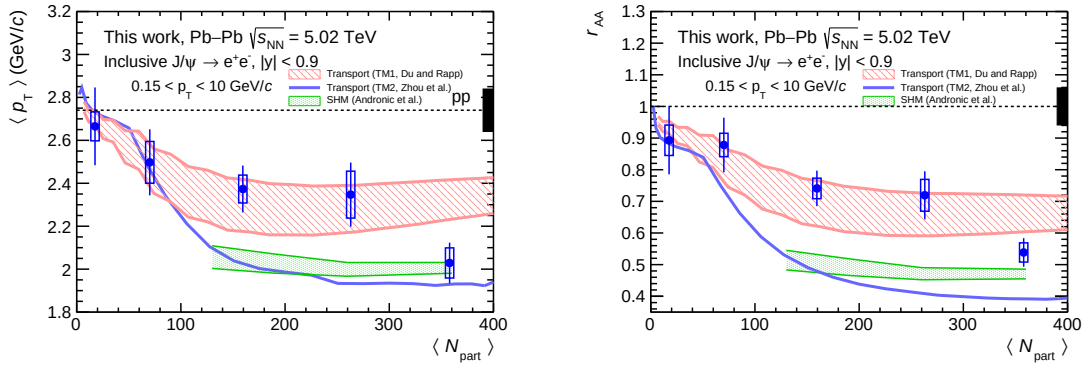

Figure 6.11: Comparison of the $\langle p_{\mathrm{T}} \rangle$ and $r_{\mathrm{AA}} = \langle p_{\mathrm{T}}^2 \rangle^{\mathrm{Pb–Pb}} / \langle p_{\mathrm{T}}^2 \rangle^{\mathrm{pp}}$ results to model predictions by the SHM [224], the transport model by Rapp et al. [143, 144] and the transport model by Zhou et al. [145, 146].

into account. Clearly, the imperfection of the knowledge of the total charm cross section is not reflected in the prediction.
Interestingly, in a prediction for the $\langle p_{\mathrm{T}}^2 \rangle$ of J/ψ by Kang et al. [122] only initial-state parton scattering is taken into account, neglecting final-state QGP medium effects. This assumption leads to an increase of the $\langle p_{\mathrm{T}}^2 \rangle$ with centrality, larger than the value in pp collisions. Hence final state QGP effects such as J/ψ production by (re)combination of deconfined charm quarks are necessary to describe the data.
In Fig. 6.12 a comparison of the $\langle p_{\mathrm{T}} \rangle$ and $\langle p_{\mathrm{T}}^2 \rangle$ in pp and Pb–Pb collisions as obtained in this work to results at lower collision energies is shown. The results of the NA50 experiment are taken from [232]. The values for pp collisions at PHENIX are obtained from a fit to the measured spectrum as shown in Sec. 5.8. The values for Au–Au and Cu–Cu collisions at PHENIX are obtained from a discretized calculation based on the measured spectra due to the specific spectral shape which complicates the fitting procedure. At the lowest collision energy at NA50 at the SPS an increase of $\langle p_{\mathrm{T}} \rangle$ and r_{AA} with increasing centrality is observed. This broadening can be interpreted to be due to initial state scattering effects. The PHENIX data indicates a flat behavior as a function of centrality which is interesting since the yield is increasingly suppressed as a function of centrality (see Fig. 2.5). A possible interpretation is that initial state broadening and final state softening cancel each other. However, the most central PHENIX point may indicate a beginning softening, although the uncertainty does not allow one to draw a strong conclusion. The results obtained in this work clearly show a different trend than the lower energy results. As explained earlier the decrease of $\langle p_{\mathrm{T}} \rangle$ and $\langle p_{\mathrm{T}}^2 \rangle$ with centrality can be explained with QGP related effects. Most importantly the J/ψ production by (re)combination leads to a softening of the moments of J/ψ spectra. Due to the significantly lower charm cross section at RHIC energies the (re)combination should not play a big role there. The $\langle p_{\mathrm{T}} \rangle$ and $\langle p_{\mathrm{T}}^2 \rangle$ results at NA50 are even consistent with no QGP related effects. In summary, this comparison shows that heavy-ion collisions at different center of mass energies

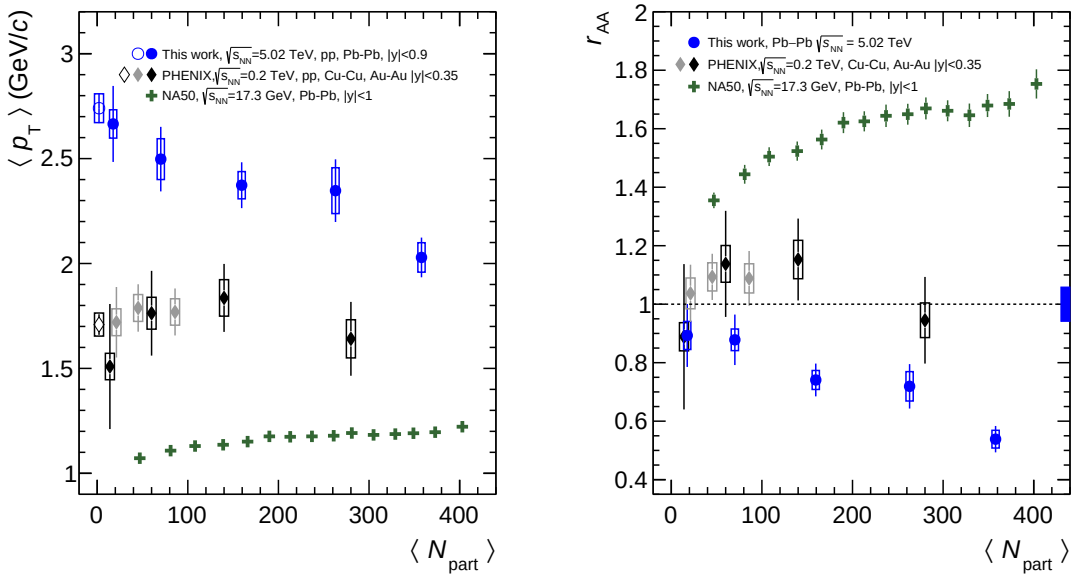

Figure 6.12: Comparison of the $\langle p_{\mathrm{T}} \rangle$ and $r_{\mathrm{AA}} = \langle p_{\mathrm{T}}^2 \rangle^{\mathrm{Pb-Pb}} / \langle p_{\mathrm{T}}^2 \rangle^{\mathrm{pp}}$ results to results obtained at lower collision energies at NA50 [232] and PHENIX [212, 233, 234].

exhibit significantly different properties.
Another interesting comparison is the comparison of the J/ψ $\langle p_{\mathrm{T}} \rangle$ and $\langle p_{\mathrm{T}}^2 \rangle$ to the results of light flavor hadrons. The comparison to inclusive charged particles (which are dominated by pions) is shown in Fig. 6.13. The values are obtained with the discretized calculation explained in Sec. 5.8 using the spectra published in [226]. The inclusive charged particles show an increase in $\langle p_{\mathrm{T}} \rangle$ and $\langle p_{\mathrm{T}}^2 \rangle$ with increasing centrality which becomes more visible when the values are normalized to the pp values. As explained in Sec. 1.3.2 the increase of the $\langle p_{\mathrm{T}} \rangle$ with centrality is understood by collective flow. The flow field adds radial momentum to the particles momentum distribution and hence leads to an increase of $\langle p_{\mathrm{T}} \rangle$. It is plausible that the observed increase of $\langle p_{\mathrm{T}}^2 \rangle$ with centrality is also due to the flattening of the spectra induced by radial flow. Interestingly, while the results of the inclusive charged particles show an increase with centrality the J/ψ results show a decrease. In order to better understand this comparison in the context of flow the $\langle p_{\mathrm{T}} \rangle$ of J/ψ mesons is compared to lighter identified hadrons in Fig. 6.14. For the light flavor hadrons and nuclei an increase in $\langle p_{\mathrm{T}} \rangle$ with centrality is observed which gets larger for particles with larger mass. This is the pattern which is expected by a hydrodynamic behavior. The J/ψ mesons, however, do not obey this pattern although the $\langle p_{\mathrm{T}} \rangle$ is of similar magnitude as for the neighboring nuclei. On the other hand it is known that J/ψ mesons exhibit elliptic flow at the LHC [208]. The absence of radial flow in the presence of elliptic flow would be implausible. Hence additional effects are necessary to explain the pattern observed for J/ψ mesons. The model comparisons of the J/ψ spectra, nuclear modification factor and $\langle p_{\mathrm{T}} \rangle$ and $\langle p_{\mathrm{T}}^2 \rangle$ imply solid evidence for the importance of J/ψ

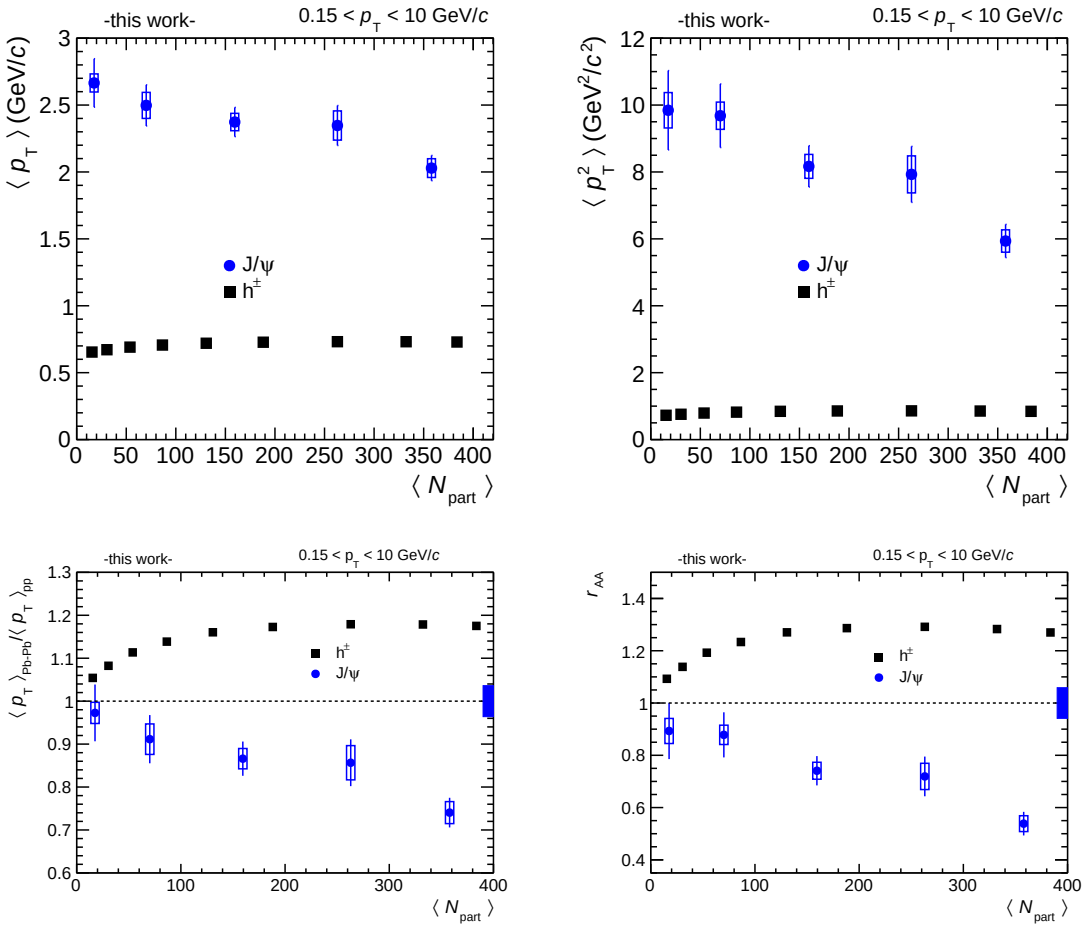

Figure 6.13: Comparison of the $\langle p_{\mathrm{T}} \rangle$, $\langle p_{\mathrm{T}}^2 \rangle$ and $r_{\mathrm{AA}} = \langle p_{\mathrm{T}}^2 \rangle^{\mathrm{Pb–Pb}} / \langle p_{\mathrm{T}}^2 \rangle^{\mathrm{pp}}$ results to inclusive charged particles. The charged particle results are calculated from the spectra published in [226].

production by (re)combination of thermalized charm quarks. Those charm quarks move with very low momenta and hence result in low momenta of the J/ψ mesons. One important difference between the J/ψ and the light flavor hadrons is that light flavor hadrons are produced thermally (see e.g. the statistical model predictions in Sec. 1.3.1). The charm quarks, however, are produced in initial hard scatterings and are not equilibrated with the medium initially. They have to subsequently interact with and thermalize in the medium in order to produce (re)generated J/ψ mesons at the phase boundary. Unfortunately the J/ψ is the only particle containing charm in Fig. 6.14. The measurement of D meson spectra as function of centrality and the determination of their $\langle p_{\mathrm{T}} \rangle$ would provide valuable insights into the comparison shown in Fig. 6.14. It could be clarified whether the pattern observed for J/ψ mesons can be attributed to (re)combination or whether it is an imprint of heavy quark thermalization in the medium. However, the measurement of D mesons down to $p_{\mathrm{T}} = 0$ in Pb–Pb collisions is currently not feasible and their reconstruction suffers

from large uncertainties at low p_{T} [227]. Precise measurements of D meson spectra in Pb–Pb collisions down to vanishing transverse momentum are planned after the ALICE upgrade [235].

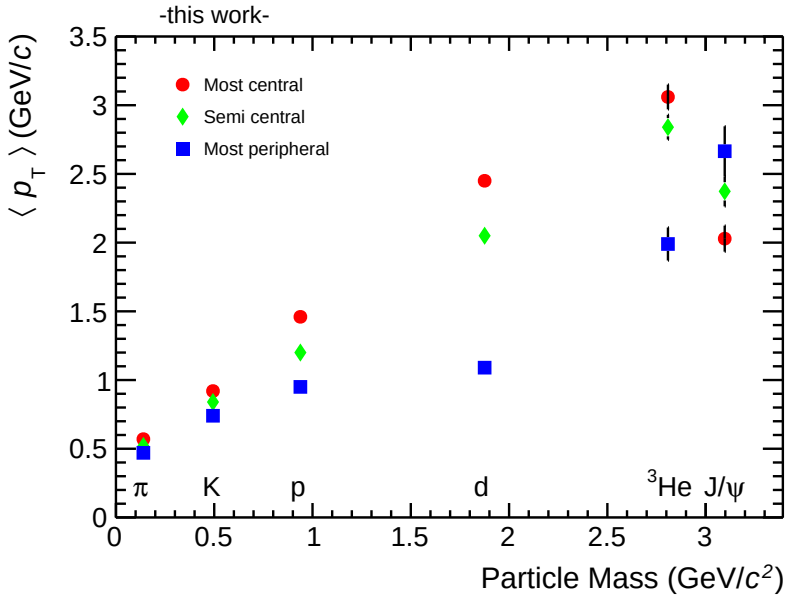

Figure 6.14: Comparison of the J/ψ $\langle p_{\mathrm{T}} \rangle$ results in 0–10%, 20–40% and 60–90% central collisions to light flavor particles. Only statistical uncertainties are shown for better visibility. The pion, kaon and proton data are shown in the centrality intervals 0–5%, 40–50%, 80–90% and are taken from [236]. The results of deuterons are shown in the centrality bins 0–5%, 30–40% and 80–90%, the ^{3}He results are shown in the bins 0–10%, 10–40%, 40–90%. The results of deuterons and ^{3}He and are taken from [237].

In Fig. 6.15 a comparison to the forward rapidity results is shown. The forward rapidity results are obtained for $p_{\mathrm{T}} < 8$ GeV/c, thus slightly smaller values of $\langle p_{\mathrm{T}} \rangle$ and $\langle p_{\mathrm{T}}^2 \rangle$ than at mid rapidity are expected. However, even if both moments are calculated for $p_{\mathrm{T}} < 12$ GeV/c in pp collisions the moments are still smaller than at mid-rapidity[1]. This implies that the J/ψ spectra in pp collisions are harder at mid-rapidity compared to forward rapidity. As discussed in [238] this can be attributed to the increase in longitudinal momentum at forward rapidity implying less available transverse momentum compared to mid rapidity.
The Pb–Pb data at forward and mid rapidity show similar decreasing trends with centrality. However, the relative suppression in most central collisions compared to pp collisions is slightly higher at mid rapidity. In the picture of J/ψ production by (re)combination this is a consequence of the higher charm cross section at mid rapidity and thus greater importance of the (re)generation at mid rapidity.

[1]For $p_{\mathrm{T}} < 12$ GeV/c the forward rapidity results are: $\langle p_{\mathrm{T}} \rangle = 2.368 \pm 0.020$ (stat.) $\pm$ 0.023 (syst.) GeV/c and $\langle p_{\mathrm{T}}^2 \rangle = 8.084 \pm 0.136$ (stat.) $\pm$ 0.121 (syst.) GeV^2/c^2 [114].

Finally, a comparison to the ALICE results obtained at $\sqrt{s_{\mathrm{NN}}} = 2.76$ TeV [152] is shown in Fig. 6.16. In order to be able to compare both center of mass energies $\langle p_{\mathrm{T}} \rangle$ and $\langle p_{\mathrm{T}}^2 \rangle$ are both normalized to their values in pp collisions. In the lower collision energy the moments do not show a significant centrality dependence. However, no strong conclusions can be drawn from the observed centrality dependence due to the limited precision of the measurement in peripheral collisions. In most central collisions the $\langle p_{\mathrm{T}} \rangle$ is slightly smaller at $\sqrt{s_{\mathrm{NN}}} = 5.02$ TeV, consistent with the expectation of a greater importance of low p_{T} J/ψ production by (re)combination at the higher collision energy. For the $\langle p_{\mathrm{T}}^2 \rangle$ a hint of higher values at semi central and peripheral collisions is found for the higher collision energy points while the most central data points are consistent. At forward rapidity also slightly higher values for $\langle p_{\mathrm{T}}^2 \rangle$ have been found at the higher collision energy. Possibly, this can be traced back to a higher flow velocity at the higher collision energy and hence a broadening of the J/ψ spectra.

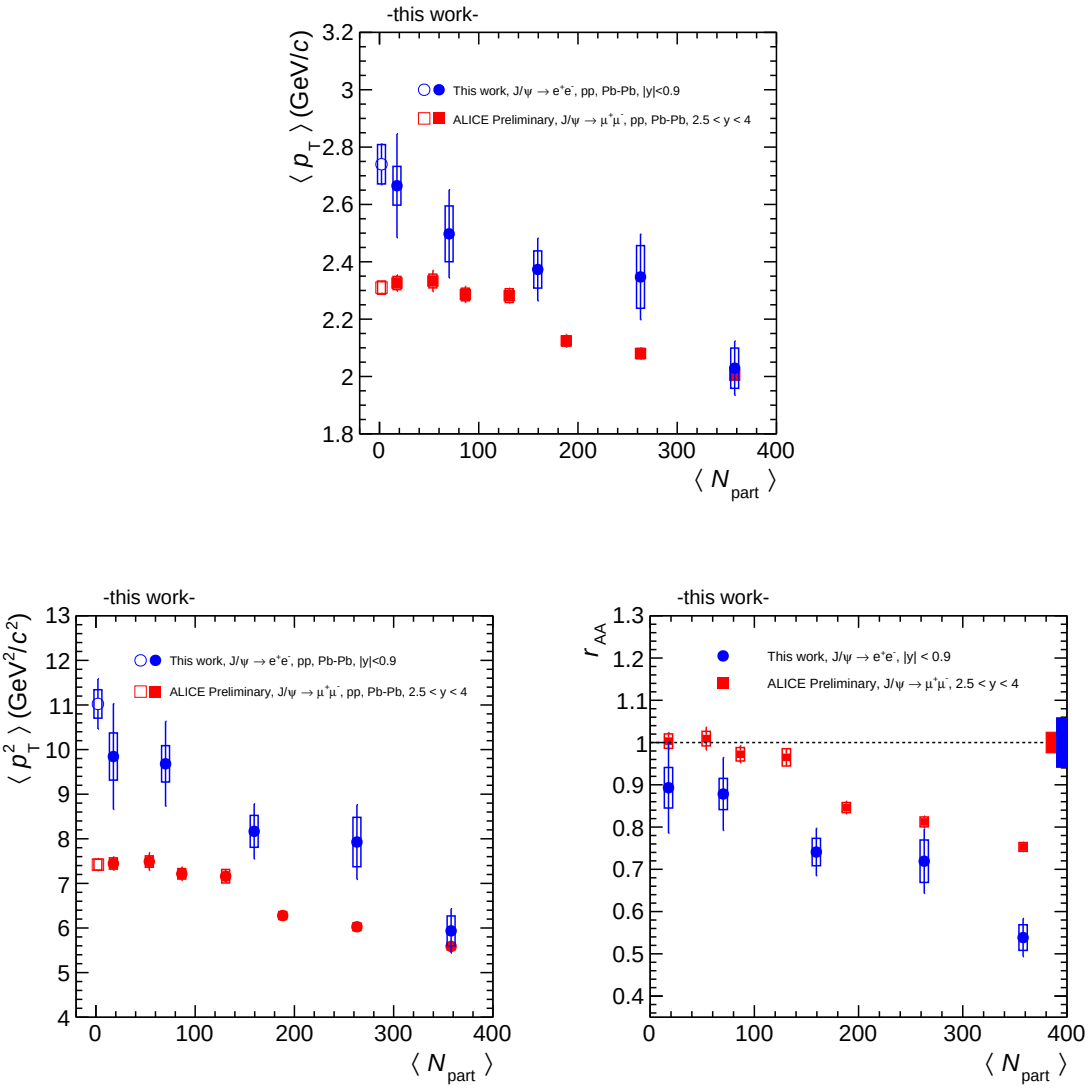

Figure 6.15: Comparison of $\langle p_{\mathrm{T}} \rangle$, $\langle p_{\mathrm{T}}^2 \rangle$ and $r_{\mathrm{AA}} = \langle p_{\mathrm{T}}^2 \rangle^{\mathrm{Pb–Pb}} / \langle p_{\mathrm{T}}^2 \rangle^{\mathrm{pp}}$ results to the forward rapidity results. The forward rapidity pp results are taken from [114], while the forward rapidity Pb–Pb results are taken from [239].

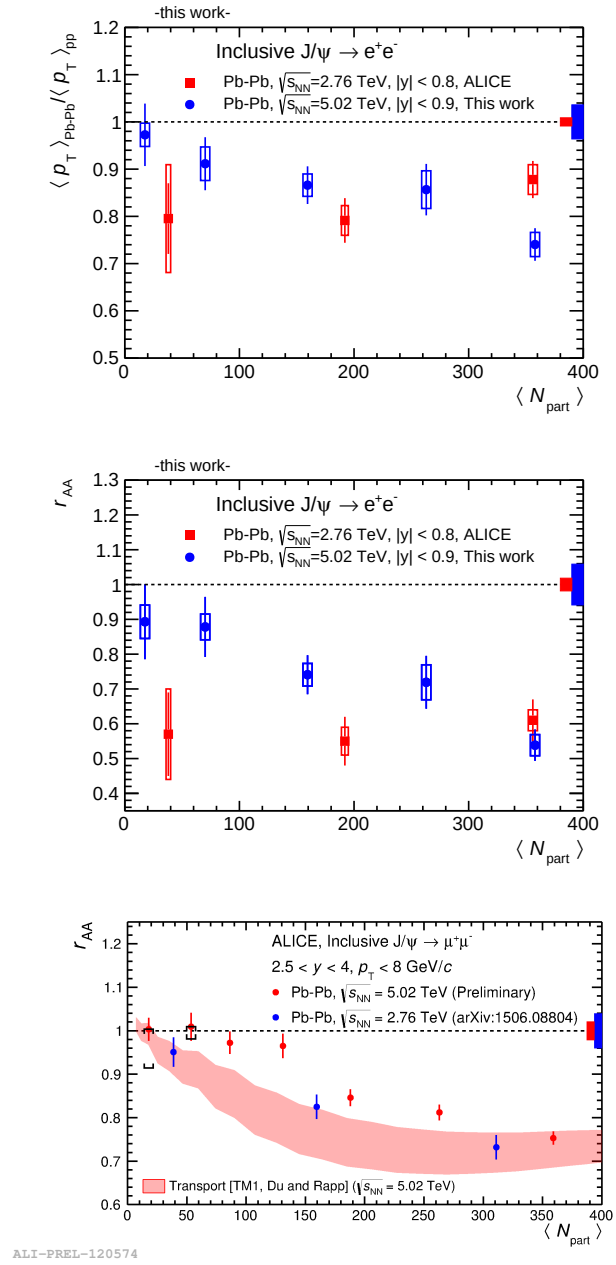

Figure 6.16: Comparison of $\langle p_{\mathrm{T}} \rangle$ and $r_{\mathrm{AA}} = \langle p_{\mathrm{T}}^2 \rangle^{\mathrm{Pb–Pb}} / \langle p_{\mathrm{T}}^2 \rangle^{\mathrm{pp}}$ results to the ALICE results at $\sqrt{s_{\mathrm{NN}}} = 2.76$ TeV which are taken from [152]. For the r_{AA} this comparison is also shown for the forward rapidity data where the figure is taken from [240].

7 Summary and outlook

The measurement of J/ψ production in different collision systems offers an excellent testing ground for QCD in different environments. In particular, in heavy-ion collisions J/ψ production is expected to be sensitive to medium properties such as deconfinement.

In this thesis the measurement of J/ψ production at mid-rapidity in Pb–Pb collisions at $\sqrt{s_{\mathrm{NN}}} = 5.02$ TeV has been presented. The J/ψ mesons were reconstructed in the e^+e^- decay channel, making use of the particle identification via $\mathrm{d}E/\mathrm{d}x$ in the TPC. Fully corrected J/ψ spectra have been obtained in three centrality classes. In the 0–20% most central collisions an increasing suppression with p_{T} is observed while at low momentum the R_{AA} is consistent with unity or an enhancement above 1. The comparison to model calculations indicate that at low transverse momentum the J/ψ production by (re)combination of deconfined and thermalized charm quarks is important. At high transverse momentum on the other hand the strong suppression is indicative of a J/ψ dissociation and/or parton energy loss of the charm quarks due to interactions with the surrounding medium. The measurement of the mean transverse momentum and mean transverse momentum square of J/ψ mesons has shown an increasing suppression with increasing centrality. It can be inferred that J/ψ spectra in peripheral Pb–Pb collisions are very similar to the spectrum observed in pp collisions. However, with increasing collision centrality the spectra are softened. This is mainly due to the increase in soft J/ψ production by (re)combination as indicated by model comparisons. Other comparisons shown in Chapter 6 support the importance of the J/ψ production by (re)combination at low transverse momentum. In summary, the analyses presented in this thesis show strong indications that in Pb–Pb collisions at an unprecedented collision energy of $\sqrt{s_{\mathrm{NN}}} = 5.02$ TeV a state of deconfined quarks and gluons is formed. Charm quarks which are produced in early hard scatterings subsequently thermalize in the medium during its evolution. When this state of matter freezes out J/ψ mesons are produced by (re)combination of charm quarks at the phase boundary.

Future measurements should address the open questions of the production mechanisms of charmonia in different collision systems.
In Pb–Pb collisions strong evidence for J/ψ production from deconfined and thermalized charm quarks by (re)combination is observed. It will be important to verify this production mechanism by more precise measurements in the future. The first opportunity will be the Pb–Pb data taking in the end of 2018 where an increase in statistics of at least one order of magnitude is anticipated in the 0–10% most

central collisions. This will allow one to measure precisely the J/ψ spectrum in the most central collisions and to confront it with model predictions. In addition it will be important that the model uncertainties will be reduced. This will be made possible by precise measurements of the total charm cross-section in pp collisions and the relevant p–Pb effects. However, ultimately a determination of the total charm cross-section in Pb–Pb collisions might be possible in LHC Run 3 after 2021. Then, a differentiation between the different models should be possible and answer the questions whether bound states can exist in the medium and what is the degree of charm thermalization close to the critical temperature T_{c}. In addition, the measurements of the higher states ψ(2S) and χ_{c} are expected to yield higher separation power between the statistical hadronization model and transport models [235]. The ψ(2S) state is expected to be measurable in LHC Run 3 at mid-rapidity while the measurement of the χ_{c} needs more detailed studies.
In Sec. 4.4 the combined TPC-TRD electron identification approach was discussed. For the higher mass state ψ(2S) and for the measurement $\Upsilon(n\mathrm{S})$ states this approach might be superior to the TPC standalone approach. Due to the higher mass of these states their decay electrons exhibit higher momenta than electrons from J/ψ decays in a decay at rest. In addition, the ψ(2S) and Υ(1S) spectra are harder than J/ψ spectra at forward rapidity in pp collisions [106, 114]. Hence for the reconstruction of those states it will be very important to reconstruct high p_{T} electrons efficiently. With the help of the TRD it might be possible to enhance the sample of electrons from the decays of those states compared to the TPC standalone approach. However, this should be studied in detail in simulations.
In pp collisions the production of J/ψ mesons is not fully understood yet given the measurements of the polarization [117, 118] and the measurement of J/ψ production in jets [119]. Further studies are clearly necessary, and ALICE can contribute with measurements at mid-rapidity in the future. The polarization of inclusive or prompt J/ψ mesons has not yet been measured at the LHC at mid-rapidity down to low transverse momentum. This can be done with a larger pp data sample in the future. Also, J/ψ-hadron and J/ψ-jet correlation measurements by ALICE at mid-rapidity can complement the existing measurement by LHCb at forward-rapidity. These measurements should improve the understanding of the J/ψ production mechanism in pp collisions and potentially clarify the role of J/ψ production in jet fragmentation.
Recently, collective effects and effects usually attributed to QGP formation have been observed in high multiplicity pp and p–Pb collisions (see [174] and references therein). These results raise the question about the potential creation of a QGP also in smaller collision systems or at least about the similarity of those collision systems. In the J/ψ sector it would be interesting to expand current multiplicity dependent studies by measurements of $\langle p_{\mathrm{T}} \rangle$ and $\langle p_{\mathrm{T}}^2 \rangle$ in pp and p–Pb collisions. In [241] an increase of the $\langle p_{\mathrm{T}}^2 \rangle$ as a function of the collision multiplicity has been suggested based on a similarity of pp and p–Pb collisions. The basis for this measurement in pp collisions at $\sqrt{s} = 5.02$ TeV has been created by the application of the template fit extraction method of the $\langle p_{\mathrm{T}} \rangle$ and $\langle p_{\mathrm{T}}^2 \rangle$ to pp collision data in Chapter 5. By slicing the data in multiplicity bins the $\langle p_{\mathrm{T}} \rangle$ and $\langle p_{\mathrm{T}}^2 \rangle$ can be extracted as a function

of multiplicity.

Very interesting years lie ahead in the field of heavy-ion physics. The ALICE upgrade and the following data taking at unprecedented readout rates of 50 kHz will allow one to study low p_{T} physics in Pb–Pb collisions in the domain of vanishing baryochemical potential with high precision. The long awaited data taking of the CBM experiment at FAIR is also anticipated to start during the next decade. It is expected to deliver invaluable information about the state of matter at high baryochemical potential. The synergy of those and other experiments will ensure a detailed characterization of the QCD phase diagram and perhaps ultimately shed significant light on hadronization, one of the great riddles of contemporary physics.

Appendix

A Result tables

p_{T} (GeV/c)	$1/\mathrm{N}_{\mathrm{evt}}\mathrm{d}N_{\mathrm{J}/\psi}/\mathrm{d}p_{\mathrm{T}}\mathrm{d}y$ $(\mathrm{GeV}/c)^{-1}$	R_{AA}
	Centrality: 0 – 20%	
0.15 – 1.3	$(2.57 \pm 0.42 \pm 0.26) \cdot 10^{-2}$	$1.31 \pm 0.24 \pm 0.15$
1.3 – 3	$(2.96 \pm 0.36 \pm 0.21) \cdot 10^{-2}$	$1.07 \pm 0.15 \pm 0.10$
3 – 5	$(0.91 \pm 0.11 \pm 0.08) \cdot 10^{-2}$	$0.77 \pm 0.11 \pm 0.08$
5 – 10	$(0.63 \pm 0.14 \pm 0.08) \cdot 10^{-3}$	$0.29 \pm 0.07 \pm 0.04$
	Centrality: 20 – 40%	
0.15 – 1.3	$(0.40 \pm 0.14 \pm 0.09) \cdot 10^{-2}$	$0.55 \pm 0.20 \pm 0.13$
1.3 – 3	$(1.04 \pm 0.12 \pm 0.09) \cdot 10^{-2}$	$1.02 \pm 0.14 \pm 0.11$
3 – 5	$(0.28 \pm 0.04 \pm 0.03) \cdot 10^{-2}$	$0.64 \pm 0.11 \pm 0.08$
5 – 10	$(0.38 \pm 0.05 \pm 0.04) \cdot 10^{-3}$	$0.47 \pm 0.08 \pm 0.06$
	Centrality: 40 – 90%	
0.15 – 1.3	$(1.05 \pm 0.21 \pm 0.16) \cdot 10^{-3}$	$0.99 \pm 0.22 \pm 0.16$
1.3 – 3	$(0.84 \pm 0.17 \pm 0.15) \cdot 10^{-3}$	$0.57 \pm 0.13 \pm 0.11$
3 – 5	$(0.55 \pm 0.07 \pm 0.07) \cdot 10^{-3}$	$0.86 \pm 0.12 \pm 0.12$
5 – 10	$(0.71 \pm 0.10 \pm 0.07) \cdot 10^{-4}$	$0.60 \pm 0.10 \pm 0.07$

Table A.1: Results for the J/ψ yield in Pb–Pb collisions in p_{T} bins ($1/\mathrm{N}_{\mathrm{evt}}\mathrm{d}N_{\mathrm{J}/\psi}/\mathrm{d}p_{\mathrm{T}}\mathrm{d}y$) and for the R_{AA}, both differential in centrality. The first uncertainty is statistical while the second one is systematic.

Centrality	$\langle p_{\mathrm{T}} \rangle$ (GeV/c)	$\langle p_{\mathrm{T}}^2 \rangle$ (GeV^2/c^2)
0 – 10%	2.03 ± 0.09 ± 0.07	5.94 ± 0.50 ± 0.33
10 – 20%	2.35 ± 0.15 ± 0.11	7.93 ± 0.84 ± 0.55
20 – 40%	2.37 ± 0.11 ± 0.07	8.17 ± 0.62 ± 0.36
40 – 60%	2.50 ± 0.15 ± 0.10	9.68 ± 0.95 ± 0.41
60 – 90%	2.67 ± 0.18 ± 0.07	9.84 ± 1.19 ± 0.53
pp	2.74 ± 0.07 ± 0.07	11.02 ± 0.56 ± 0.32

Table A.2: Results for $\langle p_{\mathrm{T}} \rangle$ and $\langle p_{\mathrm{T}}^2 \rangle$ in Pb–Pb and pp collisions at 5.02 TeV using the template fit method. In Pb–Pb collisions the results are given for $0.15 < p_{\mathrm{T}} < 10$ GeV/c while in pp collisions the results are given for $p_{\mathrm{T}} < 10$ GeV/c. The first uncertainty is statistical while the second one is systematic.

Centrality	$\langle p_{\mathrm{T}} \rangle$ (GeV/c)	$\langle p_{\mathrm{T}}^2 \rangle$ (GeV^2/c^2)
0 – 20%	2.13 ± 0.08 ± 0.05	6.14 ± 0.44 ± 0.27
20 – 40%	2.43 ± 0.10 ± 0.08	8.17 ± 0.62 ± 0.48
40 – 90%	2.59 ± 0.15 ± 0.12	9.42 ± 0.84 ± 0.62
pp	2.66 ± 0.06 ± 0.03	10.20 ± 0.46 ± 0.24

Table A.3: Results for $\langle p_{\mathrm{T}} \rangle$ and $\langle p_{\mathrm{T}}^2 \rangle$ in Pb–Pb and pp collisions at 5.02 TeV using fits to the measured spectra. In Pb–Pb collisions the results are given for $0.15 < p_{\mathrm{T}} < 10$ GeV/c while in pp collisions the results are given for $p_{\mathrm{T}} < 10$ GeV/c. The first uncertainty is statistical while the second one is systematic.

Experiment	$\sqrt{s}$ (TeV)	p_{T} range	$\langle p_{\mathrm{T}} \rangle$ (GeV/c)	$\langle p_{\mathrm{T}}^2 \rangle$ (GeV^2/c^2)
PHENIX	0.2	0–9 GeV/c	1.78 ± 0.02 ± 0.02	4.40 ± 0.13 ± 0.10
CDF	1.96	0–10 GeV/c	2.47 ± 0.01 ± 0.02	8.53 ± 0.03 ± 0.08
ALICE	7.0	0–10 GeV/c	2.84 ± 0.15 ± 0.12	11.19 ± 1.09 ± 0.77

Table A.4: Results for $\langle p_{\mathrm{T}} \rangle$ and $\langle p_{\mathrm{T}}^2 \rangle$ in pp collisions at different energies as extracted from the published spectra. The first uncertainty is statistical while the second one is systematic.

B Selection of electrons from photon conversions

For the selection of electrons from photon conversion processes different selection criteria are applied. The selection criteria which act on the properties of the e^+e^- pair are listed in Tab. B.1.

Variable	minimum	maximum
$\mathrm{Cos}(\theta_{\mathrm{pointing}})$	cos(0.02)	1.0
χ^2/n.d.f.	0.0	10.0
leg distance	0.0	0.25
$\mathrm{R}_{\mathrm{conversion}}$	3.0	90.0
ψ_{pair}	0.0	0.05
$m_{e^+e^-}$	0.0	0.05
q_{T}	0.0	0.05
ϕ_{v}	2.7	3.2

Table B.1: Pair selection criteria for e^+e^- pairs from photon conversion processes.

In addition to the pair selection criteria also constraints are placed on the properties of the individual tracks in order to assure similar properties as for primary electrons:

- $|n_{\sigma,e}^{\mathrm{TOF}}| < 3$ (if available)
- $p > 1.5$ GeV/c
- reject kinks
- $|\mathrm{DCA}_{xy}| < 1$ cm
- $|\mathrm{DCA}_z| < 3$ cm
- $\chi^2/n_{\mathrm{cls}}^{\mathrm{TPC}} < 4$
- $|\eta| < 0.9$
- $n_{cls}^{\mathrm{TPC}} > 70$

C TPC PID studies in pp collisions

Analogous to the TPC PID studies in Pb–Pb collisions the TPC PID is studied in pp collisions using electrons from photon conversions. However, the selected electron sample is very pure as can be seen in Fig. C.1.

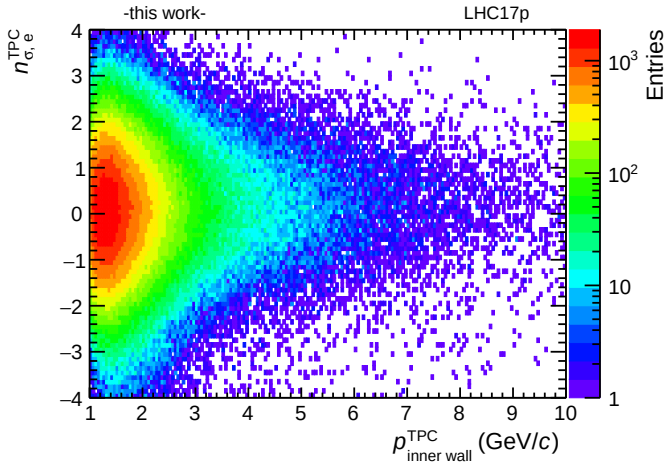

Figure C.1: The $n_{\sigma,\mathrm{e}}^{\mathrm{TPC}}$ distribution of selected electrons from photon conversion processes in pp collisions in the period LHC17p.

Hence, in the fits of the $n_{\sigma,\mathrm{e}}^{\mathrm{TPC}}$ distribution no pion tail needs to be included. Only the electron distribution in fit with a gaussian consequently. During the quality assurance phase small dependencies of the $n_{\sigma,\mathrm{e}}^{\mathrm{TPC}}$ on the momentum and η were observed for the pp data sample. Hence, the post calibration maps are created as a function of the momentum at the TPC inner wall and η. The maps corresponding to the data period LHC17p are shown in Fig. C.2 and C.3. Since the data period LHC17q represents only a small fraction of the total statistics, calibration maps can not be obtained with the same granularity as for LHC17p. However, one dimensional fit studies indicate that the difference of the mean in both periods can be described with a small offset. Thus, calibration maps for LHC17q are created using the maps of LHC17p and adding a constant derived from one dimensional studies.
The overall correction factors are very small compared to the ones reported for Pb–Pb collisions in Sec. 4.4.2. In addition it was verified that the PID in the simulation has the expected shape of an ideal gaussian with a mean of 0 and a width of 1.
Hence only the data is post calibrated with the reported maps.

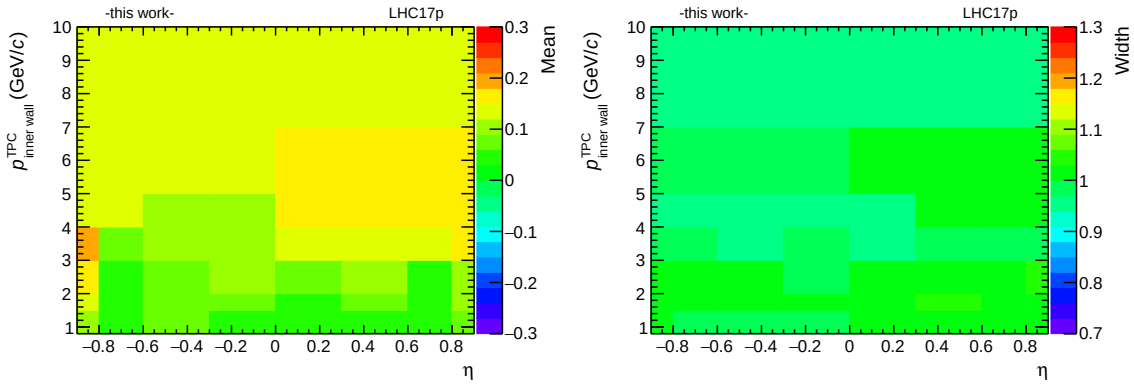

Figure C.2: The created post calibration maps in pp collisions for the period LHC17p.

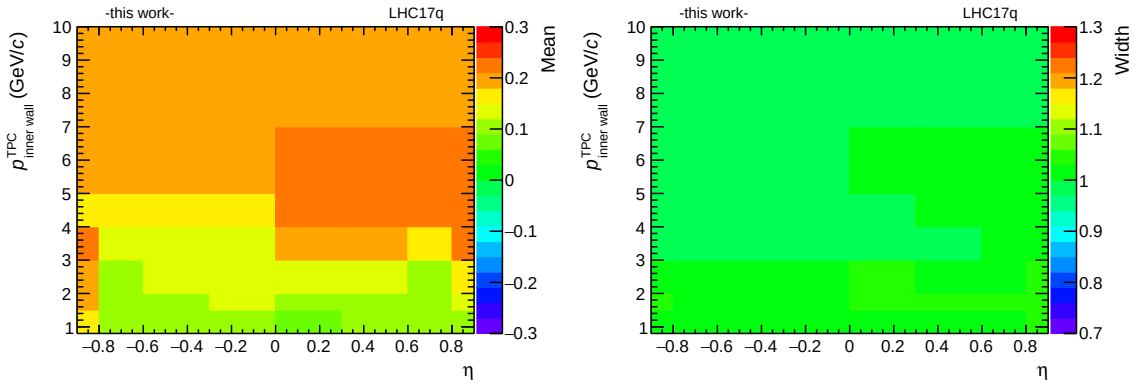

Figure C.3: The created post calibration maps in pp collisions for the period LHC17q.

D Supplemental figures for statistical uncertainties of $\langle p_{\mathrm{T}} \rangle$ and $\langle p_{\mathrm{T}}^2 \rangle$

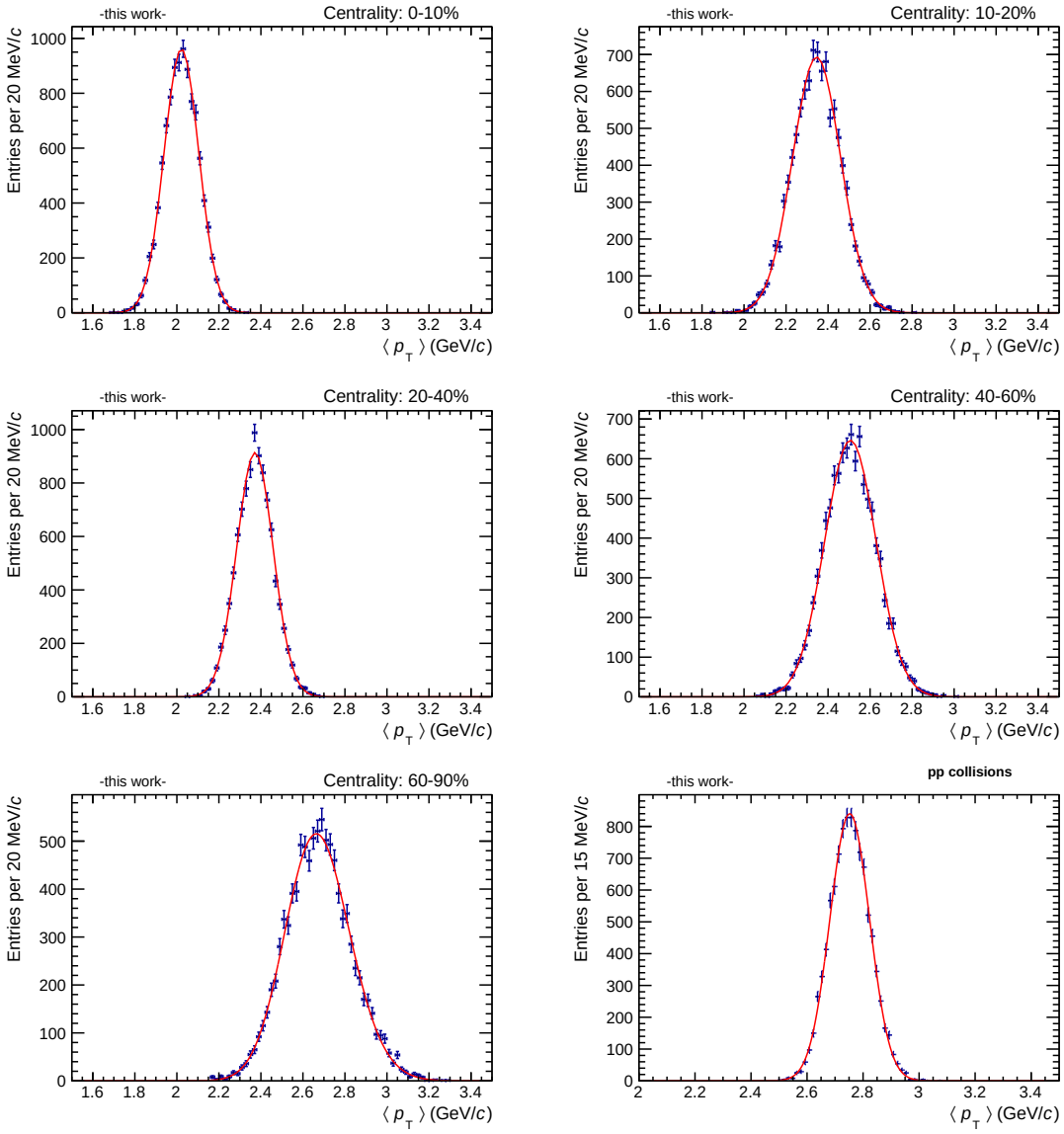

Figure D.1: Distribution of $\langle p_{\mathrm{T}} \rangle$ results obtained by smearing the same event $\langle p_{\mathrm{T}}(m_{e^+e^-})_{\mathrm{S+B}} \rangle$ distribution.

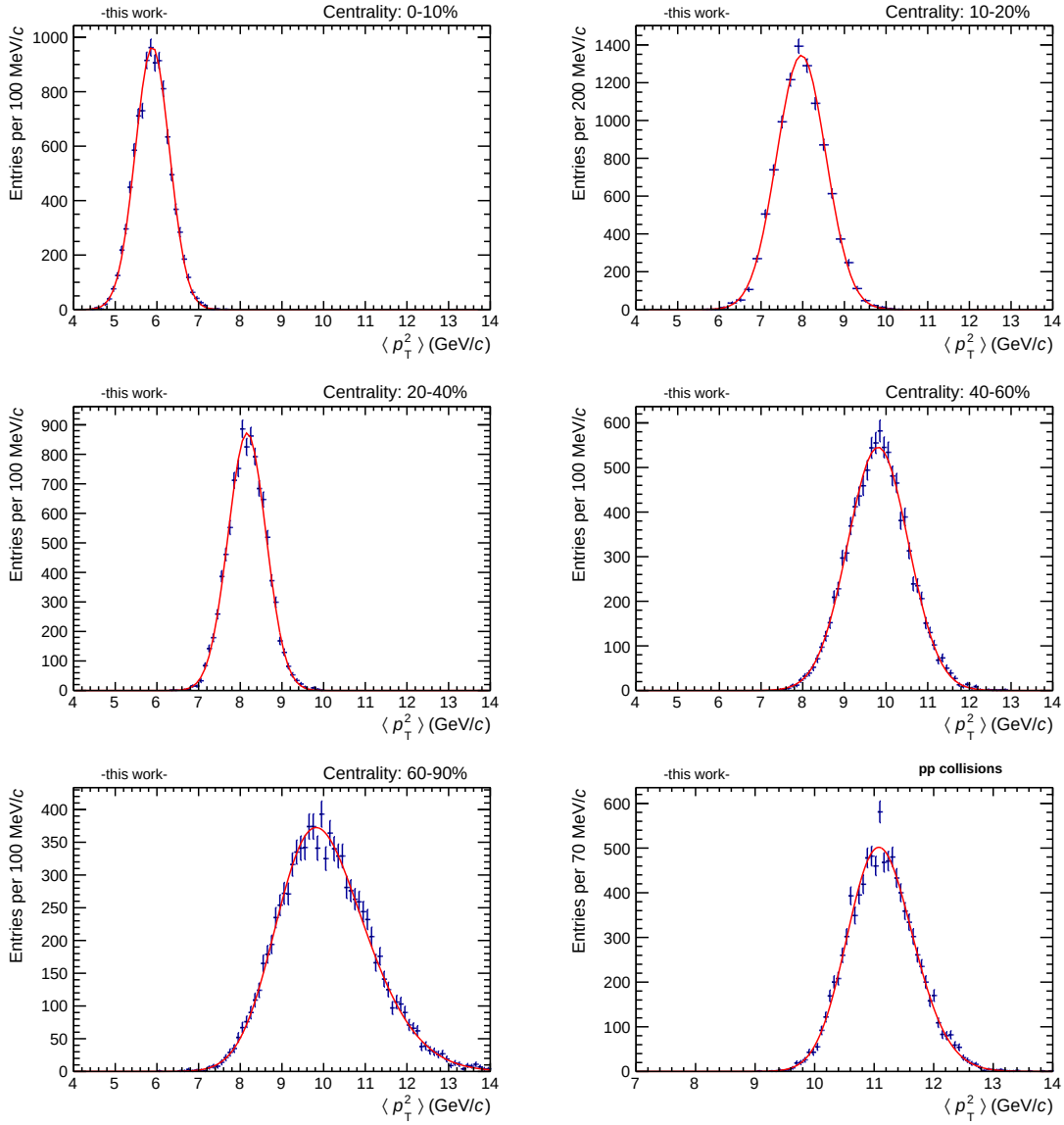

Figure D.2: Distribution of $\langle p_{\mathrm{T}}^2 \rangle$ results obtained by smearing the same event $\langle p_{\mathrm{T}}^2(m_{e^+e^-})_{\mathrm{S+B}} \rangle$ distribution.

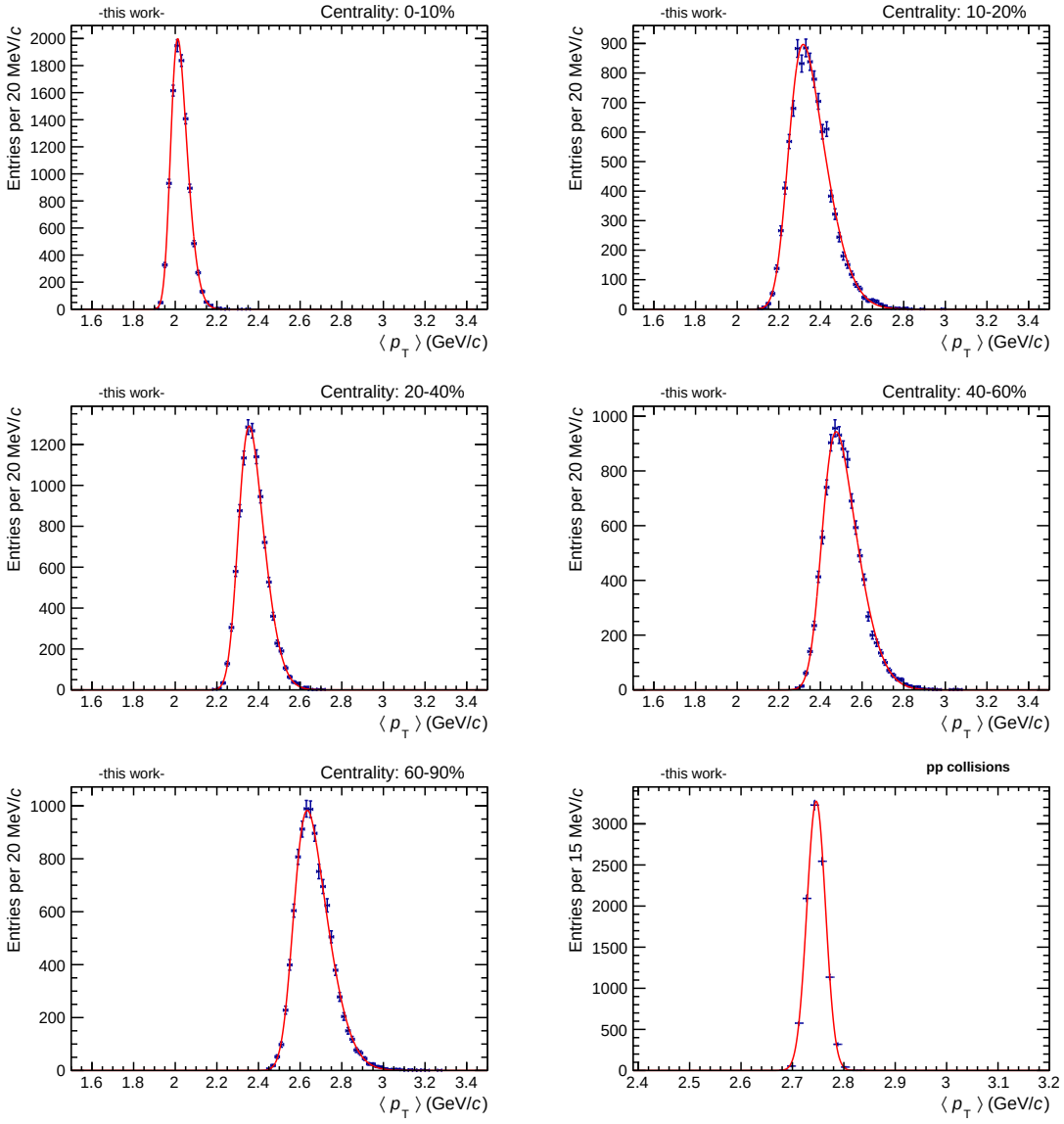

Figure D.3: Distribution of $\langle p_{\mathrm{T}} \rangle$ results obtained by varying the $N_{\mathrm{S}}(m_{e^+e^-})$ distribution.

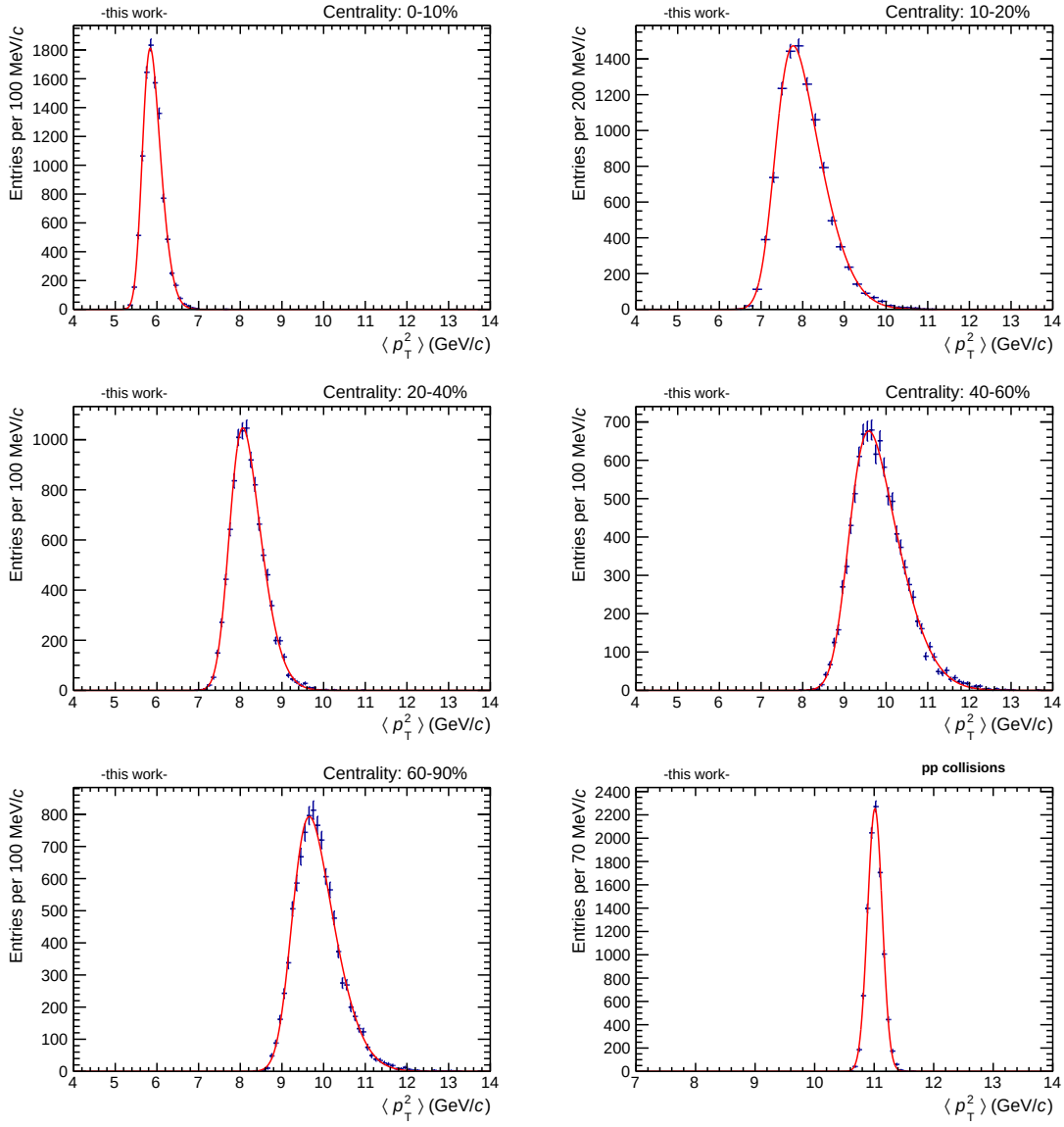

Figure D.4: Distribution of $\langle p_{\mathrm{T}}^2 \rangle$ results obtained by varying the $N_{\mathrm{S}}(m_{e^+e^-})$ distribution.

E The TRD FeeServer and control engine

E.1 Front-end electronics

The general functionality of the TRD has already been explained in Sec. 3.2.3, in this chapter the focus lies on the front-end electronics (FEE) and the Detector Control System (DCS). As already mentioned earlier the TRD is built of 18 supermodules which are comprised of 5 stacks of 6 read-out chambers (ROCs) each (see Fig. E.1). The ROCs have 6–8 read-out boards (ROBs) mounted on top (depending on the stack position). On each ROB 16 so-called Multi-Chip-Modules (MCMs) are mounted which directly process the data coming from the detector read-out pads. The MCMs contain a PreAmplifier and ShAper (PASA) and a TRAcklet Processor (TRAP) which can be adopted to different data taking modes by applying different configurations via the DCS (will be explained in Sec. E.2). The MCMs enable the processing of the raw data (on-line tracking) already at the level of the FEE in a short time (6 μs) which is needed for the TRD to provide fast triggers on rare signals. The data is merged per half-chamber and then sent out via the readout tree for more advanced processing (global TRD tracking).

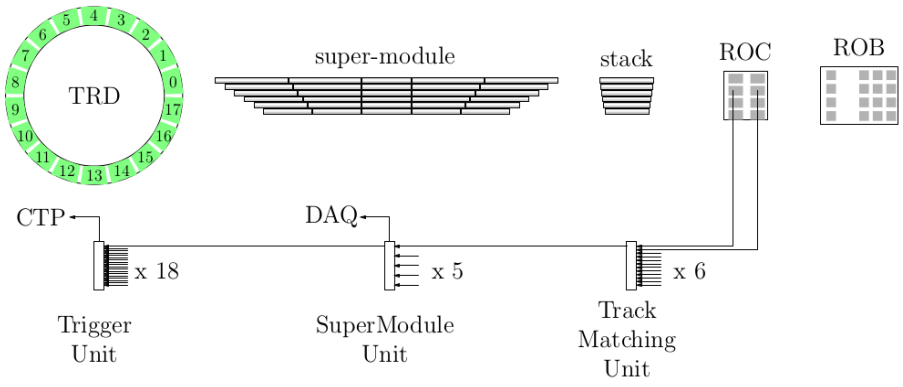

Figure E.1: Overview of the TRD front-end electronics [242]. The upper panel shows a subsequent zoom into the structure of the TRD (from left to right). The data is sent out from the ROC to the different stations of the read-out tree (lower panel).

For the configuration of the FEE and for monitoring tasks a dedicated DCS board on which an embedded Linux operating system is running is mounted on every ROC. For the purpose of the FEE configuration the MCMs are connected with a so-called Slow Control Serial Network (SCSN) which forms two individual rings connecting the MCMs in a redundant way. In this network the DCS board represents the master

and the MCMs represent the slaves. Incoming data from the master is forwarded from one slave to the next until it arrives at the master again (unbridged mode). In case of broken connections between MCMs (or broken MCMs) the SCSN can be reconfigured to form a different ring of master and slaves where the unreachable MCM is spared from the network (bridged configuration).

E.2 Detector Control System

The TRD Detector Control System (DCS), as part of the ALICE DCS, has the purpose to ensure a safe operation of the detector, to provide monitoring and configuration of the subsystems and to provide calibration information to the offline data reconstruction. The Supervisory Control and Data Acquisition (SCADA) system SIMATIC WinCC is used in the ALICE DCS for the control and automation of the systems and processes. The ALICE DCS has a tree-like architecture representing different levels in the architecture or infrastructure of the experiment/detectors. On every level finite-state-machines (FSMs) are used to represent the current status of the respective element in the tree. The states are logically propagated upwards in the tree to ensure safe operation and to indicate problems. The DCS of the TRD FEE (called FED in the following) for example has the following structure (from top to bottom): FED, sector, stack, layer. An overview of the FED DCS software can be found in Fig. E.2.

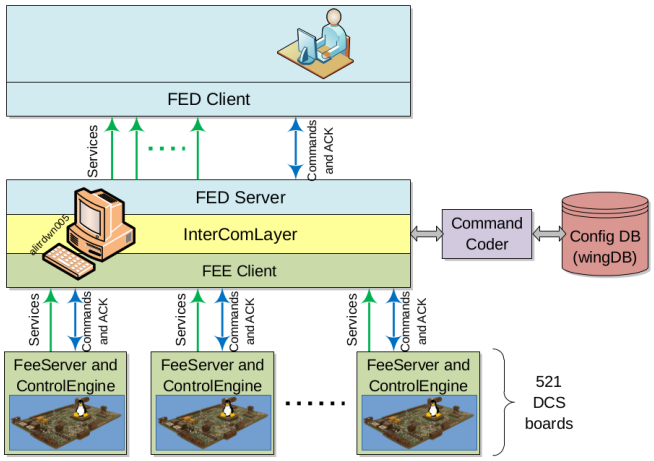

Figure E.2: Schematic of the FED DCS [243]. The communication between the individual entities is established with the Distributed Information Management System (DIM) via Ethernet connections. In this system servers publish information which is received by clients (subscribers).

When a configuration command is issued from the top layer of the FED DCS the InterComLayer (ICL) will build the necessary commands and data structure which

will be sent to the DCS boards. For this task it can access via the CommandCoder a dedicated SQL database (wingDB) which contains necessary information about the chamber types, defects in the electronics and gain calibration constants (gain tables). New items can be added easily by users to this database if for instance new defects show up.

The data structure that is built by the ICL is shown in Fig. E.3. The header of the data block is the `cfdat_header` which most importantly contains the tag of the transition command (internal numbering scheme) and offsets to the other data structures. The basic logic is that by adding the offsets to the `cfdat_header` pointer the pointers to the respective data structures are obtained (pointer arithmetic). Thus the offsets represent the starting positions of the structures in the memory with respect to the first entry. The structure `cfdat_error` contains basic information about defects in the electronics, specifically of the network interface of the readout tree (NI), the MCM internal ADC and the MCMs in general. It also contains offsets to the structures `cfdat_nistat`, `cfdat_adcstat` and `cfdat_mcmstat` which contain the position of the damaged MCM (rob, mcm) and the corresponding mask to exclude damaged electronic parts. In case of MCM defects it contains a status number which represents the type of defect. The structure `cfdat_temp_calib` was intended to contain temperature calibration constants of the MCM internal temperature sensors. However these sensors (and thus the data structure) are not used today due to the limited additional information which is gained from these temperature sensors as compared to the DCS board air temperature sensor and also due to involved maintenance requirements.

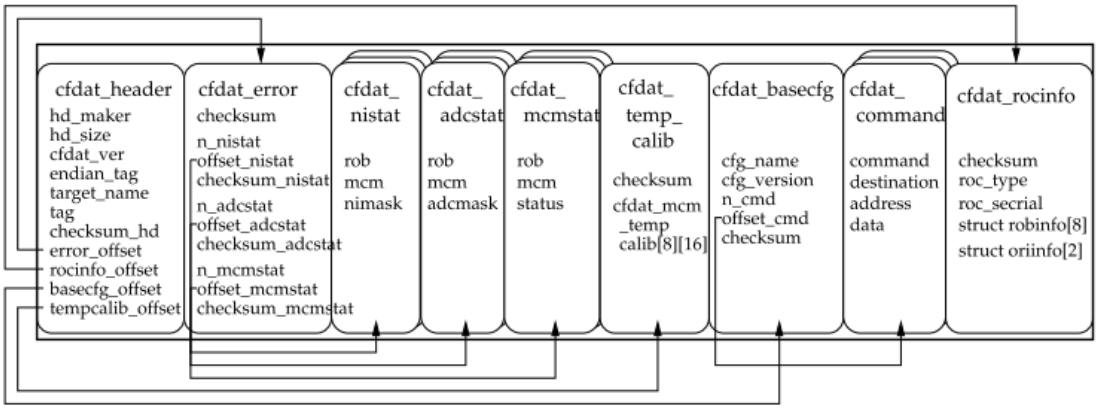

Figure E.3: FED configuration data block [244].

The structures `cfdat_basecfg` contains several details about the configuration which will be applied to the MCMs (encoded in one long string `cfg_name`), the number of SCSN commands with which this configuration can be applied (*n_cmd*) and the offset to the details of the respective SCSN commands (structures `cfdat_command`).

The structure `cfdat_rocinfo` contains mostly basic architectural information about the chamber. Finally also dedicated data structures containing the aforementioned gain tables are created and sent to the DCS boards.

E.3 FeeServer and control engine

The FeeServer is the lowest logical layer in the DCS of the front-end electronics. On every DCS board a dedicated FeeServer is running which is used for configuring and monitoring of the front-end devices.
The software logically consists of two parts: The FeeServer and the control engine. The FeeServer acts as a DIM server and provides a command channel to receive commands and a DIM data channel to publish information. The control engine is split into the libraries `libTRD` and `trdce`.
The `libTRD` provides the basic hardware interface and can be used to communicate with the MCMs via the SCSNBus or to control ROB power regulators for instance. The `trdce` package contains high level functions like a finite state machine (FSM) and the handling of incoming commands from the higher logical layers in the DCS. The central class of the control engine in which the FSM is implemented is `CEStateMachine`. When a data block is received from the ICL the corresponding actions are triggered depending on the desired transition. Important classes in this context are `roc_control` and `roc_executor`. The class `roc_control` is mainly used to parse the configuration data block and to call initializing functions with the received configuration values. The class `roc_executor` enables the hardware access by being linked to `libTRD` classes like `SCSNBus`.

The state diagram of a single read-out chamber is shown in Fig. E.4. Except for the states OFF and READY all states are implemented in `CEStateMachine`. The OFF state is only realized if the read-out chamber and the DCS board are powered off. Once the DCS board is powered on it boots and the FeeServer starts running. In this STANDBY state the chamber is still powered off. From the STANDBY state different testing procedures are available. The purpose of these tests is for instance to identify broken lines in the SCSNBus (bridge test) or to check the connectivity of the network interface of the readout tree (network interface test). A detailed description of the available tests can be found in [244].

During the initialization the FeeServer receives a configuration data block that contains in particular information about the chamber type (`cfdat_rocinfo`), the defects of the electronics `cfdat_error` and the gain tables `cfdat_gaintbl` for this chamber. The general chamber information (`cfdat_rocinfo`) is passed to the ROCInfo class which stores this information and provides get-functions to access it. The list of defects (`cfdat_error`) is passed to the `patch_maker` class which calculates the necessary configuration to circumvent these damages (in case of the SCSNBus: bridged configuration). Additionally the necessary SCSN commands are

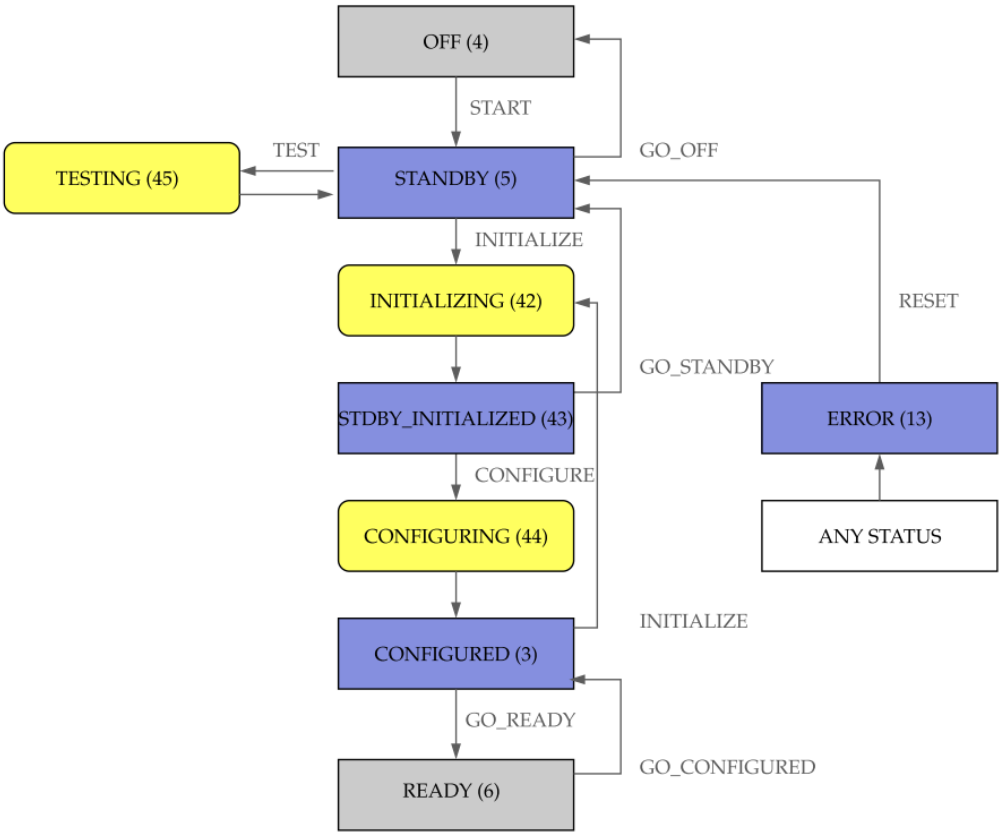

Figure E.4: State diagram of the front-end electronics. Transitional states are marked yellow, the numbers in brackets are the official ALICE numbers for the corresponding states [244].

produced which are needed to apply the calculated configuration to the front-end electronics later in the CONFIGURE state transition. The gain tables are parsed by the `gaintbl_handler` and also sent to the MCMs in the later stage of the CONFIGURE transition.
If the initialization was successful the state is changed to STDBY_INITIALIZED and the FeeServer is ready to receive new transition commands.

When the FeeServer receives the CONFIGURE command it receives again a new configuration data block, this time mainly with new information in the `cfdat_basecfg` relevant for the MCM configuration. All this information is encoded in one long configuration string `cfg_name` which can look like '`cf_pg-fpnp32_zs-s16-deh_tb24_trkl-b5p-fs1e24-ht200-qs0e24s24e23-pidlinear-pt100_ptrg`' for example. This string is chopped by the `roc_info` class and the relevant information is extracted.
In a last step all the SCSN commands which are necessary to configure the MCMs are executed by the `roc_executor` class. In the end the FSM state is set to

CONFIGURED.

Having two steps (INITIALIZE and CONFIGURE) towards the final configuration of the chamber effectively decouples the initialization of the software and the hardware. This enables to reconfigure the electronics with a different configuration without the need to reset the chamber (high current changes) in case of a B field change or a change of the run type from PHYSICS to COSMICS or vice versa. Such a reconfiguration is needed since the Lorentz angle of particles traversing the TRD active volume depends on the magnetic field (direction and strength). For cosmics data taking it is necessary to also allow the reconstruction of tracks that do not directly point towards the nominal interaction vertex. This also requires a reconfiguration of the readout electronics.

In addition to the already discussed state transitions a transition from every state to the ERROR state is possible. This is usually triggered if a transition is not allowed or when an internal error occurs and should indicate a problem to the outside. Also, it is possible to issue a reset command from every state which shuts down the voltage of the read-out boards and thus resets the configuration of the MCMs since they do not have non-volatile memory. The READY state only exists in the higher logic of the full FSM of the front-end devices. If all chambers are CONFIGURED then the top FMS node will show up in READY.

If during data taking the FeeServer restarts (which can happen due to a reboot of a DCS board or a crash of the FeeServer, both can be caused by single-event upsets (SEUs[1])) then the FeeServer was forced to ERROR state if the ROBs are powered on. The reason is that in this situation the FeeServer has lost the above described information from the initialization and configuration steps. This mainly affects the configuration of the SCSNBus and the information about the MCM configuration (long config string). In this case a proper communication to the MCMs can not be guaranteed and also the offline required information about the chamber type, applied config string and gain tables are not available. In addition the data taking efficiency of the whole experiment is deteriorated if the data taking has to be stopped in order to manually recover those problems. To ensure a more smooth operation of the TRD it was decided to upgrade the FeeServer such that this information is available after a restart which makes it possible to avoid the ERROR state. In the next Section we will describe which modifications of the control engine were necessary in order to achieve a survival of FeeServer restarts.

[1] single-event upsets refer to the change of the state of electronic devices/circuits due to ionizing radiation

E.4 Upgrade of the control engine

In order to operate the TRD chambers after a restart/reboot of the FeeServer/DCS board it is necessary to write out a certain information to a non-volatile memory area of the DCS boards. The DCS boards are equipped with a 2 kByte SRAM memory which fulfills this requirement and is thus used as storage. The access to this memory is provided by the kernel module `kmod-sram` which is permanently running and mounts the memory in `/dev/sram`. The actual writing of the information is realized by using binary serialization. It enables the writing of full data structures and is more memory efficient compared to string-based serialization.

For the writing of the information a dedicated data structure `rebootInfo` was introduced in the class `roc_control` which contains a 32bit bitmask to check the data integrity after a reboot, an integer representing the version of rebootInfo (`rebootInfoVersion`), an integer corresponding to the old FSM state (before reboot) (`oldstate`), the number of defects in the SCSNBus (`nscsndefects`), an integer which counts the number of reboots for a given DCS board (`rebootCounter`) and the name of the applied gaintable (`gaintbl_name`).
One should note here that checking the 32bit bitmask after a reboot is already a good validation procedure to see if the memory was filled with useful information before. However, it is not rigorous in a sense that it would be sensitive to possible bitflips in the full used memory block due to SEUs and thus corrupted data. The possibility of a detailed data integrity check will be discussed in section E.5. The value of `rebootInfoVersion` is defined in `roc_control.hh` and should be incremented if the structure of `rebootInfo` is changed to avoid crashes after installation of a new version due to inconsistencies. The number of defects in the SCSNBus is written out since it depends on the ROC and thus defines the length of the data block for the MCM defects. Finally, since the full gain table structures would use much more memory than is available in the SRAM, only the name of the applied gain table is written out. It is needed for proper offline data reconstruction.

The data structure `rebootInfo` represents the header of the complete data structure which is written out. In addition also the data structures `cfdat_basecfg_header`, `cfdat_header`, `cfdat_rocinfo` and the necessary number of `cfdat_mcmstat` structures are written out. Let us again point out that the number of `cfdat_mcmstat` structures is defined dynamically since it depends on the number of defects of the SCSNBus.

During the normal INITIALIZING transition the function `ROCControl::saveRebootInfo()` is called which collects the necessary information or data structures and saves them to the SRAM memory. Note that the FEE is only configured in the CONFIGURING transition, so the information about the applied configuration has to be written out separately during this transition. This is handled by `ROCControl::writeBaseCfg()` which opens the

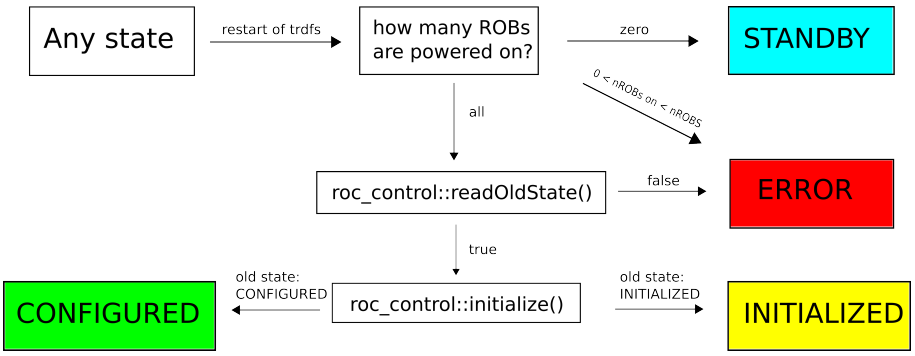

Figure E.5: Stateflow after startup of the FeeServer (trdfs) after the upgrade.

memory, seeks the corresponding positions of the structures `cfdat_basecfg_header` and `cfdat_header` and updates them. In addition, after every state transition the function `ROCControl::updateSavedInfo()` is called which opens the memory and updates the `rebootCounter` and `oldstate` to the current values. The rebootCounter is published by the FeeServer as a DIM data point and is available online during data taking in WinCC. This helps to keep record of the reboot events and is useful for debugging purposes. After a new INITIALIZING transition the `rebootCounter` is reset.

When a reboot of a DCS board occurs the FeeServer will check during startup if a reboot has occurred by first checking how many ROBs are powered on. In case all ROBs on this chamber are powered on a reboot is likely and the information in the SRAM memory is read by `ROCControl::readOldState()`. First only the header, namely the `rebootInfo` structure is read in. Subsequently the bitmask, the version of the rebootInfo and the old state is read and only in case all the information is correct and supported the other data structures are read in, otherwise the FSM will change the state to ERROR. Afterwards the rebootCounter is incremented and the function `ROCControl::initialize()` is called which lets the FeeServer learn the old configuration analogous to what is done during a normal INITIALIZING transition. Afterwards the FSM state is set to the old state (either CONFIGURED or INITIALIZED) and the last applied configuration string is set (`last_cfg_tag`). The state flow after a reboot is depicted in Fig. E.5.

E.5 Implications for TRD operation in LHC Run 3

With the aforementioned software upgrades a much smoother operation of the TRD is achieved. No human intervention is needed anymore in case of reboots of DCS boards during data taking. For LHC Run 2 data taking no serious problems were observed with the software (operational since late summer 2016). However, in Run 3 the expected luminosities are up to a factor 10 higher than in Run 2 which leads to a much higher radiation dose on the DCS boards and thus a higher reboot rate. Careful considerations have to be made when attempting extrapolations of the performance to this higher dose level. A simplified assumption would be to assume the same scaling for the number of reboot events as for the expected luminosity (assuming the same number of ions per bunch). Thus, instead of a few tens of reboots during a long fill (let's say 10 hours for simplicity) at the highest interaction rates in Run 2 a few hundreds of reboots would occur during a long fill in Run3. This could mean that statistically every DCS board reboots once per fill if the distribution of rebooting boards is homogeneous in space. This will have several consequences:
First of all, during a reboot a DCS board is not reachable and thus the FSM state is NO_CONN. After the boot and the software startup (which takes in total about two minutes) the FeeServer should publish the old FSM state. To avoid that during this time period the TRD FSM shows an ERROR state (and ALICE data taking is stopped) there is a so called majority unit in place currently. It allows up to two DCS boards in a stack to show an ERROR or NO_CONN state without switching the TRD FSM to ERROR. However, with the much higher reboot rate in Run 3 an increase in allowed DCS boards per stack might be necessary.
Secondly, due to the lack of the full gain table information after a reboot it is not possible to simply reconfigure chambers without resetting them. Currently this is handled by resetting the chambers with rebooted DCS boards before a new configuration. Since in a long fill in Run 3 statistically every DCS board might have rebooted all chambers would have to be reset before reconfiguration. To avoid this (since the reconfiguration would then come at the cost of high current changes) a new implementation could be envisaged: By sending the gain tables to the chambers in a reconfiguration process the resetting of the chambers could be potentially avoided.
Lastly, as mentioned earlier the data integrity of the full SRAM content is not checked thoroughly (like with a checksum for instance). One could imagine that SEUs also lead to bit flips in this memory and thus corrupted data is read in after reboots. However, in all data taking periods since the software upgrade no indication for such an event was observed. Thus it should also not be a big issue for Run 3.

F Lists

F.1 List of Figures

1.1 The strong coupling constant $\alpha_s(Q^2)$ as a function of the energy transfer Q, extracted from different measurements and compared to the QCD prediction. The order of QCD perturbation theory used for the extraction is given in brackets. The world average value of $\alpha_s(Q^2)$ at the mass of the Z^0 boson is given [22]. 2
1.2 Qualitative picture of different stages of hadronization of a high momentum quark-antiquark pair [24]. 3
1.3 Sketch of a conjectured QCD phase diagram [34]. 4
1.4 Thermodynamical bulk properties as calculated in lattice QCD [40]. . 5
1.5 Schematic of the space-time evolution of ultra-relativistic heavy-ion collisions [57]. 7
1.6 Illustration of the geometrical concept used in heavy-ion collisions. Left: Before the collision the incoming nuclei are separated by an impact parameter b. Right: During the collision the participant nucleons in the overlap region interact while the spectator nucleons outside of the overlap region continue propagating [64]. 10
1.7 Illustration of optical Glauber model geometry shown in the transverse plane (left) and in beam direction (right) [63]. 11
1.8 Glauber Monte Carlo simulation of a Pb–Pb collision at the LHC viewed in beam direction. Participating nucleons are represented with solid circles while spectator nucleons are marked with dotted circles [65]. 13
1.9 Sketch illustrating the slicing of the measured charged particle distribution into percentiles of the inelastic cross-section (centrality classes). The corresponding geometrical quantities like impact parameter $\langle b \rangle$ and $\langle N_{\mathrm{part}} \rangle$ can be obtained via a mapping procedure [63]. 14
1.10 Statistical model fit to particle yields measured in the 0–10% most central collisions at $\sqrt{s_{\mathrm{NN}}} = 2.76$ TeV. Mean values of the result are given in the figure [72]. 16
1.11 Blast wave fits to spectra of light flavor hadrons as measured by ALICE [78]. 17
1.12 Left: Results for the kinetic freeze-out temperature T_{kin} and mean transverse expansion velocity $\langle \beta_{\mathrm{T}} \rangle$ as extracted from blast wave fits to ALICE and STAR data [78]. Right: Mean transverse momentum of different light flavor hadrons as function of centrality as extracted from blast wave fits [80] 17

1.13 Left: Sketch of the almond shaped overlap zone created in semi-central heavy-ion collisions [64]. Right: ALICE measurement of the elliptic flow coefficient v_2 of inclusive charged particles and D mesons [82]. . . 18
1.14 Results for the nuclear modification factor of different particle types in p–Pb and Pb–Pb collisions [88]. 19

2.1 The spectrum of charmonia and non-conventional charmonium(-like) states X. Radiative transitions are not shown [93]. 22
2.2 Fraction f_{B} of non-prompt J/ψ measured by CDF [100], ALICE [101], ATLAS [102] and CMS [103]. 23
2.3 Left: Illustration of the fit function used in the extraction of the EPPS16 nPDFs. Right: Ratio R_g^{Pb} for gluons at $Q^2 = 10$ GeV^2. The mean value is indicated as black line while the total uncertainty is indicated as grey band. Both taken from [127]. 25
2.4 Left: ALICE measurement of the R_{pPb} of J/ψ as a function of rapidity compared to shadowing (EPS09), CGC and energy loss calculations [130, 131]. Right: Measurement of the transverse momentum broadening of J/ψ as a function of the average number of nucleon-nucleon collisions [132]. 26
2.5 Left: Results for J/ψ and ψ(2S) production at SPS in different p–A and A–A configurations as a function of the effective traversed length in the nuclear medium [136]. Right: Nuclear modification factor of J/ψ measured at SPS and RHIC as a function of the number of participating nucleons [136]. 28
2.6 Sketch of the dynamics of $c\bar{c}$ pairs produced in nucleus-nucleus collisions. At low collision energy the charm quarks are separated due to color screening and form open charm mesons at freeze-out. At high collisions energy J/ψ might be formed by combinations of charm and anticharm quarks from the medium due to their large abundance [142]. 30
2.7 Time evolution of a $c\bar{c}$ pair in an expanding fireball within a transport model [147]. 31
2.8 Left: Centrality dependence of the nuclear modification factor compared to model predictions [151]. Right: Transverse momentum dependence of the nuclear modification factor compared to transport model predictions and lower energy results from PHENIX [152]. In both cases the model uncertainties reflect the imprecise knowledge of the charm cross-section in Pb–Pb collisions. 32
2.9 Left: Transport model predictions for the centrality dependence of r_{AA} at different collision energies compared to available data from SPS, RHIC and LHC. Right: Expectation for a hard pQCD charm quark distribution (a) and effect of nuclear shadowing of the PDFs (b) [145]. 33
2.10 Sketch of the equivalent photon flux in UPC [153]. 35
2.11 Exclusive photoproduction of J/ψ (left) and dilepton pairs (right) [158]. 35

2.12 Left: Measurement of e^+e^- pair transverse momentum in exclusive events at mid-rapidity in the mass interval $2.2 < m_{e^+e^-} < 3.2$ GeV/c. The contributions are obtained from a fit based on simulated templates [159]. Right: Observation of an excess at very low p_{T} in the dimuon transverse momentum distribution consistent with photoproduced J/ψ in 70–90% Pb–Pb collisions at forward-rapidity [160]. 36

3.1 The CERN accelerator complex with the LHC and its accelerator chain [163]. 38
3.2 Schematic view of the ALICE detector [173]. 39
3.3 The ALICE TPC. Left: Geometry [175]. Right: Sketch of the working principle [176]. 41
3.4 Specific energy loss $\mathrm{d}E/\mathrm{d}x$ as a function of the rigidity p/z measured with the TPC in Pb–Pb collisions at 5.02 TeV. Solid lines represent the expected energy loss for different particles [173]. 44
3.5 Slice of the ALICE central barrel in beam direction [184]. 45
3.6 Left: Illustration of generated ionization along the path of electrons and pions through a TRD chamber. Right: Measured average puls height distribution as a function of the signal arrival time. Both taken from [184]. 45
3.7 Schematic of the event reconstruction sequence [172]. 47
3.8 Fit of the V0 amplitude distribution with the NBD-Glauber model. Centrality percentiles are indicated as slices of the distribution [185]. 48
3.9 Kinematic acceptance of the LHC experiments for J/ψ measurements in Pb–Pb collisions based on Run 1 publications [189]. 50

4.1 Transverse momentum distribution of generated J/ψ signals. 52
4.2 Multiplicity measured in V0 scintillators versus number of tracks in the TPC. Left: Low interaction rate data. Right: High interaction rate data. 53
4.3 Left: Distribution of the z coordinate of the interaction vertex for the selected events. Right: Centrality distribution of the selected events. . 54
4.4 Double Gaussian fit to the $n_{\sigma,\mathrm{e}}^{\mathrm{TPC}}$ distribution of conversion electrons in most central (left) and most peripheral collisions (right). 57
4.5 Centrality dependence of the mean and the width of the electron Gaussian in the fit for both data periods. 58
4.6 Pseudorapidity dependence of the mean and the width of the electron Gaussian in the fit for both data periods. 58
4.7 Momentum dependence of the mean and the width of the electron Gaussian in the fit for both data periods. 59
4.8 Correction maps for the mean and the width of the electron $n_{\sigma,\mathrm{e}}^{\mathrm{TPC}}$ distribution for the two data periods. 60

4.9 Selected calibrated electrons after applying a selection of -2 $< n_{\sigma,\mathrm{e}}^{\mathrm{TPC,\ corr}} <$ 3 and excluding protons and pions by requiring $n_{\sigma,\mathrm{p}}^{\mathrm{TPC}} > 3.5$ and $n_{\sigma,\pi}^{\mathrm{TPC}} > 3.5$. 61
4.10 Comparison of electron selection efficiency defined in Eq. 4.3 for J/ψ legs and conversion electrons in the simulation. 61
4.11 Comparison of electron selection efficiency in the simulation compared to the data periods LHC15o_highIR (left) and LHC15o_pidfix (right). 62
4.12 Example of the parameterization of the hadron rejection lines in the centrality class 0–5%. 63
4.13 Transverse momentum dependent signal extraction in the centrality class 0–20%. 66
4.14 Transverse momentum dependent signal extraction in the centrality class 20–40%. 67
4.15 Transverse momentum dependent signal extraction in the centrality class 40–90%. 68
4.16 Obtained $A \times \epsilon$ factors as a function of p_{T} shown in centrality intervals. 69
4.17 Transverse momentum dependence of the $A \times \epsilon$ shown together with its partial efficiencies and the acceptance for the most central (left) and most peripheral collisions (right). 70
4.18 Fits to the J/ψ spectra measured at forward rapidity in Pb–Pb collisions at $\sqrt{s_{\mathrm{NN}}} = 5.02$ TeV in different centrality bins. 72
4.19 Left: Toy measurement obtained from sampling the parameterization of the forward J/ψ spectrum in 0–10% centrality drawn together with different drawing positions. Right: Fit to the toy measurement together with the true x_{lw}. 76
4.20 Fits to measured spectra together with 1σ uncertainty band. 78
4.21 Interpolation of the J/ψ $\langle p_{\mathrm{T}} \rangle$ at mid-rapidity [206]. 79

5.1 Left: Acceptance × efficiency map used for the correction of the Pb–Pb data. Right: Acceptance × efficiency as function of p_{T} with its different steps in pp collisions. 84
5.2 Inclusive signal extraction in Pb–Pb collisions in the centrality intervals up to 60%. 86
5.3 Inclusive signal extraction for Pb–Pb collisions in the centrality interval 60–90% (left) and for pp collisions (right). 87
5.4 Parameterization of the background $\langle p_{\mathrm{T}} \rangle$ and $\langle p_{\mathrm{T}}^2 \rangle$ in pp collisions. . . 88
5.5 Extraction of the J/ψ $\langle p_{\mathrm{T}} \rangle$ with the template fit method in Pb–Pb and pp collisions. 89
5.6 Extraction of the J/ψ $\langle p_{\mathrm{T}}^2 \rangle$ with the template fit method in Pb–Pb and pp collisions. 90
5.7 Summary of the relative statistical uncertainties of the $\langle p_{\mathrm{T}} \rangle$ and $\langle p_{\mathrm{T}}^2 \rangle$ in Pb–Pb collisions. 91

5.8 Fit to the ALICE J/ψ spectrum measured at $\sqrt{s} = 7$ TeV where the quadratic sum of statistical and systematic uncertainty is assigned to the points. In the fit the integral of the bins is used. The data is taken from [101, 199]. 96
5.9 Fit to the PHENIX J/ψ spectrum measured at $\sqrt{s} = 200$ GeV where the sum of statistical and systematic uncertainty is assigned to the points. In the fit the integral of the bins is used. The data is taken from [212]. 97

6.1 Left: Centrality dependence of the J/ψ nuclear modification factor compared to model calculations. Right: Rapidity dependence of the nuclear modification factor. The correlated uncertainty only represents the reference uncertainty of the forward measurement. The figures are taken from [214]. 99
6.2 Transverse momentum dependent J/ψ production cross-section in pp collisions. Left: Comparison to model predictions. Right: Comparison to the reference obtained from the interpolation explained in Sec. 4.9. The figures are taken from [214]. 101
6.3 Left: Transverse momentum differential cross-section of prompt J/ψ and prompt D^0 mesons. Right: Ratio of J/ψ and D^0 cross-sections. The D^0 meson data is taken from [222]. 102
6.4 J/ψ transverse momentum spectra in three centrality classes together with statistical hadronization model [224] predictions. 104
6.5 Transverse momentum dependent nuclear modification factor of J/ψ in three centrality classes. Statistical uncertainties are indicated with vertical error bars while systematic uncertainties are indicated with boxes around the points. The horizontal error bars reflect the bin width of the measurement. The box around unity reflects the correlated systematic uncertainty (luminosity in pp collisions and T_{AA}). 105
6.6 Transverse momentum dependent nuclear modification factor compared to predictions by the SHM and the transport model by Du and Rapp. Statistical uncertainties are indicated with vertical error bars while systematic uncertainties are indicated with boxes around the points. The horizontal error bars reflect the bin width of the measurement. The box around unity reflects the correlated systematic uncertainty (luminosity in pp collisions and T_{AA}). 106
6.7 Transverse momentum dependent nuclear modification factor compared to the forward rapidity measurement. Statistical uncertainties are indicated with vertical error bars while systematic uncertainties are indicated with boxes around the points. The horizontal error bars reflect the bin width of the measurement. The box around unity reflects the correlated systematic uncertainty (luminosity in pp collisions and T_{AA}). 107

6.8 Results for $\langle p_{\mathrm{T}} \rangle$ and $\langle p_{\mathrm{T}}^2 \rangle$ in pp collisions compared to the values obtained by the interpolation. . . . 108
6.9 World data for J/ψ $\langle p_{\mathrm{T}} \rangle$ and $\langle p_{\mathrm{T}}^2 \rangle$ at mid-rapidity in pp collisions. Error bars represent the quadratic sum of statistical and systematic uncertainties. . . . 108
6.10 Results for $\langle p_{\mathrm{T}} \rangle$, $\langle p_{\mathrm{T}}^2 \rangle$ and $r_{\mathrm{AA}} = \langle p_{\mathrm{T}}^2 \rangle^{\mathrm{Pb–Pb}} / \langle p_{\mathrm{T}}^2 \rangle^{\mathrm{pp}}$ as a function of centrality in Pb–Pb collisions. Also shown is the pp data point as a reference. . . . 110
6.11 Comparison of the $\langle p_{\mathrm{T}} \rangle$ and $r_{\mathrm{AA}} = \langle p_{\mathrm{T}}^2 \rangle^{\mathrm{Pb–Pb}} / \langle p_{\mathrm{T}}^2 \rangle^{\mathrm{pp}}$ results to model predictions by the SHM [224], the transport model by Rapp et al. [143, 144] and the transport model by Zhou et al. [145, 146]. . . . 111
6.12 Comparison of the $\langle p_{\mathrm{T}} \rangle$ and $r_{\mathrm{AA}} = \langle p_{\mathrm{T}}^2 \rangle^{\mathrm{Pb–Pb}} / \langle p_{\mathrm{T}}^2 \rangle^{\mathrm{pp}}$ results to results obtained at lower collision energies at NA50 [232] and PHENIX [212, 233, 234]. . . . 112
6.13 Comparison of the $\langle p_{\mathrm{T}} \rangle$, $\langle p_{\mathrm{T}}^2 \rangle$ and $r_{\mathrm{AA}} = \langle p_{\mathrm{T}}^2 \rangle^{\mathrm{Pb–Pb}} / \langle p_{\mathrm{T}}^2 \rangle^{\mathrm{pp}}$ results to inclusive charged particles. The charged particle results are calculated from the spectra published in [226]. . . . 113
6.14 Comparison of the J/ψ $\langle p_{\mathrm{T}} \rangle$ results in 0–10%, 20–40% and 60–90% central collisions to light flavor particles. Only statistical uncertainties are shown for better visibility. The pion, kaon and proton data are shown in the centrality intervals 0–5%, 40–50%, 80–90% and are taken from [236]. The results of deuterons are shown in the centrality bins 0–5%, 30–40% and 80–90%, the ^{3}He results are shown in the bins 0–10%, 10–40%, 40–90%. The results of deuterons and ^{3}He and are taken from [237]. . . . 114
6.15 Comparison of $\langle p_{\mathrm{T}} \rangle$, $\langle p_{\mathrm{T}}^2 \rangle$ and $r_{\mathrm{AA}} = \langle p_{\mathrm{T}}^2 \rangle^{\mathrm{Pb–Pb}} / \langle p_{\mathrm{T}}^2 \rangle^{\mathrm{pp}}$ results to the forward rapidity results. The forward rapidity pp results are taken from [114], while the forward rapidity Pb–Pb results are taken from [239]. . . . 116
6.16 Comparison of $\langle p_{\mathrm{T}} \rangle$ and $r_{\mathrm{AA}} = \langle p_{\mathrm{T}}^2 \rangle^{\mathrm{Pb–Pb}} / \langle p_{\mathrm{T}}^2 \rangle^{\mathrm{pp}}$ results to the ALICE results at $\sqrt{s_{\mathrm{NN}}} = 2.76$ TeV which are taken from [152]. For the r_{AA} this comparison is also shown for the forward rapidity data where the figure is taken from [240]. . . . 117

C.1 The $n_{\sigma,\mathrm{e}}^{\mathrm{TPC}}$ distribution of selected electrons from photon conversion processes in pp collisions in the period LHC17p. . . . 129
C.2 The created post calibration maps in pp collisions for the period LHC17p. . . . 130
C.3 The created post calibration maps in pp collisions for the period LHC17q. . . . 130

D.1 Distribution of $\langle p_{\mathrm{T}} \rangle$ results obtained by smearing the same event $\langle p_{\mathrm{T}}(m_{e^+e^-})_{\mathrm{S+B}} \rangle$ distribution. . . . 131

D.2 Distribution of $\langle p_{\mathrm{T}}^2 \rangle$ results obtained by smearing the same event $\langle p_{\mathrm{T}}^2(m_{e^+e^-})_{\mathrm{S+B}} \rangle$ distribution. 132
D.3 Distribution of $\langle p_{\mathrm{T}} \rangle$ results obtained by varying the $N_{\mathrm{S}}(m_{e^+e^-})$ distribution. 133
D.4 Distribution of $\langle p_{\mathrm{T}}^2 \rangle$ results obtained by varying the $N_{\mathrm{S}}(m_{e^+e^-})$ distribution. 134

E.1 Overview of the TRD front-end electronics [242]. The upper panel shows a subsequent zoom into the structure of the TRD (from left to right). The data is sent out from the ROC to the different stations of the read-out tree (lower panel). 135
E.2 Schematic of the FED DCS [243]. The communication between the individual entities is established with the Distributed Information Management System (DIM) via Ethernet connections. In this system servers publish information which is received by clients (subscribers). 136
E.3 FED configuration data block [244]. 137
E.4 State diagram of the front-end electronics. Transitional states are marked yellow, the numbers in brackets are the official ALICE numbers for the corresponding states [244]. 139
E.5 Stateflow after startup of the FeeServer (trdfs) after the upgrade. . . 142

F.2 List of Tables

2.1 Charmonium properties derived from Non-Relativistic Potential Theory. The different χ_{c} states are not resolved in this consideration. . . 27

4.1 Number of events after selection for the datasets used in the Pb–Pb analysis presented in this thesis. 54
4.2 Summary of applied track selection criteria. 55
4.3 Summary of systematic uncertainties of the fully corrected J/ψ yields and the nuclear overlap function in percent. 75
4.4 Results for x_{lw} (GeV/c) for the different centrality intervals and p_{T} bins. 77
4.5 Results of the $\langle p_{\mathrm{T}} \rangle$ interpolation at $\sqrt{s} = 5$ TeV for $p_{\mathrm{T}} < 10$ GeV/c. . 80
4.6 Results of the p_{T} differential pp cross section interpolation at $\sqrt{s} =$ 5 TeV. The values reflect the integral in the p_{T} ranges. 80

5.1 Number of events after selection for the Pb–Pb and pp datasets used in the analysis presented in this chapter. 82
5.2 Summary of applied electron selection criteria used in pp collisions. . 82
5.3 Summary of statistical uncertainties for $\langle p_{\mathrm{T}} \rangle$ and $\langle p_{\mathrm{T}}^2 \rangle$ in pp collisions. 92
5.4 Summary of systematic uncertainties for the $\langle p_{\mathrm{T}} \rangle$ analysis. 93
5.5 Summary of systematic uncertainties for the $\langle p_{\mathrm{T}}^2 \rangle$ analysis. 94

6.1 Summary of model input parameters. The charm cross section is listed prior to the shadowing reduction. The values are obtained by private communication with the authors. 100

A.1 Results for the J/ψ yield in Pb–Pb collisions in p_{T} bins $(1/\mathrm{N_{evt}}\mathrm{d}N_{\mathrm{J}/\psi}/\mathrm{d}p_{\mathrm{T}}\mathrm{d}y)$ and for the R_{AA}, both differential in centrality. The first uncertainty is statistical while the second one is systematic. 125
A.2 Results for $\langle p_{\mathrm{T}} \rangle$ and $\langle p_{\mathrm{T}}^2 \rangle$ in Pb–Pb and pp collisions at 5.02 TeV using the template fit method. In Pb–Pb collisions the results are given for $0.15 < p_{\mathrm{T}} < 10$ GeV/c while in pp collisions the results are given for $p_{\mathrm{T}} < 10$ GeV/c. The first uncertainty is statistical while the second one is systematic. 126
A.3 Results for $\langle p_{\mathrm{T}} \rangle$ and $\langle p_{\mathrm{T}}^2 \rangle$ in Pb–Pb and pp collisions at 5.02 TeV using fits to the measured spectra. In Pb–Pb collisions the results are given for $0.15 < p_{\mathrm{T}} < 10$ GeV/c while in pp collisions the results are given for $p_{\mathrm{T}} < 10$ GeV/c. The first uncertainty is statistical while the second one is systematic. 126
A.4 Results for $\langle p_{\mathrm{T}} \rangle$ and $\langle p_{\mathrm{T}}^2 \rangle$ in pp collisions at different energies as extracted from the published spectra. The first uncertainty is statistical while the second one is systematic. 126

B.1 Pair selection criteria for e^+e^- pairs from photon conversion processes. 127

Bibliography

[1] E. Rutherford, "The scattering of α and β particles by matter and the structure of the atom," *The London, Edinburgh, and Dublin Philosophical Magazine and Journal of Science* **21** no. 125, (1911) 669–688.

[2] E. Rutherford, "Collision of α particles with light atoms. An anomalous effect in nitrogen," *The London, Edinburgh, and Dublin Philosophical Magazine and Journal of Science* **37** no. 222, (1919) 581–587.

[3] E. Rutherford, "LVII. The structure of the atom," *The London, Edinburgh, and Dublin Philosophical Magazine and Journal of Science* **27** no. 159, (1914) 488–498.

[4] J. Chadwick, "Possible Existence of a Neutron," *Nature* **129** (1932) 312.

[5] H. Yukawa, "On the Interaction of Elementary Particles I," *Proc. Phys. Math. Soc. Jap.* **17** (1935) 48–57. [Prog. Theor. Phys. Suppl.1,1(1935)].

[6] G. P. S. Occhialini and C. F. Powell, "Observations on the Tracks of Slow Mesons in Photographic Emulsions," *Nature* **160** (1947) 453.

[7] M. Gell-Mann, "The Eightfold Way: A Theory of strong interaction symmetry," *California Institute of Technology Report CTSL-20, 1961 (unpublished), reprinted in Gell-Mann, Ne'eman: The Eightfold Way, W.A. Benjamin, New York, 1964., pp. 11–57.* (1961) .

[8] Y. Ne'eman, "Derivation of strong interactions from a gauge invariance," *Nucl. Phys.* **26** (1961) 222–229. [,34(1961)].

[9] M. Gell-Mann, "A Schematic Model of Baryons and Mesons," *Phys. Lett.* **8** (1964) 214–215.

[10] G. Zweig, "An SU(3) model for strong interaction symmetry and its breaking. Version 2," in *DEVELOPMENTS IN THE QUARK THEORY OF HADRONS. VOL. 1. 1964 - 1978*, D. Lichtenberg and S. P. Rosen, eds., pp. 22–101. 1964.

[11] M. Breidenbach et al., "Observed Behavior of Highly Inelastic Electron-Proton Scattering," *Phys. Rev. Lett.* **23** (1969) 935–939.

[12] E. D. Bloom et al., "High-Energy Inelastic $e - p$ Scattering at 6° and 10°," *Phys. Rev. Lett.* **23** (1969) 930–934.

[13] G. Miller et al., "Inelastic electron-Proton Scattering at Large Momentum Transfers," *Phys. Rev.* **D5** (1972) 528.

[14] J. D. Bjorken, "Asymptotic Sum Rules at Infinite Momentum," *Phys. Rev.* **179** (1969) 1547–1553.

[15] J. J. Aubert et al., "Experimental Observation of a Heavy Particle J," *Phys. Rev. Lett.* **33** (1974) 1404–1406.

[16] J. E. Augustin et al., "Discovery of a Narrow Resonance in e^+e^- Annihilation," *Phys. Rev. Lett.* **33** (1974) 1406–1408.

[17] S. L. Glashow, J. Iliopoulos and L. Maiani, "Weak Interactions with Lepton-Hadron Symmetry," *Phys. Rev. D* **2** (1970) 1285–1292.

[18] H. Fritzsch and M. Gell-Mann, "Current algebra: Quarks and what else?," *eConf* **C720906V2** (1972) 135–165, arXiv:hep-ph/0208010 [hep-ph].

[19] H. Fritzsch, M. Gell-Mann and H. Leutwyler, "Advantages of the Color Octet Gluon Picture," *Phys. Lett. B* **47** (1973) 365–368.

[20] D. J. Gross and F. Wilczek, "Ultraviolet Behavior of Non-Abelian Gauge Theories," *Phys. Rev. Lett.* **30** (1973) 1343–1346.

[21] H. D. Politzer, "Reliable Perturbative Results for Strong Interactions?," *Phys. Rev. Lett.* **30** (1973) 1346–1349.

[22] **Particle Data Group** Collaboration, C. Patrignani et al., "The Review of Particle Physics," *Chin. Phys. C* **40** (2016 and 2017 update) .

[23] "Millennium Problems." http://www.claymath.org/millennium-problems. (accessed on May 18th 2018).

[24] M. Thomson, *Modern particle physics*. Cambridge University Press, New York, 2013.

[25] S. L. Glashow, "Partial-symmetries of weak interactions," *Nuclear Physics* **22** no. 4, (1961) 579 – 588.

[26] S. Weinberg, "A Model of Leptons," *Phys. Rev. Lett.* **19** (1967) 1264–1266.

[27] A. Salam, "Weak and Electromagnetic Interactions," *Conf. Proc.* **C680519** (1968) 367–377.

[28] G. 't Hooft and M. Veltman, "Regularization and renormalization of gauge fields," *Nuclear Physics B* **44** no. 1, (1972) 189 – 213.

[29] G. Aad et al., "Observation of a new particle in the search for the Standard Model Higgs boson with the ATLAS detector at the LHC," *Physics Letters B* **716** no. 1, (2012) 1 – 29.

[30] S. Chatrchyan et al., "Observation of a new boson at a mass of 125 GeV with the CMS experiment at the LHC," *Physics Letters B* **716** no. 1, (2012) 30 – 61.

[31] R. Hagedorn, "Statistical thermodynamics of strong interactions at high energies," *Nuovo Cimento, Suppl.* **3** no. CERN-TH-520, (1965) 147–186.

[32] J. C. Collins and M. J. Perry, "Superdense Matter: Neutrons or Asymptotically Free Quarks?," *Phys. Rev. Lett.* **34** (1975) 1353–1356.

[33] N. Cabibbo and G. Parisi, "Exponential Hadronic Spectrum and Quark Liberation," *Phys. Lett. B* **59** (1975) 67–69.

[34] H.-T. Ding, F. Karsch and S. Mukherjee, "Thermodynamics of strong-interaction matter from Lattice QCD," *Int. J. Mod. Phys. E* **24** no. 10, (2015) 1530007, arXiv:1504.05274 [hep-lat].

[35] C. Ratti, "Lattice QCD and heavy ion collisions: a review of recent progress," *Reports on Progress in Physics* **81** no. 8, (2018) 084301.

[36] K. G. Wilson, "Confinement of Quarks," *Phys. Rev. D* **10** (1974) 2445–2459. [,319(1974)].

[37] **Wuppertal-Budapest** Collaboration, S. Borsanyi et al., "Is there still any T_C mystery in lattice QCD? Results with physical masses in the continuum limit III," *JHEP* **09** (2010) 073, arXiv:1005.3508 [hep-lat].

[38] **HotQCD** Collaboration, A. Bazavov et al., "Chiral and deconfinement aspects of the QCD transition," *Phys. Rev. D* **85** (2012) 054503.

[39] Y. Aoki et al., "The Order of the quantum chromodynamics transition predicted by the standard model of particle physics," *Nature* **443** (2006) 675–678, arXiv:hep-lat/0611014 [hep-lat].

[40] **HotQCD** Collaboration, A. Bazavov et al., "Equation of state in (2+1)-flavor QCD," *Phys. Rev. D* **90** (2014) 094503, arXiv:1407.6387 [hep-lat].

[41] R. V. Gavai and S. Gupta, "Quark number susceptibilities, strangeness and dynamical confinement," *Phys. Rev. D* **64** (2001) 074506, arXiv:hep-lat/0103013 [hep-lat].

[42] C. R. Allton et al., "The QCD thermal phase transition in the presence of a small chemical potential," *Phys. Rev. D* **66** (2002) 074507, arXiv:hep-lat/0204010 [hep-lat].

[43] P. de Forcrand and O. Philipsen, "The QCD phase diagram for small densities from imaginary chemical potential," *Nucl. Phys. B* **642** (2002) 290–306, arXiv:hep-lat/0205016 [hep-lat].

[44] M. D'Elia and M.-P. Lombardo, "Finite density QCD via an imaginary chemical potential," *Phys. Rev. D* **67** (2003) 014505.

[45] Z. Fodor and S. D. Katz, "A New method to study lattice QCD at finite temperature and chemical potential," *Phys. Lett. B* **534** (2002) 87–92, arXiv:hep-lat/0104001 [hep-lat].

[46] Z. Fodor and S. D. Katz, "Critical point of QCD at finite T and μ, lattice results for physical quark masses," *JHEP* **04** (2004) 050, arXiv:hep-lat/0402006 [hep-lat].

[47] S. Datta, R. V. Gavai and S. Gupta, "QCD at finite chemical potential with $N_t = 8$," *PoS* **LATTICE2013** (2014) 202.

[48] M. G. Alford, "Color superconductivity in ultra-dense quark matter," *PoS* **LAT2006** (2006) 001, arXiv:hep-lat/0610046 [hep-lat].

[49] I. Tews, T. Krüger, K. Hebeler and A. Schwenk, "Neutron matter at next-to-next-to-next-to-leading order in chiral effective field theory," *Phys. Rev. Lett.* **110** no. 3, (2013) 032504, arXiv:1206.0025 [nucl-th].

[50] E. Annala, T. Gorda, A. Kurkela and A. Vuorinen, "Gravitational-wave constraints on the neutron-star-matter Equation of State," *Phys. Rev. Lett.* **120** no. 17, (2018) 172703, arXiv:1711.02644 [astro-ph.HE].

[51] D. Boyanovsky, H. J. de Vega and D. J. Schwarz, "Phase transitions in the early and the present universe," *Ann. Rev. Nucl. Part. Sci.* **56** (2006) 441–500, arXiv:hep-ph/0602002 [hep-ph].

[52] D. J. Schwarz, "The first second of the universe," *Annalen Phys.* **12** (2003) 220–270, arXiv:astro-ph/0303574 [astro-ph].

[53] T. Boeckel, S. Schettler and J. Schaffner-Bielich, "The Cosmological QCD Phase Transition Revisited," *Prog. Part. Nucl. Phys.* **66** (2011) 266–270, arXiv:1012.3342 [astro-ph.CO].

[54] P. Castorina, D. Lanteri and S. Mancani, "Deconfinement transition effects on cosmological parameters and primordial gravitational waves spectrum," *Phys. Rev. D* **98** no. 2, (2018) 023007, arXiv:1804.04989 [hep-ph].

[55] E. Shuryak, "Quark-gluon plasma and hadronic production of leptons, photons and psions," *Physics Letters B* **78** no. 1, (1978) 150 – 153.

[56] J. D. Bjorken, "Highly relativistic nucleus-nucleus collisions: The central rapidity region," *Phys. Rev. D* **27** (1983) 140–151.

[57] R. Stock, "Relativistic Nucleus-Nucleus Collisions and the QCD Matter Phase Diagram," arXiv:0807.1610 [nucl-ex].

[58] **ALICE** Collaboration, K. Aamodt et al., "Two-pion Bose-Einstein correlations in central Pb-Pb collisions at $\sqrt{s_{NN}} = 2.76$ TeV," *Phys. Lett. B* **696** (2011) 328–337, arXiv:1012.4035 [nucl-ex].

[59] J.-Y. Ollitrault, "Relativistic hydrodynamics for heavy-ion collisions," *Eur. J. Phys.* **29** (2008) 275–302, arXiv:0708.2433 [nucl-th].

[60] R. Baier, P. Romatschke and U. A. Wiedemann, "Dissipative hydrodynamics and heavy ion collisions," *Phys. Rev. C* **73** (2006) 064903, arXiv:hep-ph/0602249 [hep-ph].

[61] R. S. Bhalerao and S. Gupta, "Aspects of causal viscous hydrodynamics," *Phys. Rev. C* **77** (2008) 014902, arXiv:0706.3428 [nucl-th].

[62] F. Cooper and G. Frye, "Single-particle distribution in the hydrodynamic and statistical thermodynamic models of multiparticle production," *Phys. Rev. D* **10** (1974) 186–189.

[63] M. L. Miller, K. Reygers, S. J. Sanders and P. Steinberg, "Glauber Modeling in High-Energy Nuclear Collisions," *Annual Review of Nuclear and Particle Science* **57** no. 1, (2007) 205–243.

[64] R. Snellings, "Elliptic Flow: A Brief Review," *New J. Phys.* **13** (2011) 055008, arXiv:1102.3010 [nucl-ex].

[65] B. Alver, M. Baker, C. Loizides and P. Steinberg, "The PHOBOS Glauber Monte Carlo," arXiv:0805.4411 [nucl-ex].

[66] J. E. Elias et al., "Projectile Dependence of Multiparticle Production in Hadron-Nucleus Interactions at 100 GeV/c," *Phys. Rev. Lett.* **41** (1978) 285–287.

[67] **PHOBOS** Collaboration, B. B. Back et al., "Centrality and energy dependence of charged-particle multiplicities in heavy ion collisions in the context of elementary reactions," *Phys. Rev. C* **74** (2006) 021902.

[68] **PHOBOS** Collaboration, B. B. Back et al., "Charged-particle pseudorapidity distributions in Au+Au collisions at $\sqrt{s_{NN}} = 62.4$ GeV," *Phys. Rev. C* **74** (2006) 021901.

[69] **STAR** Collaboration, B. I. Abelev et al., "Systematic Measurements of Identified Particle Spectra in pp, $d+\mathrm{Au}$, and $\mathrm{Au}+\mathrm{Au}$ Collisions from STAR," *Phys. Rev. C* **79** (2009) 034909, arXiv:0808.2041 [nucl-ex].

[70] **ALICE** Collaboration, K. Aamodt et al., "Centrality Dependence of the Charged-Particle Multiplicity Density at Midrapidity in Pb-Pb Collisions at $\sqrt{s_{\mathrm{NN}}} = 2.76$ TeV," *Phys. Rev. Lett.* **106** (2011) 032301.

[71] P. Braun-Munzinger and J. Wambach, "The Phase Diagram of Strongly-Interacting Matter," *Rev. Mod. Phys.* **81** (2009) 1031–1050, arXiv:0801.4256 [hep-ph].

[72] A. Andronic, P. Braun-Munzinger, K. Redlich and J. Stachel, "Hadron yields, the chemical freeze-out and the QCD phase diagram," *J. Phys. Conf. Ser.* **779** no. 1, (2017) 012012, arXiv:1611.01347 [nucl-th].

[73] **ALICE** Collaboration, B. Abelev et al., "Pion, Kaon, and Proton Production in Central Pb-Pb Collisions at $\sqrt{s_{\rm NN}}$=2.76 TeV," *Phys. Rev. Lett.* **109** (2012) 252301.

[74] A. Andronic et al., "Thermal description of hadron production in e^+e^- collisions revisited," *Phys. Lett. B* **675** (2009) 312–318, arXiv:0804.4132 [hep-ph].

[75] S. Das, D. Mishra, S. Chatterjee and B. Mohanty, "Freeze-out conditions in proton-proton collisions at the highest energies available at the BNL Relativistic Heavy Ion Collider and the CERN Large Hadron Collider," *Phys. Rev. C* **95** no. 1, (2017) 014912, arXiv:1605.07748 [nucl-th].

[76] A. Andronic, P. Braun-Munzinger, K. Redlich and J. Stachel, "Decoding the phase structure of QCD via particle production at high energy," *Nature* **561** no. 7723, (2018) 321–330, arXiv:1710.09425 [nucl-th].

[77] E. Schnedermann, J. Sollfrank and U. Heinz, "Thermal phenomenology of hadrons from 200A GeV S+S collisions," *Phys. Rev. C* **48** (1993) 2462–2475.

[78] **ALICE** Collaboration, B. Abelev et al., "Centrality dependence of π, K, p production in Pb-Pb collisions at $\sqrt{s_{NN}}$ = 2.76 TeV," *Phys. Rev. C* **88** (2013) 044910, arXiv:1303.0737 [hep-ex].

[79] J. Sollfrank, P. Koch and U. W. Heinz, "Is there a low p(T) 'anomaly' in the pion momentum spectra from relativistic nuclear collisions?," *Z. Phys. C* **52** (1991) 593–610.

[80] **ALICE** Collaboration, J. Adam et al., "Production of light nuclei and anti-nuclei in pp and Pb-Pb collisions at energies available at the CERN Large Hadron Collider," *Phys. Rev. C* **93** no. 2, (2016) 024917, arXiv:1506.08951 [nucl-ex].

[81] S. A. Voloshin, A. M. Poskanzer and R. Snellings, "Collective phenomena in non-central nuclear collisions," *Landolt-Bornstein* **23** (2010) 293–333, arXiv:0809.2949 [nucl-ex].

[82] **ALICE** Collaboration, B. Abelev et al., "D meson elliptic flow in non-central Pb-Pb collisions at $\sqrt{s_{\rm NN}}$ = 2.76TeV," *Phys. Rev. Lett.* **111** (2013) 102301, arXiv:1305.2707 [nucl-ex].

[83] D. Teaney, "Effect of shear viscosity on spectra, elliptic flow, and Hanbury Brown–Twiss radii," *Phys. Rev. C* **68** (2003) 034913.

[84] J. Noronha-Hostler, B. Betz, J. Noronha and M. Gyulassy, "Event-by-Event Hydrodynamics + Jet Energy Loss: A Solution to the $R_{\rm AA} \otimes v_2$ Puzzle," *Physical Review Letters* **116** (2016) .

[85] J. Bjorken, "Energy Loss of Energetic Partons in Quark - Gluon Plasma: Possible Extinction of High $p_{\rm T}$ Jets in Hadron - Hadron Collisions," *FERMILAB-PUB-82-059-THY* (1982) .

[86] **STAR** Collaboration, C. Adler et al., "Disappearance of Back-To-Back High-p_T Hadron Correlations in Central Au + Au Collisions at $\sqrt{s_{NN}} = 200$ GeV," *Phys. Rev. Lett.* **90** (2003) 082302.

[87] B. G. Zakharov, "Parton energy loss in an expanding quark-gluon plasma: Radiative versus collisional," *JETP Lett.* **86** (2007) 444–450, arXiv:0708.0816 [hep-ph].

[88] **ALICE** Collaboration, B. B. Abelev et al., "Transverse momentum dependence of inclusive primary charged-particle production in p-Pb collisions at $\sqrt{s_{\rm NN}} = 5.02$ TeV," *Eur. Phys. J. C* **74** no. 9, (2014) 3054, arXiv:1405.2737 [nucl-ex].

[89] **ALICE** Collaboration, S. Acharya et al., "Analysis of the apparent nuclear modification in peripheral Pb-Pb collisions at 5.02 TeV," arXiv:1805.05212 [nucl-ex].

[90] **ALICE** Collaboration, B. Abelev et al., "Centrality Dependence of Charged Particle Production at Large Transverse Momentum in Pb–Pb Collisions at $\sqrt{s_{\rm NN}} = 2.76$ TeV," *Phys. Lett. B* **720** (2013) 52–62, arXiv:1208.2711 [hep-ex].

[91] **JET** Collaboration, K. M. Burke et al., "Extracting the jet transport coefficient from jet quenching in high-energy heavy-ion collisions," *Phys. Rev. C* **90** no. 1, (2014) 014909, arXiv:1312.5003 [nucl-th].

[92] Z. Liu, H. Zhang, B.-W. Zhang and E. Wang, "Extracting jet quenching parameters from large pT hadron suppression at RHIC/LHC," *Nuclear and Particle Physics Proceedings* **289-290** (2017) 425 – 428. 8th International Conference on Hard and Electromagnetic Probes of High Energy Nuclear Collisions.

[93] **Particle Data Group** Collaboration, M. Tanabashi et al., "The Review of Particle Physics," *Phys. Rev. D* **98** (2018) .

[94] E. Eichten et al., "Spectrum of Charmed Quark-Antiquark Bound States," *Phys. Rev. Lett.* **34** (1975) 369–372.

[95] C. Ayala, P. Gonzalez and V. Vento, "Heavy quark potential from QCD-related effective coupling," *J. Phys. G* **43** no. 12, (2016) 125002, arXiv:1509.01382 [hep-ph].

[96] N. Brambilla and S. Eidelman, "QCD and strongly coupled gauge theories: challenges and perspectives," *The European Physical Journal C* **74** no. 10, (2014) 2981.

[97] **LHCb** Collaboration, R. Aaij et al., "Determination of the X(3872) meson quantum numbers," *Phys. Rev. Lett.* **110** (2013) 222001, arXiv:1302.6269 [hep-ex].

[98] **LHCb** Collaboration, R. Aaij et al., "Observation of $J/\psi p$ Resonances Consistent with Pentaquark States in $\Lambda_b^0 \to J/\psi K^- p$ Decays," *Phys. Rev. Lett.* **115** (2015) 072001, arXiv:1507.03414 [hep-ex].

[99] **Belle** Collaboration, C. P. Shen et al., "Search for XYZ states in $\Upsilon(1S)$ inclusive decays," *Phys. Rev. D* **93** no. 11, (2016) 112013, arXiv:1605.00990 [hep-ex].

[100] **CDF** Collaboration, D. Acosta et al., "Measurement of the J/ψ meson and b-hadron production cross sections in $p\overline{p}$ collisions at $\sqrt{s} = 1960$ GeV," *Phys. Rev. D* **71** (2005) 032001.

[101] **ALICE** Collaboration, B. Abelev et al., "Measurement of prompt J/ψ and beauty hadron production cross sections at mid-rapidity in pp collisions at $\sqrt{s} = 7$ TeV," *JHEP* **11** (2012) 065, arXiv:1205.5880 [hep-ex].

[102] **ATLAS** Collaboration, G. Aad et al., "Measurement of the differential cross-sections of inclusive, prompt and non-prompt J/ψ production in proton-proton collisions at $\sqrt{s} = 7$ TeV," *Nucl. Phys. B* **850** (2011) 387–444, arXiv:1104.3038 [hep-ex].

[103] **CMS** Collaboration, S. Chatrchyan et al., "J/ψ and $\psi(2S)$ production in pp collisions at $\sqrt{s} = 7$ TeV," *JHEP* **02** (2012) 011, arXiv:1111.1557 [hep-ex].

[104] **CDF** Collaboration, F. Abe et al., "Production of J/ψ Mesons from χ_c Meson Decays in $p\overline{p}$ Collisions at $\sqrt{s} = 1.8$ TeV," *Phys. Rev. Lett.* **79** (1997) 578–583.

[105] **LHCb** Collaboration, R. Aaij et al., "Measurement of the ratio of prompt χ_c to J/ψ production in pp collisions at $\sqrt{s} = 7$ TeV," *Phys. Lett. B* **718** (2012) 431–440, arXiv:1204.1462 [hep-ex].

[106] **ALICE** Collaboration, B. B. Abelev et al., "Measurement of quarkonium production at forward rapidity in pp collisions at $\sqrt{s} = 7$ TeV," *Eur. Phys. J. C* **74** no. 8, (2014) 2974, arXiv:1403.3648 [nucl-ex].

[107] M. B. Einhorn and S. D. Ellis, "Hadronic production of the new resonances: Probing gluon distributions," *Phys. Rev. D* **12** (1975) 2007–2014.

[108] S. D. Ellis, M. B. Einhorn and C. Quigg, "Comment on Hadronic Production of Psions," *Phys. Rev. Lett.* **36** (1976) 1263–1266.

[109] H. Fritzsch, "Producing heavy quark flavors in hadronic collisions—' A test of quantum chromodynamics," *Physics Letters B* **67** no. 2, (1977) 217 – 221.

[110] F. Halzen, "CVC for gluons and hadroproduction of quark flavours," *Physics Letters B* **69** no. 1, (1977) 105 – 108.

[111] Y.-Q. Ma and R. Vogt, "Quarkonium Production in an Improved Color Evaporation Model," *Phys. Rev. D* **94** no. 11, (2016) 114029, arXiv:1609.06042 [hep-ph].

[112] G. T. Bodwin, E. Braaten and G. P. Lepage, "Rigorous QCD analysis of inclusive annihilation and production of heavy quarkonium," *Phys. Rev. D* **51** (1995) 1125–1171, arXiv:hep-ph/9407339 [hep-ph]. [Erratum: Phys. Rev.D55,5853(1997)].

[113] G. C. Nayak, "Proof of NRQCD factorization at all orders in the coupling constant in heavy quarkonium production," *The European Physical Journal C* **76** no. 8, (2016) 448.

[114] **ALICE** Collaboration, S. Acharya et al., "Energy dependence of forward-rapidity J/ψ and ψ(2S) production in pp collisions at the LHC," *Eur. Phys. J. C* **77** no. 6, (2017) 392, arXiv:1702.00557 [hep-ex].

[115] **LHCb** Collaboration, R. Aaij et al., "Measurement of forward J/ψ production cross-sections in pp collisions at $\sqrt{s} = 13$ TeV," *JHEP* **10** (2015) 172, arXiv:1509.00771 [hep-ex]. [Erratum: JHEP05,063(2017)].

[116] **ATLAS** Collaboration, G. Aad et al., "Measurement of the differential cross-sections of prompt and non-prompt production of J/ψ and ψ(2S) in pp collisions at $\sqrt{s} = 7$ and 8 TeV with the ATLAS detector," *Eur. Phys. J. C* **76** no. 5, (2016) 283, arXiv:1512.03657 [hep-ex].

[117] **ALICE** Collaboration, S. Acharya et al., "Measurement of the inclusive J/ ψ polarization at forward rapidity in pp collisions at $\sqrt{s} = 8$ TeV," *Eur. Phys. J. C* **78** no. 7, (2018) 562, arXiv:1805.04374 [hep-ex].

[118] **LHCb** Collaboration, R. Aaij et al., "Measurement of J/ψ polarization in pp collisions at $\sqrt{s} = 7$ TeV," *Eur. Phys. J. C* **73** no. 11, (2013) 2631, arXiv:1307.6379 [hep-ex].

[119] **LHCb** Collaboration, R. Aaij et al., "Study of J/ψ Production in Jets," *Phys. Rev. Lett.* **118** no. 19, (2017) 192001, arXiv:1701.05116 [hep-ex].

[120] R. Venugopalan, "The Color glass condensate: An Overview," *Eur. Phys. J. C* **43** (2005) 337–344, arXiv:hep-ph/0502190 [hep-ph].

[121] F. Arleo and S. Peigné, "Quarkonium suppression in heavy-ion collisions from coherent energy loss in cold nuclear matter," *JHEP* **10** (2014) 073, arXiv:1407.5054 [hep-ph].

[122] Z.-B. Kang and J.-W. Qiu, "Transverse momentum broadening of vector boson production in high energy nuclear collisions," *Phys. Rev. D* **77** (2008) 114027, arXiv:0802.2904 [hep-ph].

[123] Z.-B. Kang and J.-W. Qiu, "Nuclear modification of vector boson production in proton-lead collisions at the LHC," *Phys. Lett. B* **721** (2013) 277–283, arXiv:1212.6541 [hep-ph].

[124] K. J. Eskola, H. Paukkunen and C. A. Salgado, "EPS09: A New Generation of NLO and LO Nuclear Parton Distribution Functions," *JHEP* **04** (2009) 065, arXiv:0902.4154 [hep-ph].

[125] D. de Florian, R. Sassot, P. Zurita and M. Stratmann, "Global analysis of nuclear parton distributions," *Phys. Rev. D* **85** (2012) 074028.

[126] K. Kovařík et al., "nCTEQ15: Global analysis of nuclear parton distributions with uncertainties in the CTEQ framework," *Phys. Rev. D* **93** (2016) 085037.

[127] K. J. Eskola, P. Paakkinen, H. Paukkunen and C. A. Salgado, "EPPS16: Nuclear parton distributions with LHC data," *Eur. Phys. J. C* **77** no. 3, (2017) 163, arXiv:1612.05741 [hep-ph].

[128] N. Armesto, "Nuclear shadowing," *J. Phys. G* **32** (2006) R367–R394, arXiv:hep-ph/0604108 [hep-ph].

[129] K. Rith, "Present Status of the EMC effect," *Subnucl. Ser.* **51** (2015) 431–449, arXiv:1402.5000 [hep-ex].

[130] **ALICE** Collaboration, B. B. Abelev et al., "J/ψ production and nuclear effects in p-Pb collisions at $\sqrt{s_{NN}} = 5.02$ TeV," *JHEP* **02** (2014) 073, arXiv:1308.6726 [nucl-ex].

[131] **ALICE** Collaboration, J. Adam et al., "Rapidity and transverse-momentum dependence of the inclusive J/ψ nuclear modification factor in p-Pb collisions at $\sqrt{s_{NN}} = 5.02$ TeV," *JHEP* **06** (2015) 055, arXiv:1503.07179 [nucl-ex].

[132] **ALICE** Collaboration, J. Adam et al., "Centrality dependence of inclusive J/ψ production in p-Pb collisions at $\sqrt{s_{\rm NN}} = 5.02$ TeV," *JHEP* **11** (2015) 127, arXiv:1506.08808 [nucl-ex].

[133] T. Matsui and H. Satz, "J/ψ suppression by quark-gluon plasma formation," *Physics Letters B* **178** no. 4, (1986) 416 – 422.

[134] H. Satz, "Colour deconfinement and quarkonium binding," *J. Phys. G* **32** (2006) R25, arXiv:hep-ph/0512217 [hep-ph].

[135] A. Mocsy, "Potential Models for Quarkonia," *Eur. Phys. J. C* **61** (2009) 705–710, arXiv:0811.0337 [hep-ph].

[136] L. Kluberg and H. Satz, "Color Deconfinement and Charmonium Production in Nuclear Collisions," arXiv:0901.3831 [hep-ph].

[137] P. Braun-Munzinger and J. Stachel, "(Non)thermal aspects of charmonium production and a new look at J/ψ suppression," *Phys. Lett. B* **490** (2000) 196–202, arXiv:nucl-th/0007059 [nucl-th].

[138] R. L. Thews, M. Schroedter and J. Rafelski, "Enhanced J/ψ production in deconfined quark matter," *Phys. Rev. C* **63** (2001) 054905, arXiv:hep-ph/0007323 [hep-ph].

[139] A. Andronic, P. Braun-Munzinger, K. Redlich and J. Stachel, "Statistical hadronization of heavy quarks in ultra-relativistic nucleus-nucleus collisions," *Nucl. Phys. A* **789** (2007) 334–356, arXiv:nucl-th/0611023 [nucl-th].

[140] P. Braun-Munzinger and J. Stachel, "Charmonium from Statistical Hadronization of Heavy Quarks: A Probe for Deconfinement in the Quark-Gluon Plasma," *Landolt-Bornstein* **23** (2010) 424, arXiv:0901.2500 [nucl-th].

[141] A. Andronic, P. Braun-Munzinger, K. Redlich and J. Stachel, "The thermal model on the verge of the ultimate test: particle production in Pb-Pb collisions at the LHC," *J. Phys. G* **38** (2011) 124081, arXiv:1106.6321 [nucl-th].

[142] P. Braun-Munzinger and J. Stachel, "The quest for the quark-gluon plasma," *Nature* **448** (2007) 302–309.

[143] X. Zhao and R. Rapp, "Medium Modifications and Production of Charmonia at LHC," *Nucl. Phys. A* **859** (2011) 114–125, arXiv:1102.2194 [hep-ph].

[144] X. Du and R. Rapp, "Sequential Regeneration of Charmonia in Heavy-Ion Collisions," *Nucl. Phys. A* **943** (2015) 147–158, arXiv:1504.00670 [hep-ph].

[145] K. Zhou, N. Xu, Z. Xu and P. Zhuang, "Medium effects on charmonium production at ultrarelativistic energies available at the CERN Large Hadron Collider," *Phys. Rev. C* **89** no. 5, (2014) 054911, arXiv:1401.5845 [nucl-th].

[146] Z. Tang, N. Xu, K. Zhou and P. Zhuang, "Charmonium Transverse Momentum Distribution in High Energy Nuclear Collisions," *J. Phys. G* **41** no. 12, (2014) 124006, arXiv:1409.5559 [nucl-th].

[147] R. Rapp and X. Du, "Theoretical Perspective on Quarkonia from SPS via RHIC to LHC," *Nucl. Phys. A* **967** (2017) 216–224, arXiv:1704.07923 [hep-ph].

[148] A. Capella, A. Kaidalov, A. Kouider Akil and C. Gerschel, "J/ψ and ψ' suppression in heavy ion collisions," *Phys. Lett. B* **393** (1997) 431–436, arXiv:hep-ph/9607265 [hep-ph].

[149] N. Armesto and A. Capella, "A quantitative reanalysis of charmonium suppression in nuclear collisions," *Physics Letters B* **430** no. 1, (1998) 23 – 31.

[150] E. G. Ferreiro, "Charmonium dissociation and recombination at LHC: Revisiting comovers," *Phys. Lett. B* **731** (2014) 57–63, arXiv:1210.3209 [hep-ph].

[151] A. Andronic, "An overview of the experimental study of quark-gluon matter in high-energy nucleus-nucleus collisions," *Int. J. Mod. Phys. A* **29** (2014) 1430047, arXiv:1407.5003 [nucl-ex].

[152] **ALICE** Collaboration, J. Adam et al., "Inclusive, prompt and non-prompt J/ψ production at mid-rapidity in Pb-Pb collisions at $\sqrt{s_{\rm NN}} = 2.76$ TeV," *JHEP* **07** (2015) 051, arXiv:1504.07151 [nucl-ex].

[153] C. A. Bertulani, S. R. Klein and J. Nystrand, "Physics of ultra-peripheral nuclear collisions," *Ann. Rev. Nucl. Part. Sci.* **55** (2005) 271–310, arXiv:nucl-ex/0502005 [nucl-ex].

[154] C. F. v. Weizsäcker, "Ausstrahlung bei Stößen sehr schneller Elektronen," *Zeitschrift für Physik* **88** no. 9, (1934) 612–625.

[155] E. J. Williams, "Nature of the High Energy Particles of Penetrating Radiation and Status of Ionization and Radiation Formulae," *Phys. Rev.* **45** (1934) 729–730.

[156] A. J. Baltz, "The Physics of Ultraperipheral Collisions at the LHC," *Phys. Rept.* **458** (2008) 1–171, arXiv:0706.3356 [nucl-ex].

[157] **CMS** Collaboration, V. Khachatryan et al., "Coherent J/ψ photoproduction in ultra-peripheral PbPb collisions at $\sqrt{s_{NN}} = 2.76$ TeV with the CMS experiment," *Phys. Lett. B* **772** (2017) 489–511, arXiv:1605.06966 [nucl-ex].

[158] **ALICE** Collaboration, J. Nystrand, "Photonuclear vector meson production in ultra-peripheral Pb-Pb collisions studied by the ALICE experiment at the LHC," arXiv:1303.2009 [nucl-ex]. [PoSConfinementX,199(2012)].

[159] **ALICE** Collaboration, E. Abbas et al., "Charmonium and e^+e^- pair photoproduction at mid-rapidity in ultra-peripheral Pb-Pb collisions at $\sqrt{s_{\rm NN}}$=2.76 TeV," *Eur. Phys. J. C* **73** no. 11, (2013) 2617, arXiv:1305.1467 [nucl-ex].

[160] **ALICE** Collaboration, J. Adam et al., "Measurement of an excess in the yield of J/ψ at very low $p_{\rm T}$ in Pb-Pb collisions at $\sqrt{s_{\rm NN}} = 2.76$ TeV," *Phys. Rev. Lett.* **116** no. 22, (2016) 222301, arXiv:1509.08802 [nucl-ex].

[161] L. Evans and P. Bryant, "LHC Machine," *Journal of Instrumentation* **3** no. 08, (2008) S08001.

[162] M. Benedikt et al., "LHC Design Report. 3. The LHC injector chain," Tech. Rep. CERN-2004-003-V-3, CERN-2004-003, 2004.

[163] E. Mobs, "The CERN accelerator complex. Complexe des accélérateurs du CERN," 2016. https://cds.cern.ch/record/2197559. (accessed on July 16th 2018).

[164] **ATLAS** Collaboration, G. Aad et al., "The ATLAS Experiment at the CERN Large Hadron Collider," *JINST* **3** (2008) S08003.

[165] **CMS** Collaboration, S. Chatrchyan et al., "The CMS Experiment at the CERN LHC," *JINST* **3** (2008) S08004.

[166] **LHCb** Collaboration, S. Amato et al., "LHCb technical proposal," Tech. Rep. CERN-LHCC-98-04, CERN-LHCC-98-4, CERN-LHCC-P-4, 1998.

[167] **LHCb** Collaboration, "LHCb technical design report: Reoptimized detector design and performance," Tech. Rep. CERN-LHCC-2003-030, 2003.

[168] **ALICE** Collaboration, K. Aamodt et al., "The ALICE experiment at the CERN LHC," *JINST* **3** (2008) S08002.

[169] **LHCf** Collaboration, O. Adriani et al., "Technical design report of the LHCf experiment: Measurement of photons and neutral pions in the very forward region of LHC," Tech. Rep. CERN-LHCC-2006-004, 2006.

[170] **MoEDAL** Collaboration, J. Pinfold et al., "Technical Design Report of the MoEDAL Experiment," Tech. Rep. CERN-LHCC-2009-006, MoEDAL-TDR-001, 2009.

[171] **TOTEM** Collaboration, V. Berardi et al., "TOTEM: Technical design report. Total cross section, elastic scattering and diffraction dissociation at the Large Hadron Collider at CERN," Tech. Rep. CERN-LHCC-2004-002, TOTEM-TDR-001, 2004.

[172] **ALICE** Collaboration, B. B. Abelev et al., "Performance of the ALICE Experiment at the CERN LHC," *Int. J. Mod. Phys. A* **29** (2014) 1430044, arXiv:1402.4476 [nucl-ex].

[173] **ALICE** Collaboration, E. Botta, "Particle identification performance at ALICE," in *5th Large Hadron Collider Physics Conference (LHCP 2017) Shanghai, China, May 15-20, 2017*. 2017. arXiv:1709.00288 [nucl-ex].

[174] **ALICE** Collaboration, J. Adam et al., "Enhanced production of multi-strange hadrons in high-multiplicity proton-proton collisions," *Nature Phys.* **13** (2017) 535–539, arXiv:1606.07424 [nucl-ex].

[175] J. Alme et al., "The ALICE TPC, a large 3-dimensional tracking device with fast readout for ultra-high multiplicity events," *Nuclear Instruments and Methods in Physics Research Section A: Accelerators, Spectrometers, Detectors and Associated Equipment* **622** no. 1, (2010) 316 – 367.

[176] A. Kalweit, *Production of light flavor hadrons and anti-nuclei at the LHC*. Doctoral thesis, TU Darmstadt, 2012.

[177] M. Arslandok, *Event-by-Event Identified Particle Ratio Fluctuations in Pb–Pb Collisions with ALICE*. Doctoral thesis, Universität Frankfurt, 2017.

[178] C. Lippmann, "A continuous-readout TPC for the ALICE upgrade." EPS Conference on High Energy Physics, 8th July 2017. https://indico.cern.ch/event/466934/contributions/2613254/attachments/1487589/2310867/EPS_ALICE_TPC_170708.pdf. (accessed on July 19th 2018).

[179] A. u. Rehman, "Performance of the ALICE TPC Readout Electronics," in *2011 IEEE Nuclear Science Symposium Conference Record*, pp. 1014–1018. 2011.

[180] C. Lippmann, "Particle identification," *Nucl. Instrum. Meth. A* **666** (2012) 148–172, arXiv:1101.3276 [hep-ex].

[181] **Particle Data Group** Collaboration, C. Amsler et al., "The Review of Particle Physics," *Physics Letters B* **667** (2008 and 2009 partial update for the 2010 edition) .

[182] B. Hess, *Particle Identification in Jets and High-Multiplicity pp Events with the ALICE TPC*. Doctoral thesis, Universität Tübingen, 2015.

[183] **ALICE** Collaboration, P. Cortese, "ALICE transition-radiation detector," Tech. Rep. ALICE-TDR-9, CERN-LHCC-2001-021, LYCEN-2001-97, 2001.

[184] "The ALICE Transition Radiation Detector: Construction, operation, and performance," *Nuclear Instruments and Methods in Physics Research Section A: Accelerators, Spectrometers, Detectors and Associated Equipment* **881** (2018) 88 – 127.

[185] **ALICE** Collaboration, "Centrality determination in heavy ion collisions," 2018. https://cds.cern.ch/record/2636623. ALICE-PUBLIC-2018-011.

[186] "ROOT a Data analysis Framework." https://root.cern.ch/.

[187] "ALICE Software Framework." https://github.com/alisw/AliRoot.

[188] "ALICE Analysis Repository." https://github.com/alisw/AliPhysics.

[189] M. Winn, "Prospects for quarkonium measurements in p-A and A-A collisions at the LHC," *Few Body Syst.* **58** no. 2, (2017) 53, arXiv:1609.01135 [hep-ex].

[190] M. Winn, "Heavy flavour production in proton–lead and lead–lead collisions with LHCb," *Nucl. Phys. A* **967** (2017) 596–599, arXiv:1704.04217 [nucl-ex].

[191] M. Gyulassy and X.-N. Wang, "HIJING 1.0: A Monte Carlo program for parton and particle production in high-energy hadronic and nuclear collisions," *Comput. Phys. Commun.* **83** (1994) 307, arXiv:nucl-th/9502021 [nucl-th].

[192] R. Brun et al., "GEANT Detector Description and Simulation Tool," Tech. Rep. CERN-W5013, CERN-W-5013, W5013, W-5013, 1994.

[193] T. Sjostrand, S. Mrenna and P. Z. Skands, "PYTHIA 6.4 Physics and Manual," *JHEP* **05** (2006) 026, arXiv:hep-ph/0603175 [hep-ph].

[194] F. Bossu et al., "Phenomenological interpolation of the inclusive J/psi cross section to proton-proton collisions at 2.76 TeV and 5.5 TeV," arXiv:1103.2394 [nucl-ex].

[195] Z. Zhou. Doctoral thesis, University of Bergen. In preparation.

[196] D. J. Lange, "The EvtGen particle decay simulation package," *Nuclear Instruments and Methods in Physics Research Section A: Accelerators, Spectrometers, Detectors and Associated Equipment* **462** no. 1, (2001) 152 – 155. BEAUTY2000, Proceedings of the 7th Int. Conf. on B-Physics at Hadron Machines.

[197] E. Barberio and Z. Was, "PHOTOS - a universal Monte Carlo for QED radiative corrections: version 2.0," *Computer Physics Communications* **79** no. 2, (1994) 291 – 308.

[198] I. Arsene. Private communication.

[199] **ALICE** Collaboration, K. Aamodt et al., "Rapidity and transverse momentum dependence of inclusive J/ψ production in pp collisions at $\sqrt{s} = 7$ TeV," *Phys. Lett. B* **704** (2011) 442–455, arXiv:1105.0380 [hep-ex]. [Erratum: Phys. Lett.B718,692(2012)].

[200] **CMS** Collaboration, S. Chatrchyan et al., "Measurement of the prompt J/ψ and ψ(2S) polarizations in pp collisions at $\sqrt{s} = 7$ TeV," *Phys. Lett. B* **727** (2013) 381–402, arXiv:1307.6070 [hep-ex].

[201] **CDF** Collaboration, A. Abulencia et al., "Polarizations of J/ψ and $\psi(2S)$ Mesons Produced in $p\bar{p}$ Collisions at $\sqrt{s} = 1.96$ TeV," *Phys. Rev. Lett.* **99** (2007) 132001.

[202] R. Arnaldi. Private communication.

[203] R. Barlow, "Systematic errors: Facts and fictions," in *Advanced Statistical Techniques in Particle Physics. Proceedings, Conference, Durham, UK, March 18-22, 2002*, pp. 134–144. 2002. arXiv:hep-ex/0207026 [hep-ex].

[204] G. Lafferty and T. Wyatt, "Where to stick your data points: The treatment of measurements within wide bins," *Nuclear Instruments and Methods in Physics Research Section A: Accelerators, Spectrometers, Detectors and Associated Equipment* **355** no. 2, (1995) 541 – 547.

[205] J. Book, J/ψ *Production in Pb–Pb Collisions with ALICE at the LHC*. Doctoral thesis, Universität Frankfurt, 2014.

[206] M. K. Köhler. Private communication.

[207] N. Borghini and J. Y. Ollitrault, "Azimuthally sensitive correlations in nucleus-nucleus collisions," *Phys. Rev. C* **70** (2004) 064905, arXiv:nucl-th/0407041 [nucl-th].

[208] **ALICE** Collaboration, S. Acharya et al., "J/ψ elliptic flow in Pb-Pb collisions at $\sqrt{s_{\rm NN}} = 5.02$ TeV," *Phys. Rev. Lett.* **119** no. 24, (2017) 242301, arXiv:1709.05260 [nucl-ex].

[209] **ALICE** Collaboration, B. Abelev et al., "Inclusive J/ψ production in pp collisions at $\sqrt{s} = 2.76$ TeV," *Phys. Lett. B* **718** (2012) 295–306, arXiv:1203.3641 [hep-ex]. [Erratum: Phys. Lett.B748,472(2015)].

[210] **ALICE** Collaboration, J. Adam et al., "Differential studies of inclusive J/ψ and ψ(2S) production at forward rapidity in Pb-Pb collisions at $\sqrt{s_{\rm NN}} = 2.76$ TeV," *JHEP* **05** (2016) 179, arXiv:1506.08804 [nucl-ex].

[211] M. Winn, *Inclusive* J/ψ *production at mid-rapidity in p–Pb collisions at* $\sqrt{s_{\rm NN}}$ *= 5.02 TeV*. Doctoral thesis, Universität Heidelberg, 2016.

[212] **PHENIX** Collaboration, A. Adare et al., "Ground and excited charmonium state production in $p+p$ collisions at $\sqrt{s} = 200$ GeV," *Phys. Rev. D* **85** (2012) 092004, arXiv:1105.1966 [hep-ex].

[213] T. Bustamante, *Inclusive* J/ψ *production at mid-rapidity in Pb–Pb collisions at* $\sqrt{s_{\rm NN}}$ *= 5.02 TeV*. Doctoral thesis, Universität Heidelberg, 2018.

[214] "ALICE public preliminary figures." http://alice-figure.web.cern.ch/preliminary_fig_pub. (accessed on November 24th 2018).

[215] A. Andronic, P. Braun-Munzinger, K. Redlich and J. Stachel, "Hadron yields, the chemical freeze-out and the QCD phase diagram," *J. Phys. Conf. Ser.* **779** no. 1, (2017) 012012, arXiv:1611.01347 [nucl-th].

[216] M. Cacciari et al., "Theoretical predictions for charm and bottom production at the LHC," *JHEP* **10** (2012) 137, arXiv:1205.6344 [hep-ph].

[217] M. Cacciari, M. L. Mangano and P. Nason, "Gluon PDF constraints from the ratio of forward heavy-quark production at the LHC at $\sqrt{S} = 7$ and 13 TeV," *Eur. Phys. J. C* **75** no. 12, (2015) 610, arXiv:1507.06197 [hep-ph].

[218] Y.-Q. Ma and R. Venugopalan, "Comprehensive Description of J/ψ Production in Proton-Proton Collisions at Collider Energies," *Phys. Rev. Lett.* **113** no. 19, (2014) 192301, arXiv:1408.4075 [hep-ph].

[219] Y.-Q. Ma, K. Wang and K.-T. Chao, "$J/\psi(\psi')$ production at the Tevatron and LHC at $\mathcal{O}(\alpha_s^4 v^4)$ in nonrelativistic QCD," *Phys. Rev. Lett.* **106** (2011) 042002, arXiv:1009.3655 [hep-ph].

[220] M. Butenschoen and B. A. Kniehl, "Reconciling J/ψ production at HERA, RHIC, Tevatron, and LHC with NRQCD factorization at next-to-leading order," *Phys. Rev. Lett.* **106** (2011) 022003, arXiv:1009.5662 [hep-ph].

[221] **ALICE** Collaboration, S. Acharya et al., "Measurement of D-meson production at mid-rapidity in pp collisions at $\sqrt{s} = 7$ TeV," *Eur. Phys. J. C* **77** no. 8, (2017) 550, arXiv:1702.00766 [hep-ex].

[222] **ALICE** Collaboration, "Preliminary Physics Summary: Measurement of $\rm D^0$, $\rm D^+$, $\rm D^{*+}$ and $\rm D_s^+$ production in pp collisions at $\sqrt{s} = 5.02$ TeV with ALICE," 2018. https://cds.cern.ch/record/2317187.

[223] T. Sjöstrand et al., "An Introduction to PYTHIA 8.2," *Comput. Phys. Commun.* **191** (2015) 159–177, arXiv:1410.3012 [hep-ph].

[224] A. Andronic, P. Braun-Munzinger, M. K. Koehler and J. Stachel, "Testing charm quark thermalisation within the Statistical Hadronisation Model," arXiv:1807.01236 [nucl-th].

[225] "ALICE luminosity determination for pp collisions at $\sqrt{s} = 5$ TeV using 2017 data.". Public note, in preparation.

[226] **ALICE** Collaboration, S. Acharya et al., "Transverse momentum spectra and nuclear modification factors of charged particles in pp, p-Pb and Pb-Pb collisions at the LHC," arXiv:1802.09145 [nucl-ex].

[227] **ALICE** Collaboration, S. Acharya et al., "Measurement of D^0, D^+, D^{*+} and D_s^+ production in Pb-Pb collisions at $\sqrt{s_{\mathrm{NN}}} = 5.02$ TeV," *Submitted to: JHEP* (2018) , arXiv:1804.09083 [nucl-ex].

[228] **ATLAS** Collaboration, M. Aaboud et al., "Prompt and non-prompt J/ψ and $\psi(2\mathrm{S})$ suppression at high transverse momentum in 5.02 TeV Pb+Pb collisions with the ATLAS experiment," *Eur. Phys. J. C* **78** no. 9, (2018) 762, arXiv:1805.04077 [nucl-ex].

[229] **ALICE** Collaboration, J. Adam et al., "J/ψ suppression at forward rapidity in Pb-Pb collisions at $\sqrt{s_{\mathrm{NN}} = 5.02}$ TeV," *Phys. Lett. B* **766** (2017) 212–224, arXiv:1606.08197 [nucl-ex].

[230] O. Drapier, *Étude des disitributions en impulsion transverse des dimuons produits dans les collisions noyau-noyau auprès du SPS du CERN.* Habilitation thesis, Université Claude Bernard LYON I, 1998.

[231] R. Rapp. Private communication.

[232] **NA50** Collaboration, M. Abreu et al., "Transverse momentum distributions of J/ψ, ψ', Drell–Yan and continuum dimuons produced in Pb–Pb interactions at the SPS," *Physics Letters B* **499** no. 1, (2001) 85 – 96.

[233] **PHENIX** Collaboration, A. Adare et al., "J/ψ Production in $\sqrt{s_{\mathrm{NN}}} = 200$ GeV Cu+Cu Collisions," *Phys. Rev. Lett.* **101** (2008) 122301, arXiv:0801.0220 [nucl-ex].

[234] **PHENIX** Collaboration, A. Adare et al., "J/ψ Production vs Centrality, Transverse Momentum, and Rapidity in Au+Au Collisions at $\sqrt{s_{NN}} = 200$ GeV," *Phys. Rev. Lett.* **98** (2007) 232301, arXiv:nucl-ex/0611020 [nucl-ex].

[235] **ALICE** Collaboration, B. Abelev et al., "Upgrade of the ALICE Experiment: Letter Of Intent," *Journal of Physics G: Nuclear and Particle Physics* **41** no. 8, (2014) 087001.

[236] **ALICE** Collaboration, F. Bellini, "Testing the system size dependence of hydrodynamical expansion and thermal particle production with π, K, p, and ϕ in Xe-Xe and Pb-Pb collisions with ALICE," in *27th International Conference on Ultrarelativistic Nucleus-Nucleus Collisions (Quark Matter 2018) Venice, Italy, May 14-19, 2018*. 2018. arXiv:1808.05823 [nucl-ex].

[237] M. Puccio, *Study of the production of nuclei and anti-nuclei at the LHC with the ALICE experiment*. Doctoral thesis, Università degli studi di Torino, 2017.

[238] **PHENIX** Collaboration, A. Adare et al., "J/ψ production versus transverse momentum and rapidity in p^+p collisions at $\sqrt{s}$ = 200-GeV," *Phys. Rev. Lett.* **98** (2007) 232002, arXiv:hep-ex/0611020 [hep-ex].

[239] M. Tarhini, *Measurement of Z-boson and J/ψ Production in p–Pb and Pb–Pb Collisions at $\sqrt{s_{\mathrm{NN}}}$ = 5.02 TeV with ALICE at the LHC*. Doctoral thesis, Université Paris-Saclay, 2018.

[240] M. Tarhini, "Charmonium production in Pb–Pb and p–Pb collisions at forward rapidity measured with ALICE," *Nuclear Physics A* **967** (2017) 588 – 591. The 26th International Conference on Ultra-relativistic Nucleus-Nucleus Collisions: Quark Matter 2017.

[241] B. Z. Kopeliovich et al., "J/ψ in high-multiplicity pp collisions: Lessons from pA collisions," *Phys. Rev. D* **88** no. 11, (2013) 116002, arXiv:1308.3638 [hep-ph].

[242] J. Klein, *Jet Physics with A Large Ion Collider Experiment at the Large Hadron Collider*. Doctoral thesis, Universität Heidelberg, 2014.

[243] J. Mercado Pérez, *Development of the control system of the ALICE Transition Radiation Detector and of a test environment for quality-assurance of its front-end electronics*. Doctoral thesis, Universität Heidelberg, 2008.

[244] U. Westerhoff, *The FEE Server Control Engine of the ALICE-TRD*. Diploma thesis, Universität Münster, 2009.

Acknowledgements

First of all I would like to thank Prof. Dr. Johanna Stachel for the opportunity to pursue a PhD project in her group. It was a great pleasure to work in this fruitful environment on all these interesting topics. Also, I am very grateful for the support of my supervisor Prof. Dr. Klaus Reygers who always had an open door and with whom I had a lot of useful and motivating discussions. I would also like to thank Prof. Dr. Tilman Plehn for acting as a co-advisor and for the rich discussions in our regular meetings. Also, I would like to thank Prof. Dr. Norbert Herrmann for the willingness to act as a referee for this thesis.
Many thanks goes to the ALICE group in Heidelberg for creating such a nice and prolific working environment and for all the cake at various occasions.
For all the support and the creation of a motivating working environment for TRD related topics I would like to thank Dr. Jochen Klein, Dr. Jorge Mercado, Dr. Leticia Cunqueiro, Dr. Hans Beck and Sebastian Klewin.
I would like to thank the ALICE analysis group $J/\psi \rightarrow e^+e^-$ for the productive working environment and for all the productive discussions. I wish to thank Dr. Michael Winn for introducing me to the topic of J/ψ production and for all the answered questions. I owe my gratitude to Dr. Ionut Arsene for introducing me to the reducedTree framework and for a lot of support on analysis related topics.
I wish to thank Dr. Hans Beck, Sebastian Klewin and Ole Schmidt for the support with our computing farm and the fast problem solving.
For proof reading of this thesis I would like to thank Dr. Hans Beck, Dr. Alexander Schmah and Dr. Markus K. Köhler.
Last but not least I would like to thank my wonderful girlfriend and my friends in Heidelberg. The last years would not have been that great without you!

Deposition

Erklärung:

Ich versichere, dass ich diese Arbeit selbstständig verfasst habe und keine anderen als die angegebenen Quellen und Hilfsmittel benutzt habe.

Heidelberg, den 26.11.2018 .....